JOURNAL OF THE AERONAUTICAL SCIENCES

VOLUME 10 OCTOBER, 1943 NUMBER 8

# Experimental Investigations in Aircraft Dynamics

WILLIAM B. BERGEN*

*The Glenn L. Martin Company*

ABSTRACT

This paper represents a report on some of the vibration studies that have been made at The Glenn L. Martin Company. It is divided into three sections in which vibrations emanating from the power plant, flutter, and dynamic loads are discussed. With the exception of power-plant vibrations, where methods of design control are treated from an analytic point of view, the main body of the paper is concerned with experimental vibration studies involving both wind-tunnel and flight tests.

The development of electrical vibration recording equipment especially designed to meet the rigid requirements of aircraft flutter testing is described in the light of tests first conducted in 1937 on an early Martin Clipper and continued on other models, including the large Navy flying boat, Mars. One particular feature of these tests is the use of a mechanical vibrator that is remotely controlled to produce artificial excitation in flight.

The third phase of the paper is concerned with measurements made to determine dynamic loads encountered by aircraft structures under service conditions. It is shown, for example, that dynamic loads whose magnitudes exceed present static requirements are encountered on nose-wheel struts. In conclusion, the paper discusses the preliminary results of a program, conducted in cooperation with the Bureau of Aeronautics, to measure the landing and take-off accelerations encountered by flying boat hulls.

## INTRODUCTION

VIBRATION HAS only recently been recognized as one of the major problems confronting the aircraft designer. Actually, the problem is as old as the industry itself, but in the early days of flying, problems of stability, power plant, and primary strength were of such importance that vibration was accepted as a necessary evil. To be sure failures were common, but it was not until the other phases of design were well under control that vibration problems began to be perceived in their true perspective. The destructive nature of vibratory forces was first apparent in power-plant design. As early as 1925 many authorities believed further improvement of the radial engine was limited by vibration considerations and the development of the metal propeller was seriously retarded by a lack of knowledge of propeller vibratory stresses. Today, the airplane itself has reached a similar stage, where vibration problems must be solved if the present rate of development is to be maintained.

Aircraft vibration embraces the broad field of structural dynamics, but the problems can be generally classified under three main categories. The first group comprises those vibrations that originate in the power plant. Although not normally dangerous, they may excite components of the airplane structure, resulting in noisy and uncomfortable aircraft and, in many cases, causing fatigue failures. The second group consists of instability phenomena that are aerodynamically excited, such as flutter, wing divergence, and aileron reversal. All these are important, but particular emphasis is placed on flutter because of its vicious nature and its disastrous consequences. The third group includes the problems that are associated with the behavior of elastic structures under dynamic loads. Two examples of this group, which will be treated later in some detail, are the accelerations encountered by flying boats during take-offs and landing maneuvers and the dynamic loads imposed on landing-gear struts.

## POWER-PLANT VIBRATION

In dealing with the power plant, the object of the aircraft designer is to prevent either the engine unbalanced forces from reaching vital components or to design these components in such a manner that the impressed engine vibratory forces are minimized. A complete analysis of the vibration problems involved in the power plant is beyond the scope of this article, but, as the basic principles have such extensive ap-

Presented at the Structures Session, Eleventh Annual Meeting, I.A.S., New York, January 25–29, 1943.

* Vibration Engineer.

plications in almost all phases of aircraft design, they will be discussed briefly. Four general methods of attacking vibrations that originate from the power plant are:

(1) Removal of sources of excitation.
(2) Control of natural frequency of excited member.
(3) Introduction of friction or viscous damping.
(4) Installation of dynamic damper.

Method (1), while obviously the most effective, is seldom possible, and the present trend toward increased power-plant output has increased the attendant difficulties. The sources of excitation may be controlled to some extent in the design of the power plant itself—for example, the arrangement of cylinders, the choice of the engine-propeller gear ratio, and the incorporation of dynamic dampers. But, as the power plant is an inherently unbalanced machine, certain exciting forces will always be present. These forces are not simple harmonic but consist of a number of simple harmonic forces acting simultaneously.

In view of these conditions the most effective method of vibration improvement at the designer's disposal is the control of the natural frequencies of the excited members. The efficiency of vibration isolation is expressed as the "transmissibility" of a supported unit. Transmissibility[1] is defined as the ratio of the transmitted force to the impressed force and its significance is graphically illustrated in Fig. 1 as a function of the

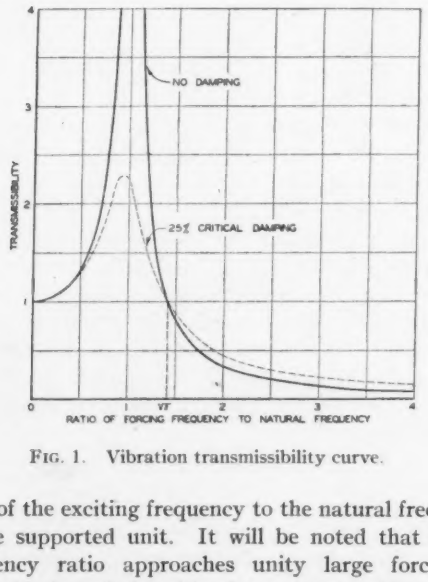


FIG. 1. Vibration transmissibility curve.

ratio of the exciting frequency to the natural frequency of the supported unit. It will be noted that as the frequency ratio approaches unity large forces (or amplitudes) are induced in the supported object. The actual magnitudes of these forces will depend on the damping in the system, but it is apparent that maximum vibration isolation is obtained when the natural frequency of the excited system is placed well below the frequency of the exciting force.

***Frequencies of Exciting Forces***

The frequencies of the exciting forces emanating from the power plant are a direct function of the engine speed and may be represented as a spectrum in which the engine r.p.m. is plotted against the various forcing frequencies. A typical engine spectrum of this type, showing some of the engine orders that are important to the aircraft engineer, is shown in Fig. 2. This

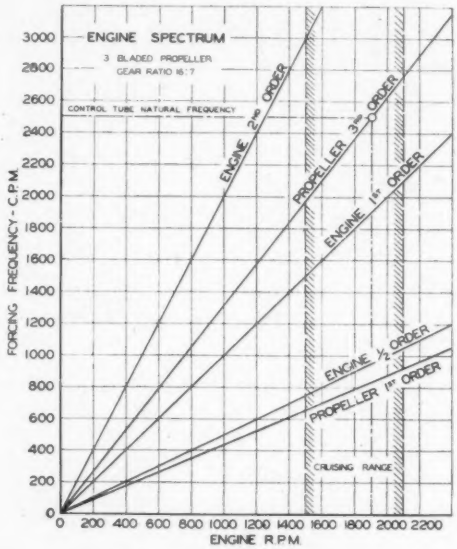


FIG. 2. Engine frequency spectrum.

spectrum indicates that at an engine r.p.m. of 1,800, for example, forcing impulses of 900 (one-half order), 788 (propeller first order), 1,800 (engine first order), and 3,600 (engine second order) are generated. The spectrum is used to determine which frequency ranges must be avoided and which frequency ranges will result in maximum vibration isolation. The control tube with a natural frequency of 2,500 cycles per min. as plotted on the spectrum cannot be considered satisfactory, since it will be excited by the propeller third order impulses at the engine cruising speed of 1,900 r.p.m. From an examination of Figs. 1 and 2 it can be seen that maximum vibration isolation is obtained when the natural frequency of any unit is kept below 700 cycles per min., and this is exactly what is done with instrument panels, delicate accessories, and the power plant itself. Where rigidity requirements preclude low frequencies, as in the case of throttle control tubes, a higher range that is free from engine excitation must be chosen. For many engine-propeller combinations there is no clear region, and in this case an arbitrary lower frequency limit is set. For all types of control tubes, a lower limit of 4,000 cycles per min. has been found to work very well, but in the attachment of accessories directly to the engine a lower limit of 10,000 cycles per min. has often been found necessary.

### *Damping*

The introduction of friction or viscous damping is generally not satisfactory and should be accomplished only as a last resort. Under certain conditions where a high-frequency ratio exists, damping may actually be harmful. This can be seen from Fig. 1 where, above a frequency ratio of $\sqrt{2}$, the presence of damping increases the transmissibility. On the other hand, the dynamic damper may often be used with good results. The dynamic damper usually consists of an elastically suspended mass whose natural frequency is chosen to correspond to that of the disturbing frequency. An interesting example in which excessive amplitudes of a flying-boat float were eliminated by a dynamic damper is illustrated in Fig. 3. The damper consisted of a

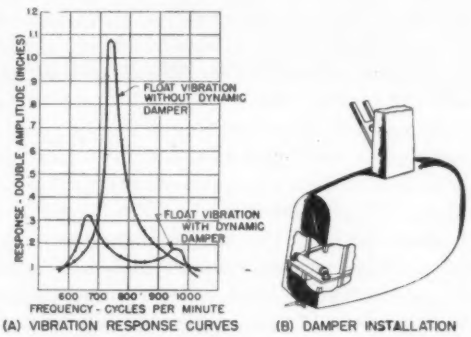
RESPONSE - DOUBLE AMPLITUDE (INCHES)
FLOAT VIBRATION WITHOUT DYNAMIC DAMPER
FLOAT VIBRATION WITH DYNAMIC DAMPER
600 700 800 900 1000
FREQUENCY - CYCLES PER MINUTE
(A) VIBRATION RESPONSE CURVES
(B) DAMPER INSTALLATION

FIG. 3. Effect of dynamic damper installation on float vibration.

spring-mounted mass, tuned to the torsional frequency of the float strut as shown in Fig. 3 (B). The damper mass was damped by hydraulic fluid contained in the cylinder. The effect of this installation was to transform the large single resonance peak into two highly damped peaks of the coupled system as shown in Fig. 3 (A), thus effectively diminishing the float amplitudes.

Experience has shown that the greatest problem in connection with isolating power-plant vibration is one of design control. Designs that have been analyzed from a vibration point of view have given little trouble, and the majority of annoying vibration troubles that do arise in service can be foreseen if proper control is exercised in the design stage. To accomplish this, it is now standard practice to assign experienced vibration personnel to each project. Rigid vibration criteria for the design of control tubes, hydraulic lines, electrical equipment, and accessories have been established and shock mounts are carefully designed for all delicate instruments and control equipment.

## FLUTTER

The importance of flutter was recognized early by the Martin company in conjunction with its development of large ocean transports. Although several cases of flutter were encountered in World War I, the fundamental concepts of aerodynamic oscillatory flow were not generally understood, and progress in the theoretic solution of the flutter problem was slow. In 1935 the N.A.C.A. published an excellent report[2] on the mechanism of flutter in which the expressions for the aerodynamic forces and moments acting on an oscillating two-dimensional wing were derived. With this theoretic background it was possible, by making rough estimates of the fundamental flutter parameters and neglecting parameters of secondary importance, to obtain a fair estimate of the critical speed. Unlike power-plant excitation, there was no direct theoretic solution to the flutter problem, and engineering progress has been dependent largely upon experimental research.

### *Experimental Studies*

Although the theoretic aspects of the flutter problem have by no means been neglected, the experimental studies involving ground vibration tests, flight tests, and wind-tunnel tests have proved to be the most interesting. When these studies were begun by the Martin company in 1936, two difficult problems were faced. First, the catastrophic nature and complexity of flutter precluded the use of the normal engineering procedure of "cut and try" and dictated the necessity for obtaining reliable data in a scientific manner. Second, the instruments that would satisfy the rigid requirements of aircraft flutter testing were not available. It was only natural, therefore, that the program should consist of a cooperative research in which flutter-testing technique and flutter-testing instruments were developed simultaneously.

Initial research was concerned with the development of vibration measuring equipment which had to have specialized characteristics in order to make it suitable for aircraft flutter measurements. First of all it was necessary to design a vibration pickup unit that was sufficiently small to be located in remote parts of the aircraft and yet was sufficiently sensitive to respond to the small magnitude accelerations associated with flutter measurements. Second, it was necessary to design auxiliary equipment that was capable of amplifying and recording these pickup responses without itself introducing any extraneous errors. Because of the nature of flight testing, the equipment had to maintain its calibration over long periods of time and through wide ranges of pressure and temperature variations. It had to be sufficiently rugged to withstand abnormal operating accelerations encountered in test flying and, above all, the equipment had to be light and compact.

### *Instrumentation*

The instrumentation question has been attacked from many angles and, as in several related problems, the aircraft industry has borrowed heavily from the field

of electronics. In 1934 a joint instrument-development program between the Bureau of Aeronautics of the U.S. Navy and the Massachusetts Institute of Technology resulted in electrical equipment[3] suitable for the quantitative study of engine vibrations. This equipment demonstrated the advantages of electrical vibration-recording devices and resulted in many improvements in power-plant design. However, the M.I.T. equipment, being designed to measure vibrations at frequencies above 15 cycles per sec., was not well suited to the low-frequency vibrations encountered in aircraft structural components. The range of pertinent frequencies in this field extends from nearly 0 cycles per sec., which would be encountered, for example, in a pull-out maneuver, to approximately 75 cycles per sec. as an upper limit. In general, the motions of low frequencies and high amplitudes are the most important.

With this in mind it was decided that an electrical type pickup designed to operate as an accelerometer, in which the displacement of a spring supported element relative to the frame of the pickup is proportional to the acceleration imposed on the pickup as a unit, offered the best possibilities. The first accelerometer developed consisted of two tandem carbon stacks supported in a flexible frame. Accelerations imposed on the pickup varied the resistances of the stacks, which were connected as two active arms of an electrical bridge. The bridge output was amplified by a d.c. amplifier and fed to a cathode ray oscillograph. This equipment, shown in Fig. 4, was first used in 1937 to determine the flight flutter characteristics of the Martin Model 156, more commonly known as the Russian Clipper.

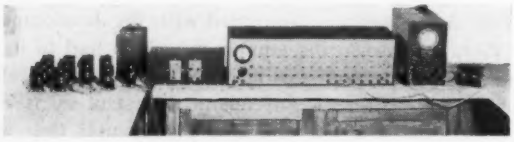

FIG. 4. Early Martin vibration measuring equipment.

### *Test Methods*

In making these tests, two modifications of the flutter test method introduced in Germany by von Schlippe[4] were used in conjunction with the electrical equipment. The basic principle of the method is simple and has been likened by von Schlippe to the flexural failure of a compressed member. If an axial compressive load, applied eccentrically to the member, is successively increased, the deflection is first proportional to the load, then increases more rapidly until quite severe. By plotting the load-deflection curve for the member, as shown in Fig. 5, it is possible to determine the buckling load of a thin bar without breaking it. In a similar manner, the flutter speed of an airplane can be determined by setting the airfoil surfaces into oscillation in flight and then plotting their amplitudes as a function of the air speed to determine the critical velocity.

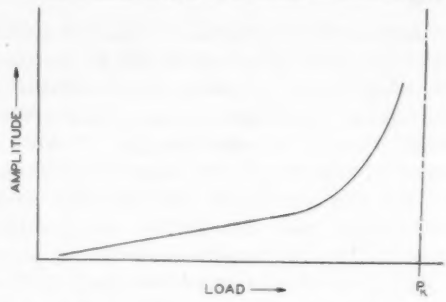


FIG. 5. Load-deflection curve of an eccentrically compressed bar.

Results of a test conducted on a Junkers Ju 86 airplane to determine the critical speed of a rudder-fuselage flutter coupling are shown in Fig. 6.

The first method used on the Model 156 tests in 1937 consisted of plotting the average and transient amplitudes of a surface as a function of the air speed. In this case gusts were used as the source of excitation. In the second method, a refinement of the first, a known initial static displacement was given to the surface by a mechanical device. The surface was then released quickly and the transient motion recorded. The equipment and technique employed for these tests seem crude in the light of present developments, but it was possible to predict and correct a flutter condition involving the rudder before any danger to the airplane became imminent.

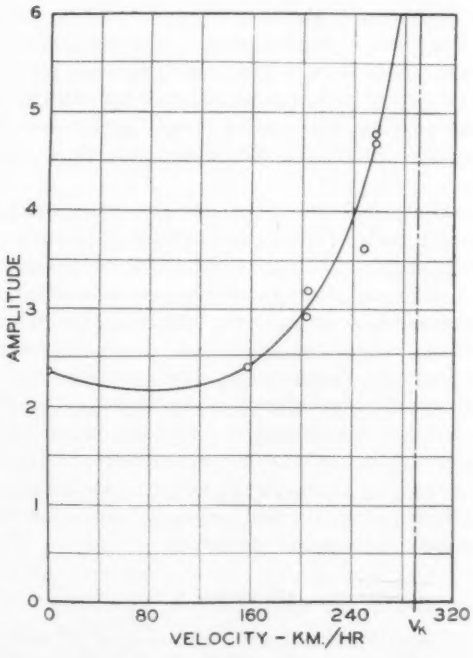


FIG. 6. Results of flight oscillations test on a Junkers Ju 86 airplane.

As a result of these flight tests the original carbon stack pickup, which was found to have many inherent faults, was replaced with an induction type accelerometer. Extensive changes were made in the amplifying equipment, the most important being the incorporation of a "carrier signal" that resulted in greatly increased sensitivity throughout the entire frequency range. This modified equipment, as used for testing the Model XPBM-1 airplane, is shown in Fig. 7.

FIG. 7. Installation of vibration equipment in the Model XPBM-1 airplane.

### *The Mechanical Vibrator*

The XPBM-1 tests were particularly interesting since a mechanical vibrator was used for the first time in this country as the source of excitation in flight. The advantages of a mechanical vibrator were recognized prior to the 1937 tests on the Model 156, but the crash of a Junkers airplane in Germany while undergoing flight flutter tests aroused considerable doubt as to the safety of the method. For this reason a vibrator was not used for the earlier tests. However, subsequent theoretic forced frequency studies not only vindicated the vibrator but also disclosed additional variables that could serve as "flutter indicators." Accordingly, a vibrator was installed on the leading edge of the XPBM-1 wing at 75 per cent of the semispan. The large rheostats shown in Fig. 7 were used to control the vibrator speed through variation of the motor armature resistance. The test procedure consisted of measuring wing amplitudes, frequencies, and vibrator power inputs as functions of airspeed. The amplitude and power input data were used to calculate the wing damping, the change in which indicated any approach to a flutter condition. The data obtained during these tests demonstrated both the safety of the airplane and the value of the vibrator in obtaining flutter information.

The tests could not be called completely successful from a quantitative point of view, however, for the following reasons:

(a) The method of varying the armature resistance resulted in poor control characteristics of the vibrator. The vibrator speeds could not be held constant near resonant frequencies, and thus it was difficult to plot accurately the all-important resonant peaks.

(b) Friction losses in the vibrator exceeded the power required to vibrate the wing. This made wing damping measurements unreliable.

(c) The large temperature differences caused by dives from high altitudes resulted in wide variations in pickup response.

(d) The sensitivities of the electrical components were not sufficiently independent of battery voltage variations, mechanical vibrations, and numerous small but important sources of "hash."

Finally, it was concluded that, although a visual oscilloscope offered an excellent means of immediately evaluating the test data, simultaneous recording of all data in permanent form, together with the visual features, was to be preferred.

### *Measuring Equipment Improvement*

The experience gained during these early flutter tests was largely responsible for many refinements in the equipment. Improvements in the pickup design, for example, have resulted in a linear response to accelerations ranging from 0 to ±20 times gravity at frequencies from 0 to 5,000 cycles per min. The weight of the pickups has been reduced from 16 to 2 oz. and, at the same time, the sensitivity increased. The amplifier design has been revised to incorporate extensive shielding and automatic voltage regulation, and particular attention has been given to stability of operation under extreme conditions of mechanical shock and fluctuations of battery power supply. From a practical testing point of view, light weight and compactness have been found to be important factors. A complete set of twelve amplifiers, together with the power supply, weighs 100 lbs., and some idea of the relative size of the equipment may be gained from Fig. 8, which shows a set of equipment in its present form. This equipment has demonstrated its practicability during extensive service operation, not only on flutter tests but on many varied researches, some of which will be discussed in the latter part of the paper.

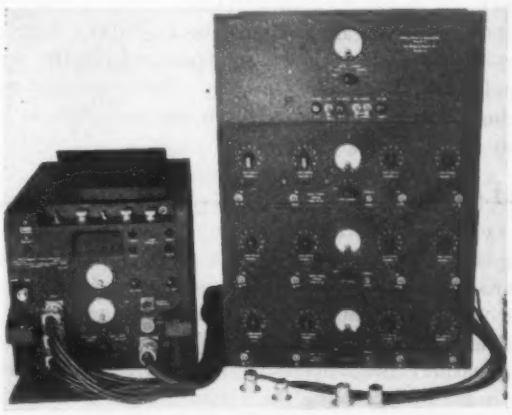

FIG. 8. Latest vibration equipment, developed by The Glenn L. Martin Company, with recording oscillograph.

The latest flutter test, which was an extension of the earlier tests conducted on the Russian Clipper and the Model XPBM-1 airplanes, has recently been completed on the Navy flying boat Mars. Excepting the improvements in the measuring equipment and in the vibrator control circuit, the experimental setup for making the test was essentially the same as that used on the Model XPBM-1 airplane. The vibrator installation in the leading edge of the wing at 75 per cent of the semispan is shown in Fig. 9. The vibrator consisted of two opposite-rotating weights driven by a special 1-hp. d.c. electric motor. The unbalance of the vibrator was adjustable, but 40 in.lbs. of unbalance was used throughout the tests. The vibrator was provided with an electric tachometer generator to give a visual indication of the vibrator r.p.m. The difficulties encountered with the vibrator speed control on the earlier test were eliminated by incorporating a special type motor generator in the vibrator circuit. This resulted in excellent frequency control at all vibrator speeds. Pickups, as shown in Fig. 8, were mounted along the front and rear spars of both wings.

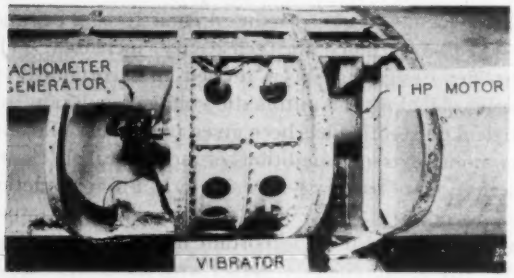


FIG. 9. Installation of vibrator in the wing.

### *Test Procedure*

The test procedure consisted of varying the vibrator r.p.m. from 0 to 1,100 cycles per min. while the air speed was held constant. This procedure was repeated in uniform speed increments from 42.5 up to 75 per cent of the design dive speed of the airplane. While the pickup responses for each frequency survey were recorded, a visual check was maintained on the wing amplitudes throughout the tests. Using this test procedure, it was possible to obtain complete data in less than 30 min. flying time.

### *Test Results*

Typical results of the flight test are illustrated in Fig. 10. Response curves for a pickup located on the rear spar at approximately 75 per cent of the semispan are plotted for three of the air speeds tested. The resonance peaks are characteristic and correspond to the natural frequencies of the wing-aileron system. In order to determine the actual-deflection shapes of these modes, cross plots of the pickups have been made and these results are also shown in Fig. 10. Because of

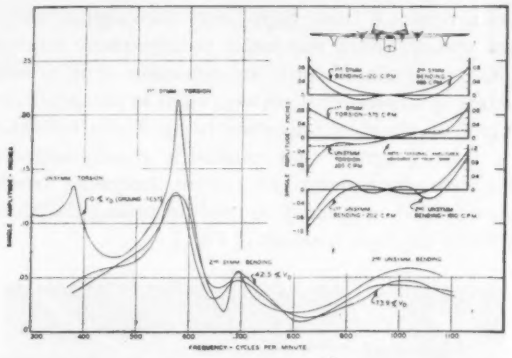

FIG. 10. Response of wing to forced vibration in flight, showing deflection curves.

the low frequencies involved, the shapes of the first symmetric and the first unsymmetric bending modes were determined from ground-test results. The shapes of the other modes were determined from flight results. These plots identify the shapes of the modes quite accurately but are not too reliable in the regions of low response near the nodes. For example, it would be expected that the first symmetric bending frequency exhibit a node on either side of the ship centerline ininstead of the apparent single node at the centerline as shown in Fig. 10.

The unsymmetric torsional frequency that occurs at 385 cycles per min. is of particular interest as this mode may lead to a low calculated flutter speed if the calculations are based on conventional two-dimensional flutter theory. Acutally, the mode is not pure torsion but is strongly coupled both with the pitching and translational frequencies of the power plant and the first unsymmetric bending frequency of the wing that occurs at 202 cycles per min. This mode was first detected in connection with an earlier airplane, and a flutter model, which will be described later, was constructed to check the existence of the low flutter speed.

The wind-tunnel tests did not disclose the suspected low flutter speed, and the present flight results, which show that this mode is heavily damped in flight, substantiate these results.

The most predominant peak is that of the symmetric wing torsion mode that occurs at 570 cycles per min. Its characteristics, as a function of air speed, are plotted in Fig. 11. In this figure it will be noted that the maximum amplitude as measured on the rear spar occurs at zero air speed. Between 0 and 42.5 per cent of the design dive speed there is a rather sharp decrease in amplitude, but beyond this speed the amplitude remains virtually constant up to the maximum speed tested.

Another method of presenting the flutter characteristics of the torsion mode consists in plotting the damping coefficients as a function of air speed. In this case, the damping coefficients are computed from

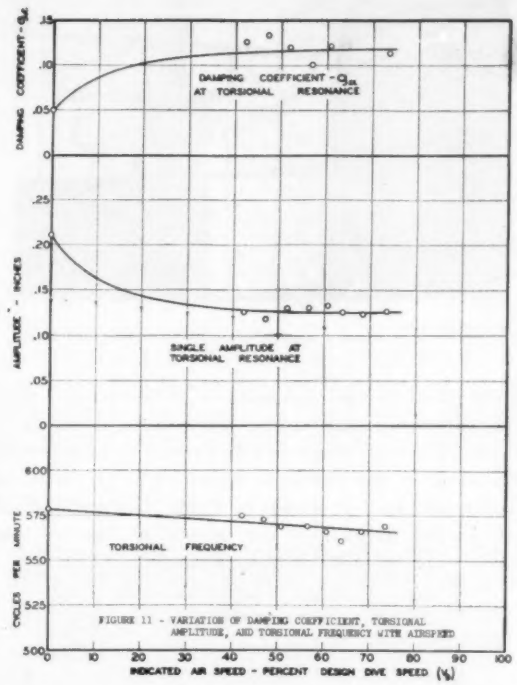
DAMPING COEFFICIENT - $Q_{ss}$
AT TORSIONAL RESONANCE
SINGLE AMPLITUDE AT TORSIONAL RESONANCE
TORSIONAL FREQUENCY
INDICATED AIR SPEED - PERCENT DESIGN DIVE SPEED (%)

FIGURE 11 - VARIATION OF DAMPING COEFFICIENT, TORSIONAL AMPLITUDE, AND TORSIONAL FREQUENCY WITH AIRSPEED

FIG. 11. Variation of damping coefficient, torsional amplitude, and torsional frequency with air speed.

the test curves of Fig. 10, in accordance with the formula:

$$g = \Delta N/N$$

where $\Delta N$ is the width of the resonance curve measured at 0.707 of its maximum height and $N$ is the resonant frequency. As the flutter speed is approached, the damping coefficient decreases, becoming zero at the critical velocity. It will be noted that the damping curve plotted in Fig. 11 is almost a mirrored image of the amplitude curve as would be expected. Since the coefficient calculations are quite sensitive to the width of the resonance peak, the experimental error is greater than that of the amplitude curve. The plot of torsional resonance versus air speed shows that there is a slight tendency for the torsional frequency to decrease. With regard to the higher order modes, it is again apparent that there is no tendency toward dangerously increasing amplitudes.

The immediate object of any flight flutter test is to prove the safety of the airplane. While the present tests have shown no increasing amplitudes, the question often arises as to whether, if a critical speed does exist, the amplitudes will increase so rapidly that insufficient warning is given. Present experience, which is based on both wind-tunnel and flight experience, has indicated that, at least for a two-degree coupling involving a control surface, the increase in amplitude with speed is sufficiently gradual to give advance warning. Little data is available, however, on the characteristics of a flexure-torsion coupling, and this subject is an important one for further research.

### *Evaluating Flutter Characteristics*

Perhaps of even more importance than the immediate object of the flutter test is the application of the experimental data in evaluating the flutter characteristics of new designs. It is generally conceded that as the size and speed of aircraft are increased, it will become necessary to fly airplanes much closer to critical flutter speeds than is now thought safe. This will require more accurate flutter analyses involving higher order modes and three-dimensional considerations. The mathematical background for making these analyses, of which papers recently published by Bleakney[5] and Loring[6] are good examples, has been established. Hence, the next important step is to supplement the theoretic results with actual experimental data obtained from flight flutter tests.

The tests are being continued not only in flight but in the wind tunnel where data may be obtained up to and even beyond the flutter speed. The field is so extensive that much still remains to be learned, but it is felt that the vibration equipment, together with the testing technique, now constitutes a practical tool for flight flutter research.

## WIND-TUNNEL FLUTTER TESTS

While the final demonstration of flutter characteristics is dependent on full-scale flights, valuable data can be obtained from wind-tunnel tests of flutter models. These provide an excellent means for checking flutter theory experimentally. From an engineering point of view, the advantages of wind-tunnel tests on a flutter model, while the prototype airplane is still in the design stage, are apparent.

## WING-FLUTTER MODEL

The first flutter model studies conducted by the Martin company were made in conjunction with the design of the Model XPBM-1 airplane. This twin-engined patrol bomber employed a high aspect ratio, cantilever wing with severe spanwise mass, and structural discontinuities. Large float retraction cutouts in the outer panels and the use of two-spar construction, in which shear stresses were carried by flat sheet, resulted in a torsionally flexible wing. Flutter calculations indicated that the lowest critical speed was 60 per cent higher than the design dive speed of the airplane, but it was felt that an experimental check of the flutter speed was advisable because of the many assumptions made in the theoretic analysis. In addition, it was desired to investigate the possible existence of the flutter coupling involving the inner panel torsion of the wing, engine translation, and wing bending, as discussed in the previous section.

### Dynamic and Geometric Similarity

In order to obtain a direct correlation between the speeds obtained in the wind tunnel and the speeds of the full-scale airplane, a model must satisfy the requirements of dynamic and geometric similarity.[7] In terms of the flutter parameters this means that the reduced frequency $k$, mass ratio $\kappa$, and location of elastic, gravity, and hinge axes, and mass radii of gyration, expressed nondimensionally, must have the same respective values. It can be shown that, if these conditions are met and if complete geometric similarity is maintained, the flutter speed of the model will be exactly the same as the flutter speed of the full-scale airplane. For the case at hand, this was not a satisfactory situation. First, the possible flutter speeds were above the speed range of any available tunnel and, second, it was not practical to scale geometrically the aluminum-alloy skin gauges. After considerable investigation it was found that the use of pyralin (cellulose nitrate) would permit low speeds with practical material thicknesses. The low modulus-density ratio ($E/\rho$) of pyralin resulted in a model to full-scale speed ratio of 1:4.3. The model was built to a geometric scale ratio of 7.87 and is shown in Fig. 12. The bomb and fuel loads were represented by attaching lead weights to the ribs, and the engines were simulated by rubber-mounted steel masses having vibrational characteristics similar to those of the full-scale engines. The fuselage and tail surfaces consisted of dummy structures whose weights and moments of inertia were similar to those of the prototype. The total weight of the model was 80 lbs.

Fig. 12. Pyralin wing-flutter model.

The model, mounted in the tunnel as shown in Fig. 13, permitted limited freedom in roll, pitch, and vertical motion. The aerodynamic angle of attack was varied by adjusting a turnbuckle in series with the pitching restraint wire attached to the nose of the model. As the electrical vibration equipment was not available at this date, bending and torsional deflections were measured by observing the movement on the test chamber floor of a spot of light reflected from a small

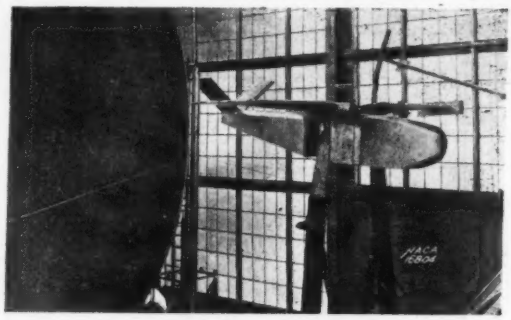

Fig. 13. Flutter model mounted in wind tunnel.

mirror glued to the undersurface of the wing. Static deflection and vibration tests were made on the model to check the conformance of its dynamic characteristics with those of the full-scale wing. The excellent correlation obtained is shown in Table 1, where the full-scale model frequencies for several modes are compared. The theoretic frequency ratio was 0.545.

Table 1

| Mode | Natural Frequency, Cycles per Min. — Airplane | Model | Ratio |
|---|---|---|---|
| Low torsion—engine predominant | 377 | 695 | 0.542 |
| Second bending (float retracted) | 495 | 895 | 0.553 |
| High torsion—outer panel predominant | 697 | 1,315 | 0.530 |
| Wing tip torsion | 982 | 1,765 | 0.556 |

#### *Duplicating Free Flight Conditions*

Although good correlation was obtained between the full-scale and model dynamic characteristics, duplicating free flight conditions in the wind tunnel proved to be difficult. The location of the model supports was chosen to coincide with the theoretic full-scale nodal locations, and the model was provided limited freedom to simulate free flight conditions. It was found that the irregularities in the tunnel slipstream caused such violent motions of the model on its supports that it became necessary to clamp the left wing as shown in Fig. 13. This problem is particularly acute in dynamic flutter models because of their relative lightness, and the only answer appears to be in taking special precautions to obtain smooth airflow. Another difficulty encountered was caused by the abnormal bending deflections of the wing. A possible explanation for these deflections is that the restraint of the model supports permitted the wing lift forces to build up and to exceed by many times the normal load factor for which the wing was designed. An attempt was made to reduce the wing lift force by initially setting the wing at an aerodynamic angle of attack of zero, but even under this condition it was found that the wing tip twist under aerodynamic loading was sufficient to build up

loads that greatly exceeded those of the equivalent normal air-borne condition. The magnitude of the bending deflections is shown in Fig. 14, which was made at 70 m.p.h.

In spite of these difficulties, it was demonstrated that the prototype airplane had a high flutter speed. Final structural failure of the model occurred at 96 m.p.h. when the rear spar buckled. As this speed corresponded to a full-scale speed of over 400 m.p.h., it was evident that a wide margin existed between the design diving speed of the prototype airplane and the lowest speed at which flutter could be anticipated.

While these tests were hampered by the difficulties described above, the important fact of the safety of the prototype airplane was fully established. In the case of unconventional airplanes, whose flutter characteristics are shown to be marginal by theoretic calculations, the test of a flutter model may well prove or disprove the integrity of the design.

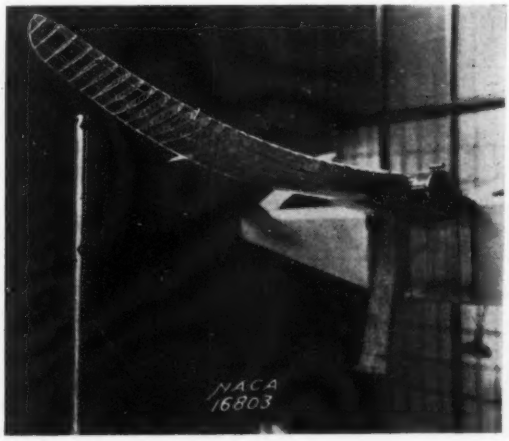


FIG. 14. Bending deflection of flutter model.

## TAIL-FLUTTER MODEL

Unlike the pyralin model, which was tested to verify the lowest critical speed of a particular prototype design, the second series of flutter model tests were undertaken to check the general application of the flutter theory to tail surfaces. Theodorsen and Garrick[8] had already performed a large number of tests and shown that good agreements existed for cantilever wing sections within the limits of error in the determination of the primary parameters. However, practically no experimental data were available on the application of theory to tail flutter, even though the majority of reported flutter cases had involved tail surfaces.

Accordingly, in 1940 a wind-tunnel investigation was initiated, in cooperation with the Bureau of Aeronautics of the United States Navy, to make a generalized study of the tail-flutter problem. For this study, a balsa wood model was constructed in such a manner that practically all of the major flutter parameters could be adjusted and a wide range of design variables tested. The model itself, Fig. 15, consisted of a fuselage section fitted with conventional stabilizer, fin, and control surfaces. The fuselage was mounted at its forward nodal point to pivot in roll, pitch, and yaw. The frequencies of these modes were controlled by external springs. A "cutaway" sketch, illustrating details of the elevator construction, is shown in Fig. 16. This design permitted a variation of the aerodynamic balance of the elevators from a hinge position of 7 per cent of the elevator chord to 31 per cent of the chord and a wide variation of mass balance.

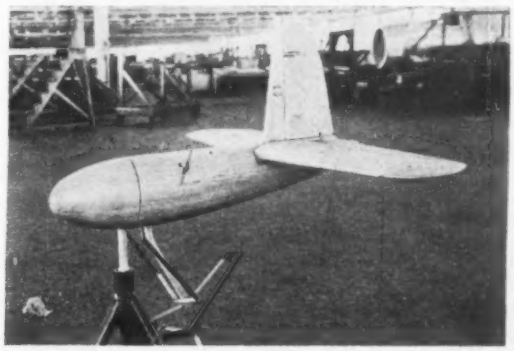

FIG. 15. Tail-flutter model.

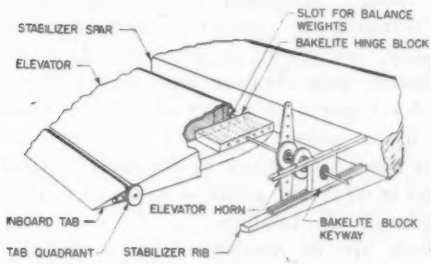


FIG. 16. Details of tail-flutter model elevator construction.

### *Obtaining Dynamic Data*

In order to obtain the pertinent dynamic data, which included frequencies, phase angles, and damping coefficients, small inductor-type accelerometers were installed on the model. These pickups, weighing less than $\frac{1}{2}$ oz., could be mounted within the fuselage, stabilizer, and control surfaces of the model without introducing any appreciable errors. One of the pickups is shown installed in the vertical fin of the model in Fig. 15. These pickups were used in conjunction with the vibration measuring equipment and their responses recorded on a twelve-element oscillograph. Several representative test records are shown in Fig. 17. The use of the vibration recording equipment proved to be successful, since it not only provided accurate test data but also enabled over 1,000 separate flutter tests to be made within a six-week period.

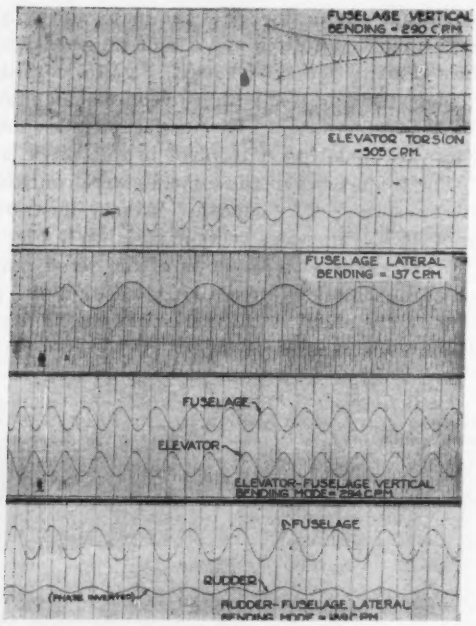


FIG. 17. Representative records of tail-flutter model test

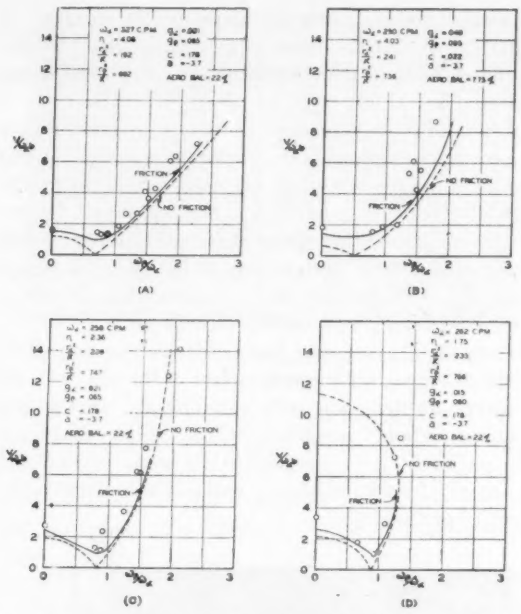


FIG. 18. Experimental and theoretic results of elevator-fuselage vertical bending coupling.

### *Plotting Test Results*

In general, the test results were plotted in terms of the nondimensional flutter speed versus the "control surface-fuselage" frequency ratio. Typical test results, illustrating the correlation between experiment and theory, are shown in Fig. 18. The theoretic flutter speeds were obtained from flutter charts that were a development of similar wing-flutter charts described in an earlier paper.[9] A discussion of these charts is beyond the scope of the present paper, but the forms in which the physical constants of the model were reduced are tabulated in Table 2. As these parameters are in nondimensional form, they are equally applicable to full-scale airplanes.

It will be noted that good agreement was obtained in practically every case. Of particular interest is the effect of friction in raising the theoretic minimum speed from zero to a value approaching the test results. The flutter curves exhibit the characteristic loop enclosing an unstable region, which is typical of wing-aileron binary flutter. For the case of tail flutter the limiting frequency ratio may be much higher and flutter was obtained with frequency ratios as high as 2.5.

These results also indicate that if the frequency ratio exceeds a well-defined value the control surface has a high flutter speed, and mass balance is of secondary importance. If the frequency ratio is less than this value, it is necessary to eliminate completely the unstable region, for, so long as a lower branch remains, flutter usually occurs in a low speed range.

TABLE 2

Flutter Parameters

| Notation | Definition | Theodorsen[2] Notation |
|---|---|---|
| $\frac{I_\alpha L_\alpha}{\pi\rho b^4 L_\alpha}$ | Ratio of supporting surface inertia to the air cylinder inertia. $I_\alpha L_\alpha$ is equal to the total mass moment of inertia of the entire system in rotation about its node, $L_\alpha$ is the effective span of the supporting surface, and $\pi\rho b^4$ is the inertia of the reference air cylinder. | $\frac{r_\alpha^2}{\kappa}$ |
| $\frac{I_\beta L_\beta}{\pi\rho b^4 L_\beta}$ | Ratio of control surface inertia to the air cylinder inertia. $I_\beta L_\beta$ is equal to the mass moment of inertia of the control surface about its hinge axis, and $L_\beta$ is the span of the control surface. | $\frac{r_\beta^2}{\kappa}$ |
| $\eta$ | $\eta = \frac{1}{\pi\rho b^4}\left[\frac{I_\beta L_\beta + b(c-a)S_\beta L_\beta}{L_\beta}\right]$ where $I_\beta L_\beta + b(c-a)S_\beta L_\beta$ is the product of inertia of the control surface about the coupling nodes. | $\frac{r_\beta^2}{\kappa} + (c-a)\frac{x_\beta}{\kappa}$ |
| $\omega_\beta$, $\omega_\alpha$ | Control surface and fuselage natural frequencies, respectively. | $\omega_\beta$, $\omega_\alpha$ |
| $g_\alpha$, $g_\beta$ | Friction coefficients of fuselage and control surface, respectively. | $g_\alpha$, $g_\beta$ |

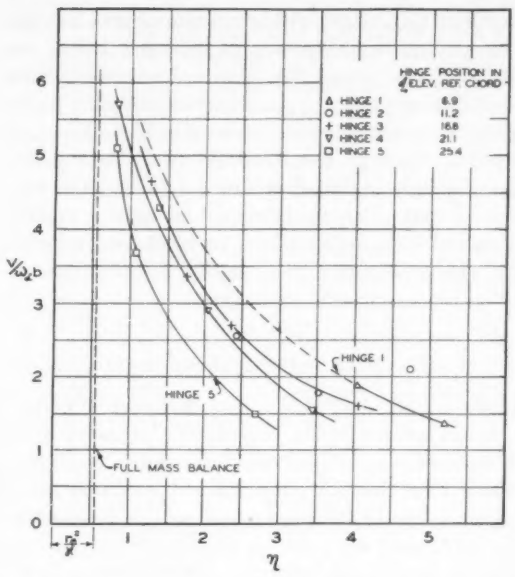


FIG. 19. Flutter speed factor versus rotational parameter for various values of hinge location.

### *Effect of Control Surface Balance*

During this series of tests the effect of control surface aerodynamic balance was found to be most pronounced at frequency ratios near zero. Fig. 19 shows test curves obtained by plotting the rotational unbalance parameter $\eta$ versus the speed coefficient for several different hinge locations. It was found that the speed at which flutter occurred was largely dependent on the initial elevator angle, and this accounts for the scattering of the test points. The net result is that, at low frequency ratios, the area forward of the hinge line tends to reduce the critical flutter speed slightly for a given unbalanced mass moment. Fig. 20 shows the results of a test in which the hinge line was located behind the aerodynamic center of the control surface.

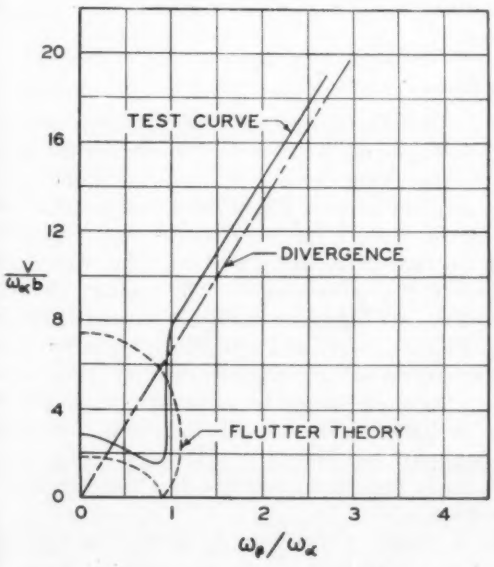


FIG. 20. Divergence resulting from aft hinge location.

In this case flutter was encountered below a frequency ratio of 1, as anticipated by theory. Above this ratio, torsional divergence occurred because of the relative positions of the aerodynamic center and rudder hinge line. As the phenomenon consisted of alternate stalling of the rudder in each extreme position, the divergence oscillations had the same appearance as a flutter coupling and were identified only from the oscillograph records. The speed at which these oscillations occurred was checked fairly closely by divergence calculations, and it will be noted that this critical speed is directly proportional to the frequency of the control surface.

### *Advantages of Aerodynamic Balance*

From a practical design point of view, aerodynamic balance has many advantages. Area forward of the hinge line is not only an effective means of reducing the control forces but permits a much lower value of $\eta$ to be obtained for a given amount of nonstructural balance weight. For example, the amount of balance weight required in the leading edge of the model to obtain full mass balance for a hinge line at 7 per cent of the elevator chord was approximately 15 times the weight required for full mass balance for a hinge line at 25 per cent of the chord.

One of the surprising results of the tests was that flutter could not be excited in the rudder-hull torsion mode. Even though a complete range of frequency ratios was investigated and additional unbalance in the form of lead was attached to the rudder trailing edge, no flutter could be maintained within the speed range of the tunnel. Flutter involving unsymmetric motion of the elevators could be excited, but only at extremely high speeds. These results are explainable when the rudder and elevators are considered as partial span flaps.

In the case of the rudder, both the vertical fin and the horizontal stabilizer contributed velocity damping, and the effective span ratio for the rudder was less than 0.2. For the unsymmetric mode the effective span ratio was approximately 0.6. These tests were extended to include twin rudders. In this case the upper flutter limit was reduced because of the increased inertia of the system, but there was practically no change in the lower speed curve. These results indicate that flutter involving fuselage torsion is normally less critical than either of the fuselage bending modes, and, if the surfaces are adequately balanced against the bending modes, a considerable safety margin for fuselage torsion coupled flutter exists.

***Balance Tabs***

Preliminary data, obtained on both balance tabs and control tabs, indicated the importance of tabs in the consideration of tail flutter. Balance tabs are constrained to move about their hinge axes an amount proportional to the main control surface motion. A tab movement in the same direction as the motion of the control surface is designated as leading, while a tab movement opposite to the motion of the control surface is designated as lagging. The degree of lead or lag, defined as the ratio of tab to control surface angular displacement, is illustrated in Fig. 21.

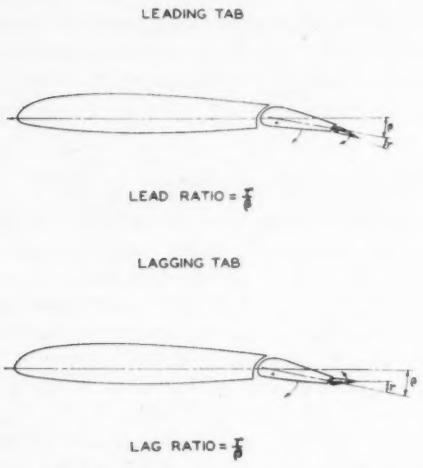


FIG. 21. Leading and lagging tabs.

The results of the balance tab tests are shown in Fig. 22. With a large elevator mass unbalance and an elevator-fuselage frequency ratio near unity, the leading tab was found to raise the flutter speed markedly, while the lagging tab slightly reduced the flutter speed. This effect was even more pronounced for the case of full mass balance of the elevators, where no flutter could be excited with the leading tab ratio 1:1 or more.

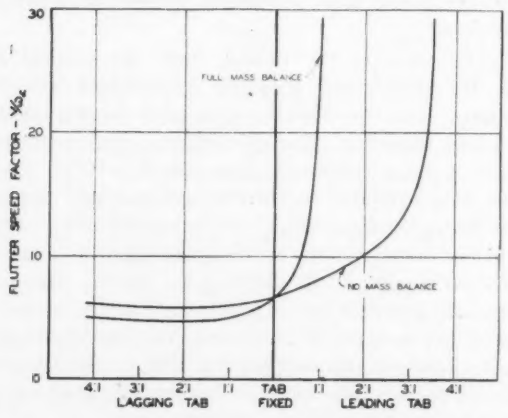


FIG. 22. Effect of leading and lagging tabs on flutter speed.

These tests were made with a tab whose area was 12.5 per cent of the elevator area and covered 45 per cent of the elevator span. The pronounced effect of the balance tabs suggests the possibility of designing control surfaces with considerable aerodynamic balance area forward of the hinge line to obtain a forward c.g. mass location with a minimum of added ballast. The hinge moments may then be increased to satisfy stability and control force requirements by employing a leading tab. This arrangement has actually been used successfully on several Martin airplanes.

## DYNAMIC LOAD MEASUREMENTS

While a great deal of attention has been devoted to the flutter problem, the remarkable increases in size and performance of aircraft have introduced many additional problems of vital interest to the structural designer. One of the most important is the design of large structures that are necessarily flexible and are subjected to dynamic loadings. Under certain landing conditions, for example, a fuselage may tend to vibrate or "whip" at one or more of its natural frequencies, and it is possible for this whipping to build up vibratory stresses that may exceed considerably the anticipated static stresses. A number of cases may be cited where major structural components—such as fuselages, stabilizers, and landing gear struts—whose strengths exceeded static load requirements have failed in service. On the other hand, there are indications that as airplanes increase in size there is a tendency for certain load factors to decrease and the design may be severely penalized by arbitrarily assuming large values. In any event, it is apparent that the design of flexible structures is not subject to the well-defined empirical rules associated with the design of small aircraft and that both theoretic and experimental data are urgently needed.

***Load Factors***

As a step in this direction, a rather extensive program has been in progress for some time to measure the actual load factors being encountered on large flying boats. This program is being conducted in cooperation with the Bureau of Aeronautics and measurements are being made on three large flying boats ranging from 52,000 to 140,000 lbs. gross weight. The primary object of these tests is to obtain a sufficient amount of experimental data to serve as a foundation for rationalizing the structural design requirements for large flying boats. As the tests are by no means completed, the data available at the present time must necessarily be considered as preliminary. However, certain trends are already apparent which are directly applicable to new designs.

As a result of the instrumentation development program necessitated by the experimental flutter investigations, the vibration measuring equipment has

proved to be ideally suited for obtaining dynamic load data. The inherent characteristics of the equipment make it possible to record simultaneously a large number of pickup units located in remote parts of the airplane. In addition to the accelerometers, the equipment is used in conjunction with standard wire-wound strain gauges[10] and special control surface displacement indicators to obtain a complete time history of accelerations, stresses, and control displacements.

## Flying-Boat Tests

A typical equipment installation is shown in Fig. 23. The accelerometers are located in the wing, hull, and tail surfaces in sufficient numbers to record the accelerations in the following modes:

(a) Translation and rotation along and about the three principal axes.

(b) Total vertical accelerations of the hull at the tail surfaces.

(c) Total vertical accelerations of the hull at the bow.

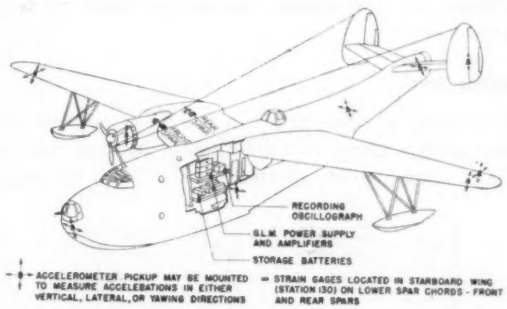
RECORDING OSCILLOGRAPH
G.L.M. POWER SUPPLY AND AMPLIFIERS
STORAGE BATTERIES
= ACCELEROMETER PICKUP MAY BE MOUNTED TO MEASURE ACCELERATIONS IN EITHER VERTICAL, LATERAL, OR YAWING DIRECTIONS
= STRAIN GAGES LOCATED IN STARBOARD WING (STATION 130) ON LOWER SPAR CHORDS - FRONT AND REAR SPARS

Fig. 23. Installation of acceleration measuring equipment in the Model PBM-3 airplane.

The control surface displacement indicators consist of wire-wound potentiometers connected in electrical bridge circuits whose outputs are directly proportional to the surface displacements. These are recorded by the oscillograph together with the strain gauge responses. A typical oscillograph record showing a time history of these responses is illustrated in Fig. 24. It will be noted that the master oscillator signal is recorded as a check on the stability of the electrical equipment. During some early landing tests, the carrier oscillator signal was found to be distorted by the impact accelerations. It has since been redesigned, and in several cases where the landing impacts have been sufficiently severe to damage flight instruments the electrical equipment has remained perfectly stable.

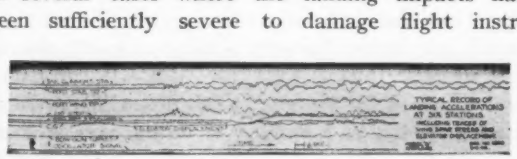

Fig. 24. Typical oscillograph record of landing accelerations.

The majority of test data available at present pertains to the landing accelerations encountered on two of the flying boats. Although measurements are being made during all of the flight maneuvers that this type of aircraft is expected to perform, the measured accelerations are all quite low. Similarly, no appreciable load factors have been encountered on normal take-offs. However, complete rough water tests are in progress at this writing. The landings themselves are quite representative and cover a wide range of loadings and landing techniques.

## Landing Accelerations

Several typical landing acceleration curves are plotted in Fig. 25. These three-dimensional plots offer the most comprehensive means of illustrating the data since they show a time history of acceleration distribution. The occurrence of the acceleration peaks is characteristic of all the landings, and their frequency is largely dependent on the wave formation and natural frequencies of the hull. The closeness of these frequencies in many cases suggests the possibility of building up large hull amplitudes when the frequency of the wave formation coincides with one of the hull natural frequencies.

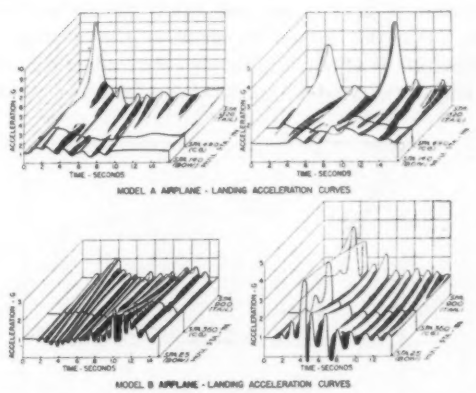


Fig. 25. Three-dimensional plots of landing accelerations.

The effect of hull flexibility is shown by the shape of the acceleration curve along the hull span, particularly on the initial impacts. The slope of this curve is practically linear back to the rear step where it assumes a parabolic shape characteristic of the hull vertical bending mode. As is to be expected, this effect becomes more pronounced as the length of the hull is increased. For extremely large airplanes, it may prove desirable to proportion the hull load factor in accordance with the type of parabolic acceleration distribution shown in Fig. 25.

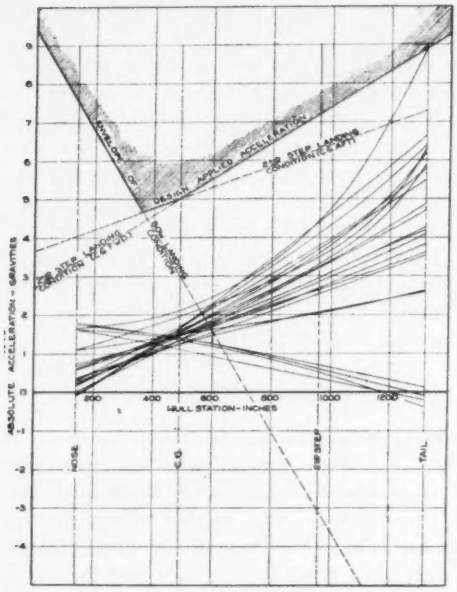


FIG. 26. Model A airplane, landing and take-off accelerations.

### *Test Data*

The relations between the test data and present design requirements are illustrated in Figs. 26 and 27. In examining these curves, two facts are immediately apparent. First, the accelerations encountered at the center of gravity are well below the design limitations. For the Model B airplane the average c.g. acceleration is about 2.2*g*, while the average c.g. acceleration for the Model A airplane is even lower, at about 1.7*g*. The angular accelerations, however, are considerably higher than the design values, as evidenced by the rather steep slope of the test curves. As a net result, the design requirements are apparently conservative for the major portion of the hull span, but, toward the tail, design accelerations have actually been encountered on the Model A airplane.

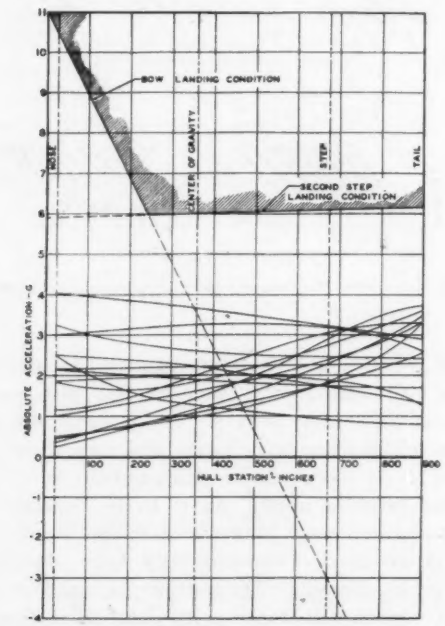


FIG. 27. Model B airplane, landing and take-off accelerations.

In drawing any conclusions from these data, it must be remembered that all of the landings made to date may be classed as smooth or moderate. The c.g. accelerations will undoubtedly be found to increase in magnitude when rough water tests are made, and it will be interesting to see the effects on the angular accelerations. Similarly, while the bow load factor requirements appear conservative on the basis of the available data, no true bow landings have been made to date. Although the stabilizer acceleration data are not plotted, the accelerations encountered at the stabilizer tips have often exceeded the hull accelerations at the tail. In one case a total acceleration at the stabilizer of 10*g* was recorded when the acceleration at the hull tail was only 6.5*g*. These stabilizer tip accelerations are particularly important for twin-tail airplanes where the heavy fin and rudder masses can build up large inertial forces.

### *Landing Data*

As a step in predicting the trends of applied load factors with increase in airplane size, landing data for the two airplanes are plotted in Fig. 28 as statistical

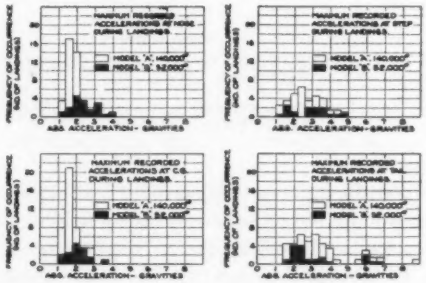
MAXIMUM RECORDED ACCELERATIONS AT NOSE DURING LANDINGS
MAXIMUM RECORDED ACCELERATIONS AT STEP DURING LANDINGS
MAXIMUM RECORDED ACCELERATIONS AT C.G. DURING LANDINGS
MAXIMUM RECORDED ACCELERATIONS AT TAIL DURING LANDINGS
MODEL 'A' 140,000#
MODEL 'B' 52,000#
ABS. ACCELERATION - GRAVITIES
FREQUENCY OF OCCURRENCE (NO. OF LANDINGS)

FIG. 28. Trends of maximum recorded accelerations during landings.

frequency curves. In constructing these curves, each single nose acceleration represents the maximum acceleration encountered during any one landing and is not necessarily related to the c.g. or tail accelerations encountered at the same instant. From an examination of Fig. 28 two trends are apparent. First, there is a definite indication that the applied vertical load factor at the center of gravity is less for the 140,000-lb. gross weight airplane than the 52,000-lb. airplane. The average vertical load factor for the smaller airplane averages about 2.2*g* (absolute) while the average load factor for the larger is only about 1.7*g*. This would indicate that the vertical load factor tends to decrease

with size. On the other hand, the average tail acceleration encountered on the larger model is higher than the average for the smaller airplane. Part of this increase would be expected because of the difference in hull spans, but it is evident from the slope of the curves of Figs. 26 and 27 that angular accelerations do increase with size.

In predicting design trends on comparative data, as plotted in Fig. 28, it must be remembered that the load factors are not only a function of airplane size but also depend upon pilot technique, water conditions, and hull design. For these particular tests all pilots can be considered as experienced and in many cases both ships were flown by the same pilot. As previously mentioned, no rough water or bow landings have yet been made and the present data should be used with caution.

## Flight Maneuvers

A sample record obtained during a demonstration pull-out dive is plotted in Fig. 29. This type of record

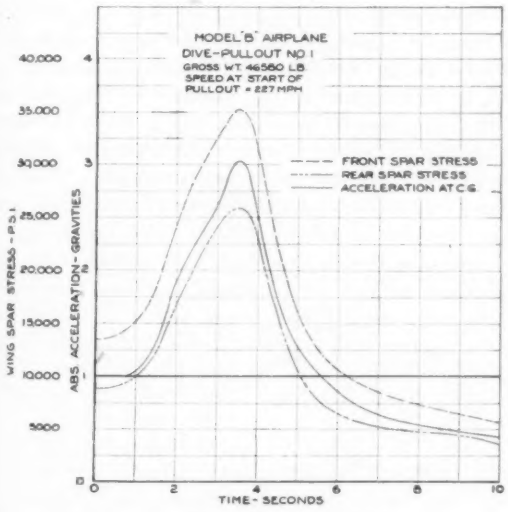


Fig. 29. Pull-out record showing correlation between acceleration and stress.

is useful in showing not only the duration of the applied "steady-state" acceleration but the phase relationships between this acceleration and the spar stresses. The results of a number of pull-out records have been correlated with the computed stresses and the good agreement obtained is shown in Fig. 30. The elevator control position indicator was not installed for these tests, but, at present, interesting data are being obtained on the relationships between the elevator movements and "build up" of load factor. The results of a typical stall record are plotted in Fig. 31. In this case it is noted that in recovering from the stall the elevator was reversed from $+12°$ to $-9°$ and back to $+15°$ in $3\frac{1}{2}$ sec. In spite of large variation in elevator

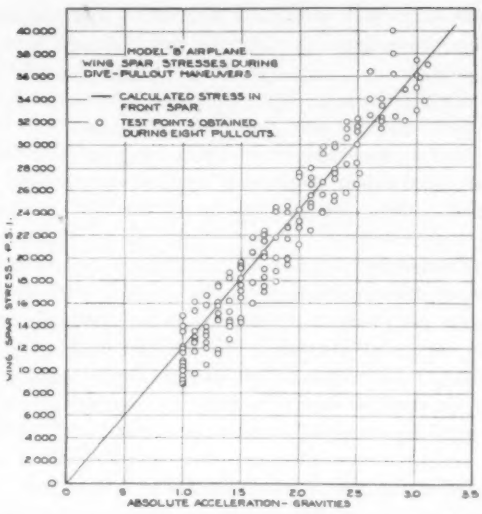
MODEL 'B' AIRPLANE
WING SPAR STRESSES DURING DIVE-PULLOUT MANEUVERS
CALCULATED STRESS IN FRONT SPAR
TEST POINTS OBTAINED DURING EIGHT PULLOUTS
WING SPAR STRESS - P.S.I.
ABSOLUTE ACCELERATION - GRAVITIES

Fig. 30. Correlation of measured and calculated stresses.

angle, the acceleration at the center of gravity only varied from $+0.7g$ to $+1.25g$ (absolute). These types of measurements will be particularly valuable in investigating the load factors built up on fighter-type airplanes, which are designed to execute much more violent maneuvers than are expected of the large flying boats on which the present measurements are being made.

## Nose-Wheel Load Measurements

Load factors, expressed in terms of applied accelerations, are usually of greater significance than actual loads. Often, however, it is desirable to measure loads directly, and such a case was recently encountered

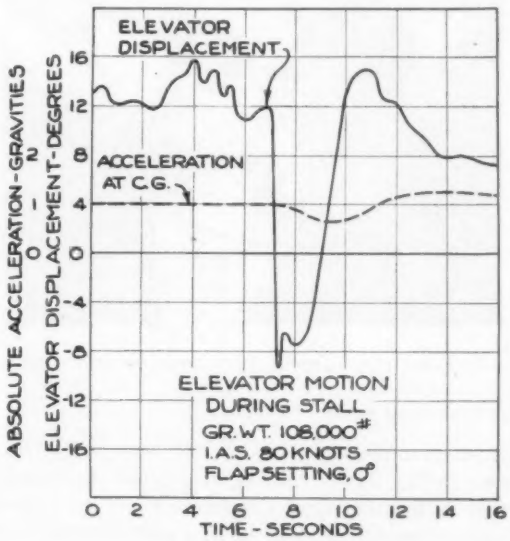


Fig. 31. Typical elevator displacement and c.g. acceleration during stall.

in connection with structural difficulties with the nose wheel of a medium bomber. In this instance, several failures of the nose gear downlock fitting indicated that high drag loads were being realized. As static tests had proved that the gear would sustain 150 per cent of the specified three-wheel landing condition, which was critical, flight-test results were needed to determine the exact magnitudes of the loads actually being encountered.

The nose-wheel loads were determined by measuring the strut stresses at four points equally spaced around the strut periphery and then computing the loads from these measured stresses and the known nose-wheel geometry. The installation of the strain gauges on the nose strut is shown in Fig. 32. In order to correlate the nose-gear loads with the applied load factors, four accelerometer pickups were installed along the fuselage at the nose, center of gravity, deck turret, and tail. The tests were conducted in cooperation with the Air Forces Matériel Center. The particular field chosen for the tests was in a rutted condition and represented the most severe type of service conditions likely to be encountered. Nose-gear strut stresses were measured during more than 25 take-offs and landings.

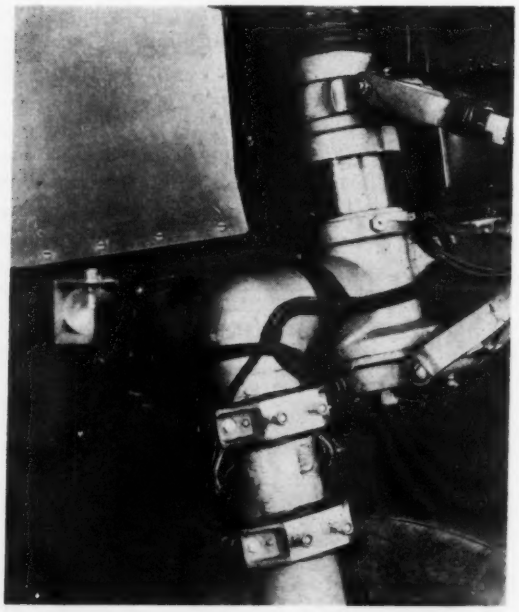

FIG. 32. Installation of strain gauges on nose wheel.

### *The Nose-Gear Strut*

A diagrammatic sketch of the nose-gear strut is shown in Fig. 33. It will be noted that the downlock fitting is located approximately 29 per cent of the distance between the rotation axis and the centerline of the axle. The load on the downlock is composed of the components of the vertical and drag loads normal

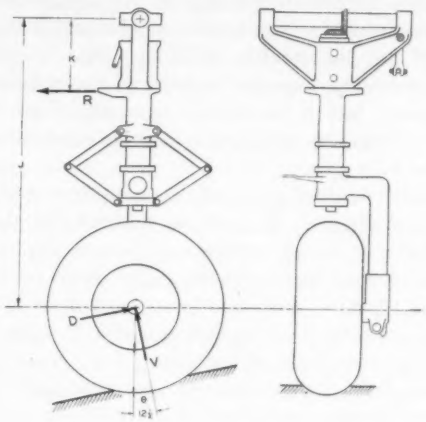


FIG. 33. Nose-gear diagram.

to the strut in accordance with the following equation:

$$R = J/K(D \cos \theta - V \sin \theta)$$

It is apparent that the vertical load is a relieving load and, for a given drag load, the downlock load is increased as the vertical load is reduced. The significance of this feature in the design of the downlock fitting is graphically illustrated in Fig. 34. The drag load is plotted versus the vertical load and lines of constant $D/V$ are plotted for ready reference. Superimposed on this curve are the various limit design conditions for the downlock fitting. The lowest curve represents the design downlock load specified by the three-wheel landing with inclined reactions condition. In this case, the applied vertical load was 18,680 lbs. and the applied drag load was 25 per cent of this value, 4,670 lbs. Fortunately, the original downlock fitting was good for considerably more than this specified

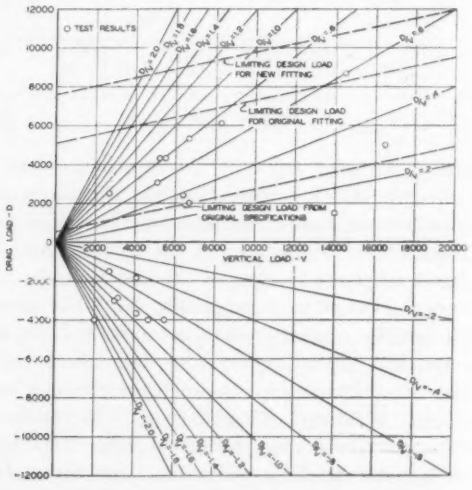


FIG. 34. Nose-gear flight-test results showing the ratio of drag to vertical loads under rough field landing conditions.

load because of an arbitrary ground turning condition assumed in the analysis, and the actual strength is plotted as the intermediate curve. The highest curve represents the design strength of the final reinforced downlock fitting. As the fitting itself was well over-strength in compression, no compressive limit is shown.

The results of a typical landing record are plotted in Fig. 35. The most striking feature is that both the drag and downlock reactions exhibit stress reversals that occur at the fore-and-aft natural bending frequency of the strut. The vertical reaction, on the other hand, remains positive throughout the landing run. The accelerations recorded in these tests were not particularly high, varying between two to three gravities immediately above the nose gear.

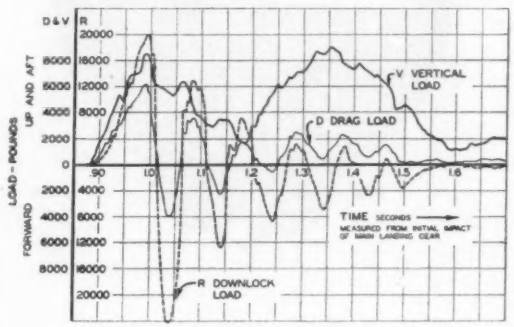


FIG. 35. Nose-gear landing loads.

### *Design Loads*

The relations between the test points and design loads are shown in Fig. 34. In practically every case the test points fall above the limit specified by the three-wheel landing with inclined reactions condition. For this particular design there is an indication that the $D/V$ ratio is most often near 0.8, and the maximum load imposed on the downlock fitting was caused by a vertical load that was 78 per cent of the design vertical reaction combined with a drag load 60 per cent of the vertical. In some instances the whipping may result in high forward loads, for, in this case, the vertical load adds to the negative drag load. Again, there is a tendency for the test points to cluster around the $D/V = 0.8$ ratio, although the vertical loads are relatively low. These results lead to the conclusion that the original design load, specified as 25 per cent of the vertical reaction, was unconservative. The present specified percentage of 0.33 does not appear too stringent, and there is experimental justification for increasing this value.

## CONCLUSIONS

Until recently, experimental checks on the flutter characteristics of a new model consisted of ground oscillation tests. The results of these tests were limited to the determination of natural frequencies, which, while important, are only a part of the data required to establish the flutter speeds of an airplane. The present investigations have advanced the test technique to the point where more complete flutter data may now be measured in flight. In one instance a rudder flutter condition has actually been predicted from flight data, while the recent tests on the Mars have shown that the instrumentation difficulties encountered on earlier tests have been eliminated. A substantial back-log of experience has been obtained and this is being supplemented with continued flight and wind-tunnel experience. As airplane design speeds approach estimated flutter speeds, it is anticipated that flight flutter tests will become a required acceptance item.

Although the vibration measuring equipment was developed primarily for flutter testing, it has proved to be suited ideally for measuring all types of accelerations, stresses, and displacements. In addition to recording many types of dynamic data, which heretofore has not been possible, the ability of the equipment to record simultaneously the responses of a large number of remotely located indicators has resulted in a tremendous saving in flight time. The economic aspects of this, particularly for flight tests on large airplanes, are apparent. Practically all of the tests discussed in the paper are being extended, and the results are already contributing materially to more refined aircraft design.

## REFERENCES

[1] Den Hartog, J. P., *Mechanical Vibrations*, p. 77; The McGraw-Hill Book Company, Inc., New York, 1934.

[2] Theodorsen, Theodore, *General Theory of Aerodynamic Instability and the Mechanism of Flutter*, N.A.C.A. T.R. No. 496, 1934.

[3] Draper, C. S., Bentley, G. P., and Willis, H. H., *The M.I.T. Sperry Apparatus for Measuring Vibration*, Journal of the Aeronautical Sciences, Vol. 4, No. 7, p. 281, May, 1937.

[4] von Schlippe, B., *The Question of Spontaneous Wing Oscillations*, N.A.C.A. T.M. No. 806, October, 1936.

[5] Bleakney, W. M., *Three-Dimensional Flutter Analysis*, Journal of the Aeronautical Sciences, Vol. 9, No. 2, pp. 56–63, December, 1941.

[6] Loring, S. J., *Outline of a General Approach to the Flutter Problem*, S.A.E. Journal, Vol. 49, No. 2, August, 1941.

[7] Nagel, Felix, *Static and Dynamic Model Similarity*, Journal of the Aeronautical Sciences, Vol. 6, No. 11, p. 468, September, 1939.

[8] Theodorsen, Theodore, and Garrick, I. E., *Mechanism of Flutter, A Theoretical and Experimental Investigation in the Flutter Problem*, N.A.C.A. T.R. No. 685, 1940.

[9] Bergen, W. B., and Arnold, Lee, *Graphical Solution of the Bending-Aileron Case of Flutter*, Journal of the Aeronautical Sciences, Vol. 7, No. 12, p. 495, October, 1940.

[10] de Forest, A. V., *Characteristics and Aircraft Applications of Wire Resistance Strain Gages*, Instruments, Vol. 15, No. 4, p. 112, April, 1942.

# Altimeter Setting Indicator

CHARLES H. COLVIN*
*New York University*

SUMMARY

The paper describes a new instrument, the Altimeter Setting Indicator, developed in the Instrument Division of the Weather Bureau under the direction of the author. The instrument is intended for installation at airports and is a special form of aneroid barometer in which the mechanism is so designed and the scale so graduated that the "altimeter setting number" is read directly. An adjustment is provided for adapting the instrument for use at airports at various elevations above sea level. The paper includes an analysis of the relation between barometric pressure and altimeter setting numbers. The old techniques of determining and making available altimeter setting information are compared with that made possible by the use of the Altimeter Setting Indicator.

THE ALTIMETER SETTING INDICATOR is an aneroid barometer from which, when the instrument is adjusted for the surveyed elevation of the airport upon which it is installed, the altimeter setting number may be read directly.

The instrument was developed, under the author's direction, by the U.S. Weather Bureau, and an initial quantity has been manufactured for the Bureau.

## THE BAROMETRIC SCALE

To understand why such an instrument is needed, it is necessary to recall that the Sensitive Altimeter (Fig. 1), as used on all transport and military aircraft to indicate altitude, is provided with a so-called "barometric scale" by means of which the instrument may be adjusted to compensate for barometric pressure changes. In flight this scale is set by the pilot to the number of which he is advised by radio from an airport. With its barometric scale set to this number, the hands of the altimeter will, if the instrument has no calibration error, read the altitude of the airport when the plane lands on that airport. (It is assumed that the position of the altimeter in the airplane is such that the instrument is 10 ft. above the ground when the wheels touch the runway.) The number to which the pilot sets the barometric scale of the altimeter is known officially as the "altimeter setting number" and colloquially as the "kollsman number."†

FIG. 1. Sensitive altimeter.

TABLE 1

| Altimeter Setting Number | Change in Altimeter Reading, Ft. |
|---|---|
| 28.0 | 1,824 |
| 28.1 | 1,727 |
| 28.2 | 1,630 |
| 28.3 | 1,533 |
| 28.4 | 1,436 |
| 28.5 | 1,340 |
| 28.6 | 1,244 |
| 28.7 | 1,148 |
| 28.8 | 1,052 |
| 28.9 | 957 |
| 29.0 | 863 |
| 29.1 | 768 |
| 29.2 | 673 |
| 29.3 | 579 |
| 29.4 | 485 |
| 29.5 | 392 |
| 29.6 | 298 |
| 29.7 | 205 |
| 29.8 | 112 |
| 29.9 | 20 |
| 30.0 | − 73 |
| 30.1 | −165 |
| 30.2 | −257 |
| 30.3 | −348 |
| 30.4 | −440 |
| 30.5 | −531 |
| 30.6 | −622 |
| 30.7 | −712 |
| 30.8 | −803 |
| 30.9 | −893 |
| 31.0 | −983 |

Presented at the Radio and Instruments Session, Eleventh Annual Meeting, I.A.S., New York, January 25–29, 1943.

* Director, Daniel Guggenheim School of Aeronautics, and Coordinator of Research, College of Engineering. Also Technical Adviser to the Chief, U.S. Weather Bureau.

† It is also referred to as the "standard atmosphere sea level pressure," not to be confused with the "standard pressure at sea level" which is 29.92 in. of mercury.

### Altitude Correctons

Although called the "barometric scale" and apparently graduated in inches of mercury, the adjustment of this scale actually changes the reading of the altimeter by a certain number of feet regardless of the altitude or barometric pressure. For example, changing the barometric scale setting from 29.9 to 30.1 causes the altimeter to read 185 ft. higher, regardless of the initial reading. Table 1 gives, for each value of the altimeter setting number, the correction to be applied to the altitude indication (in feet) to obtain the corresponding altitude reading for a setting of 29.92—that is, to obtain the so-called "pressure altitude." The values in the table equal the altitude in the standard atmosphere[1] for the barometric pressure in inches of mercury of the same values as the altimeter setting numbers; hence, the name "barometric scale." However, at no other altitude are the numbers on the altimeter setting scale readable in inches of mercury, while they do correspond to the figures in feet, as given in Table 1, at all altitudes.

As it is necessary to determine the altimeter setting number and to transmit it by radio at frequent intervals and as this is merely a reference number that is only indirectly related to the ambient barometric pressure at the airport, some accurate and simple method or instrument for determining the number was desirable.

### Correction Methods

Two methods have been in use. In one the ambient pressure is determined from the mercurial or other barometer in the Airport Weather Bureau Office. This is reduced to the station pressure (for the field elevation) and from this pressure value the corresponding altitude in the standard atmosphere (or "pressure altitude") may be determined by reference to appropriate tables.[1] Adding 10 ft. (the assumed height of the airplane's altimeter above the ground) and subtracting the actual altitude of the airport from this "pressure altitude" gives the altimeter setting value in feet. Reference to Table 1 or its equivalent in the standard atmosphere tables gives the corresponding altimeter setting number. In practice, the procedure is simplified by the use of special tables prepared for each airport.

In another method a station barometer,[2] comprising a Sensitive Altimeter identical with those carried by the airplanes, is installed in the airport Operations Office. When the altimeter setting number is desired, the adjustment knob of the altimeter is turned until the hands read 10 ft. below the airport altitude.* The instrument is then vibrated or tapped and again set to the field altitude less 10 ft. After repeated setting and tapping, the desired altitude indication is obtained, and the setting number is then read from the barometric scale.

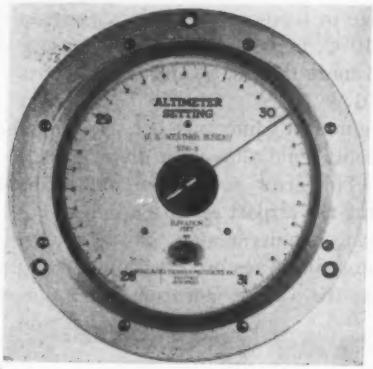


Fig. 2. Altimeter setting indicator.

### The Altimeter Setting Indicator

On the other hand, from the Altimeter Setting Indicator (Fig. 2), the altimeter setting number is read directly. Once installed and set for the height of the airport, no manipulation or reference to tables is required.

In the Altimeter Setting Indicator the mechanism of the Sensitive Altimeter has, in effect, been turned inside out. Adjustment is made for altitude with the hand indicating altimeter setting numbers. Each instrument is built to cover a range of airport elevation of 200 ft. To allow for the assumed height of the altimeter (10 ft. above the field) the instrument is set to an airport elevation 10 ft. below the actual altitude of the airport. The altimeter setting scale is calibrated in the pressure equivalents of altitude in accordance with the Standard Atmosphere Tables but is graduated in the corresponding altimeter setting numbers (from Table 1) with 29.92 placed at the altitude of the midpoint of the airport elevation scale. For example, an Altimeter Setting Indicator designed for airport elevations from 900 to 1,100 ft. has the 29.9 graduation line at the pressure corresponding to 1,020 ft. (1,000 being the midpoint of the airport elevation scale and 20 the altitude equivalent of 29.9 in Table 1), the 29.0 line at a pressure corresponding to 1863 ft., the 31.0 line at a pressure corresponding to 17 ft., etc.

The instrument is enclosed in a sealed case with provision for connection to a static head for elimination of effects of wind pressure.

#### *Specifications*

The specification against which the initial purchase was made by the Weather Bureau requires that errors at room temperature shall not exceed ±0.02 and that the maximum error shall not exceed the minimum error by more than 0.02. Resetting of the airport elevation index can, therefore, keep all readings within ±0.01 of the correct value.

* It should, perhaps, be explained that, since it is desired that the airplane's altimeter read the field altitude when 10 ft. above the field, it must be set to read 10 ft. below the field altitude when at the field elevation. Hence, the correct setting number is that corresponding to an altitude 10 ft. less than the actual elevation of the field.

A change in temperature of 20°C. within the range between 10°C. and 40°C. may not cause a change in reading of more than 0.02, and friction errors may not exceed 0.01.

A position error (difference between the reading with dial horizontal and that with dial vertical) of 0.01 is allowed. This error may be minimized or eliminated by resetting the airport elevation index.

The aging requirement is that after six months the calibration shall be restored, within the original limits, by moving the airport elevation index not more than 20 ft.

***Test Results***

The maximum and average errors of the first 13 instruments received and tested for the Weather Bureau of Standards, were:

| | Maximum | Average |
|---|---|---|
| Calibration at room temperature | 0.028 | 0.012 |
| Difference between maximum and minimum error | 0.015 | 0.010 |
| Temperature error, for change of 20°C. | 0.014 | 0.008 |
| Friction error | not readable | |
| Position error | less than 0.01 | |
| Aging | no readable change in two months | |

The Altimeter Setting Indicator is installed in the Operations Office, rather than in the Weather Bureau Office, where it can be read at any time by operating personnel and where the altimeter setting number can be transmitted immediately without reference to the Weather Bureau Office. Until the rate of drift is established for each instrument, their readings are being compared daily with the computed values of altimeter setting numbers as determined from the Weather Bureau mercurial barometer. It is anticipated that after an initial period of such daily comparisons it will be found unnecessary to check the Altimeter Setting Indicator more often than once per month. It is estimated that the use of these instruments will effect a saving to the Weather Bureau of some 400 man-hours per year per instrument.

REFERENCES

[1] Brombacher, W. G., *Altitude-Pressure Tables Based on the United States Standard Atmosphere*, N.A.C.A. Report No. 538.

[2] Colvin, Charles H., *Flight Altitude Control*, Journal of the Aeronautical Sciences, Vol. 6, No. 5, pp. 206-210, March, 1939.

# Mechanical Properties of Austenitic Stainless Steels

R. A. LINCOLN* AND W. H. MATHER†

*Allegheny-Ludlum Steel Corporation*

## INTRODUCTION

MUCH HAS BEEN WRITTEN and said about the corrosion and the heat-resistant properties of austenitic stainless steel. However, relatively little consideration has been given to their mechanical properties, in spite of the fact that a variety of remarkable and useful properties can be obtained. Changes in chemical composition produce considerable differences in mechanical properties, so that, within the range of compositions of austenitic stainless steel that can be obtained commercially, it is possible to obtain a wide variety of different alloys. These range from a relatively soft metal with a low rate of work-hardening that lends itself readily to spinning operations to alloys that are slightly harder and have a rate of work-hardening that makes them well suited to drawing and, finally, to alloys that have a high rate of work-hardening that can be cold-rolled to extremely high tensile strengths and still have sufficient ductility to allow strip and sheet to be formed into structural shapes.

## EFFECT OF COMPOSITION

This marked effect of composition on mechanical properties is the result of the effect of slight changes in composition affecting the stability of austenite with respect to its tendency to transform into ferrite at room temperature. The effect of composition on the stability of the austenite is clearly shown in the curves taken from a paper published by Wever and Jellinghaus of the Kaiser Wilhelm Institute. Fig. 1 shows cross sections of the constitution diagram for ternary alloys containing iron, chromium, and nickel. These cross sections are drawn at constant iron content so that along their length relative proportions of chromium and nickel vary. The cross sections at 75 per cent and 70 per cent iron cover the range of alloys that will be discussed and referred to as austenitic stainless steel. These two cross sections show that when the nickel content exceeds approximately 11 per cent the alloy at room temperature consists of a stable austenitic structure with no tendency to transform into ferrite. However, when the nickel content drops below 11 per cent, there is a tendency for ferrite to form in the vicinity of room temperature. For example, on the cross section for 75 per cent iron, an alloy containing 17 to 18 per cent chromium and 7 to 8 per cent nickel is completely austenitic in the temperature range from 1,100°C. down to approximately 100°C. However, below 100°C. the stable structure would consist of a mixture of austenite and ferrite. In the annealed condition such an alloy would exist at room temperature with a completely austenitic structure because of the fact that at the low temperature it is too sluggish to transform. However, when the material is deformed through cold-work, the energy imparted to the structure by the working of the metal causes the transformation from austenite into ferrite to start taking place. Thus, in such an alloy the normal increase in hardness produced by cold-work is exaggerated and added to by increase in hardness, which results from the transformation of austenite into ferrite.

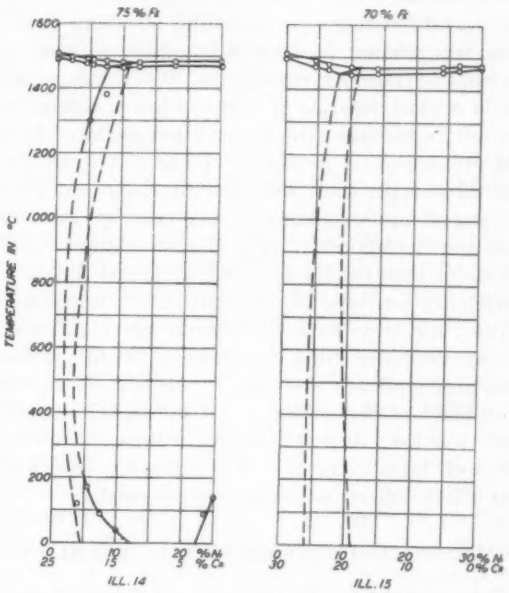


FIG. 1. Cross sections of equal iron content through the three component systems Fe–Cr–Ni. From Wever and Jellinghaus, *Mitt. Kais.-Wilh.-Inst. Eisenf.*, Vol. 13, p. 103, 1931.

On the other hand, when an alloy in this range of compositions contains more than 11 per cent nickel and is subjected to cold deformation, the work-hardening that results is not added to by any tendency for the aus-

Presented at the Materials Session, Eleventh Annual Meeting, I.A.S., New York, January 25–29, 1943.

* Associate Director of Research.

† Metallurgist.

tenite to transform, and such alloys therefore have the lowest rate of work-hardening.

### *Composition Control*

The primary requisite, necessary in order to obtain an alloy with the desired mechanical properties, is to control the composition so that an austenitic structure that has the necessary tendency to transform into ferrite is obtained. For example, with approximately 18 per cent chromium, the addition of approximately 12 per cent nickel produces an austenitic structure that at room temperature is completely stable without any tendency to transform into ferrite. When such an alloy is cold-worked, the rate of work-hardening is relatively low and the increase in hardness is that produced by the cold-working of the austenite. If the nickel content is lowered to 8 per cent, with the chromium content remaining at approximately 18 per cent, an austenitic structure is obtained which at room temperature is less stable than the higher nickel alloy, and there exists a tendency for some of the austenite to transform to ferrite. As alloys with successively lower nickel content are examined it will be found that the rate of work-hardening gradually increases as a result of a decrease in stability of the austenite. If the nickel content is made too low, then the austenite becomes unstable, and such large quantities of it transform into ferrite that alloys difficult to control are obtained.

## Mechanical Properties of Annealed Alloys

Before taking up the properties of cold-worked material, it might be well to consider the mechanical properties of annealed alloys as they are affected by composition. Fig. 2 shows stress-strain curves for annealed austenitic stainless steel of different compositions. As can be seen from this figure, the yield strength of the various alloys is controlled more by carbon content than by any other variation in composition. It will be noted that, regardless of chromium and nickel content within the range being considered, as the carbon content increases from 0.056 per cent up to 0.13 per cent the yield strength increases from approximately 24,000 up to 36,000 lbs. per sq.in. On the other hand, after the range of elastic deformation has been passed and the metal is being plastically deformed while being pulled in the tensile test, widely different stresses are obtained, depending on the chromium and nickel content. Thus, the alloy containing approximately 16.5 per cent chromium and 11 per cent nickel breaks with an ultimate strength of 74,000 lbs. per sq.in. and 60 per cent elongation in a 2-in. gauge length. The alloy containing 17.90 per cent chromium and 6.72 per cent nickel breaks with an ultimate tensile strength of 146,000 lbs. per sq.in. and an elongation of 72½ per cent in a 2-in. gauge length. The alloys containing approximately 19 per cent chromium and 9 per cent nickel all break with tensile strengths in the range from 85,000 to 95,000 lbs. per sq.in. Thus it appears that, up to the yield strength and before any plastic deformation has taken place in the metal, all of these compositions have approximately similar strengths that vary slightly in proportion to the amount of carbon dissolved in the austenite. However, after plastic deformation starts taking place, the actual breaking load varies widely depending on the relative chromium and nickel content, which in turn influences the transformation of austenite into ferrite during cold deformation.

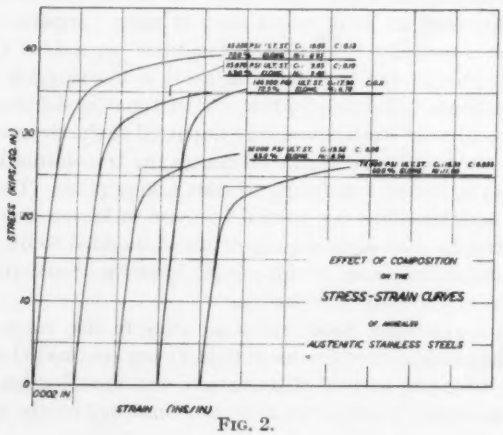


FIG. 2.

### *Drawing Properties*

With regard to the drawing properties of these alloys in the annealed condition, we regard the composition containing 0.08 to 0.12 per cent carbon with approximately 19 per cent chromium and 9 per cent nickel as being the composition best suited for all round deep drawing. This composition is known as Type 302 stainless steel, and we believe it to be best suited for straight tension draws where the metal is being pulled through a drawing ring and must elongate uniformly all over after passing through the ring. The proper rate of work-hardening of this composition of chromium and nickel together with carbon content in the vicinity of 0.10 per cent, results in an alloy that does not tend to neck down in one place while being drawn but tends to cause the deformation to be spread uniformly over a larger area.

### *Spinning Operations*

An alloy containing approximately 17 per cent chromium and 11 per cent nickel with carbon content in the vicinity of 0.05 per cent is one that we would consider best suited for spinning operations or for mild drawing and forming operations, which are similar to spinning operations. The extremely low rate of work-hardening introduced by the high nickel content, together with the low yield strength accompanying the low carbon content, results in an alloy well suited for such applications. This alloy is known as the free spinning grade of Type 304 stainless steel.

TABLE 1

Density of Dural = 2.8; Density of 18–8 = 7.95

$$\text{Ratio} \frac{\text{Density of 18–8}}{\text{Density of Dural}} = 2.83$$

Comparison of Mechanical Properties

| | Yield Strength, Lbs. | Tensile Strength, Lbs. | Per Cent Elongation in 2 In. | Modulus of Elasticity, Lbs. per Sq.In. | Deflection at Yield Strength, In./In. |
|---|---|---|---|---|---|
| Hardened Dural with a 1 sq.in. cross section | 40,000 | 62,000 | 10 | 10,000,000 | 0.0062 |
| Hardened Dural with a 2.83 sq.in. cross section | 113,200 | 175,400 | .. | 10,000,000 | 0.0062 |
| Cold-rolled stainless steel strip (0.11 per cent C, 19 per cent Cr, 9 per cent Ni) with a 1 sq.in. cross section | 113,200 | 140,000 | 20 | 27,000,000 | 0.0062 |

Regular Type 304 stainless steel, which has a low carbon content with approximately 19 per cent chromium and 9 per cent nickel, has properties intermediate between the two previously mentioned ones and would undoubtedly be satisfactory for many drawing operations. However, we believe that the two first-named compositions are sufficient to cover most requirements.

***High Strength Alloys***

The composition containing approximately 18 per cent chromium and slightly less than 7 per cent nickel is not suggested for most applications in the annealed condition unless the high rate of work-hardening of this composition is desirable for special reasons. We believe that its best field of usefulness lies in the cold-rolled condition because it can be rolled to relatively high strength and still retain sufficient ductility to allow itself to be formed.

By carefully controlling the relative amounts of chromium, nickel, manganese, and carbon present in austenitic stainless steel, it is possible to obtain alloys that can be rolled to extremely high tensile strengths and still have good ductility. In considering material from the point of view of its strength-weight ratio, it is natural to compare it with aluminum alloys because of their well-known high strength-weight ratio. From this point of view it is of interest to determine the properties that the stainless steel would have to have in order to compare favorably with Dural. Table 1 gives such a comparison.

As shown in the table, the density of Dural is approximately 2.8, while that of 18–8 is about 7.95. Thus, the ratio of the density of stainless steel to that of Dural is 2.83 to 1. The best mechanical strength that can be obtained with aluminum alloys is a tensile strength of approximately 62,000 lbs. per sq.in. and a yield strength of approximately 40,000 lbs. per sq.in. When we take into account that a given volume of stainless steel is 2.83 times as heavy as the same volume of aluminum alloy, it is evident that, in order to have as good a strength-weight ratio, stainless steel must have a yield strength of at least 113,200 lbs. per sq.in. and a tensile strength of at least 175,460 lbs. per sq.in. For example: a square inch section of stainless steel of a given length is equivalent in weight to a 2.83-sq.in. section of Dural of the same length. In order to have the same weight-strength ratio, the piece of stainless steel would have to withstand 113,200 lbs. before arriving at its yield strength because this is the stress at which such a section of Dural in its hardened condition would be at its yield strength. Since Dural has a modulus of elasticity of approximately 10,000,000 lbs. per sq.in. and stainless steel has a modulus of elasticity of approximately 27,000,000 lbs. per sq.in., the above-described bar of Dural would deflect 0.0062 in. per in. at a yield strength of 113,200 lbs. total load on a 2.83 sq.in. cross section, while the above-described bar of stainless steel would deflect approximately the same at a yield strength of 113,200 lbs. on a 1 sq.in. cross section. In other words, there would be almost no difference in the deflection produced by a given stress.

It should be borne in mind that because of its lower density a given section of Dural will have a greater thickness than a similar stainless-steel section of the same strength-weight ratio. Similarly, the Dural section would be more resistant to buckling under compression. For this reason designs that have been made with Dural might not be satisfactory if the Dural were replaced by stainless steel. In order to make use of the high strength-weight ratio of stainless steel, it will be necessary to use designs favorable to the characteristics of stainless steels where the rigidity of thin sections are stiffened by corrugating or some similar forming.

On the basis of past experience cold-rolled stainless-steel strip that has an elongation of approximately 15 per cent, in the 2-in. gauge length of the standard tensile test, should have sufficient ductility to make the bends that would be expected in the forming of such parts as angles and I-beams that are used as structural members. Taking this figure of 15 per cent elongation

in the standard 2-in. gauge length tensile test as a requirement to be met, let us consider what mechanical properties can be obtained with stainless steel (see Table 2).

TABLE 2

| Alloy and Treatment | Yield Strength, Lbs. per Sq.In. | Tensile Strength, Lbs. per Sq.In. | Per Cent Elongation in 2 In. |
|---|---|---|---|
| Cold-rolled stainless-steel strip (0.11 per cent C 19–9) with a 1 sq.in. cross section | 129,000 | 145,000 | 15 |
| Cold-rolled stainless-steel strip (0.10 per cent C 18–8) with a 1 sq.in. cross section | 140,000 | 160,000 | 15 |
| Cold-rolled stainless-steel strip (0.13–0.15 per cent C, 17–18 per cent Cr, 7.0–7.2 per cent Ni, 0.50 per cent Mn) with a 1 sq.in. cross section | 170,000 | 200,000 | 15 |
| Minimum strength that stainless steel must have in order to compete with aluminum | 113,000 | 175,000 | .. |

### *Composition Variations*

With 0.11 per cent carbon and approximately 19 per cent chromium and 9 per cent nickel, by the proper cold-rolling, strip can be obtained which together with 15 per cent elongation, has a yield strength of 129,000 lbs. per sq.in. and a tensile strength of 145,000 lbs. per sq.in. With 0.10 per cent carbon and approximately 18 per cent chromium and 8 per cent nickel, cold-rolled strip can be obtained with an elongation of 15 per cent, a yield strength of 140,000 lbs. per sq. in., and a tensile strength of 160,000 lbs. per sq.in. This range of compositions from 18 to 19 per cent chromium and 8 to 9 per cent nickel represents the compositions that most likely would be obtained when ordering regular 18–8 under Type 302 specifications. It can be seen that the properties that can be obtained with these alloys are not good enough to compete with aluminum on the basis of the weight-strength ratio. It was pointed out previously that, in order to compete with Dural stainless steel would have to have a yield strength of approximately 113,200 lbs. per sq.in. and a tensile strength of 175,000 lbs. per sq.in. Thus, the regular Type 18–8 is slightly better than Dural when we consider the yield strength on a weight-strength basis but falls below Dural when tensile strength is considered.

Most of the 17–7 Type 301 stainless steel which is made has had sufficient manganese added to it so that the effect of the combined nickel and manganese contents is such that an alloy with properties similar to those described above for 18–8 and 19–9 is obtained.

### *Obtaining High Mechanical Properties*

If the composition is closely controlled so that the nickel content falls between 7.0 to 7.2 per cent, the chromium content is 17 to 18 per cent, and the carbon content is 0.13 to 0.15 per cent with the manganese content close to 0.50 per cent, cold-rolled strip and sheets can be obtained that have a yield strength of 170,000 lbs. per sq.in. and a tensile strength of 200,000 lbs. per sq.in. with 15 per cent elongation. When this is compared with the previously stated figures for Dural, it is evident that this stainless steel has a tensile strength 15 per cent greater and a yield strength 42 per cent greater than Dural when equal weights of the two alloys are compared on a strength-weight basis.

Table 3 gives compositions with which high tensile strengths can be obtained accompanied by good ductility. The first composition in this table is the one that has just been discussed. If the chromium content of this composition is held close to 18.00 per cent, then alloys that have the same desirable properties can be produced that contain 0.10 to 0.12 per cent carbon. Other variations in composition are possible within the limits of the present Type 301 analysis and still maintain the high mechanical properties stated above. If the carbon content is 0.10 to 0.12 per cent and the chromium content close to 17 per cent, the nickel content must be about 7.5 per cent, or approximately 1 per cent manganese must be present with 7.0 to 7.2 per cent nickel. The only requirement of chemical composition is that the elements be balanced so as to obtain an austenitic structure with the proper tendency to transform into ferrite.

TABLE 3

Compositions with Which High Mechanical Properties Can Be Obtained

| Per Cent C | Per Cent Mn | Per Cent Cr | Per Cent Ni |
|---|---|---|---|
| 0.13–0.15 | 0.50–0.70 | 17 –18 | 7.0 –7.2 |
| 0.10–0.12 | 0.50–0.70 | 17.90–18.25 | 7.0 –7.2 |
| 0.10–0.12 | 1.20–1.40 | 17.00–17.40 | 7.0 –7.2 |
| 0.09–0.13 | 0.50–0.70 | 18 –19 | 6.25–7.0 |

### *Cold-Rolling Tests*

Tests have shown that a relatively wide range of compositions exists with nickel contents of less than 7 per cent which have the same desirable mechanical properties described above. The narrow limits of compositions described above lie on the upper edge of this relatively wide range of compositions. The wide range existing at nickel contents of less than 7 per cent have been overlooked up to the present time, and it has been generally assumed that more than 7 per cent nickel is necessary in order to produce an austenitic structure sufficiently stable to be useful unless relatively large quantities of manganese were present. Our experiments show that alloys falling in the range of compositions 0.09 to 0.13 per cent carbon, 0.50 to 0.70 per cent man-

ganese, 18 to 19 per cent chromium, and 6.25 to 7.0 per cent nickel have the same high mechanical properties described above after cold-rolling.

An example of the mechanical properties that can be obtained with an alloy in this last-named range of compositions is shown by the data in Table 4, obtained from an alloy containing 0.11 to 0.12 per cent carbon, 18 55 per cent chromium, 6.84 per cent nickel, and 0.50 per cent manganese.

TABLE 4

Mechanical Properties That Can Be Obtained with Alloys Containing Less Than 7 Per Cent Nickel

| Treatment | Yield Strength (0.2 Per Cent Offset), Lbs. per Sq.In. | Tensile Strength, Lbs. per Sq.In. | Per Cent Elongation in 2 In. |
|---|---|---|---|
| 1,950°F., air-cooled | 38,000 | 124,000 | 86.0 |
| Cold-rolled (12.5 per cent) | 60,000 | 152,000 | 55.0 |
| Cold-rolled (22.5 per cent) | 118,000 | 176,000 | 36.5 |
| Cold-rolled (30 per cent) | 151,000 | 193,000 | 25.0 |
| Cold-rolled (41.5 per cent) | 184,000 | 214,000 | 16.0 |

### *Test Results*

The results of our tests on these alloys indicate that, in certain ranges of composition, changes in the concentration of chromium affected the stability of the austenite with respect to its tendency to transform into ferrite in a manner that is contrary to the relationship that we had thought to be true. We had, in the past, believed that increasing the chromium content would make the austenite less stable. However, in the alloys containing from approximately 5.5 to 7.5 per cent nickel and chromium contents in the range from 17 to 21 per cent, increasing the chromium content produced an alloy that, at room temperature, appeared to have more stable austenite when judged on the basis of work-hardening and mechanical properties. Table 5 illustrates this behavior.

### *Effect of Increasing Chromium*

We have just considered the properties of an alloy containing 0.11 to 0.12 per cent carbon, 18.55 per cent chromium, and 6.84 per cent nickel. Compare this with an alloy containing 0.11 per cent carbon, 20.88 per cent chromium, 6.66 per cent nickel, and 0.50 per cent manganese. In the annealed condition this latter alloy has a yield strength of 40,000 lbs. per sq.in., a tensile strength of 105,000 lbs. per sq.in., and an elongation of 65.0 per cent in a 2-in. gauge length. As shown before, the former alloy has a yield strength of 38,000 lbs. per sq.in., a tensile strength of 125,000 lbs. per sq.in., and an elongation of 86.0 per cent. After cold-rolling 30 per cent, the alloy containing 20.88 per cent chromium had a yield strength of 125,000 lbs. per sq.in., a tensile strength of 167,000 lbs. per sq.in., and an elongation of 25 per cent, while the alloy with 18.55 per cent chromium had a yield strength of 151,000 lbs. per sq.in., a tensile strength of 193,000 lbs. per sq.in., and an elongation of 25 per cent. Thus the alloy with the higher chromium content appears to be made up of austenite that is more stable than that in the lower chromium alloy. It can be seen that the tensile strength in the annealed condition as well as the rate of work-hardening of the higher chromium alloy are less than the equivalent properties in the low chromium alloy.

On the basis of the above data it can be seen that in order to obtain high-tensile stainless steel with the highest mechanical properties and at the same time have the broadest range of chemical compositions to work to, it will be desirable for the minimum nickel content of 7 per cent present in most specifications to be lowered to about 6 per cent.

## SPECIFYING MECHANICAL PROPERTIES

In order to specify the desired mechanical properties in these alloys to best advantage, it will be necessary to discard the old classification of tempers that connects the various tempers with yield and tensile strengths. In place of this some classification will have to be adopted that connects the various tempers with yield strengths and allows the tensile strengths to fall where they may, or a different relationship between temper, yield strength, and tensile will have to be used for compositions showing different rates of work hardening.

As an example of what might be encountered if the various tempers were specified on the basis of tensile strength alone, consider some of the properties already described. When considering the properties of regular 18–8 and 19–9, it was pointed out that in this range of compositions cold-rolled strip can be obtained which has a tensile strength of 145,000 to 160,000 lbs. per sq.in.,

TABLE 5

Effect of Varying Chromium Content in the Range of Compositions 5.5 to 7.5 Per Cent Nickel and 17 to 21 Per Cent Chromium

| Alloy | Treatment | Yield Strength, Lbs. per Sq.In. | Tensile Strength, Lbs. per Sq.In. | Per Cent Elongation in 2 In. |
|---|---|---|---|---|
| 18.55 per cent Cr, 6.84 per cent Ni | 1,950°F., air-cooled | 38,000 | 124,000 | 86.0 |
| 18.55 per cent Cr, 6.84 per cent Ni | Cold-rolled 30 per cent | 151,000 | 193,000 | 25.0 |
| 20.88 per cent Cr, 6.66 per cent Ni | 1,950°F., air-cooled | 40,000 | 105,000 | 65.0 |
| 20.88 per cent Cr, 6.66 per cent Ni | Cold-rolled 30 per cent | 125,000 | 167,000 | 25.0 |

TABLE 6

Effect of Composition on the Relationship Between Tensile Strength and Yield Strength

| Alloy | Treatment | Tensile Strength, Lbs. per Sq.In. | Yield Strength, Lbs. per Sq.In. | Per Cent Elongation in 2 In. |
|---|---|---|---|---|
| 302 stainless steel (0.11 per cent C, 19–9) | Half-hard type | 150,000 (min.) | 110,000 (min.) | 8.0 (min.) |
| 18.55 per cent Cr, 6.84 per cent Ni | Cold-rolled (12.5 per cent) | 152,000 | 60,000 | 55.0 |
| 18.55 per cent Cr, 6.84 per cent Ni | Cold-rolled (22.5 per cent) | 176,000 | 118,000 | 36.5 |
| 302 stainless steel (0.11 per cent C, 19–9) | Annealed | 95,000 | 38,000 | 65 |
| 18.5 per cent Cr, 6.8 per cent Ni | Annealed | 124,000 | 38,000 | 86 |

and a yield strength of 129,000 to 140,000 lbs. per sq.in., and an elongation of 15 per cent. Thus, with half-hard 18–8 strip, when a minimum tensile strength of 150,000 lbs. per sq.in. is specified, a minimum yield strength of 110,000 lbs. per sq.in. is obtained. However, if the alloy with 18.55 per cent chromium and 6.84 per cent nickel were supplied to meet a minimum tensile strength of 150,000 lbs. per sq.in., a yield strength of only 60,000 lbs. per sq.in. might be obtained. This latter alloy can be supplied with a yield strength of 110,000, but, in order to obtain it, a tensile strength of 175,000 lbs. per sq.in. must accompany it. With these properties an elongation of 36 per cent is obtained.

Thus it can be seen that this composition has properties superior to the regular 18–8, but that, in order to specify the desired properties, it will be necessary to have specifications different from those in existence for regular 18–8.

### *Effect of Different Compositions*

It is interesting to generalize a little on a comparison of the mechanical properties of the different compositions. In the annealed condition all of the austenitic chromium nickel steels with the same carbon content have approximately the same yield strength. As shown previously, this holds true for the 18.5 per cent chromium, 6.8 per cent nickel analysis as well as for the regular 19–9 composition. However, beyond the elastic range where plastic deformation takes place in the tensile test, the various rates of work-hardening of different compositions influence the stress at which breaking occurs. The compositions with the greatest rate of work-hardening show higher breaking strengths than the ones with lower rates of work-hardening. Thus, the tensile strength of the annealed 19–9 composition is approximately 95,000 lbs. per sq in., while that of the 18.5 per cent chromium, 6.8 per cent nickel composition is approximately 125,000 to 145,000 lbs. per sq.in., although the yield strength of the two are approximately the same. In other words, the yield strength is dependent on the amount of cold work that the alloy has had before being subjected to the tensile test.

In the previously cited case where a wide difference in yield strengths existed at 150,000 lbs. per sq.in. tensile in two different compositions, the 18.5 per cent chromium, 6.8 per cent nickel composition required only 12.5 per cent reduction in cold rolling in order to attain a tensile strength of 150,000 lbs. per sq.in., while the 19–9 composition required approximately 35 per cent cold reduction. When the former composition is given 35 per cent cold reduction, its tensile strength becomes 195,000 lbs. per sq.in. and its yield strength is 165,000 lbs. per sq.in., wth 20 per cent elongation. It has been our experience that approximately 30 per cent reduction in thickness by cold rolling is necessary in order to raise the yield strength so that it is within 75 per cent of the tensile strength (see Table 6).

### *Effect of Cold-Rolling*

In considering the use of strip whose mechanical properties have been obtained through cold-rolling for applications as load bearing structural members, it is natural that attention be given to the variations in properties in different directions resulting from the rolling. Such variations in properties with direction would naturally be different with different lots of material depending primarily upon processing conditions. The following are the results of tests conducted in tension, as well as in compression, on samples taken from strip in both the longitudinal and the transverse directions. The composition of the material tested was 0.12 per cent carbon, 0.47 per cent manganese, 17.96 per cent chromium, and 7.02 per cent nickel. The strip was cold-rolled in our mill as a regular commercial material to a thickness of 0.027 in. It was then stress relieved at a low temperature and tested (see Table 7).

TABLE 7

| | Tension | | | Compression |
|---|---|---|---|---|
| Direction Tested | Yield Strength (0.2 Per Cent Offset), Lbs. per Sq.In. | Tensile Strength, Lbs. per Sq. In. | Per Cent Elongation in 2 In. | Yield Strength, (0.2 Per Cent Offset), Lbs. per Sq.In. |
| Longitudinal | 174,800 | 199,200 | 16.0 | 169,800 |
| Transverse | 184,300 | 203,000 | 13.0 | 199,900 |

Approximately the same results have been obtained by The Union Carbide and Carbon Laboratories using a different lot of strip material containing 0.11 per cent

carbon, 1.32 per cent manganese, 17.15 per cent chromium, and 7.17 per cent nickel which was cold-rolled to a thickness of 0.035 in. Tests were made in the longitudinal and transverse directions in both tension and compression on the material in the as-rolled condition and after stress-relieving as well (see Table 8).

TABLE 8

| | Tension | | | |
|---|---|---|---|---|
| | Yield Strength (0.2 Per Cent Offset), Lbs. per Sq.In. | Tensile Strength, Lbs. per Sq.In. | Per Cent Elongation in 2 In. | Compression |
| Longitudinal, as-rolled | 162,000 | 196,000 | 15 | 146,000 |
| Transverse, as-rolled | 140,000 | 201,000 | 10 | 185,000 |
| Longitudinal, stress-relieved | 181,000 | 198,000 | 14 | 163,000 |
| Transverse, stress-relieved | 172,000 | 202,000 | 10 | 201,000 |

## FATIGUE STRENGTH

Fatigue strength is another property that should be considered in connection with material of this type. The first work that we did in connection with fatigue strength of cold-rolled, high tensile stainless steel strip was a number of years ago on a strip to be used as a spring contact that had to withstand 500,000 reversals of stress from 0 to 110,000 lbs. per sq.in. without breaking. After some experimenting, it was found that results lined up as shown in Table 9. In the as-rolled condition the fatigue strength of the strip was less than half the tensile strength. If the reductions between anneals were kept to less than 40 per cent, stress-relieving at a low temperature raised the fatigue strength to approximately one-half the tensile strength. If, between intermediate anneals, the material had been over-rolled, stress-relieving had only slight effect on the fatigue strength and it remained less than half the tensile strength.

### *Tests on Strip Material*

More recently we have been running fatigue tests on strip material and attempting to actually determine the endurance limit. Fig. 3 is self-explanatory and shows results of fatigue tests carried out on cold-rolled strip containing 0.11 per cent carbon, 17.90 per cent chromium, and 6.72 per cent nickel after having been cold-rolled to a tensile strength of 190,000 lbs. per sq.in. The results of tests are shown in the as-rolled condition as well as after stress-relieving at 300°C. for 24 hours. It can be seen that the fatigue strength of the stress-relieved material is in the vicinity of 100,000 lbs. per sq.in. or approximately 52 per cent of the tensile strength, while the fatigue strength of the as-rolled material is approximately 80,000 lbs. per sq.in., which is

TABLE 9

C 0.16 Mn 0.37 Cr 17.22 Ni 7.20 Si 0.427

Material hot-rolled to 0.250-in. strip. Cold-rolled to 0.040-in. strip with anneals at 2,050°F. spaced at every 30 to 35 per cent cold reduction. After annealing at 0.040 in., the material was cold-rolled 50 per cent to a thickness of 0.020 in. and a tensile strength of 215,000 to 220,000 lbs. per sq.in.

| Results of Fatigue Test Run with Bend Across Rolling Direction and Stress Varying from 0 to 110,000 Lbs. per Sq.In. on Each Flex | Treatment |
|---|---|
| Broke after 115,000 flexes | As-cold-rolled |
| Broke after 101,000 flexes | ..... |
| Broke after 323,000 flexes | After cold-rolling, heated eight hours at 800° to 850°F. Tensile strength unchanged |
| Unbroken after 10,500,000 flexes<br>Unbroken after 10,290,000 flexes | After cold-rolling, heated 16 hours at 800° to 850°F. Tensile strength unchanged |

C 0.16 Mn 0.37 Cr 17.22 Ni 7.20 Si 0.427

Material hot-rolled to 0.250-in. strip. Cold-rolled to 0.040-in. strip with anneals at 2,050°F. spaced at every 60 per cent cold reduction. After annealing at 0.040 in., the material was cold-rolled 50 per cent to a thickness of 0.020 in. and a tensile strength of 215,000 to 220,000 lbs. per sq.in.

| Results of Fatigue Test Run with Bend Across Rolling Direction and Stress Varying from 0 to 110,000 Lbs. per Sq.In. on Each Flex | Treatment |
|---|---|
| Broke after 116,000 flexes | As-cold-rolled |
| Broke after 37,000 flexes | ..... |
| Broke after 285,000 flexes<br>Broke after 84,000 flexes | After cold-rolling, heated five hours at 800° to 850°F. Tensile strength unchanged |
| Broke after 251,000 flexes<br>Broke after 95,000 flexes | After cold-rolling, heated 15 hours at 800° to 850°F. Tensile strength unchanged |
| Broke after 175,000 flexes<br>Broke after 163,000 flexes | After cold-rolling, heated 24 hours at 800° to 850°F. Tensile strength unchanged |

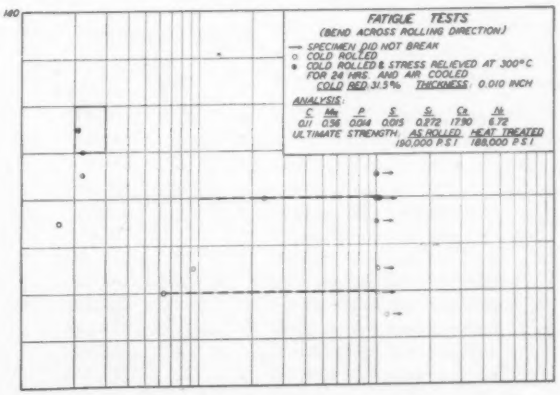
140
FATIGUE TESTS
(BEND ACROSS ROLLING DIRECTION)
SPECIMEN DID NOT BREAK
COLD ROLLED
COLD ROLLED & STRESS RELIEVED AT 300°C FOR 24 HRS. AND AIR COOLED
COLD RED. 31.5%
THICKNESS 0.010 INCH
ANALYSIS:
C Mn P S Si Cr Ni
0.11 0.56 0.014 0.015 0.272 17.90 6.72
ULTIMATE STRENGTH: AS ROLLED HEAT TREATED
190,000 P.S.I. 188,000 P.S.I.

FIG. 3.

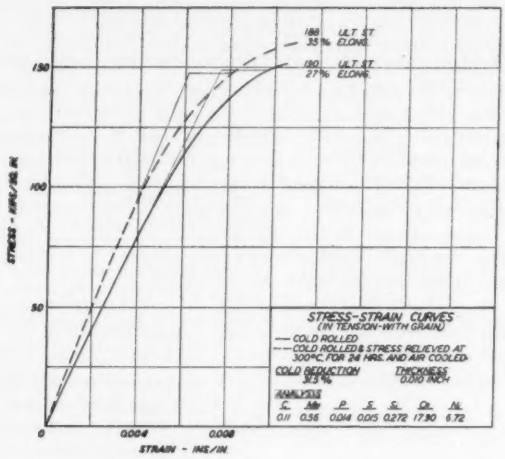


FIG. 4.

in the vicinity of 43 per cent of the tensile strength. These figures are in line with the data that have been reported in the literature for other ferrous alloys.

It is interesting to compare these results on fatigue strength with the stress-strain curves for the same material. Fig. 4 shows the stress-strain curve for the two materials whose fatigue characteristics were shown in the previous graph. In this connection it is worthy of noting that the stress-relieved material at a stress of 100,000 lbs. per sq.in. has undergone approximately the same amount of strain as the unstress-relieved material has undergone at a stress of 80,000 lbs. per sq.in.

Thus, it appears that both the stress-relieved and unstress-relieved materials fail in fatigue at approximately the same deflection but that, in the case of the stress-relieved material, a greater pressure was necessary in order to produce this amount of deflection.

### *Use of Manganese*

The ability of manganese to replace nickel in austenitic stainless steel has been recognized for a number of years. At the present time, with a scarcity of nickel existing, it has become desirable to attempt to replace as much nickel as possible with manganese. Thus, attempts have been made to produce a high tensile material with the properties just described but containing as low an amount of nickel as possible. In making such a substitution, the effect on the stability of the austenite, both at room temperature and at elevated temperatures, should be considered. The stability at elevated temperatures is of importance in connection with the hot-rolling characteristics of the material. It will be recalled from data previously shown that the alloy containing 18 per cent chromium and 7 per cent nickel consisted of more stable austenite at elevated temperatures than it did at room temperature. However, this condition does not appear to remain if too much nickel is replaced by manganese, because alloys are produced that have a tendency to break up during hot-rolling. Increase in the carbon content or the addition of nitrogen may help to relieve this condition and permit the substitution of a greater quantity of manganese. However, at the present time this is at an experimental stage.

Table 10 gives mechanical properties obtained with one of our experimental heats which we believed represents about the greatest practical substitution of manganese. It will be noted that the tensile properties of the annealed as well as the cold-rolled material do not differ materially from the properties of the material discussed previously containing approximately 18 per cent chromium, 7 per cent nickel, and 0.50 per cent manganese. Thus, 3 per cent nickel has been replaced with approximately $4^1/_2$ per cent manganese and an alloy with similar characteristics has been obtained.

(*Continued on page 272*)

TABLE 10

| Heat | C | Mn | P | S | Si | Cr | Ni |
|---|---|---|---|---|---|---|---|
| 32,985 | 0.10 | 4.98 | 0.028 | 0.013 | 0.418 | 18.01 | 4.40 |

Laboratory annealed—1,925°F., 5 min., a.c. on 0.032-in. sheet

| Condition | Tensile Strength, Lbs. per Sq.In. | Yield Strength,* Lbs. per Sq.In. | Per Cent Elongation in 2 In. | Hardness |
|---|---|---|---|---|
| Lab annealed | 126,600 | 43,960 | 82.0 | |
| | 121,800 | 42,980 | 79.0 | |
| | 130,800 | 42,980 | 76.0 | 86 86.5 87 R B |
| | 125,250 | 42,850 | 68.0 | |
| 8.3 per cent cold-reduced | 162,000 | 77,400 | 58.0 | |
| 8.1 per cent cold-reduced | 156,000 | 766,600 | 55.0 | |
| 22.3 per cent cold-reduced | 178,900 | 114,400 | 35.0 | |
| 22.3 per cent cold-reduced | 182,900 | 108,800 | 36.0 | |
| 35.3 per cent cold-reduced | 226,500 | 184,250 | 14.0 | |
| 35.3 per cent cold-reduced | 224,100 | 182,000 | 13.0 | |
| 40.6 per cent cold-reduced | 232,800 | 198,400 | 12.0 | |
| 40.6 per cent cold-reduced | 234,000 | 192,700 | 12.0 | |

* Yield strength taken at offset of 0.002 in. from modulus line on stress-strain curve.

# Temperature Effects on Turbine Supercharger Installations

PHILIP COLMAN*

*Lockheed Aircraft Corporation*

ABSTRACT

In order to obtain consistent flight test data for airplanes with turbine superchargers, account must be taken of the variation of engine brake horsepower with changes in atmospheric conditions. The variation of power available with the change of free air temperature is greatly magnified by the complexity of the induction system when the turbine supercharger and intercooler are included. The limits of power available on any day are dictated by one of the following three conditions: (1) the engine manufacturer's specified manifold pressure and engine r.p.m. values; (2) the turbine manufacturer's specified maximum allowable turbine wheel speed; and (3) the engine manufacturer's specified maximum allowable intake port temperature. The power available at any altitude may be calculated. However, these calculations can only be approximate, and therefore it is suggested that complete charts be derived based on the data available and that all flight test data be corrected to standard conditions by use of the increments shown on these charts. Once a standard day power chart has been derived for a turbine-equipped airplane from flight test data and the correction charts, all future flight tests may be corrected to this power chart. The steps then become identical to those currently used to correct flight test data for airplanes with only single-speed geared engine superchargers.

## INTRODUCTION

WHEN THE INDUCTION SYSTEM of the power plant of an airplane engine includes a turbine-type supercharger in series with a gear-driven integral supercharger, the variation of atmospheric conditions greatly affects the brake horsepower output of the engine. In the procedure of flight testing the airplane to establish its performance and to determine the effects of changes of configuration on that performance, the methods of reduction of the test data must include a consideration of the engine operation considerably more accurate than is normally undertaken in the test procedure with other types of power plants. This is a result of the greater complexity of the induction system, which includes a variable speed supercharger, an air cooler, a carburetor, and a constant-speed supercharger, as shown diagrammatically in Fig. 1.

Engineering flight tests are made for the following purposes: a check of the general flying qualities of the airplane; a development of improvements to the design; a determination of the performance of the aircraft; and a study of the effects of variations of configuration on the airplane's performance. In all types of flight tests, especially for the last two purposes, it is necessary to reduce the actual data obtained to a common basis so that although atmospheric conditions may change between tests the corrected results are directly comparable. This means in particular that the flight data must be corrected for atmospheric conditions, which is accomplished by reducing all data to the norm—the defined N.A.C.A. standard day. The actual performance of the airplane is corrected for two effects: the aerodynamic variation of air forces with the change of the density of the air and the variation of brake horsepower available from the engine. The first effect is unchanged by the introduction of the turbine supercharger, except insofar as the basic characteristics of the airplane are changed by the movement of the flap-type doors that adjust the air flow across the radiators to maintain the engine air, coolant, and oil temperatures at the required values. This is an effect that is not considered in this study but which may be a large factor in the performance of the airplane

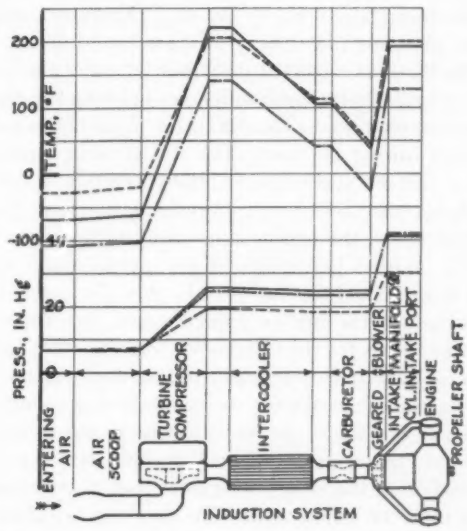


FIG. 1. Example of temperature and pressure variation through induction system. Conditions: pressure altitude = 35,000 ft.; airplane indicated air speed = 120 m.p.h.; and engine speed = 2,900 r.p.m.

| Notation | Variation from Standard Temperature | Limitation | Turbine Speed, R.P.M. | Shaft Power Delivered, B.H.P. |
|---|---|---|---|---|
| Dot-dash line | − 40°F. | Maximum manifold pressure | 23,200 | 2,040 |
| Full line | 0°F. | Maximum turbine speed | 25,000 | 1,880 |
| Dotted line | + 40°F. | Maximum port temperature | 22,350 | 1,230 |

Presented at the Power Plants and Propellers Session, Eleventh Annual Meeting, I.A.S., New York, January 25–29, 1943.

* Chief Aerodynamics Engineer.

under varying atmospheric conditions. The correction for radiator door drag variation with door angle requires a knowledge of the magnitude of the drag increments plus the standard aerodynamic formulas.

### Flight Test Power Correction

The effect to be studied is the variation of brake horsepower delivered by the engine with the change of atmospheric conditions. Normally, in flight test for the determination of rate of climb (for example), engine power, pressure and density altitudes are derived, and the climb rate is corrected for power by use of the increment of brake horsepower difference between the engine manufacturer's power chart and the actual horsepower obtained during the test. For the airplane equipped with a turbine supercharger, the correction is not so simple because there is no calibrated power-plant power chart to which the performance at altitude can be corrected. With a knowledge of the manufacturer's sea-level power chart for the engine, plus the characteristic curves for the turbine supercharger, plus the effectiveness curves for the intercooler, the theoretic power-plant power chart for brake horsepower versus altitude can be calculated for the standard day conditions. Methods for this type of calculation are available. However, there are so many variables that enter the calculation of the complete system that many assumptions must be made which can give rise to much inaccuracy. Therefore, it is suggested that correction charts be prepared from the basic data on hand and that the actual flight test data for brake horsepower versus altitude be corrected by the increments derived from these charts, thereby establishing a standard day reference power chart. Once this reference chart is established from preliminary flight test, all future test data may be corrected for power by adding the difference between the power obtained on the flight and the power read off the reference chart at the required altitude. The flight test procedure then becomes identical to that for airplanes equipped only with single-stage geared blowers.

The induction system consists of the air scoop, turbine supercharger, intercooler, carburetor, geared supercharger, and engine intake manifold and port. A schematic diagram of the system is shown in Fig. 1. The engine port is the orifice through which the charge of vaporized gasoline and air is delivered to the cylinder —labeled "cylinder intake port" in Fig. 1. When the engine is operating at a constant number of revolutions per minute, set by the propeller governor, the power delivered by each cylinder to the propeller shaft is dependent on the number of pounds of fuel plus air flowing into the cylinder on each intake stroke. The number of pounds of the mixture which enters the cylinder is a direct function of the pressure and temperature of that charge in the cylinder intake port. This study is made to show how the pressure and temperature of the charge may vary because of a change of the temperature of the entering air at a constant outside pressure—that is, for each pressure altitude. From this, the variation in engine brake horsepower available for various atmospheric conditions may be derived. The pressure in the intake manifold and at the engine port is the same, and therefore the terms "port pressure" and "manifold pressure" may be used interchangeably.

The type of turbine considered here is driven by the exhaust gas flow that connects the engine cylinder exhaust ports and the gas turbine of the supercharger into the system. Each of the component parts of the induction system will be considered separately.

### Air Scoop

The engine air is normally obtained from a forward-facing duct opening that "scoops" the required amount of air, as dictated by the power and specific air consumption of the engine. The velocity of the entering air is thus dependent on the engine requirements, the density of the incoming air, and the area of the duct. The curves for the efficiency of the turbine supercharger are based on the pressure rise in compressor, the rise being measured from the inlet pressure and density at the entrance flange of the compressor. There is a total head pressure, the sum of the dynamic plus static pressures, of the air available at the scoop entrance. This total available head is converted, according to Bernoulli's equation, into a pressure and an air velocity according to the dictates of the system. The velocity at the compressor entrance and the attendant static pressure can be determined from the engine power and the specific air consumption.

$$V_c = Q/A_c = KP/60\sigma\rho_0 g A_c$$

where

$V_c$ = air velocity at the compressor entrance in ft. per sec.
$A_c$ = compressor entrance area in sq.ft.
$Q$ = quantity of air in cu.ft. per min.
$K$ = specific air consumption in lbs. per min. per b.hp.
$P$ = engine b.hp.
$\sigma$ = relative density
$\rho_0$ = sea-level air density = 0.002378 slugs per cu.ft.
$g$ = acceleration of gravity = 32.2 ft. per sec. per sec.

Neglecting the change of density, which is normally small:

$$\Delta p_c = 0.001189(1 - C)(\sigma V_a^2) - \left(\frac{0.0000563}{\sigma}\right)\left(\frac{KP}{A_c}\right)^2$$

where

$\Delta p_c$ = difference of static pressure between the compressor entrance and the atmosphere in lbs. per sq.ft.

$C$ = per cent loss in total head between that available in the free stream and the total head at the compressor entrance

$V_a$ = airplane speed in ft. per sec.

In this equation the total loss of available head is taken as a function of the dynamic pressure based on the airplane velocity. This is a good approximation because of the fact that with a well-formed air scoop the major part of the head loss is due to the drag of the airplane component parts ahead of the scoop plus losses at the scoop entrance due to the convergence or divergence of the stream lines. For intake systems comprised of long ducts plus turns, an added factor should be included because the duct losses may reach relatively large values. This factor would take the form of a constant times the dynamic pressure of the air in the duct.

This static pressure difference $\Delta p_c$ is often called ram pressure. Ram, defined as an increment in altitude gained due to the ram pressure, may be written by combining the previous equation with the pressure-altitude relationship:

$$dp/dh = \sigma/13.05$$

$$\Delta h = 0.0155(1 - C)(V_a)^2 - 0.00072\,(KP/\sigma A_c)^2$$

= ram increment of altitude in ft.

This ram increment of altitude is plotted in Fig. 2 for various air speeds and altitudes. As an example, with the 2,000-b.hp. engine chosen, 3,450 ft. of ram is available at 400 m.p.h. true air speed at 30,000 ft. corresponding to a ram pressure of 1.39 in. of mercury. For the case shown in Fig. 1, for standard atmospheric conditions at 35,000 ft. at an indicated speed of 120 m.p.h. and true air speed of 216 m.p.h., the ram is 3.6 lbs. per sq.ft. (0.05 in. Hg) or 152 ft. of altitude. The atmospheric pressure is 7.04 in. Hg; the compressor entrance pressure is 7.09 in. Hg. It is interesting to note that at climb speeds at high altitudes the ram may become negative because of the fact that the air in the compressor entrance is flowing at a velocity greater than that of the airplane. The value of $C$ is a function of the installation and may be considerably greater than 20 per cent used in Fig. 2. The value $K$ is a function of engine operation and varies with power and carburetor mixture setting, usually specified by the engine manufacturer.

These equations will be varied for designs in which the scoop is in the slipstream of the propeller. The factor $C$ may be changed to include the slipstream effect by using the relationship of dynamic head in the slipstream to that of the free stream, assuming a constant propeller efficiency.

$$qs/q = 1 + (590{,}000\,\eta P/V_a{}^3D^2)$$

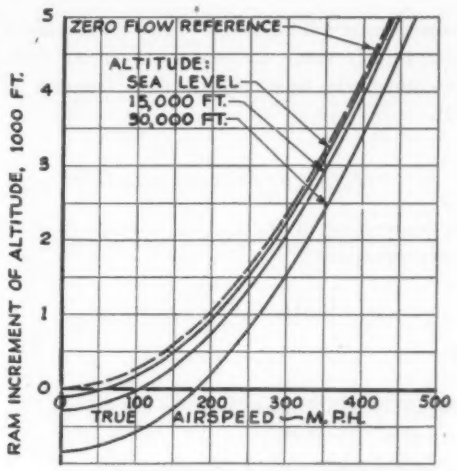


FIG. 2. Increase in critical altitude due to ram for various air speeds. $P$ = 2,000 b.hp.; $K$ = 0.12 lb. per min. per b.hp.; $A_c$ = 0.60 sq.ft.; $C$ = 0.20; $\Delta h = 0.0155\,(1 - C)(V_a{}^2) - 0.0072\,(KP/\sigma A_c)^2$, $V_a$ = airplane speed—ft. per sec.

where

$qs$ = dynamic head in the slipstream in lbs. per sq. ft.

$q$ = dynamic head in the free stream in lbs. per sq.ft.

$V_a$ = airplane speed in ft. per sec.

$D$ = propeller diameter in ft.

$\eta$ = propeller efficiency

For the sake of simplicity, the pressure equations have used the Bernoulli equation for incompressible fluids. The error caused is within the accuracy of determining the constants for the equations. However, since the pressure rise in a compressor is a function of the temperature of the entering air, the adiabatic temperature rise due to the compression of the air is important. Bernoulli's equation for the compressible fluid case is unwieldy unless simplifying assumptions are made. For the determination of temperature at the compressor intake, the temperature rise due to bringing the air from its initial free stream velocity to the airplane velocity is used. Thus, the temperature increment takes the simple form:

$$\Delta T = 0.82\,(V_a/100)^2\,\eta_s$$

where

$\Delta T$ = temperature rise of the entering air in degrees Fahrenheit

$V_a$ = true airplane speed in ft. per sec.

$\eta_s$ = correction factor for the deviation from complete stoppage of the air and for the dissipation of some of the heat before reaching the compressor ($\eta_s$ = 0.75)

For the example of 400 m.p.h. at 30,000 ft. for which the ram increment of altitude was 3,430 ft., the ram

temperature rise will be 21°F. For the standard case shown in Fig. 1, where the true air speed is 216 m.p.h., the incoming air temperature rises from −66° to −60°F.

### Turbine Supercharger

The compressor of the turbine supercharger follows the basic equation:

$$(v_t)^2 = 6{,}088\ T_c Y/\eta_p$$

where

$v_t$ = tip speed of the compressor wheel
$Y = (P_2/P_1)^{0.283} - 1$
$P_2$ = compressor outlet pressure
$P_1$ = compressor entrance pressure
$\eta_p$ = pressure coefficient
$T_c$ = compressor entrance temperature in degrees Fahrenheit, Absolute

The temperature rise across the compressor is

$$\Delta T = (v_t)^2/6{,}088 = TY/\eta_p$$

This equation makes the assumption that the temperature coefficient, $\eta_t$, is equal to the pressure coefficient. This approximation is slightly conservative. The pressure coefficient is a function of the quantity of flow and the compressor wheel speed, varying from a value of the coefficient at a low ratio of flow quantity to wheel r.p.m. corresponding to the minimum for stable operation to a pressure coefficient of zero at a high ratio of quantity to r.p.m. Data on the variation of the pressure coefficient, $\eta_p$, with these parameters must be obtained from test stand experiments for exact calculations. Since these are a function of the size and characteristics of the compressor diffuser, no general rules can be established, except that for design power in well-balanced designs close to the maximum pressure coefficient can be maintained at all altitudes. The example of Fig. 1 assumes a value of $\eta_p = 0.625$, which on a standard day at 35,000 ft. and 25,000 turbine r.p.m. results in a temperature rise across the compressor from −60° to +222°F. and a pressure rise from 7.09 in. Hg to a compressor out pressure of 25.8 in. Hg.

The turbine end of the supercharger is dependent upon the exhaust gas flow of the engine for operation. As a general rule, for a well-designed installation, the power available from the engine is never a limit of the supercharger operation. By this is meant that some other factor, usually maximum allowable turbine speed as determined from the material stress limit, is the controlling factor dictating the maximum operation of any installation. The limit of exhaust power available will only be critical for low-cruising power flight conditions. This will be discussed later in this paper.

### Intercooler

The intercooler is placed in the induction system so that advantage may be taken of the turbine supercharger pressure rise without the detrimental effects of high carburetor air temperatures. The effectiveness of the intercooler is defined as

$$E = (T_{I1} - T_{I2})/(T_{I1} - T_a)$$

where subscript $I_1$ and $I_2$ denote the entering and exiting intercooler points and $T_a$ equals the outside air temperature in degrees Fahrenheit. The effectiveness of an intercooler is a function of the cooling air pressure drop across the radiator, the air density, and the engine air mass flow. For a constant engine brake horsepower, the engine air mass flow is constant. For the standard installation with adjustable intercooler cooling air exit doors, the effective cooling air pressure drop may be held constant. Above the critical altitude, the maximum altitude to which full engine power may be maintained, the air mass flow reduces as the engine power reduces. However, the maximum angle on the cooler door is usually obtained at critical altitude. Therefore, above critical altitude, the effective pressure drop reduces approximately as the air density goes down. The result is that the intercooler effectiveness remains substantially constant.

The pressure drop of the engine air through the intercooler is a function of the dynamic head of the air in the system. For installations in which this loss is large, the variation must be taken into account. The pressure drop is thus a function of the mass flow squared and the reciprocal of the density of the engine air in the intercooler. For a constant power the mass flow remains constant, but the density decreases and the turbine speed increases with altitude.

Fig. 1 assumes an intercooler effectiveness of 0.40 and an intercooler engine air pressure loss of 1 in. of mercury. In the standard atmosphere case the temperature of the air entering the intercooler is 222°F. With an outside air temperature of −66°F., there is a temperature difference of 288°F. Thus, in passing through the intercooler, the engine air will be cooled to 106°F.

### Carburetor

The pressure drop across the carburetor and its attendant duct system for the full throttle setting conditions is more easily treated in combination with the engine-geared supercharger because of the interrelation between the two. This will be discussed in the next section. In this study, only the full throttle conditions are of interest, because in most of the operations of an installation including a turbine supercharger, the full carburetor throttle position is attained at low altitudes.

The temperature drop due to the vaporization of the gasoline may be calculated from the latent heat of

vaporization of the fuel. Using a value of 137 B.t.u. per lb.,* and a value of the specific heat of the air of 0.243 B.t.u. per lb. per degree Fahrenheit,

$$\Delta T = 563\ (F/A)$$

where $F/A$ equals the fuel to air ratio for the engine and $\Delta T$ equals the temperature decrease in degrees Fahrenheit. The fuel to air ratio varies according to the power and mixture setting of the engine from values of 0.060 to 0.130. Tests have shown that the temperature drop across the carburetor does not follow this relationship, mainly because there is not complete vaporization across the carburetor. However, here the interest lies in the ultimate conditions existing at the engine intake port, by which point complete vaporization should be accomplished in this type of installation. This assumption is valid provided it is kept in mind when considering the operation of the geared engine blower.

In Fig. 1 a fuel-air ratio of 0.12 is assumed, dropping the temperature of the engine air for the standard day condition from the carburetor in temperature of 106°F. to the geared engine blower entrance temperature of 39°F.

### Geared Engine Blower

The engine-driven compressor follows the same equations as set forth for the turbine compressor. The values of temperature, pressure, and pressure coefficient must be specified. If the equation is based on the pressure rise from the pressure at the carburetor face and if the temperature for the formula is the carburetor temperature minus the temperature change due to the vaporization of the fuel, then, with a logical value of pressure coefficient, $\eta_p$, the engine geared blower pressure rise and, thus, the pressure delivered to the engine cylinder intake port can be determined. Test data indicate that a value of $\eta_p$ between 50 and 60 per cent should approximate most designs.

The temperature change between carburetor and port is the fuel vaporization temperature drop plus the blower temperature rise, which is only a function of the engine blower speed as shown by the equation give in the turbine supercharger discussion.

In Fig. 1 a pressure coefficient of 0.50 is assumed, resulting, for a standard atmosphere case, in a pressure rise from a carburetor pressure of 24.8 to 41.3 in. Hg. The temperature rose to 193°F. from the geared blower entrance temperature of 39°F. Thus, the fuel-air charge entering the cylinder at the port has a temperature of 193°F. and a pressure of 41.3 in. Hg. Entering the assumed basic engine power chart of Fig. 3 with 41.3 in. Hg, a power of 1,960 b.hp. is obtained. This chart is based on a port mixture charge temperature of 147°F. Using the approximate rule that power varies 1 per cent for each 10° of temperature deviation,

* International Critical Tables, Vol. II.

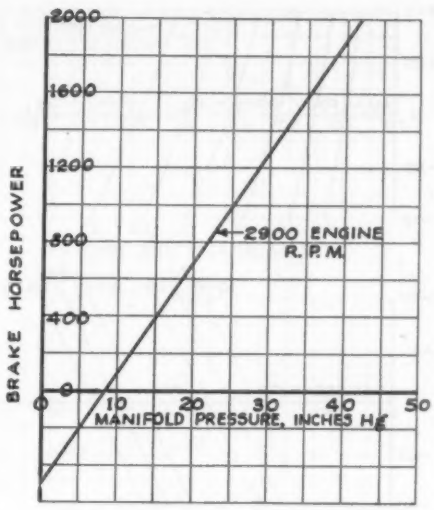


Fig. 3. Assumed power-chart brake horsepower versus manifold pressure. Back pressure = 29.92 in. Hg; carburetor temperature = 60°F.; port temperature = 147°F.

46° equals 4.6 per cent power reduction. The engine will deliver 1,880 b.hp.

### Correction Charts

The complexity of the induction system with a turbine supercharger installation necessitates the simplifications that have been discussed. The more data that can be obtained from the manufacturers of the components plus information derived in flight test with pressure and temperature measuring instruments throughout the system, the more accurate can be the computation of the brake horsepower available. But the best method is to record flight test data and correct it by increments to standard day conditions. Thus, if the increments are slightly in error because of small discrepancies in the necessary parameters, the total quantity values of power and altitude will only be slightly affected, and all flight test results may be corrected to the standard day condition, which presents the basis of comparison of one aircraft with another or of one configuration with another.

The type of correction charts recommended are shown in Figs. 4, 5, and 6. These charts show the variations of manifold pressure and altitude available with variation of atmospheric conditions from standard. Thus in Fig. 5, for the power régime where maximum turbine speed is the limitation, the change in manifold pressure between that obtained on the flight test day and that which could be obtained on a standard day can be found by plotting in the flight test point and following parallel to the lines shown to the standard day value. The variation in port temperature which affects the brake horsepower available is also shown. Thus, if a flight at 40,000-ft. pressure altitude on a −40°F. day,

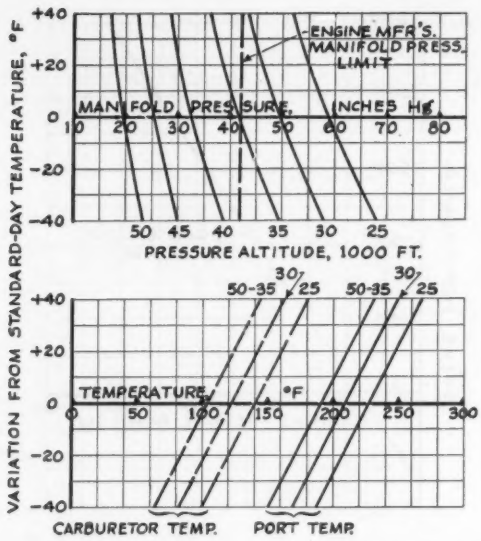


FIG. 4. Changes of pressures and temperatures with variations from a standard day, at constant engine and turbine speed. Engine speed = 2,900 r.p.m.; turbine speed = 25,000 r.p.m.

limited by the 25,000 turbine r.p.m. restriction, showed that at 38.7-in. Hg manifold pressure was available, Fig. 4 shows that at this same pressure altitude on a standard day only 32.3-in. manifold pressure would be available. The port temperature would change from 150° to 191°F. The maximum value allowable is dictated by the engine manufacturer and therefore cannot be exceeded.

Fig. 5 is a chart for correcting a power régime that is limited by an arbitrary port temperature specification. Since engine power limits and engine reliability are, besides other factors, functions of cylinder intake port temperatures, this can restrict the maximum power available before the maximum turbine speed limitation is reached. Thus, using Fig. 5, if on the flight test day the maximum pressure altitude for a given manifold pressure was obtained when the port temperature indicator read 200°F. (or the carburetor temperature indicator read 113°F.), the limiting altitude for the same temperatures on a standard atmospheric day may be determined. Entering the chart with the flight test day pressure altitude and deviation from standard temperatures, the slope of the lines may be followed to the standard day condition to find the altitude available on a standard day with the same manifold pressure and port temperature. It will be noted that for the parameters chosen to construct Fig. 5 the variation in altitude is considerable. Flying at a +40°F. day, a 42-in. Hg manifold pressure can be attained at a maximum altitude of 16,000 ft. pressure altitude. On a standard day this manifold pressure could be taken to 36,100 ft. if the 200°F. port temperature was the only limit. However, inspection of the corresponding turbine r.p.m. lines shows that the 25,000 turbine r.p.m. limit has been exceeded, so Fig. 4 will dictate the critical altitude on a standard day.

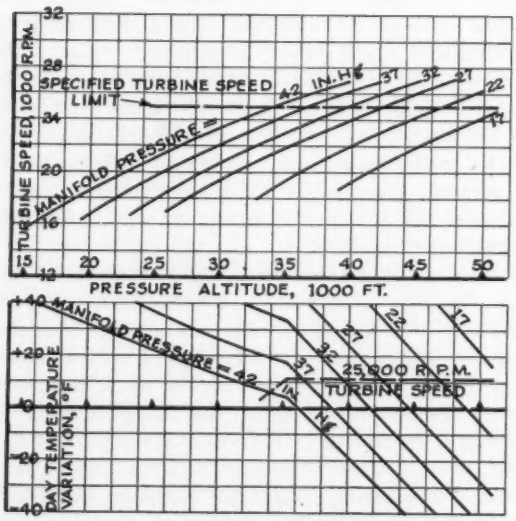


FIG. 5. Changes of turbine speed and altitude with variations from a standard day, at constant engine speed and engine port temperature. Engine speed = 2,900 r.p.m.; carburetor temperature = 113°F.; port temperature = 200°F.

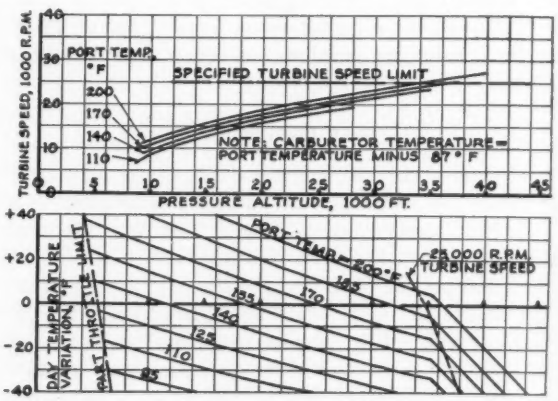
TURBINE SPEED, 1000 R.P.M.
PORT TEMP., °F
SPECIFIED TURBINE SPEED LIMIT
NOTE: CARBURETOR TEMPERATURE = PORT TEMPERATURE MINUS 87° F
PRESSURE ALTITUDE, 1000 FT.
DAY TEMPERATURE VARIATION, °F
PART THROTTLE LIMIT
25,000 R.P.M. TURBINE SPEED

FIG. 6. Changes of turbine speed and engine port temperature with variations from a standard day, at constant engine speed and manifold pressure. Engine speed = 2,900 r.p.m.; manifold pressure = 42 in. Hg.

Fig. 6 presents the derivation of a relatively minor correction that is to be used where the engine manufacturer's arbitrary manifold pressure limit is the only governing factor. This chart shows, for a given manifold pressure and pressure altitude, the change of port temperature with atmospheric conditions. This is to be used in conjunction with the power correction for port temperature, 1 per cent of power per 10° of temperature. Thus, if on a 40°F. day a flight is made at 10,000 ft. pressure altitude, the port temperature will be 48°F. higher than would be obtained with the same manifold pressure on a standard day.

These correction charts may be constructed assuming zero ram at the intake scoop. Ram affects the absolute values, but the variation with atmospheric conditions is approximately the same. Therefore, although a flight test point does not fall exactly on the calculated line, the point may be extrapolated to standard conditions by following the slope of the neighboring lines.

These charts must be calculated for each particular airplane, engine, turbine, and intercooler combination. The charts included herein are shown for extreme conditions in an effort to clarify the discussion. These are sample charts. The assumptions made for their calculation are shown in the following section.

### Sample Calculations

The sample charts, Figs. 4, 5, and 6, have been calculated based on the assumptions given in the following paragraphs. These assumptions are chosen to emphasize the limiting conditions.

(1) Ram is equal to zero.

(2) Turbine pressure coefficient is constant = 0.625. Maximum allowable turbine speed = 25,000 r.p.m. Turbine compressor wheel diameter = 1 ft. Turbine in temperature and pressure = outside air temperature and pressure.

(3) Intercooler effectiveness is constant = 0.40. Intercooler pressure drop is constant = 1 in. Hg.

(4) Carburetor fuel to air ratio = 0.12. Fuel vaporization temperature drop = 67°F.

(5) Engine-geared supercharger pressure coefficient based on carburetor air temperature less fuel vaporization temperature drop = 0.50. Engine supercharger gear ratio = 8.5 to 1. Engine compressor wheel diameter = 0.75 ft.

(6) Engine power variation with manifold pressure as shown in Fig. 3 for the conditions: (*a*) engine speed = 2,900 r.p.m.; (*b*) back pressure = 29.92 in. Hg.; and (*c*) port temperature = 147°F. Engine manufacturer's manifold pressure limit = 42 in. Hg. Engine manufacturer's port temperature limit = 200°F. Engine power variation with port temperature is 1 per cent per 10°F.

Substituting these factors into the basic equations, the charts are obtained. Each chart will be explained separately. This will include the application of the charts to the derivation of the brake horsepower available versus altitude curve, shown in Fig. 9.

*Fig. 4—Constant turbine speed and constant engine speed.* This chart is to be used for the correction of manifold pressure available above the limiting turbine speed critical altitude.

$$MP = \left[\left(\frac{P_2}{P_1}\right)_{\text{turbine}} (P_{\text{atmosphere}}) - \Delta P_{\text{intercooler}}\right] \left[\left(\frac{P_2}{P_1}\right)_{\text{carburetor to port}}\right]$$

where $MP$ equals the port manifold pressure.

$$\left(\frac{P_2}{P_1}\right)_{\text{turbine}} = (Y_{\text{turbine}} + 1)^{3.53}$$

$$Y_{\text{turbine}} = \left(\frac{\pi ND}{60}\right)^2_{\text{turbine}} \left(\frac{\eta_p}{6{,}088}\right)\left(\frac{1}{T_{\text{atmosphere}}}\right) = \frac{176.5}{T_{\text{atmosphere}}}$$

$$T_{\text{carburetor}} = T_{\text{atmosphere}} + \left(\frac{\pi ND}{60}\right)^2_{\text{turbine}} \left(\frac{1}{6{,}088}\right) - E\left[T_{\text{atmosphere}} + \left(\frac{\pi ND}{60}\right)_{\text{engine blower}} \left(\frac{1}{6{,}088}\right) - T_{\text{atmosphere}}\right]$$

$$= T_{\text{atmosphere}} + 170$$

$$\left(\frac{P_2}{P_1}\right)_{\text{engine blower}} = (Y_{\text{engine blower}} - 1)^{3.53}$$

$$Y_{\text{engine blower}} = \left(\frac{\pi ND}{60}\right)^2_{\text{engine blower}} \times \left(\frac{\eta_p}{6{,}088}\right)\left(\frac{1}{T_{\text{entrance}}}\right) = \frac{77.2}{T_{\text{entrance}}}$$

$$T_{\text{entrance}} = T_{\text{carburetor}} - \Delta T_{\text{fuel cooling}} = T_{\text{carburetor}} - 67$$

$$T_{\text{port}} = T_{\text{entrance}} + \left(\frac{\pi ND}{60}\right)^2_{\text{engine blower}} \left(\frac{1}{6{,}088}\right) = T_{\text{entrance}} + 154$$

*Fig. 5—Constant engine speed and engine port temperature.* This chart is to be used for the correction of critical altitude as limited by the arbitrary port temperature maximum for a given engine manifold pressure.

$$P_{\text{carburetor}} = \frac{MP}{(P_2/P_1)_{\text{engine blower}}}$$

$$Y_{\text{engine blower}} = \left(\frac{\pi ND}{60}\right)^2 \left(\frac{\eta_p}{6{,}088T}\right)_{\text{engine blower}} = 0.1525$$

$$(P_2/P_1)_{\text{engine blower}} = (Y + 1)^{3.53} = 1.651$$

$$T_{\text{engine blower}} = T_{\text{port}} - \left(\frac{\pi ND}{60}\right)^2_{\text{engine blower}} \left(\frac{1}{6{,}088}\right) = 506°R$$

For a $MP$ = 42 in.,

$$P_{\text{turbine out}} = 1 + (MP/1.651) = 26.4 \text{ in. Hg.}$$

$$T_{\text{atmosphere}} = \frac{T_{\text{port}} - (\pi ND/60)^2\,(1/6{,}088)_{\text{engine blower}} + \Delta T_{\text{vaporization}}}{1 + Y[1 - (E/\eta_p)]}$$

$$= 573/(1 + 0.96Y)$$

$$T_{\text{atmosphere}} = T_{\text{port}} - \left(\frac{\pi ND}{60}\right)^2 \left(\frac{1}{6{,}088}\right)_{\text{engine blower}} + \Delta T_{\text{vaporization}} = 573°R$$

$$N_{\text{turbine}} = \left[\frac{T_{\text{atmosphere}}\,(Y)(6{,}088)}{\eta_p}\right]^{1/2}\left(\frac{60}{\pi D}\right)_{\text{turbine}}$$
$$= 1{,}883\,[(OAT)(Y)]^{1/2}$$

*Fig. 6—Constant engine speed and engine manifold pressure.* This chart is to be used for the correction of port temperature at a constant altitude below critical altitude. The equations for this calculation are identical to those used for Fig. 5, except that the port temperature is varied and the manifold pressure is held constant for each line.

In Figs. 5 and 6 the variation of turbine speed with change of conditions is included as a matter of interest, although they need only be known to insure that the maximum allowable turbine speed is not exceeded. The minimum altitude limit of Fig. 5 is the altitude where the engine supercharging in itself is sufficient to obtain the desired manifold pressure, below which point part throttle carburetor settings exist.

To illustrate the use of these three charts and emphasize the effects of the temperature variation from standard day conditions, the next three figures have been constructed. Fig. 7 shows the manifold pressure

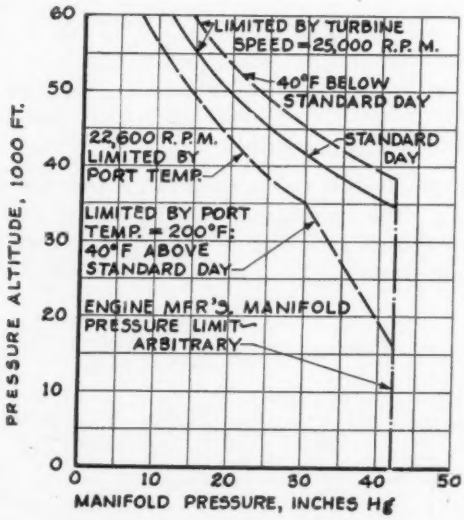


FIG. 7. Example of: manifold pressure available versus pressure altitude, for variations from a standard day. Engine speed = 2,900 r.p.m.; zero ram conditions.

available versus altitude. On a standard N.A.C.A. day, inspection of Figs. 4 and 5 reveals that the critical altitude for the engine manufacturer's 42-in. Hg maximum allowable manifold pressure is limited by maximum turbine speed before the limiting port temperature is reached. The critical altitude and the variation of manifold pressure above critical altitude is dictated solely by Fig. 4. For a cold day when the air temperatures are 40°F. below standard at all altitudes, Fig. 4 still limits the pressures available, and the increase in manifold pressure available above the standard day condition may be read directly by following the lines of

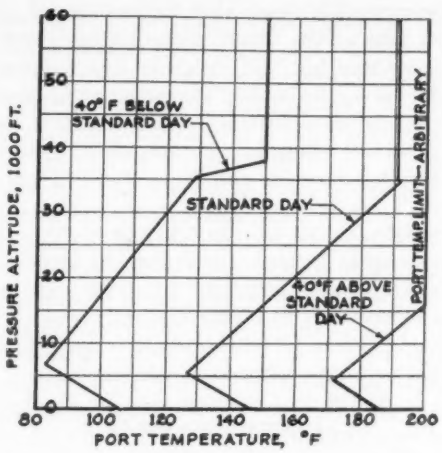


FIG. 8. Example of: engine port temperature versus pressure altitude, for variations from a standard day. Engine speed = 2,900 r.p.m.; zero ram conditions; carburetor temperature = port temperature minus 87°F.

Fig. 4 from the standard to the −40°F. condition. In Fig. 7, it can be seen that 3,500 ft. more altitude is obtainable for a given manifold pressure. On the hot day, 40°F. above standard at all altitudes, the port temperature limits of Fig. 5 become critical before maximum turbine speed is reached. Following the constant 42-in. Hg line of Fig. 5, it is seen that at 40°F. above standard, the critical altitude for 42-in. Hg manifold pressure is reduced to 16,000 ft. Fig. 5 then limits the available manifold pressure for all altitudes above 16,000 ft. Above the tropopause the standard temperature becomes a constant. Therefore, in this region the turbine speed becomes a constant at the value that results in the port temperature limit.

Similarly, the variation of port temperature with atmospheric temperature conditions can be read from Figs. 4, 5, and 6. These are plotted in Fig. 8 and follow the same limits as the manifold pressure lines. Nothing has been said of the back pressure variation with altitude. This factor is small for the maximum power conditions. At a constant altitude, changes of air temperature will have a minor effect on the back pressure. Since engine power varies approximately $^1/_2$ per cent per in. Hg back pressure, the error in the power derivation is small.

Having the correct manifold pressure and port temperature for the type of day in question, the brake horsepower versus altitude can be drawn by reference to the engine power chart. Using the assumed chart of Fig. 3, the final power-plant power chart is drawn in Fig. 9. This figure shows that 35 per cent of the standard day brake horsepower is lost for this installation on a 40°F. above standard day; 7 per cent is gained on a 40°F. below standard day. This will give a marked change in airplane performance and, if these effects of temperature on engine power are not realized and corrected for, there can be no consistency between air-

plane flight tests and no basis of airplane comparison can be obtained. If a flight test climb were made at 35,000 ft. on a 40°F. above standard day, the power would be found to be limited to 1,230 b.hp. corresponding to a manifold pressure of 30.2 in. Hg and a port temperature of 200°F. From Fig. 5, it could be found that under standard conditions, this manifold pressure could have been obtained at 43,000 ft. except that, under these conditions, the corresponding turbine speed would be 25,800 r.p.m. Being limited to 25,000 r.p.m., the cross-plotted line of Fig. 6 shows the critical altitude to be 34,800 ft. With Fig. 4, it is found that 42 in. and 192°F. port temperature will be available at 34,800 ft. under standard conditions, which corresponds to 1,910 b.hp. Similarly, from a flight test power of 1,780 b.hp. at 40,000-ft. pressure altitude (38.7-in. Hg manifold pressure, 150°F. port temperature) on a 40°F. below the standard day temperature, the standard day power obtained from the pressures and temperatures corrected by the use of Fig. 4 is 1,380 b.hp. These are extreme cases for examples.

## Cruising Power

Cruising power limits may be established in a similar way, except for the extremely low powers. Some installations may be limited by compressor surge limits. Well-balanced systems, however, will generally run into the maximum exhaust power available limits where the exhaust waste gate closes before the compressor surge is experienced. The lower extreme of power requirements is generally the power required for maximum range cruise conditions. The maximum altitudes at which the optimum power-engine r.p.m. combinations (optimum b.m.e.p. for minimum specific fuel consumption) may be maintained is limited by the altitude at which the waste gate closes at these power settings. The nature of the calculations for these critical altitudes is approximate because of the large error involved in small variations in the necessary constants of calculation. The calculation itself is involved. However, flight tests for these conditions are only made to determine the flight plan for instruction of a pilot for long-range flight operation. The pilot is instructed to fly at a specified speed and set his power required at as low an engine r.p.m. as is possible, approaching the arbitrary minimum r.p.m. and maximum b.m.e.p. limits. Establishment of the closed waste gate critical altitude for low powers on a flight test day is all that is required to obtain the approximate maximum altitude limits. Therefore, a flight can be made at various altitudes, at each setting various engine speeds and opening the throttle until the maximum (waste gate closed) manifold pressure is obtained. Plotting these limits and converting them into terms of brake horsepower, a low-power cruising limit chart can be obtained that will suffice for the data required. Thus, in Fig. 9, the dotted lines represent the minimum power limits for the power chart, the solid lines showing the maximum limits. The complete power-plant brake horsepower available chart is then represented in Fig. 9.

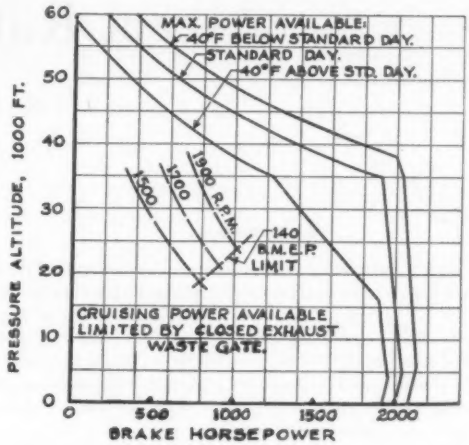


FIG. 9. Example of: brake horsepower available versus pressure altitude, for variations from a standard day. Engine speed = 2,900 r.p.m.; zero ram conditions.

## Conclusion

These calculations discussed herein may be refined by the inclusion of accurate determination of the constants involved from bench or flight tests. However, if one climb and one high-speed flight are made at various altitudes with an aircraft, the data obtained may be corrected to standard conditions once, and all future flight tests may be corrected by reference to this established power chart. The cruising régime requires one additional test flight. The correction is important for an installation including a turbine and intercooler because of the magnifying effects of these components on the engine operation with varying atmospheric conditions.

One further note should be added. If the chart is desired for a span of 50,000 ft. in altitude, the variation of the pressure coefficient $\eta_p$ with the compressor flow and r.p.m. should be accounted for by use of the characteristic curves. In the construction of Fig. 9, a constant value of $\eta_p$ was assumed. Accordingly, the altitude for zero power under standard atmospheric conditions is found to be 66,500 ft. However, the variation of the parameters with air density and pressure will reduce the actual pressure available at extreme altitudes and, except by special design, the altitude for zero power will be reduced.

# Aspect Ratio Corrections

K. D. WOOD*
*Purdue University*

SUMMARY

Customary calculations of aspect ratio correction for lift curve slope are shown to be in error by as much as 30 per cent for aspect ratios of 1.5 or less. The assumptions and results of various theoretic analyses are summarized, and a new form of plotting is proposed showing the discrepancies between various theories and between theory and experiment. Simple empirical equations consistent with acceptable theory are proposed which closely approximate the experimental results.

A new method is also proposed for estimating the airplane efficiency factor $e$ often used in aspect ratio corrections for induced drag, taking account of the size and shape of the fuselage as well as the wing aspect ratio.

## INTRODUCTION

IN AIRPLANE PERFORMANCE and stability computations it has become customary to assume that the lift and drag coefficients of the wing and tail surfaces are expressible with useful accuracy by the linear equations

$$C_L = a\alpha_a = m\alpha_a/57.3 \tag{1}$$

$$C_D = C_{DV} + KC_L^2 \tag{2}$$

where $a$ and $m$ are the lift curve slope per degree and per radian, respectively, and $C_{DV}$ and $K$ are the intercept and slope, respectively, of the best fitting straight line on a graph of $C_D$ vs. $C_L^2$ for the most important range of $C_L$ from 0.2 to 1.0. Other notation is N.A.C.A. standard. For the usual tapered wing $C_{DV}$ is the same as the value of $C_{D_{e_{min.}}}$ published in N.A.C.A. reports for all practical purposes.

Both the lift curve slope $a$ and the induced drag factor $K$ are functions of the aspect ratio $A$, determinable by theory and experiment. Tests on wing models have most often been made for $A = 6$, and corrections to other aspect ratios have been through an intermediate step involving a theoretic "infinite aspect ratio" in which the flow was supposedly two-dimensional. The equations given in reference 1 for these corrections are:

$$m = (4/3)m_6[A/(A + 2)] \tag{3}$$

$$C_D = C_{D6} - (C_L^2/6\pi) + (C_L^2/\pi A) \tag{4}$$

In Eqs. (3) and (4), the subscripts $(\ )_6$ designate test results at aspect ratio 6; the quantity $4m_6/3$ may be considered as the lift curve slope for infinite aspect ratio and may be designated $m_0 = 57.3a_0$; the quantity $C_{D6} - (C_L^2/6\pi)$ may be considered as the drag coefficient for infinite aspect ratio and may be designated $C_{D_0}$ and called the "effective profile drag coefficient."

## PRANDTL WING THEORY

The above method of aspect ratio correction is based on the classic "finite wing" theory of Prandtl,[3] involving a "lifting line" vortex in a perfect fluid, which was substantiated by a series of airfoil tests at aspect ratios of 1 to 7, all of the tests being fitted by a common line with fair accuracy when the above corrections were applied. The discovery was so outstanding and the tests so convincing that tests of this sort have rarely been repeated, but recent tests on tail surfaces of aspect ratios from 2 to 4 have consistently yielded markedly different results as may be seen in Fig. 1. Millikan[4] points out that the agreement between Prandtl's theory and data is astonishing in view of the simplicity of the assumptions.

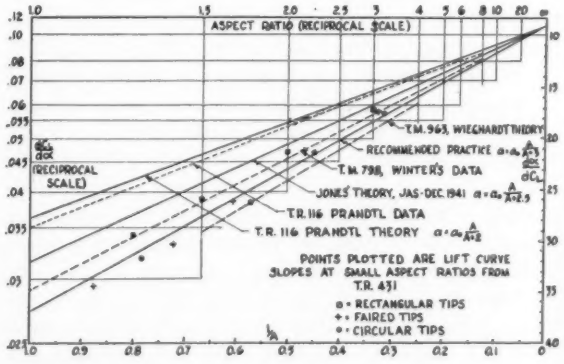
ASPECT RATIO (RECIPROCAL SCALE)
T.M. 963, WIEGHARDT THEORY
RECOMMENDED PRACTICE
T.M. 798, WINTER'S DATA
JONES THEORY, JAS-DEC. 1941
T.R. 116 PRANDTL DATA
T.R. 116 PRANDTL THEORY
POINTS PLOTTED ARE LIFT CURVE SLOPES AT SMALL ASPECT RATIOS FROM T.R. 431
o = RECTANGULAR TIPS
+ = FAIRED TIPS
• = CIRCULAR TIPS
(RECIPROCAL SCALE)

FIG. 1. Comparison of theory and experiments on slope of lift curves of wings of various aspect ratios.

## STUDIES OF THE LIFT CURVE SLOPE

Jones[5] has pointed out that the Prandtl equation for the lift curve slope of a finite elliptical wing requires a correction so that instead of having the form of Eq. (3), with $4m_6/3 = 2\pi$, it should have the form

$$m = 2\pi A/(EA + 2) \tag{5}$$

where $E$ is the ratio of the semiperimeter to the span of the ellipse and is therefore a function of $A$. Jones' equation, plotted in Fig. 1, is found to be closely approximated for $A > 1$ by the equation

$$m = 2\pi A/(A + 2.5) \tag{6}$$

Presented at the Aerodynamics Session, Eleventh Annual Meeting, I.A.S., New York, January 25–29, 1943.

* Professor of Aeronautical Engineering.

Wieghardt[6] has shown that for rectangular airfoils of small aspect ratio a close approximation of the lift curve slope requires assuming a series of vortexes distributed along the chord. A line is drawn on Fig. 1 representing the equation

$$m = 2\pi A/(A + 3) \tag{7}$$

and this is seen to lie between the Wieghardt theory and the data of Winter.[7] References 8 and 9 also present data consistent with that of Winter, typical data from reference 8 being plotted on Fig. 1. While much data on airfoils of low aspect ratio are so scattering as to make it difficult to isolate the tip-shape and aspect ratio factors, there seems to be abundant evidence to the effect that corrections made on the basis of Eq. (3), which represents current practice, are likely to give lift curve slopes as much as 30 per cent higher than experiment justifies in the region of $A = 1.5$, such as is sometimes involved in vertical tail surfaces. If a simple correction equation is desired, it is much better to use

$$m = (3m_0/2)[A/(A + 3)] \tag{8}$$

than to use Eq. (3). Eq. (8) will give values of the infinite aspect ratio slope $3m_0/2$ slightly greater than the theoretic $2\pi$ for some tests, and a good empirical practice, consistent with most test results and with theory more accurate than the lifting-line theory, is proposed as

$$\left.\begin{aligned} m &= \frac{2\pi A}{A + 2.7} \text{ for elliptical tips} \\ m &= \frac{2\pi A}{A + 3} \text{ for rectangular tips} \end{aligned}\right\} \tag{9}$$

In the light of adequate theory, the so-called infinite aspect ratio slope $a_0 = m_0/57.3$ as usually computed has no important meaning. It is the slope for two-dimensional flow if the theory applied, which it does not. Corrections have been made by going to infinity and back again, on the wrong track. The reciprocal plotting of Fig. 1 is intended not only to get infinity on the paper but also to plot theories and experiments as straight lines with engineering accuracy. If this thesis is accepted, one more of the uncertainties involved in the calculation of airplane stability is eliminated from the catchall tail efficiency factor $\eta_t$ which usually appears in such calculations.

## Correction of Induced Drag for Aspect Ratio

While a chart similar to Fig. 1 can be prepared covering the correction of induced drag for aspect ratio (such a chart is presented in reference 10), no theoretic considerations have been found showing wide departures from the Prandtl theory at low aspect ratio such as were found for the lift curve slopes. In further view of the wide adoption of Oswald's method of performance analysis[11] and the need for incorporation of fuselage drag variation with the induced drag of the wing, it is chosen to compare theory and experiments on induced drag by means of the airplane efficiency factor $e$ defined by the equation

$$K = dC_D/d(C_L^2) = 1/\pi Ae \tag{10}$$

and to consider that the drag variation of the fuselage may be added to the induced drag of the wing in the manner expressed by the equation

$$1/e = (1/e_w) + \Delta(1/e)_f \tag{11}$$

Theory and data for wings alone are compared in Fig. 2(a). The only theoretic results shown are those of Prandtl and Glauert, represented by the lines at the top of the figure. Low aspect ratio data are from references 7 and 9; high aspect ratio data are from references 12 and 13. The low aspect ratio data are scattering, so the trend of the graph is uncertain, but there is enough evidence to conclude that $e_w$ is not independent of aspect ratio. The recommended practice based on the best data available to the author is indicated by the broken lines.

The data on the effect of fuselage drag are even more sketchy. The plotting [Fig. 2(b)] assumes that the effect of the fuselage on the wing will be proportional to the ratio of fuselage frontal area to wing area for a given fuselage shape and wing incidence, though these are really separate variables that should be treated independently by drawing additional lines on the graph.

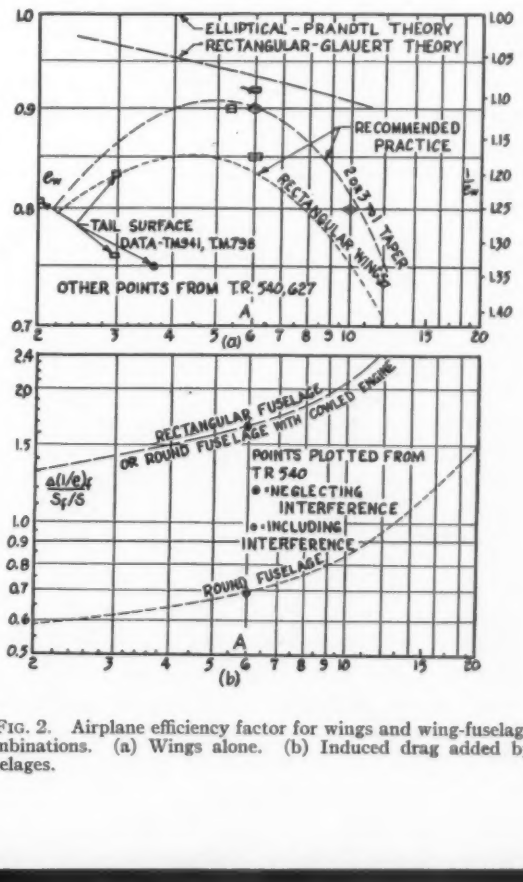


FIG. 2. Airplane efficiency factor for wings and wing-fuselage combinations. (a) Wings alone. (b) Induced drag added by fuselages.

Additional research on this point would be highly desirable. With sufficient general data, $e$ can be estimated for a new design without special wind-tunnel tests in the manner illustrated by the following *example.*

*Problem:* Estimate the airplane efficiency factor $e$ for a combination of a rectangular wing of aspect ratio 7 and $S = 180$ sq.ft. with a rectangular fuselage of frontal area $S_f = 15$ sq.ft.

*Solution:* In Fig. 2(a) read $1/e_w = 1.22$. In Fig. 2(b) read $\Delta(1/e)_f/(S_f/S) = 1.75$. Compute $\Delta(1/e)_f = (1.75)(15/180) = 0.15$. Compute by Eq. (11) $1/e = 1.22 + 0.15 = 1.37$ and $e = 1/1.37 = 0.73$.

Since $e$ need not be known closer than 5 per cent for most purposes, this treatment is believed useful in spite of the inadequacy of the data on which it is based.

### References


[1] Civil Aeronautics Administration, Air Commerce Manual 04.129B2.

[2] Jacobs, Eastman N., and Abbott, Ira H., *Airfoil Section Data Obtained in the NACA Variable-Density Tunnel as Affected by Support Interference and Other Corrections,* N.A.C.A. T.R. No. 669, 1939.

[3] Prandtl, L., *Applications of Modern Hydrodynamics to Aeronautics,* N.A.C.A. T.R. No. 116, 1921.

[4] Millikan, C. B., *Aerodynamics of the Airplane,* p. 49; John Wiley & Sons, New York, 1941.

[5] Jones, Robert T., *Theoretical Correction for the Lift of Elliptical Wings,* Journal of the Aeronautical Sciences, Vol. 9, No. 1, p. 8, November, 1941.

[6] Wieghardt, Karl, *Chordwise Load Distribution of a Simple Rectangular Wing,* N.A.C.A. T.M. No. 963, 1940.

[7] Winter, H., *Flow Phenomena on Plates and Airfoils of Short Span,* V.D.I. Special Issue (Aviation) 1936, N.A.C.A. T.M. No. 798.

[8] Zimmerman, C. H., *Characteristics of Clark-Y Airfoils of Small Aspect Ratios,* N.A.C.A. T.R. No. 431, 1932.

[9] Martinov, A., and Kolosov, E., *Some Data on the Static Longitudinal Stability and Control of Airplanes* (Design of Control Surfaces), Publication of Central Aero-Hydrodynamical Institute of Moscow, N.A.C.A. T.M. No. 941, 1940.

[10] Wood, K. D., *Technical Aerodynamics,* p. 32; The McGraw-Hill Book Company, New York, 1935.

[11] Oswald, W. B., *General Formulas and Charts for the Calculation of Airplane Performance,* N.A.C.A. T.R. No. 408, 1932.

[12] Jacobs, Eastman N., and Ward, Kenneth E., *Interference of Wing and Fuselage from Tests of 209 Combinations in the NACA Variable-Density Tunnel,* N.A.C.A. T.R. No. 540, 1935.

[13] Anderson, Raymond F., *The Experimental and Calculated Characteristics of 22 Tapered Wings,* N.A.C.A. T.R. No. 627, 1938.


---

(*Continued from page 260*)

This high manganese alloy offers difficulties in processing which, at the present time, have not been completely overcome. Whether this alloy becomes a commercial product is dependent on the ability of producers to overcome troubles encountered during rolling it. All of the material that can be processed without cracking during the initial stage of the rolling has satisfactory properties in the form of cold-rollod strip. The problem is not one of getting consistent mechanical properties but one of converting the ingot into finished strip.

# Effects of Yielding and Perforations on a Wing Tension Surface

RICHARD K. KOEGLER* AND ARTHUR SCHNITT†

*Curtiss-Wright Corporation*

SUMMARY

Two different but interdependent ideas concerning stress calculations are presented. Perforation effects on stress-strain curves are first investigated. A method of calculating these curves for any gauge length, perforation size, and spacing is shown. This method depends on an effective perforation length and an ultimate stress concentration factor. Test data are given to substantitate the method. Tentative curves are presented from which the effective perforation length and stress concentration factor for various perforations can be found for use in engineering calculations.

The method of accounting for yielding in ultimate strength calculations is next presented. It consists of applying stress-strain curves to the strain distributions found in the elastic range. Its practicability and validity depend on the fact that in the plastic range the stresses determined will not be seriously in error for moderate variations of strain. Examples based on a two-beam wing with heavy 24ST extruded flanges show that calculations neglecting yielding may indicate failure in the wrong member and at too low a load (15 per cent in a typical case). In addition, if an appreciable length of surface yields, shear lag may be seriously affected.

The method applies to many cases besides the one shown. Because of the slow increase of stress with strain after yielding, approximate calculations afford reasonably accurate results, and it may be found in the future that yielding effects will simplify many stress calculations rather than complicate them.

## INTRODUCTION

THE BASIC FUNDAMENTAL of any strength calculation is the consideration of deflection or strain. By assuming that the stress is directly proportional to the strain, it is possible to calculate stress directly. However, when the yield point is exceeded, this proportionality changes and conventional stress calculations break down. In the calculation of ultimate strengths, the effects of yielding are important and must be accounted for. This is often done by determining fictitious allowable stresses to be used with conventional formulas, as in the modulus of rupture of certain sections in bending. In many cases, such a procedure is not possible, but the fact that beyond yield the stress increases slowly with moderate strain increases makes it possible to solve satisfactorily certain problems by employing certain rough approximations.

Examples of cases where the low modulus of elasticity beyond yield affects the stress distribution at ultimate load and permits solutions by approximations are shown to be the tension surfaces of such stressed skin structures as wings, fuselages, and tail surfaces. The compression surfaces are also affected by yielding, but the effects are usually slight because of the close proximity of compression yield and compression crippling. Where materials of different properties are used acting in combination, the effects of yielding are especially important. As an illustrative example, such a case is chosen—namely, a wing tension surface constructed with thick 24ST extruded flange sections and 24ST Alclad skin with chordwise ribs and stiffeners but no spanwise stiffeners.

In this case, as in most aircraft applications, perforations such as rivet and bolt holes are present which affect the ultimate tensile strengths and elongations and the shape of the stress-strain curves of the materials used.

### *Procedure*

It is first shown that the gauge length for stress-strain curves to be used in investigating an entire wing surface should be taken as the distance between regularly repeated perforations (such as the rib or chordwise stiffener rivet holes) and should include one set of such perforations. Next it is explained why the stress-strain curves are all plotted using the stress in the unperforated region as the ordinate. This is important to remember in studying the method or the curves.

It is then established that the stress-strain curve of unperforated material for any gauge length over 2 in. can be taken the same as the curve for a 2-in. specimen for the purposes of this paper. Upon this basis a method for finding the curve for any perforated specimen is developed. This method is based on the concept that most of the material acts like an unperforated specimen but that a certain length near the perforations acts as though it were all at the net stress through the perforations. The length assumed acting at the net stress is called "effective perforation length" ($d_L$) and is expressed in terms of the perforation diameter. Calculations and test data are given to prove the method correct, to permit determination of $d_L$ for various cases, and to illustrate the dependency of $d_L$ on certain parameters. The stress at which the perforated specimen will fail is found by the use of a stress concentration factor, $K$. Tentative curves of $d_L$ and $K$ for various perforation sizes and spacing are

Presented at the Structures Session, Eleventh Annual Meeting, I.A.S., New York, January 25–29, 1943.

* Project Stress Engineer, Structures Department, Airplane Division.

† Stress Analyst, Structures Department, Airplane Division.

shown for estimating these factors for engineering use. Brief discussions of the dependence of $d_L$ and $K$ on ultimate elongation and other factors, of the interdependence of $d_L$ and $d_K$ (effective perforation width), and of the effects of yielding on stress distributions near perforations in the plastic range are also given.

### *Developing the Analysis*

To develop a method of analysis for engineering purposes, a set of skin and flange stress-strain curves for an example wing are found, and the effects of the stress-strain curves on stress distribution at ultimate load are investigated for two simplified cases and for one case which resembles a typical wing surface. In the simple example of a flat surface without shear lag, it is shown that to neglect yielding would indicate too low a flange stress at the time of failure and would predict failure in the wrong member. In the second simplified example of a flat surface with shear lag, it is shown that it is possible for yielding to practically eliminate the sag in the chordwise distribution of skin stress usually caused by shear lag. The average skin efficiencies above and below yield are compared, and the percentage of ultimate load at which flange yielding occurs is noted to be at approximately 80 per cent of ultimate.

The probable effects of yielding are then investigated by means of a typical tension surface in which shear lag and flange stress vary across the span and the skin is arched. Stress distributions at failure are determined by applying stress-strain curves to the strain distributions known to exist before yielding, and the validity of the assumption is investigated by comparison of calculated skin and flange elongations for the total span. The assumptions are shown to be reasonable provided an appreciable length of span yields.

### *Application of the Method*

The application of the method to an actual case is illustrated by means of an example. The determinations of skin efficiencies and stress calculations are shown. A comparison with the results obtained if yielding is neglected is afforded by a parallel example. It is shown that the effects on the ultimate load carried and on the calculated skin stresses are appreciable. This is especially true in the present case where the skin and flange have different properties. To neglect yielding in this case is 15 per cent too conservative.

It is concluded that the method does not entail too much extra work in actual practice and is worth using in many instances. A discussion of the approximate treatment of the subject is given.

## Effects of Perforations

### *Summary of Perforation Effects on Stress-Strain Curves*

The comparative behavior of perforated aluminum-alloy specimens and solid specimens is shown (especially in Figs. 2 and 3) to be as follows: The stress-strain curve for a perforated specimen based on the stress across the solid or gross section has a slightly lower modulus of elasticity in the elastic range, a lower yield point, and lower stress at all strains in the plastic range. The ultimate elongation is reduced, and the ultimate stress across the perforated or net section is reduced because of stress concentration. The shape of the stress-strain curve, the ultimate elongation, and the degree of stress concentration are functions of the size and spacings of the perforations and of the elastic and plastic properties of the solid material.

### *Gauge Lengths to Be Used*

When bolt and rivet holes are considered in flanges and skins in tension, the stress-strain curves for each material must contain the added local yielding at the perforations and must represent considerable lengths of the materials. This is apparent when it is considered that, with the materials acting in combination, local differentials in strain occurring in the flanges and skin are of little consequence because of the ability of the flange and skin and their attachments to absorb these small differentials. However, over appreciable lengths, the strains in each material will "average out" into average strains that will affect the general strain distribution of the surface. Thus, gauge lengths must be used which are reasonable in size and yet represent the average action of a large portion of the wing. For example, with a method of wing construction which employs chordwise stiffeners at approximately every 8 in., the gauge length for the skin would be 8 in. and would contain one row of rivets. Likewise, the gauge length for the flange might be the same, or, if there were large bolt holes only at ribs, the distance between ribs would be used.

### *Use of Gross Areas in Plotting*

Note that all data and curves are based on the stress in the gross area, the reasons for which follow. These points become apparent later in the study.

(1) In a perforated specimen with a large gauge length, more material is acting at the gross stress than at the net stress. This means, as is shown later, that the stress-strain curves for perforated and solid materials will be more nearly alike when based on gross stress than if net stress is used. This is most noticeable in the elastic range and just beyond yield. The most striking differences in the stress-strain curves are in the ultimate stress and the ultimate elongation. Thus it is easier to visualize effects of perforations on stress-strain curves.

(2) Since only the ultimate stress and elongation are appreciably affected if gross stress is considered, it is easier to visualize the effects of different perforations and materials on wing strength.

(3) From a practical point of view of the structures engineer, only approximate knowledge of the perforation sizes need be known for design purposes. This is because the shapes of the stress-strain curves in the elastic range and just beyond yield are not seriously affected by moderate changes in perforations.

(4) Finally, the load carried by each element of skin or flange for use in designing splices can be determined directly by multiplying the corresponding stress for the element by its gross area.

### *Stress-Strain Curves of Solid Specimens*

Before attempting the study of the stress-strain curves of perforated specimens, the items that affect those of solid specimens and the extent of these effects are noted.

The variations of stress with strain for solid aluminum-alloy materials are obtained by test in accordance with A.S.T.M. standards[1] in order to have a basis for comparison. Standard tensile specimens for extrusions are $^1/_2$ in. in diameter and those for sheets are $^1/_2$ in. wide. Strain measurements are gauged in approximately a 1-in. length, while ultimate elongation is measured in a 2-in. length across the fracture by matching the several ends of the specimen.

However, in actual airplane construction these materials exist in widely varying cross-sectional dimensions and lengths, both of which affect the stress-strain curves. Shanley[2] investigated the effect of the length of material over which strains are measured and found that the stress-strain curve was identical for gauge lengths from $^1/_4$ to 30 in. up to within a few per cent of the ultimate stress. In a perforated material failure occurs at the perforations, and the solid portion of the material acts at a stress less than ultimate. Therefore, the variation of stress with strain in the solid portion of a perforated material is independent of the length of the solid material.

The effect of cross-sectional area upon the stress-strain curve has been investigated by the authors. It was found that, for extrusion specimens up to 2 sq.in. in area and for various thicknesses of sheet specimens up to 5 in. wide, the shapes of the stress-strain curves were the same as those determined from standard specimens up to within a few per cent of ultimate load.

Therefore, the variation of stress with strain in the solid portion of a material is taken as that determined from standard 2-in. specimens for use in all calculations.

### *Method of Calculating Stress-Strain Curves—Concept of $d_L$*

If the local disturbance in the vicinity of a perforation (stress concentration) is disregarded and if the perforation is a circular hole of diameter $d$ in a specimen of width $w$ and thickness $t$, the stress-strain curve for a gauge length $L$ (see Fig. 1) could be calculated simply by

$$\epsilon_A = [\epsilon_N d + \epsilon_G(L - d)]/L \qquad (1)$$

In this equation $\epsilon_A$ represents the average strain per unit length in length $L$, and $\epsilon_N$ and $\epsilon_G$ are the strains per unit length corresponding to the stresses in the net and gross sections, respectively. In other words, the stress-strain curve could be obtained by summing the elongations existing in the net and gross sections and averaging them over a given length at various net and gross stresses up to the ultimate stress of the material.

However, it is known that a concentration of stress exists at a perforation in the elastic range,[3] and it has been established by numerous tests that a stress concentration continues to exist to a certain extent in the plastic range even for highly ductile materials. This is later proved by the fact that the ultimate stress of a perforated dural specimen based on net area is less than that for the solid material. The effect of stress concentration is to increase the elongation in the neighborhood of the net section and thus it seems reasonable to replace the rivet diameter, $d$, by an effective perforation diameter, $d_L$, in calculating stress-strain curves (see Fig. 1).

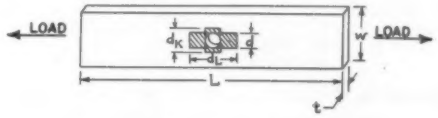


FIG. 1. Concept of $d_L$ and $d_K$.

### *Description of Specimens Tested*

In order to study the effects of perforations and stress concentration upon the stress-strain curves of 24ST Alclad sheet and 24ST extrusions, numerous solid and perforated specimens were tested.

The 24ST Alclad sheet specimens ranged in thicknesses from 0.025 to 0.081 in. and were 1, 3, and 5 in. wide. Perforations of $^1/_8$, $^5/_{32}$, and $^3/_{16}$ in. in diameter were placed at the geometric center of the specimens spaced at 1 in. so that the 1-, 3-, and 5-in. wide specimens contained 1, 3, and 5 perforations, respectively, in a row perpendicular to the sides of the specimens. The 24ST extruded specimens were machined from extrusions of two different original thicknesses (0.25 and 1.0 in.). Machined thicknesses of $^1/_4$, $^1/_2$, and $^3/_4$ in. were varied with widths of 1 and 2 in. One perforation was placed in each extruded specimen and these were from $^1/_8$ to $^3/_4$ in. in diameter. To simulate actual conditions, the sheet specimens perforations were plugged with appropriate sized flathead A-17ST rivets while the extrusion perforations were reamed and AN standard steel bolts inserted. Strains were measured in 1-, 2-, and 8-in. gauge lengths. Maximum elongations were measured in the same gauge lengths as for strains by matching the fractures of the failed specimens.

TABLE 1

Solid Material Properties

| Material Designation | 24ST Alclad | 24ST Extrusion (1 in.) | 24ST Extrusion (1/4 in.) |
|---|---|---|---|
| Actual material description | 24ST Alclad sheet, tested as received | Machined from 1 in. thick; 24ST extrusion | Machined from 0.25 in. thick; 24ST extrusion |
| Yield tensile stress, lbs. per sq.in. | 48,800 | 60,000 | 54,000 |
| Ultimate tensile stress, lbs. per sq.in. | 66,000 | 79,000 | 69,600 |
| Maximum elongation in 2 in. in per cent | 22 | 12 | 17 |
| Maximum elongation in 8 in. in per cent | 18 | 10 | 14 |
| Ratio of ultimate to yield tensile strength | 1.35 | 1.32 | 1.29 |
| Reference stress-strain curve | Fig. 2, Curve A | Fig. 3, Curve A | (None) |

TABLE 2

Sample Calculation of Stress-Strain Curve (2-In. Perforated Specimen—24ST Alclad Sheet)

| Col. Pt. Ref. | (1) Net stress (Selected) | (2) Corres. strain Curve A, Fig. 2 | (3) Gross stress 1 (0.875), Fig. 2 | (4) Corres. strain Curve A, Fig. 2 | (5) Total strain in 2 in. (0.538) (2) + (1.462) (4) | (6) Average strain, in. per in. 5/2 |
|---|---|---|---|---|---|---|
| 1 | 61,000* | 0.0725 | 53,400 | 0.0242 | 0.0744 | 0.0372 |
| 2 | 59,000 | 0.0560 | 51,600 | 0.0170 | 0.0550 | 0.0275 |
| 3 | 56,000 | 0.0370 | 49,000 | 0.0074 | 0.0307 | 0.0154 |
| 4 | 52,000 | 0.0185 | 45,500 | 0.0047 | 0.0168 | 0.0084 |
| 5 | 48,000 | 0.0058 | 42,000 | 0.0043 | 0.0094 | 0.0047 |
| 6 | 36,000 | 0.00367 | 31,500 | 0.0032 | 0.0067 | 0.0034 |

* Ultimate net stress from test (Fig. 2).

A résumé of the solid material properties appears in Table 1. For convenience, the three different aluminum-alloy materials tested are designated as 24ST Alclad, 24ST extrusion (1 in.), and 24ST extrusion (1/4 in.). Note that the maximum elongations given are those determined from the A.S.T.M. standard specimens. Also note that the skin was loaded parallel to the direction of rolling.

### *Stress-Strain Curves for Perforated Specimens and Calculations*

To find the effective perforation length $d_L$, including stress concentration effects on elongation, various points on the test stress-strain curves are selected and $d_L$ is calculated by means of Eq. (1). For example, the recorded stress-strain curve for a 2-in. gauge length specimen is reproduced in Fig. 2 as Curve B. Then, for an elongation of 0.0154 in. per in., a gross stress of 49,000 lbs. per sq.in., and a corresponding net stress of 56,000 lbs. per sq.in.

$$0.0154 = [2 - d_L)0.0074 + 0.0370d_L]/2$$

$$d_L = 0.538 \text{ in.}$$

where $\epsilon_N$ and $\epsilon_G$ are obtained from Curve A.

In all instances, upon determining the value of $d_L$ for each specimen, the shape of the stress-strain curve can be computed within the accuracy of strain measurements and small material variations. Again using Curve B of Fig. 2 for purposes of illustration, a number of points on the curve are computed by Eq. (1) and the points are noted on Fig. 2 (see Table 2).

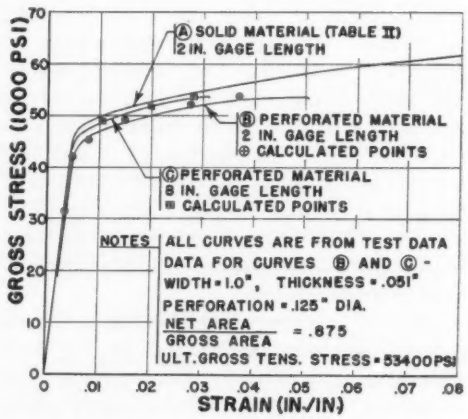
GROSS STRESS (1000 PSI)
STRAIN (IN./IN.)
Ⓐ SOLID MATERIAL (TABLE II) 2 IN. GAGE LENGTH
Ⓑ PERFORATED MATERIAL 2 IN. GAGE LENGTH ⊕ CALCULATED POINTS
Ⓒ PERFORATED MATERIAL 8 IN. GAGE LENGTH ⊞ CALCULATED POINTS
NOTES
ALL CURVES ARE FROM TEST DATA
DATA FOR CURVES Ⓑ AND Ⓒ - WIDTH = 1.0", THICKNESS = .051"
PERFORATION = .125" DIA.
NET AREA / GROSS AREA = .875
ULT. GROSS TENS. STRESS = 53400 PSI

FIG. 2. Stress-strain curves—24ST Alclad sheet.

In order to find the ultimate net stress to be used in estimating the ultimate elongation (Point 1 of Table 2) stress concentration must be accounted for. If the ultimate net stress is known from tests (Table 2), this value is used. For future use, a factor $K$ by which the ultimate tensile strength of the material can be multiplied to find ultimate net stress is determined later for various perforations.

In order to show the effect of gauge length upon the stress-strain curve, Curve C is included in Fig. 2 for strains measured in an 8-in. gauge length. The points

on this curve have been calculated for the same value of $d_L$ also by means of Eq. (1). Note how much more closely the 8-in. gauge length curve approximates that of the solid specimen than does the curve for a 2-in. gauge length.

The results of similar data and calculations for a 24ST extrusion of 1-in. original thickness are reproduced in Fig. 3.

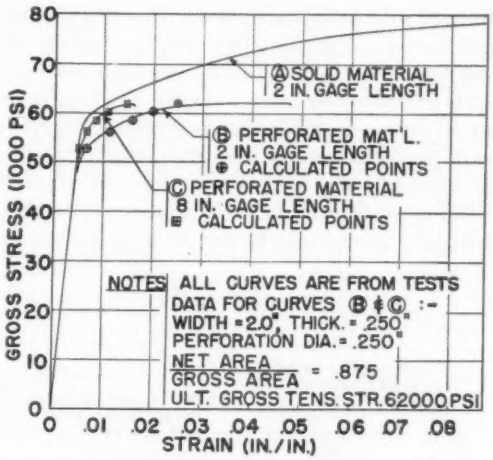
GROSS STRESS (1000 PSI)
STRAIN (IN./IN.)
Ⓐ SOLID MATERIAL 2 IN. GAGE LENGTH
Ⓑ PERFORATED MAT'L. 2 IN. GAGE LENGTH ⊕ CALCULATED POINTS
Ⓒ PERFORATED MATERIAL 8 IN. GAGE LENGTH ⊞ CALCULATED POINTS
NOTES: ALL CURVES ARE FROM TESTS
DATA FOR CURVES Ⓑ & Ⓒ :-
WIDTH = 2.0", THICK. = .250"
PERFORATION DIA. = .250"
NET AREA / GROSS AREA = .875
ULT. GROSS TENS. STR. 62000 PSI

FIG. 3. Stress-strain curves—24ST extrusion (1 in.).

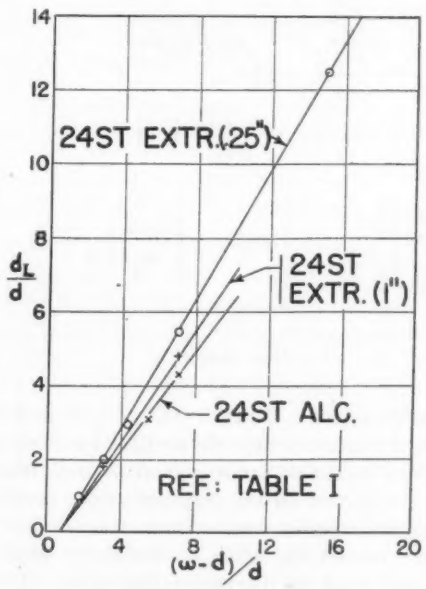


FIG. 4. Effective perforation length $d_L$ (24ST extrusions and 24ST Alclad sheet).

At the calculated Point 1 in Table 2 where the net stress is the ultimate net stress for the specimen, the ultimate elongation is computed to be 0.037 in. per in. while the measured maximum elongation was 0.05 in. per in. This occurred in every instance and is probably explained by the fact that the fracture at the perforation was not uniform, which resulted in an appreciable gap at the fracture when the broken parts were pieced together for elongation measurements. This discrepancy does not have a serious effect on the use of the curves, and the calculated maximum elongation probably represents the actual elongation at the moment of failure and is the value desired from an engineering standpoint. Better test data to explain the discrepancy, however, would be useful.

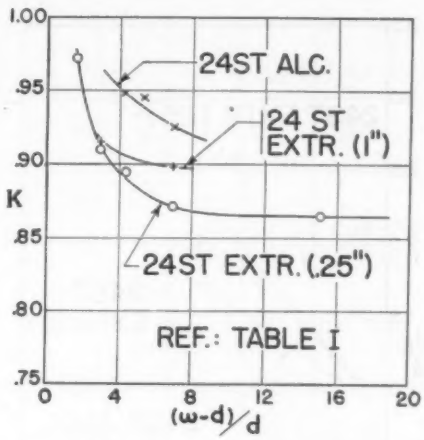


FIG. 5. Stress concentration factor $K$ (24ST extrusions and 24ST Alclad sheet).

### *Estimation of $d_L$ and $K$*

In order to find values of $d_L$ and $K$ for engineering purposes, graphs should be available showing their variation with various independent parameters.

The additional load to be carried in the net section which must make the average net stress greater than the stress in the gross area is proportional to $d$, and the area available to carry the load is $(w - d)$. Thus, the parameter $(w - d)/d$ was suggested. Nondimensional values of $d_L/d$ plotted against $(w - d)/d$ result in straight-line relationships, for a given material (see Fig. 4). Nondimensional values of $K$ plotted against $(w - d)/d$ result in curves for each given material (see Fig. 5). Since different curves are obtained for different materials, new curves will probably be needed for any other material to be used.

### *Study of Stress Concentration Effects*

Since the reason for the concept of $d_L$ is to take account of stress concentration effects and since the tests show a reduction in ultimate strength because of stress concentration (see $K$, Fig. 5), further study of these effects is of interest.

Fig. 5 shows that the smaller the perforation with respect to the width, the greater the stress concentration effect. For extremely large widths, however, a limiting value is reached.

In the elastic range or for nonductile materials, the stress concentration at the edge of the perforation has

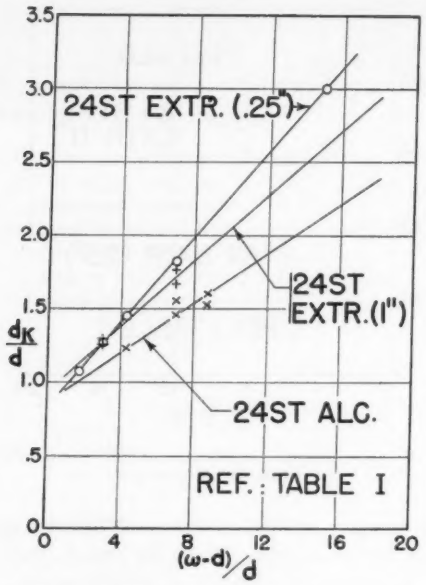


FIG. 6. Effective perforation width $d_K$ (24ST extrusions and 24ST Alclad sheet).

been proved mathematically by Kirsch[4] and by photoelasticity by Frocht[3] to be three times the normal stress.

Since stress concentration in the elastic range is a strain phenomenon, the effect of yielding in the vicinity of the perforations in the plastic range is to permit the stresses in the rest of the material to build up before failure occurs. To illustrate this, an example using test data is given. The strain distribution throughout

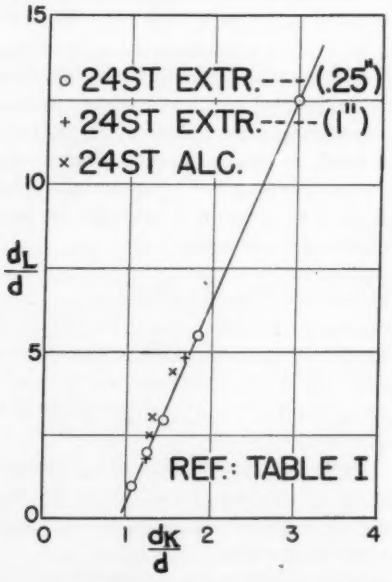


FIG. 7. Variation of effective perforation length $d_L$ with effective perforation width $d_K$.

is assumed to be similar to that in the elastic range as previously shown.[3,4] The specimen is a 24TS extrusion (1.0-in.) (see Table 1) with a 2 by 0.24-in. cross section and a 0.25-in. perforation $[(w - d)/d = 7.0)]$. Such a specimen will have an ultimate allowable stress of 79,000 lbs. per sq.in., an average stress in a net section of 79,000 × 0.898 = 70,900 lbs. per sq.in., and corresponding strains of 0.10 and 0.033 in. per in., respectively (see Table 1 and Fig. 3). The strains are taken from 8-in. gauge length data, since this eliminates most of the effects of "necking down," and it was noted in the tests that necking down was considerably restrained at the perforations. In Fig. 8 the stress distribution shape at failure is constructed. Since the stress in the region remote from the perforation will not be far different from 70,900 lbs. per sq.in., it is seen that the build-up of strain at the perforation (0.10/0.033 = 3) may remain approximately the same at failure as in

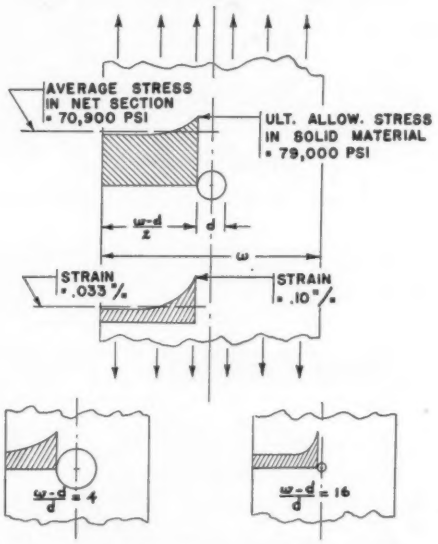
AVERAGE STRESS IN NET SECTION = 70,900 PSI
ULT. ALLOW. STRESS IN SOLID MATERIAL = 79,000 PSI
STRAIN = .033 %
STRAIN = .10 %
$\frac{\omega-d}{d} = 4$
$\frac{\omega-d}{d} = 16$

FIG. 8. Approximate stress and strain distributions at perforation—Example.

the elastic range.[3,4] Thus, a study of strain distributions in the elastic range shows that for perforations removing a relatively large amount of area, where the strain distribution all the way across the specimen is affected, the stresses remote from the perforation are allowed to build up, while for relatively small holes failure will start at the perforation before the stress remote from the perforation can build up. The larger ultimate stress concentration factor and limiting value approached for small perforations can therefore be understood. Further study by such approximate methods may be worth while.

Although not enough data has been taken to definitely prove it, it appears that stress concentration in the plastic range is a function of the ratio of the ultimate stress to the yield stress (see Table 1 and Fig. 5).

Note also that the curves of $d_L/d$ versus $(w - d)/d$ vary in the same way with the same parameters.

To show that $d_L$ is a function of stress concentration (and to present another possible method of determining stress concentration effects on ultimate load carried), the concept of an effective perforation diameter $d_K$ is introduced.

The width $d_K$ (Fig. 1) is that width of perforation which will predict the actual failing load in the net section if perforation diameter $d_K$ is used with the ultimate allowable stress of the solid material. A sample calculation of $d_K$ is as follows (see Point 1 of Table 2 and Curve B of Fig. 2).

ultimate gross stress $(w - d)$ =
ultimate allowable stress $(w - d_K)$ (2)

therefore

$$62{,}000(2 - 0.25) = 67{,}300(2 - d_K)$$

and

$$d_K = 0.38 \text{ in. or } 1.52d$$

In Fig. 6 direct relationships are shown to exist for $(w - d)/d$ versus $d_K/d$. This shows that stress concentration is a function of the proportion of the total area removed by the perforations.

The nondimensional values of $d_K$ as $d_K/d$ are plotted in Fig. 7 versus $d_L/d$. Straight-line relationships show that the effective perforation length $d_L$ is also directly related to stress concentration.

## Application of Stress-Strain Curves to Tension Surfaces

### *Example Stress-Strain Curves of Skin and Flange*

Assuming that the skin perforations are caused by $^1/_8$-in. dimpled rivets at 1-in. spacing and that the flange perforations are caused by $^3/_{16}$-in. bolts in the $1^1/_2$-in. wide flange, the value of $(w - d)/d$ in both cases is 7.0. Also, assuming that the perforations occur every 8 in., at the chordwise stiffeners, the gauge length to be used is 8 in. Therefore, the curves from Figs. 2 and 3 for corresponding parameters can be used. Note that the stresses shown are calculated values based on actual tests, that the skin is loaded parallel to the grain, and that the original extruded thickness of the flange was approximately 1 in. Since these curves will be referred to repeatedly, they are reproduced together in Fig. 9.

### *Flat Surface Without Shear Lag*

To see the effects of yielding on a wing tension surface, consider first a simple example—namely, that of a flat tension surface with all material at the same distance from the neutral axis, with uniform strain across the entire chord (no shear lag) and along the entire span.

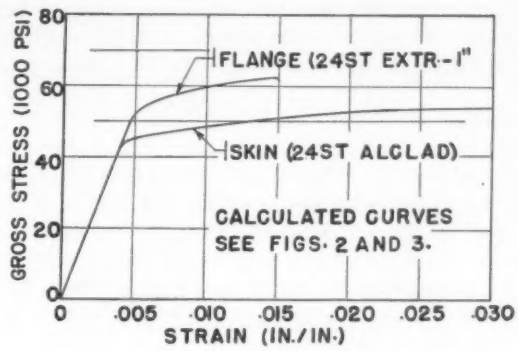


Fig. 9. Example stress-strain curves for skin and flange.

At a strain of 0.003 in. per in., both skin and flange act at 31,000 lbs. per sq.in. (Fig. 9). When the strain has reached 0.01, Fig. 9 shows that the skin stress will be 48,500 lbs. per sq.in. and the flange stress 59,500 lbs. per sq.in. The section will fail in the flange when a strain of 0.0145 is reached and, as can be seen from Fig. 9, the stresses immediately prior to failure will be 51,000 lbs. per sq.in. in the skin and 62,000 lbs. per sq.in. in the flanges. Conventional calculations according to $f = My/I$ would indicate the same stress in flange and skin, with the result that failure would occur when the stress had reached the lower of either of their allowables. Such calculations would therefore indicate failure in the skin when the stress reached 53,400 lbs. per sq. in. (see Figs. 2 and 9). From these calculations it would be expected that the skin would be the first to fail since it has the lower allowable, whereas study of Fig. 9 shows that the flange would actually fail first because its ultimate elongation is lower. More important is the fact that conventional calculations neglecting yielding would indicate less strength than is actually the case. This can be seen by the following simple calculations. Assuming half of the tension area to be in the skin and half in the flanges, conventional calculations would indicate a total load of $53{,}400A$ while calculations considering yielding show that the load would actually be $(62{,}000)(A/2) + (51{,}000)(A/2) = 56{,}500A$. This is a difference of 5.6 per cent in load. The difference would have been even greater in the case of wing bending where the skin is at a greater distance from the neutral axis than is the flange and, thus, at a higher stress than the flange (by usual calculations).

Accustomed as most engineers are to thinking of ultimate elongations in terms of tests on 2-in. solid specimens, the value of 1.45 per cent shown in Fig. 9 may seem low. Even if a large gauge length (8 in.) is taken in order to obtain an idea of the average elongation in a long length, the data given in Table 1 show that 10 to 14 per cent might be expected. Reference 2 has shown that the percentage elongation changes little for gauge lengths over 8 in. A simple example, however, will illustrate that elongations of 10 to 14 per cent and

the accompanying allowables are never attained but that the 1.45 per cent elongation and the accompanying low gross flange stress may represent the normal case.

Assume an efficient wing built in such a way that the flange yields throughout about one-third of the span. For a 10 per cent elongation in the tension flange, no yielding in the compression flange, a semispan of 200 in., and an average depth of 15 in., the tip deflection can be estimated as follows: $\alpha R$ = spanwise length of flange which yields, where $\alpha$ = angle between lines perpendicular to beam at ends of yielding section and $R$ = radius of curvature.

$$\alpha(R + 15) = \left(\frac{\text{semispan}}{3}\right) + 0.10\left(\frac{\text{semispan}}{3}\right) \qquad (3)$$

where neutral axis for estimating curvature can be taken at compression flange due to its negligible elongation. By subtraction, $15\alpha = 0.10 \times 200/3$. Therefore $\alpha = 0.44$ radians or 25.4°.

Thus it is seen that an elongation of 10 per cent will never be attained over any appreciable length, and the powerful effects of a little yielding on wing deflection are illustrated. By ratioing it can also be seen that an average elongation of 1.45 per cent in the same length will afford an angle of $(1.45/10) \times 25.4 = 3.68°$. Since this is a reasonable value, it is clear that such an elongation is a possible condition.

Thus, this simple example has afforded some insight into the behavior of an actual wing with regard to the magnitude of strains and stresses usually encountered near ultimate load, and the average strains attained due to the effects of local perforations (Fig. 9) are seen to represent a possible case.

### *Flat Surface with Shear Lag*

The possible effects of yielding on shear lag are shown by means of a second example. The same flat tension surface is assumed to have the shear lag factors shown in Fig. 10 at all spanwise locations, and the strain at any given chordwise location is assumed to be constant along the entire span. This example is inconsistent with actual shear lag characteristics, but it will serve to show the possible effects of yielding on shear lag.

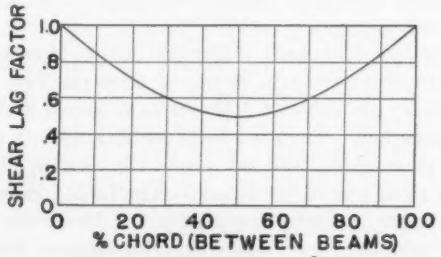


FIG. 10. Chordwise variation of shear lag factor (flat surface example).

At this point it is well to emphasize that shear lag is a strain phenomenon. It is often used in section property calculations as if it were a measure of stress, only because the calculations are made as if the material were always in the elastic range where stress is directly proportional to strain. Actually, the shear lag factor should be applied to the strain calculations and the stresses found from the resultant strain. With the flat skin of this second example, the shape of the shear lag factor curve and the strain distribution curve are geometrically similar. The shear lag curve used in this example is an extreme case, which will seldom be exceeded over any appreciable spanwise length. Winny[5] has shown a calculation of the shear lag for a typical wing, the results of which illustrate this statement.

The calculations of chordwise stress distributions are simple. Choose an arbitrary flange strain, find the corresponding stress from Fig. 9, and plot this stress on Fig. 11. At any point along the chord, multiply the arbitrarily chosen strain by the factor found from Fig. 10 and obtain the stress corresponding to the resultant strain from Fig. 9. Do this at a number of points along the chord and plot the stresses thus obtained on Fig. 11. The chordwise stress distributions corresponding to flange strains of 0.003, 0.005, 0.010, and 0.0145 are shown in Fig. 11.

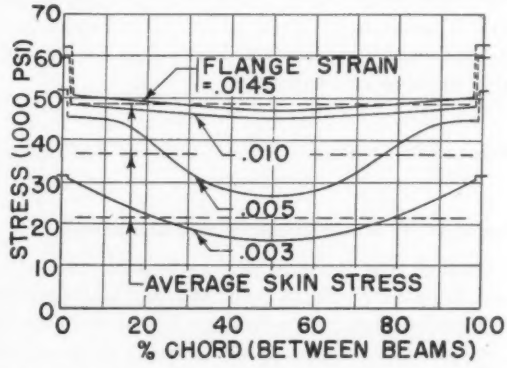


FIG. 11. Chordwise stress distribution for various flange strains (flat surface with shear lag example).

The possible effect of yielding is to reduce the effect of shear lag in the midchord fiber from 50 per cent in the elastic range to 3,500/50,500 = 6.9 per cent at ultimate load.

From Fig. 11, however, the ratio of average skin stress to flange stress in the elastic range is 0.67 and in the plastic range is 0.78, thus indicating that the reduction in the sag of the shear lag curve may in some cases be nearly used up by the reduction in skin stress due to yielding at ultimate load. This indicates that it may often be possible to use the same skin efficiency factors in the elastic and plastic ranges. In actual practice, however, calculations of stress in the elastic range are seldom necessary (although often made), since yielding will usually occur much closer to ulti-

mate load than is required by the customary 1.5 safety factor. By comparing the total load carried by the surface at the time of yielding with the load at failure this is shown to be true:

Assume the tension area to be divided equally between skin and flanges. From Fig. 9, at a strain of 0.005 the flange material has barely exceeded the proportional limit. From Fig. 11, the load carried at this strain is 52,000 $(A/2)$ + 37,000 $(A/2)$ = 44,500$A$. Also from Fig. 11, the load at failure is 62,000 $(A/2)$ + 48,000 $(A/2)$ = 55,000$A$. Thus, yielding is seen to take place at 80 per cent of ultimate load. Since this proximity of yield and ultimate stress in perforated tension surfaces has been noted in many static tests of actual wings, further study of this point seems to be worth while in the interests of more efficient design.

### *Typical Wing Tension Surface*

The possible effects of yielding have been shown by the simplified examples above. However, before drawing any conclusions, probable effects must be investigated. This is done by applying the stress-strain curves to a tension surface typical of an actual wing. The characteristics of this surface are shown in Figs. 12–14. The principal features are the following: The shear lag varies across the span in a typical fashion as calculated by Winny[5] for a similar case; the flange stress varies along the span in a typical variation; and the skin is not flat nor are the flanges both at the same distance from the neutral axis. In this example the skin is discontinuous at the inboard and outboard end ribs. It is assumed that the flange stress variation along span and chordwise strain variation in the elastic range have previously been worked out and that in these calculations all effects of the arching of the skin and plan-form taper have been taken into account. Consequently, no section properties are needed and all investigations can be made by combining the stress-strain curves with the strain distributions at the various stations.

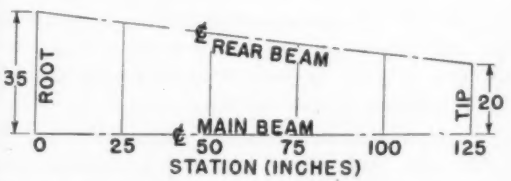


FIG. 12. Plan form of typical wing tension surface—example.

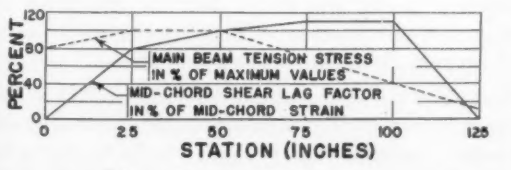


FIG. 13. Spanwise variation of main beam stress and mid-chord shear lag factor (typical wing example).

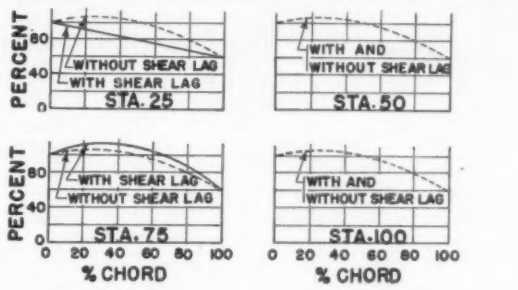


FIG. 14. Chordwise strain distribution with and without shear lag (typical wing example).

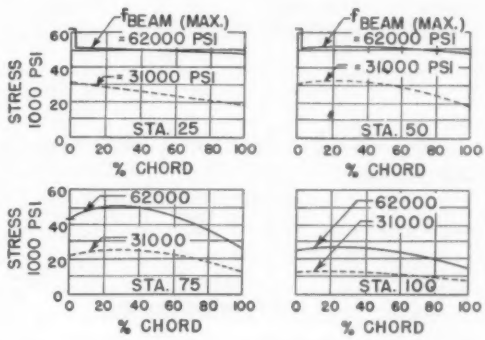


FIG. 15. Chordwise stress distribution for various maximum flange stresses (typical wing example).

The method used to find chordwise distributions of stress at various stations in the typical wing is as follows: Fig. 13 shows that the maximum main beam stress will occur at certain stations (25 and 50). Assume that the section properties will be so adjusted that the main beam stresses at these stations will be equal to those anticipated at failure (62,000 lbs. per sq.in.). From this, the main beam strain at these stations is found (see Fig. 9), and from the strain distributions at these stations (Fig. 14) and the stress-strain curves of Fig. 9, the stress distributions at these stations are found and plotted on Fig. 15. At other stations the stress is ratioed down from the maximum value of 62,000 by the ratios in Fig. 13 and the corresponding main beam strain is found from Fig. 9. The chordwise stresses are then found in the same manner as before and are plotted on Fig. 15. The curves found by the above are labeled "$f_{Beam\ (max.)}$ = 62000 psi" on Fig. 15. Another set of curves is found for a maximum beam stress (at the critical stations) of 31,000 lbs. per sq.in. (elastic range) and these curves are labeled "$f_{Beam\ (max.)}$ = 31000 psi" (Fig. 15).

However, in Fig. 15 the assumption is made that the strain distribution at any station remains the same at all stresses. From a consideration of the main beam stresses of Fig. 15 and the curves of Fig. 9, it is seen that the spanwise strain distribution along the beam (and, consequently, along skin elements) will change

TABLE 3

Determination of Skin and Flange Elongations at Various Loads (Fig. 16)

| Bay | Flange at Ult. Load Flange Stress = 62,000 lbs. per sq.in. Av. strain in bay | Flange at Ult. Load Flange Stress = 62,000 lbs. per sq.in. Av. strain × length of bay | Skin Mid-Chord at Ult. Load Flange Stress = 62,000 lbs. per sq.in. Av. strain in bay | Skin Mid-Chord at Ult. Load Flange Stress = 62,000 lbs. per sq.in. Av. strain × length of bay | Flange at Max. Flange Stress = 31,000 lbs.per sq.in. Av. strain in bay | Flange at Max. Flange Stress = 31,000 lbs.per sq.in. Av. strain × length of bay | Skin Mid-Chord at Max. Flange Stress = 31,000 lbs. per sq.in. Av. strain in bay | Skin Mid-Chord at Max. Flange Stress = 31,000 lbs. per sq.in. Av. strain × length of bay |
|---|---|---|---|---|---|---|---|---|
| 0–15 | 0.0055 | 0.083 | 0.0016 | 0.024 | 0.0026 | 0.039 | 0.0007 | 0.010 |
| 15–25 | 0.0105 | 0.105 | 0.0070 | 0.070 | 0.0028 | 0.028 | 0.0019 | 0.019 |
| 25–50 | 0.0146 | 0.365 | 0.0131 | 0.328 | 0.0031 | 0.078 | 0.0027 | 0.068 |
| 50–60 | 0.0105 | 0.105 | 0.0106 | 0.106 | 0.0027 | 0.027 | 0.0028 | 0.028 |
| 60–75 | 0.0045 | 0.068 | 0.0047 | 0.070 | 0.0024 | 0.036 | 0.0025 | 0.038 |
| 75–125 | 0.0024 | 0.120 | 0.0023 | 0.115 | 0.0012 | 0.060 | 0.0012 | 0.060 |
| Σ | .. | 0.846 | .. | 0.713 | .. | 0.268 | .. | 0.223 |

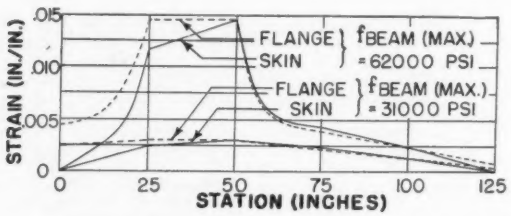


FIG. 16. Spanwise distribution of skin and flange strains for various maximum flange stresses (typical wing example).

with yielding. Therefore, it must be investigated whether or not the change in spanwise strain distribution will alter the chordwise strain distribution enough to invalidate the method.

Consider the strain changes necessary if the skin stress at mid-chord were to be 75 per cent of the main beam flange stress at ultimate load as well as in the elastic range. At Station 25, the skin near the flange is at the ultimate possible strain of 0.0145 in. per in., the stress there is 51,000 lbs. per sq.in., and the corresponding calculated strain and stress at mid-chord are $0.75 \times 0.0145 = 0.0109$ in. per in. and 49,000 lbs. per sq.in., respectively. For the stress at mid-chord to become 46,500 lbs. per sq.in. (same relation as in elastic range), the strain there would have to be reduced to 0.0065 in. per in., a considerable reduction.

This might occur if the skin inboard and outboard of this point stretched much more than expected or if the inboard and outboard end ribs bowed in severely. To investigate these possibilities, the total elongations of the main beam flange and the mid-chord skin element are determined. This is done very simply by plotting against span the strains (see Fig. 9) corresponding to the stresses shown in Fig. 15 and integrating the areas under the curves. The spanwise distributions of strains at ultimate and at a load corresponding to a maximum beam flange stress of 31,000 lbs. per sq.in. are shown in Fig. 16. The areas under the curves and the consequent elongations are found in Table 3.

From Table 3 it is noted that, at a loading corresponding to a maximum flange stress of 31,000 lbs. per sq.in., the shear lag resulted in a difference between flange and skin total elongations of $0.268 - 0.223 = 0.045$ in. In the plastic range, however, the difference is 0.133 in. The difference in elongation in the plastic range already represents more bowing in of the end ribs than would be predicted by ratioing the bowing in the elastic range in proportion to beam stress [$(62{,}000/31{,}000)\ 0.045 = 0.090$ in.].

For the skin stress at mid-chord to be 75 per cent of the beam stress (with a strain of 0.0065—see above) the total skin elongation is roughly estimated as $(0.0065/0.003)0.223 = 0.488$ in. This elongation represents yielding of the skin inboard and outboard of the region of Station 25–50. The bowing in of the end ribs in this case would be $0.846 - 0.488 = 0.358$ in. Even with yielding of the skin inboard and outboard of the region of Station 25–50, the bowing in of the end ribs is excessive, and it is clear that the actual case will be between that calculated in Fig. 15 (49,000 lbs. per sq.in.) and that mentioned above (46,500 lbs. per sq.in.).

In any case the skin at mid-chord has yielded somewhat, and the above considerations demonstrate how little error is likely to occur even with large errors in strain estimation (above yielding).

In addition, the skin stress at midpoint is not the critical value and at the critical point (adjacent to the main beam flange) there is no doubt that the effects of yielding on the skin stress will be close to those estimated. It is also noted that the chordwise distribution of skin stress is but little affected by the variations of mid-chord skin stress found above.

Some method of accounting for yielding such as outlined is reasonable for engineering use. The following example illustrates the possible effects of neglecting yielding when calculating ultimate strength and the desirability of considering such effects.

## Illustrative Example

### *Sequence of Operations*

To illustrate the use of the method and its effect, two sets of strength calculations are made. One set includes the effects of yielding, the other does not. The section chosen represents Station 25 of the foregoing example.

To use the method, the following steps would be taken. First, the shear lag distribution in the elastic range is found by the usual means. Then, using these efficiencies, the approximate flange areas and spanwise flange stress distributions are found to satisfy the various loading conditions. Then the skin and flange stress-strain curves are determined for the expected perforations. If the spanwise flange stress and strain variations are such that entire sections will be affected by yielding, the material curves are applied to each cross section where yielding is expected, and the stress distributions at ultimate load are found. At this time, estimations of the effects of changed spanwise strain distributions and such factors as slippage in skin-flange connections (near end ribs only) are made and taken into account. Finally, the efficiency factors are found and these are used in the final section property and stress calculations.

The use of the efficiency factor is similar to the method often used in problems involving shear lag in the elastic range. The affected areas are multiplied by the efficiency factor for use in section properties and the stresses calculated according to $f = My/I$ are also corrected by the factor. Any point along the chord might be used as the base in finding the factor and, since it is the principal member, the main beam flange is taken as having 100 per cent efficiency.

### *Determination of Efficiency—No Yielding*

The factor can be determined from a strain distribution such as in Fig. 17 and is equal to the ratio of the average element strain including shear lag to the average element strain neglecting shear lag. The factor determined from Fig. 17 are as shown in Table 4.

Table 4

Determination of Efficiency—No Yielding

| Col. | (1) | (2) | (3) |
|---|---|---|---|
| Element | Strain factor (no shear lag) | Strain factor (shear lag but no yielding) | Shear lag factor |
| | Fig. 17 | Fig. 17 | (2)/(1) |
| 1 | 1.04 | 0.96 | 0.92 |
| 2 | 1.07 | 0.86 | 0.80 |
| 3 | 0.96 | 0.73 | 0.76 |
| 4 | 0.72 | 0.63 | 0.87 |

### *Determination of Efficiencies—with Yielding*

When yielding is present, the factor is most easily found by constructing a chordwise stress distribution curve taking into account yielding. The factor is in terms of the main beam value, as in the case of shear lag efficiency factors. In the present case the maximum skin strain will occur at the main beam (Fig. 14) and will fail when the strain = 0.0145 in. per in. (Fig. 9). From the stress-strain curves of Fig. 9 and the strain distribution curve of Fig. 14, a curve of stress distribution at ultimate load is calculated and is shown in Fig. 17. The efficiency factors are found from the ratio of average element stress including yielding to the average element stress neglecting yielding (Table 5). The rear beam is assumed to have the same stress-strain curve as the skin.

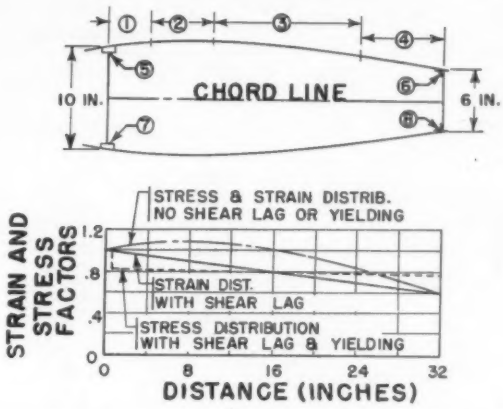


Fig. 17. Station 25—cross section and chordwise stress and strain distributions at ultimate load (typical wing example).

Table 5

Determination of Efficiencies—with Yielding

| Col. | (1) | (2) | (3) |
|---|---|---|---|
| Element | Stress (no shear yielding) | Stress factor (with shear lag and yielding) | Efficiency factor |
| Ref. | Fig. 17 | Fig. 17 | (2)/(1) |
| 1 | 1.04 | 0.84 | 0.81 |
| 2 | 1.07 | 0.83 | 0.78 |
| 3 | 0.96 | 0.80 | 0.83 |
| 4 | 0.72 | 0.78 | 1.08 |
| 5 | 1.00 | 1.00 | 1.00 |
| 6 | 0.60 | 0.78 | 1.30 |

### *Section Property Calculations*

With an ultimate bending moment of 1,347,000 in. lbs., the following stresses are obtained from the data in Table 6.

*Neglecting yielding effects:* Skin directly above main beam; shear lag efficiency = 1.00; margin of safety = −0.13.

$$f_t = My/I = 1{,}347{,}000\{[5.0 - (-0.17)]/105.4\}$$
$$= 61{,}700 \text{ lbs. per sq.in.}$$

$$F_t = 53{,}400 \text{ lbs. per sq.in. (Fig. 9)}$$

Main beam flange; margin of safety = +0.00.

TABLE 6

Section Property Calculations—Station 25

| | Col. | (1) | (2) | (3) | (4) | (5) | (6) |
|---|---|---|---|---|---|---|---|
| | Item | Area | Factor$_e$ | $A_e$ | $y$ | $(A_e)(y)$ | $(A_e)(y^2)$ |
| | Ref. | | Table 4 | 1 × 2 | Fig. 17 | 3 × 4 | 4 × 5 |
| Neglecting Yielding Effects* | 1 | 0.160 | 0.92 | 0.147 | 5.3 | 0.78 | 4.13 |
| | 2 | 0.320 | 0.80 | 0.256 | 5.4 | 1.38 | 7.46 |
| | 3 | 0.480 | 0.76 | 0.364 | 4.8 | 1.75 | 8.39 |
| | 4 | 0.320 | 0.87 | 0.278 | 3.7 | 1.03 | 3.81 |
| | 5 | 1.000 | 1.00 | 1.000 | 5.0 | 5.00 | 25.00 |
| | 6 | 0.250 | 1.00 | 0.250 | 3.0 | 0.75 | 2.25 |
| | 7 | 2.000 | 1.00 | 2.000 | −5.0 | −10.00 | 50.00 |
| | 8 | 0.500 | 1.00 | 0.500 | −3.0 | − 1.50 | 4.50 |
| | Σ | 5.230 | | 4.795 | −0.17 | − 0.81 | 105.54 |
| | Ref. | | Table 5 | (1) × (2) | Fig. 17 | (3) × (4) | (4) × (5) |
| Including Yielding Effects† | 1 | 0.160 | 0.81 | 0.130 | 5.3 | 0.69 | 3.65 |
| | 2 | 0.320 | 0.78 | 0.250 | 5.4 | 1.35 | 7.30 |
| | 3 | 0.480 | 0.83 | 0.398 | 4.8 | 1.91 | 9.16 |
| | 4 | 0.320 | 1.08 | 0.346 | 3.7 | 1.28 | 4.74 |
| | 5 | 1.000 | 1.00 | 1.000 | 5.0 | 5.00 | 25.00 |
| | 6 | 0.250 | 1.30 | 0.325 | 3.0 | 0.98 | 3.17 |
| | 7 | 2.000 | 1.00 | 2.000 | −5.0 | −10.00 | 50.00 |
| | 8 | 0.500 | 1.00 | 0.500 | −3.0 | − 1.50 | 4.50 |
| | Σ | 5.230 | | 4.949 | −0.06 | − 0.29 | 107.52 |

* $I = \Sigma[(A_e)(y^2)] - \Sigma[(A_e)(y^2)] = 105.54 - 0.139 = 105.4$.
† $I = \Sigma[(A_e)(y^2)] - \Sigma[(A_e)(y^2)] = 107.52 - 0.017 = 107.5$.

$$f_t = My/I = 1{,}347{,}000\ \{[5.0 - (-0.17)]/105.4\}$$
$$= 61{,}700 \text{ lbs. per sq.in.}$$
$$F_t = 62{,}000 \text{ lbs. per sq.in. (Fig. 9).}$$

*Including yielding effects:* Skin directly above main beam; efficiency = 51,000/62,000 = 0.823; margin of safety = +0.00.

$$f_t = My/I = 1{,}347{,}000[5.0 - (-0.06)] \times (0.823/107.5)$$
$$= 51{,}000 \text{ lbs. per sq.in.} = F_t \text{ (Fig. 9)}$$

Main beam flange; margin of safety = +0.00.

$$f_t = My/I = 1{,}347{,}000\{[5.0 - (0.06)]/107.5\}$$
$$= 62{,}000 \text{ lbs. per sq.in.} = F_t \text{ (Fig. 9)}$$

Calculations thus indicate that the wings will be able to carry 15 per cent more load when they include yielding effects than when they are neglected. In addition, calculations of skin stresses across the chord and of the rear beam stress are much closer to the actual case and the loads used to design skin and flange splices will be more accurate. Therefore it seems worth while to account for yielding in determining the ultimate strength of such surfaces.

## General Discussion of Method of Applying Stress-Strain Curves to Actual Tension Surfaces

The approximate character of the treatment given in this paper demonstrates the possible engineering usefulness of the method. In an actual case many variations occur: The stress-strain curves of the actual materials would probably differ from those used in the calculations, even if typical allowables are used; the rivet spacing at the ribs would not be known at the time it was necessary to determine efficiencies, and these spacings might vary from rib to rib; the skin gauges might change during design and would probably vary along the span; finally, an exact solution for shear lag at stresses below yield is seldom available to the stress analyst. Therefore, the fact that the efficiencies will not be seriously altered by moderate errors in determining strain is of considerable importance to the analyst in estimating skin efficiencies. With reasonably accurate and unchanging efficiencies, flange and skin areas can easily be altered to obtain the maximum allowable stresses.

It should also be noted that, while the method given is probably of some value to engineers in obtaining a more accurate analysis of a wing tension surface than is possible with present methods neglecting yielding, much more study is desirable. Better calculations or estimations of the effects of yielding upon chordwise strain variations, including possible effects of tension yielding on shear modulus and slippage in skin-flange connection, are definitely needed. This is especially important near end ribs where there is severe and rapidly changing shear lag. Although the shear lag curves are modified by yielding, the above work shows that shear lag data in the elastic range is needed as much for the tension surface as for the compression surface (where it applies directly). An attempt to ac-

(*Continued on page 321*)

# Resonant Electrical Control Systems

DAVID WILLIAM MOORE, JR.*
*Fairchild Aviation Corporation*

SUMMARY

This paper describes a simple electrical position-repeating and control system. Its operation is based upon the change in the phase relationship between the current and voltage in a series-resonant circuit as the tuning of the resonant circuit is varied. The control system sensitivity is a function of the $Q$ of the resonant circuits employed and is high for values of $Q$ which may be easily obtained in normal practice.

The application of this principle to the control of low and substantial amounts of power is discussed and practical circuits are proposed. No electrical contacts are required in any of the circuits, which permits the design of an extremely reliable instrument.

The paper is concluded with a brief description of the application of this resonant control principle to single- and multichannel radio control to which it is well suited.

## INTRODUCTION

REMOTE POSITIONING and control equipments have become essential features in the design of many types of modern aircraft. The increasing size of planes has complicated the control problem by lengthening the distance between the various control and accessory components, thereby rendering the use of flexible shafts and mechanical linkages impractical. A flexible shaft cannot be relied upon for accurate control adjustments if it is too long, or overloaded, or made to traverse short radius bends. It is often impossible to design around these limitations. To utilize all of the available space in some planes it is frequently necessary to build equipment into more components than is functionally necessary. Each unit must then be capable of proper interaction with the remaining units often requiring the translating of shaft positions from one section to the other. These units, which are of necessity tucked away wherever space is available, usually may not be successfully controlled by mechanical means.

To solve these problems, various electrical positioning and control systems have been developed, the best known of which is the self-synchronous position repeater. This device is efficient and accurate for indications that do not require the development of any appreciable amount of torque, the electrical system employed being too elastic to supply substantial torques with accuracy. Power-producing position-repeating systems have been developed, but many of them require contacts and relays for their operation, thus rendering them unsatisfactory from the maintenance point of view. Most of these contact-operated controls are of the so-called "on-off" type and do not produce a control torque proportionate to the input error signal, thereby being susceptible to hunting if adjusted to permit a high sensitivity.

Presented at the Radio and Instruments Session, Eleventh Annual Meeting, I.A.S., New York, January 25–29, 1943.

* Engineer in Charge, Control Laboratory.

## THEORY OF OPERATION

A control system will be described depending upon the phase characteristics of an electrical series-resonant circuit for its operation. This system does not require contacts and may be operated over a wire or radio channel. High-torque, low-power operation may be had with no electronic amplifiers.

The series-resonant circuit consists of inductance, capacitance, and resistance in series, the value of the resistance determining the $Q$ or efficiency of the circuit. Fig. 1 shows the current and current-voltage phase relationship as the frequency of the applied voltage is varied above and below the resonant frequency of the electrical circuit. The current is maximum and in phase with the voltage when the circuit is tuned to resonate with the frequency of the applied voltage. As the applied voltage frequency is changed slightly, the

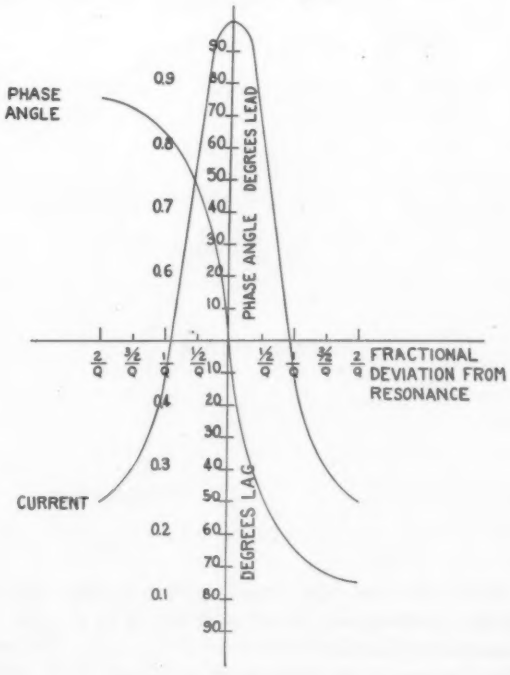


FIG. 1.

electrical circuit is no longer tuned to resonance and the phase of the current with respect to the applied voltage shifts rapidly, leading or lagging the voltage depending upon the direction of the frequency change. This phase shift is rapid to approximately 45° leading or lagging and then asymptotically approaches 90° as the frequency change is continued. The rate of change of this phase shift is a function of the efficiency or $Q$ of the electrical circuits and is greater for more efficient circuits. Since this resonant control system is operated by a phase-sensitive servo, the efficiency of the electrical circuits determines the sensitivity of the control and may be designed to a value consistent with the application and cost of the equipment. In practical resonant control apparatus operating on power frequencies, a $Q$ of five will permit sensitivities of the order of $^1/_{10}$ of 1 per cent change in frequency or in inductance.

## Basic Resonant Control

Fig. 2 is a schematic diagram of the basic series-resonant control system. The phase-sensitive servo used here is the simple two-phase electric motor that has the property of developing torque only when there is an electrical phase differential between the currents in the two phases. Maximun torque is developed when there is an electrical phase differential of 90° between the currents in the two-motor phases, and the direction of the torque produced depends upon which motor phase has leading current.

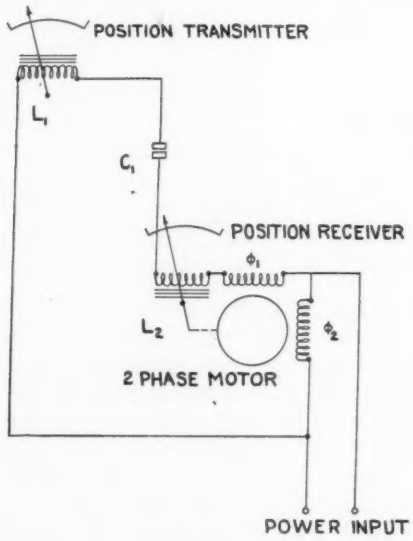


Fig. 2.

The series-resonant circuit in this system consists of the mechanically variable inductances $L_1$ and $L_2$, capacitance $C_1$, and phase one of the motor. The position transmitter of this system is inductance $L_1$ which may be varied by rotating its control shaft. It is connected to the position receiver by two electrical conductors that may be of considerable length. The position-receiving section of the control consists of inductance $L_2$ which is adjusted by the two-phase servo motor. Phase two of the servo motor is connected directly to the a.c. power supply and is adjusted to unity power factor by any convenient method so that the current passing through it is in phase with the applied power supply voltage.

### *Equilibrium Condition*

In the stand-by or equilibrium condition, the series-resonant circuit is adjusted to resonate with the applied voltage and, in this condition, also passes in-phase current. Therefore, the two-phase motor has unity power factor current in each phase, and no torque is developed because there is no electrical phase differential between the currents in the two-motor phases. If the position-transmitting inductance $L_1$ is varied by turning its control shaft, the series circuit is slightly detuned producing a shift in the phase of the current passing through it, which produces an electrical phase differential between the current in the two phases of the servo motor, causing it to develop torque. This torque is used to turn the control shaft of inductance $L_2$, in the proper sense to adjust it, until the series circuit is resonating with the power supply frequency and equilibrium again established. The servo motor at all times tends to keep a condition of resonance in the series circuit by maintaining the sum of the inductance values of $L_1$ and $L_2$ constant. Therefore, to permit accurate and linear position-repeating, it is necessary to design the mechanically variable inductances to change their value linearly with input shaft rotation and to be complementary units, since the value of the inductance in the position receiver must increase as the value of the position-transmitting inductance decreases to keep the sum constant. Fig. 3 illustrates the lamination design to produce this type of inductance change and shows its simplicity, there being no moving coils and consequently no need for brushes and slip rings. This type of inductance is linear for approximately 70° rotation of the control shaft, and accurate position-repeating throughout this

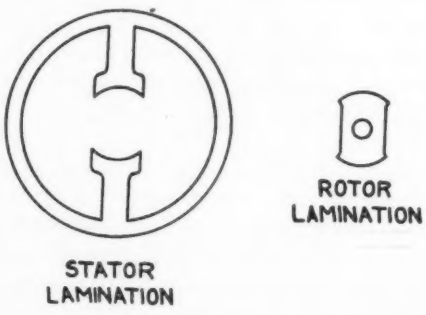


Fig. 3.

range may be obtained. Greater ranges, with no loss in the percentage of accuracy, may be had by gearing or by using different inductance design.

The sensitivity of this system is high near the balance point because the current is rising to a maximum at low electrical phase angles, permitting the development of substantial torques although the phase differential between the currents in the two motor phases is small.

### Control System Insensitive to Frequency Change

This basic control is suitable for operation on controlled frequency systems such as a 60-cycle industrial power supply but would be upset by mobile electrical systems where the frequency of the applied voltage may shift several per cent. This upsetting is caused by the electrical phase shift in the series-resonant circuit produced by the change in frequency of the power supply voltage which has the same effect on the system as the change in phase angle caused by a change in the value of inductance $L_1$.

A system (shown in Fig. 4) has been devised which is independent of reasonable changes in frequency. This system consists of the basic resonant control circuit with a second series-resonant circuit added in phase two of the two-phase servo motor. The position transmitter in this frequency insensitive system consists of inductances $L_1$ and $L_3$, which are mounted in the same case and controlled by the same control shaft. They are mechanically arranged so that as the value of inductance $L_1$ is increasing, the value of inductance $L_3$ is decreasing. This produces opposite electrical phase shifts in the two resonant circuits with a resulting electrical phase differential in the servo motor causing motor torque that adjusts inductances $L_2$ and $L_4$, which are designed to be complimentary to $L_1$ and $L_3$, until resonance is re-established. The sensitivity of this system is greater than that of the basic system, since two series-resonant circuits are being detuned, doubling the phase differential in the servo motor for a given inductance change. If the electrical power supply exciting this system shifts in frequency, each series-resonant circuit is affected in the same manner, producing equal phase shifts in the same direction in each circuit causing no electrical phase differential between the currents in the two-motor phases. Consequently, this frequency change does not affect the zero or balance point of the control. A system of this type will permit a frequency shift of 8 per cent with no serious effect on its operation. Higher frequency shifts do not cause a change in the zero position but are accompanied by serious torque reduction.

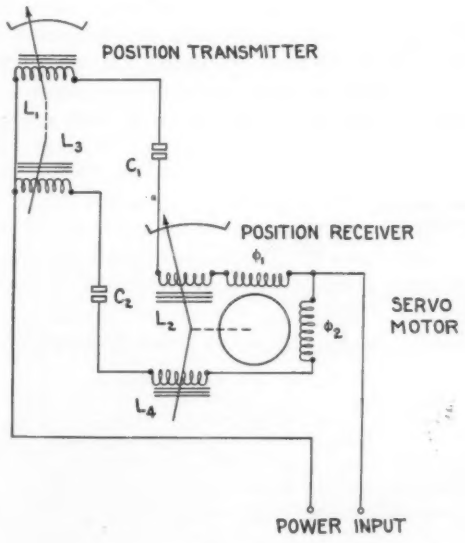


Fig. 4.

### Practical Resonant Control

A follow-up unit has been constructed in accord with the principle just described. It operates from 110 volts at 60 cycles, drawing a maximum power of 14 watts. The torque output is at least 50 in.oz. per deg. error between the position-transmitting shaft and the position-receiving shaft, with a maximum torque output of approximately 30 in.lbs. at 10° error. This unit tracks the position transmitter within 1 per cent and is sensitive to at least one-half of 1 per cent change of the maximum angular range. This particular unit was designed for operation on both 50 and 60 cycles, the value of the resonating condensers being changed by means of a toggle switch to insure maximum efficiency on both frequencies.

### High Power Output

These position-repeating systems are limited in power output since the maximum current drain is in the standby or equilibrium position. After the maximum allowable standby current is reached by a system of this type, greater torques and higher power may be obtained by using different phase-sensitive servos than the two-phase motor. Thyratron tubes are logical servos since they require little control power for large controlled power. Using these tubes as phase-sensitive servos, large powers may be controlled with moderately sized inductances and capacitances.

If the difference between the voltages across two series-resonant circuit capacitances, as shown in the vector diagram of Fig. 5, is used to control the thyratron grids, the electrical phase of this voltage will always be the optimum angle for firing the tubes. The phase of this difference voltage, as shown in the vector diagram, does not change with the changing phase of the series currents but is either leading or lagging the electrical supply voltage by 90°, depending upon the phase characteristics of the two circuits, and may consequently be utilized to fire either one of two thyratrons to control a suitable servo motor.

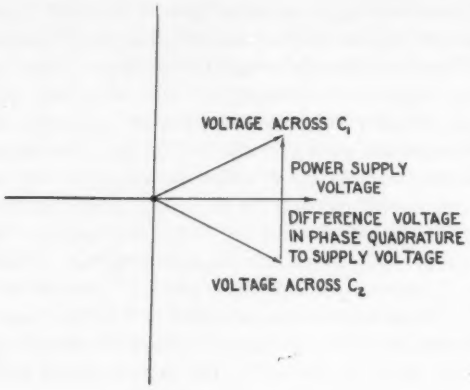


FIG. 5.

Air or hydraulic servos may also be used if desired. A direct two-phase motor resonant control system may be used to operate the servo valve, the servo adjusting the follow-up inductance and the mechanism to be controlled. Large powers may easily be handled in this manner with rapid action. Hydraulic power metered by this system could be used for control surface operation on large aircraft to enable positive positioning.

## TORQUE AMPLIFYING SYSTEM

Fig. 6 shows a torque amplifying system suitable for transmitting a low-torque shaft position to an adjacent shaft with increased torque. The resonant-control system is the frequency-insensitive circuit with the transmitting and receiving inductances combined into one unit. The low-torque shaft varies the position of the inductance rotors, and the servo motor adjusts the inductance stators, maintaining a resonant condition at all times. This assures constant mechanical relationship between the stators and rotors of the inductances. This system may be made relatively compact and, with electronic amplifiers, may be made dynamic in action. It is suitable for continuous 360° operation.

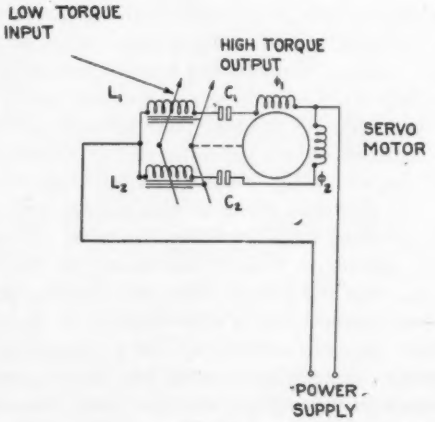


FIG. 6.

## RADIO CONTROL

All of the systems mentioned so far are suitable for wire operation. Fig. 7 illustrates a radio-position-transmission system capable of definite proportionate position control over a radio carrier. The receiving part of the radio system consists of a variable inductance $L_2$ and $C_2$ and a servo motor. Phase one of the servo motor is in series with the inductance and the capacitance, and phase two is made essentially resistive and is connected directly across the alternating voltage supply—in this case, the output of the radio receiver. Such a circuit is essentially a frequency meter and assumes a definite position for each frequency supplied from the radio receiver. The position transmitter consists of a similar circuit with the servo motor operating an audio oscillator that is used to modulate the radio transmitter. The transmitter servo motor adjusts the audio oscillator frequency to the resonant frequency of $L_1$ and $C_1$. This frequency modulates the radio transmitter and therefore excites the position-receiving circuit, which is adjusted by the receiving servo motor until it is resonating with the applied frequency. If $L_1$ and $L_2$ are identical mechanically variable inductances and if $C_1$ and $C_2$ are equal, the position of the control shaft of $L_1$ will be duplicated by the position of the control shaft of inductance $L_2$. The servo motor in the transmitter is included to permit satisfactory field operation. If the audio oscillator drifts during warm-up or at any other time, the servo motor corrects the drift, since it maintains the osciilator frequency equal to the resonant frequency of the circuit $L_1C_1$.

Multichannel radio control may be obtained with the above radio circuit by assigning a frequency band to each control or by assigning all of the controls to one frequency band and modulating different subcarrier

(*Continued on page 321*)

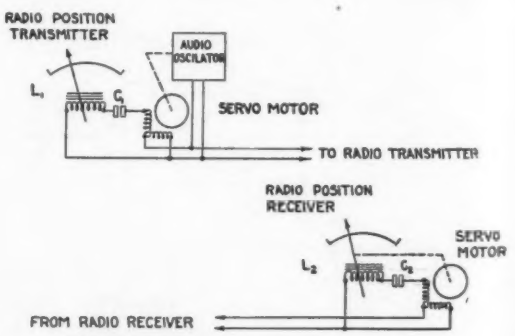


FIG. 7.

# Characteristics of Airfoils in a Cylindric Axial-Flow Grid*

JOHN R. WESKE† AND FRANK E. MARBLE‡

*Case School of Applied Science* and *N.A.C.A. Aircraft Engine Research Laboratory*

SUMMARY

Results are presented of an experimental investigation of a rotating cylindric axial-flow grid of airfoils. Measurements of pressure distribution over the cylindric mid-section of the airfoil were obtained for several blade spacings and angular settings and under various operating conditions. These data were used to compute the lift characteristics. The possibility of supplementing pressure distribution measurements by wake traverses for the determination of profile drag was explored.

## INTRODUCTION

THIS PAPER deals with an experimental investigation that was undertaken for two reasons:

(1) To explore the possibilities of an experimental method of measurements of the characteristics of airfoils in grid arrangement which corresponds closely to the assumptions made in theoretic investigations.

A review of the literature giving results of potential flow theory, and in particular of thin airfoil theory applied to plain airfoil grids, reveals an abundance of material available. In many cases there is a question, however, with regard to how far the results of theory may be applied to the flow of a real fluid through a given grid. It appeared desirable, therefore, to establish conditions of test closely analogous to those assumed in the theoretic treatment.

(2) The experimental equipment was developed also with a view to providing a means of testing cylindric grids under conditions closely approaching those encountered in practice. Grids similar to those tested are found in axial flow fans and compressors and the setup may readily be adapted to the testing of turbine grids. A good deal of information is available with regard to the action of turbine and compressor wheels. It appears desirable, however, to supplement this available data by information derived from detailed tests of the individual airfoil in grid arrangement, in particular since methods of computation of fan and turbine wheels on the basis of airfoil characteristics are commonly used.

Presented at the Aerodynamics Session, Eleventh Annual Meeting, I.A.S., New York, January 25–29, 1943.

* Essential features of the selector switch were developed and the majority of the pressure distribution tests were conducted by Morris Sable, a student at Case School of Applied Science.

† Professor of Aerodynamics.

‡ Associate Mechanical Engineer.

## PREVIOUS WORK

Grids have been investigated experimentally by Christiani,[1] Keller,[2] Shimoyana,[3] H. Kraft and T. M. Berry,[4] and W. R. New.[5] In these investigations a row of stationary airfoils has been placed into the working section of a wind tunnel or at the outlet of an air duct, and measurements of the forces acting on the airfoil were obtained either by balance measurements or by pressure distribution measurements on the central airfoil. Drag measurements were obtained from wake traverses. Because of the nature of the experimental arrangement, it was possible to test a limited number of air foils only, say, from five to seven, and there is a question as to how closely the results from the test grid may be applied to the grid of infinite extent.

## EXPERIMENTAL SETUP

In order to overcome this objection the authors have undertaken to develop a test setup in which a cylindric axial-flow grid is tested, thus satisfying the requirement with regard to the extent of the grid. Furthermore, the airfoil grid is arranged on a wheel and may be rotated. The entire setup is placed into the working section of a wind tunnel (Figs. 1a and 1b). This arrangement has the advantage that both accelerating grids and decelerating grids may be tested with equal facility. The desired condition of operation may be adjusted readily by varying the wind-tunnel speed. The technique is quite similar to that employed in conventional aerodynamic wind-tunnel tests. By using a rotating grid, it is possible for a given capacity of the wind tunnel to obtain Reynolds numbers higher than those attainable with fixed grids. The wheel carrying the airfoil grid has a tip diameter of 3 ft.; when mounting airfoils of

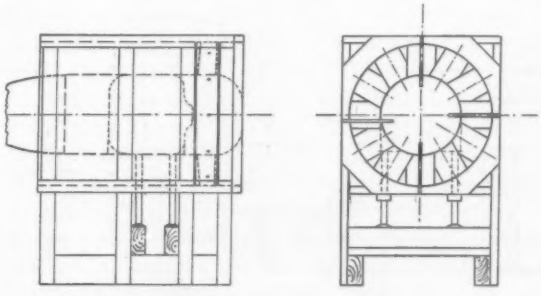

FIG. 1a. Experimental setup.

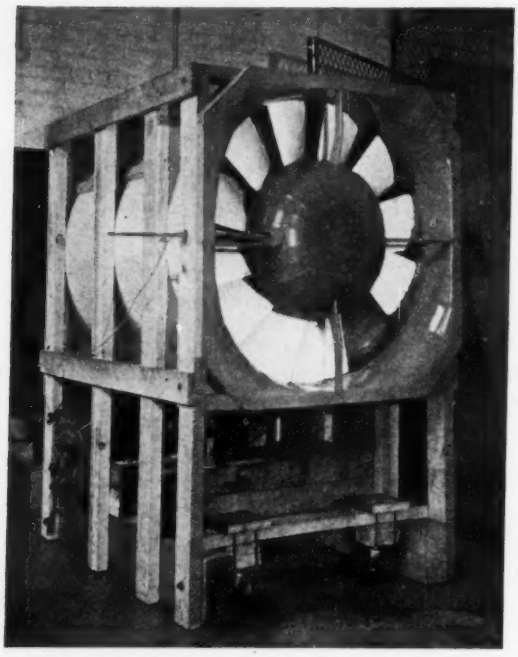

FIG. 1b. Experimental setup.

8-in. chord and operating at 1,200 r.p m., Reynolds numbers of nearly 1,000,000 may be obtained. Mach numbers, however, are of the order of 0.2 and therefore do not compare with those encountered in turbines and compressors.

## THE TESTING EQUIPMENT

The tests were conducted in the working section of a 9-sq.ft. return type wind tunnel of the Aerodynamics Laboratory of Case School of Applied Science. A plan view of this wind tunnel is shown in Fig. 2. The wind tunnel has been adapted for these tests through the installation of a fine mesh screen in the upstream plane of the nozzle. The screen has 18 meshes to the inch and is made of wire $^1/_{100}$ in. in diameter. This screen serves two purposes—it decreases the turbulence and the effect of any wake that might be carried from the downstream side of the working section all around the circuit, and it serves to measure the quantity of flow through the working section, the pressure drop across the screen having been calibrated against quantity of flow by pitot tube readings at the mouth of the nozzle in a preliminary test in which no equipment was placed in the working section. When testing decelerating grids, the resistance of the air circuit is increased further by placing a honeycomb section and a system of adjustable slats in the duct downstream of the working section.

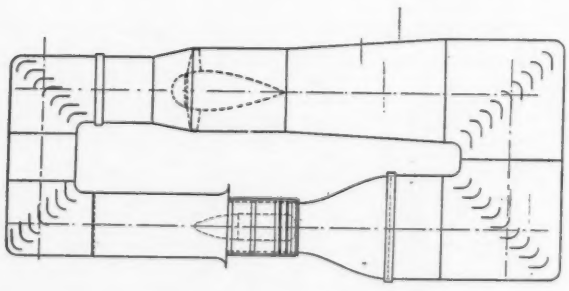

FIG. 2. Arrangement in the wind tunnel.

The test setup proper, which may be placed into the working section, is shown in elevation and side view in Fig. 1a. It consists essentially of a cylindric duct section 36 in. in diameter. Inside this section and coaxial with it, there is mounted an electric motor in a coaxial cylindric cowling of 20-in. diameter so that an annular space of 8-in. radial width is created. Motor supports and motor cowling are streamlined to offer the least air resistance. The motor shaft carries a wheel of 20-in. diameter and 8-in. width of face which is located immediately upstream of the motor cowling. On the face of this wheel may be mounted a number of airfoil-shaped blades. The tips of these blades are interconnected by a plywood ring of 36-in. inside diameter and 8-in. width. Rigidity of the wheel (consisting of the ring connecting the tips, the blades, and the hub wheel) is assured by radial stay bolts extending one through each blade. This design of the test wheel was chosen in preference to the design with a stationary wall around the tips, since it was felt that it lessened the interference from tip clearance and also provided greater rigidity for the blades.

Upstream of the wheel carrying the cylindric grid there are mounted a stationary bellmouth section and, connected to it by slender radial ribs, a fixed streamlined nose for the cylindric hub, thus providing a smooth inlet section for the air from the throat of the wind-tunnel nozzle to the cylindric grid. The clearances between the wheel and the nose fairing and motor cowling, and likewise between the rotating rim, the fixed casing and bellmouth section, are approximately $^1/_8$ in.

The test section fits tightly against the downstream inlet of the wind tunnel. A streamlined tail, which projects from the cylindric hub into the downstream section, is provided to improve the uniformity of flow in the wind tunnel, downstream of the working section, by reducing wake areas. In normal operation the pressure in the working section is atmospheric immediately upstream of the cylindric grid and either above, below, or equal to atmospheric pressure downstream of the cylindric grid, depending upon whether the latter acts as a compressor or turbine or has no effect. It was assumed that in choosing the tunnel pressure with respect to atmosphere the effect upon the grid of leakage of air through the clearances between casing and rim was reduced to a minimum.

The unit is powered by a 7-hp., 1200 r.p.m. d.-c. motor equipped with electric controls that permit oper-

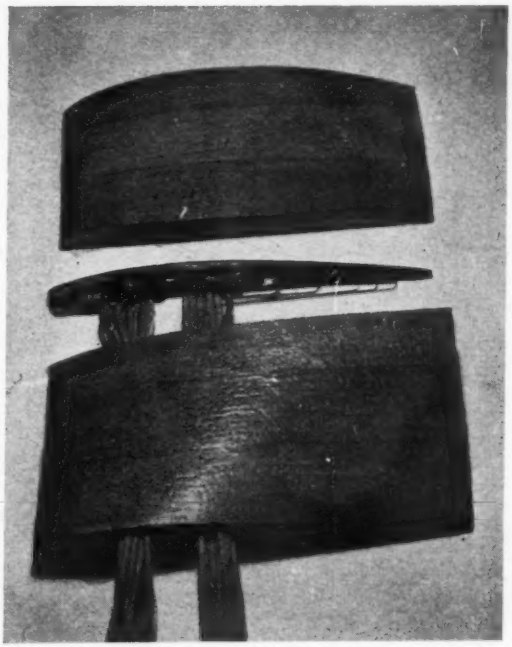

FIG. 3. The master airfoil.

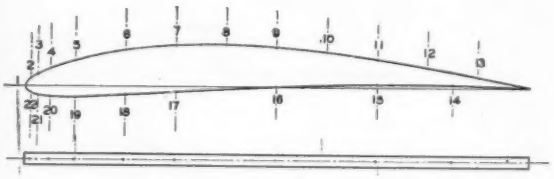


FIG. 4. The profile N.A.C.A. 4409 airfoil, showing location of pressure taps.

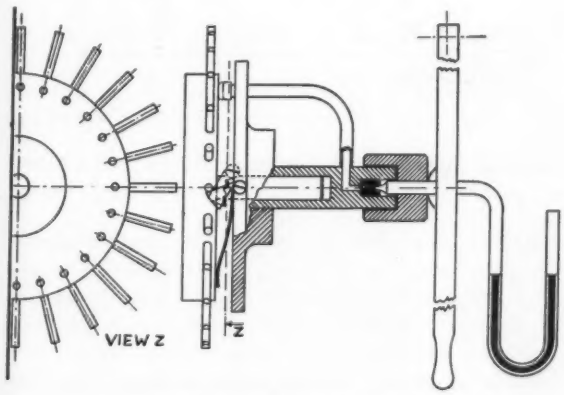


FIG. 5. Selector switch.

ation at several speeds and over a wide range of load conditions. As the lift of a pump grid becomes negative, the motor reverses its action and becomes a generator.

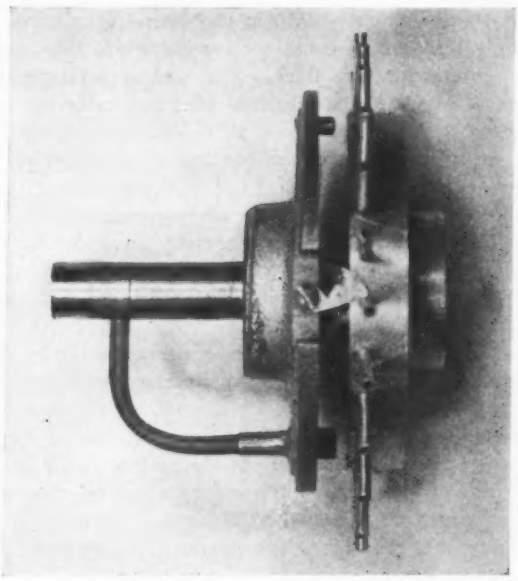

FIG. 6. Selector switch.

## THE CYLINDRIC GRID

The blades of the circular grid are composed of one master blade (see Fig. 3) and of dummy blades, all blades being of identical shape and twist. The number of the latter depends upon the spacing of the grid to be tested.

The master airfoil contains a section of brass $^1/_4$ in. wide, which is provided with 20 pressure taps, distributed over the part of its surface forming the airfoil contour as shown in Fig. 4. The remainder of this airfoil is made of wood. The section prepared for pressure measurements may be inserted at various positions along the radial span of the blade. To the pressure taps are connected rubber tubes which lead to the selector switch. The tests were conducted on a N.A.C.-A. 4409 profile.

## THE SELECTOR SWITCH

The selector switch has two purposes: (1) that of a seal transmitting the air pressure in a rotating pressure line to a stationary line, which in turn is connected to a U-tube manometer and (2) that of connecting successively the pressure line from each of the pressure taps of the master airfoil to a single line leading to the seal. A cross section of the selector switch is shown in Fig. 5 and a photograph in Fig. 6. Fig. 3 shows the mechanical details of the switch. The airtight seal between the rotating and the stationary part of the switch is produced by a rubber bushing. In order to minimize the wear of this bushing, provision has been made for continuous lubrication of the contact surfaces. Various lubricants were tried and it was found that glycerine was most suitable as a lubricating medium. The lubri-

cating system (not shown in the figure) consists of a supply reservoir, a container for the waste lubricant, and interconnecting lines. The seal is arranged in such a way that the lubricant may not enter the air lines.

The selector mechanism consists of a trigger lever operated by axial motion of the stationary part of the valve through an axial stroke of approximately $^1/_4$ in. One of two opposing discs is thereby advanced by an angle equal to the spacing of the bores connecting to the pressure lines in the rotating system, which are arranged equidistant around the circumference of the second disc. The friction in the seal, augmented by the friction of an adjustable sliding surface, supplies the force for advancing the selector switch. Contact between the pressure line coming from the seal and any of the various lines leading to the master airfoil is established by a rubber bushing. Since no relative motion occurs at this point, an airtight connection is readily obtained through adequate axial pressure.

## Testing Procedure

The following readings were taken: (1) r.p.m. of the grid; (2) quantity of airflow from pressure difference across the wind-tunnel screen; (3) static pressure upstream of the grid; (4) static pressure in the annular space downstream of the grid both adjacent to the casing and adjacent to the cylindric hub; (5) direction and velocity of flow at various radii downstream of the grid; and (6) pressure distribution over the blade element.

## Results

Plots of pressure distribution against distance along the chord of the blade section, such as shown in Figs. 7 to 9 were obtained from the pressure distribution tests. The normal force per unit radial length of the blade was obtained by integration of the area under the curve of pressure distribution plotted against distance along the chord. Similarly, the tangential force was

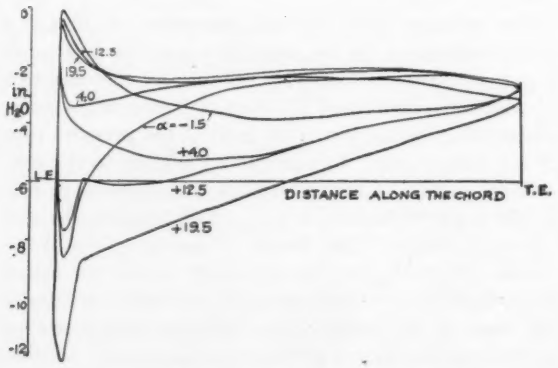


Fig. 7. Pressure distribution ($t/l$ = 12) (single airfoil); $r$ = 14 in.; $B_r$ = 30°.

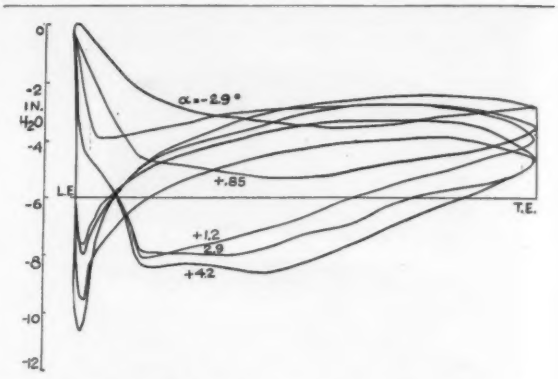


Fig. 8. Pressure distribution, grid, $t/l$ = 1.83 (six blades); $r$ = 14 in.; $B_r$ = 30°.

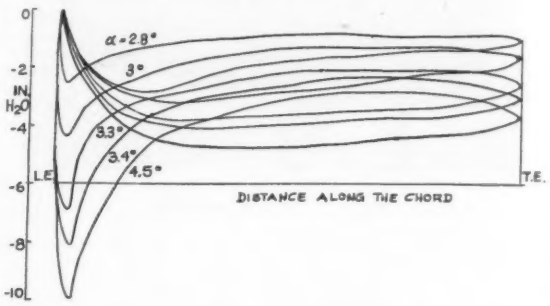


Fig. 9. Pressure distribution, grid, $t/l$ = 0.915 (twelve blades); $r$ = 14 in.; $B_r$ = 30°.

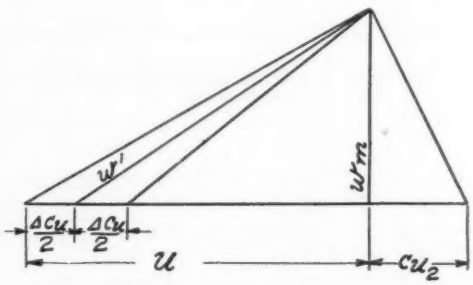


Fig. 10. Typical velocity diagram for flow through a moving pump grid.

obtained from plots of pressure distribution against distance normal to the chord. The resultant force was then found as the geometric sum of normal and tangential force. With the resultant force and its direction and with the angle of the blade section known, it is possible to obtain the component of force parallel to the grid as well as the component normal to the grid. The forces thus computed are regarded as closely approximating the actual forces, although the effect of skin friction has not been taken into account. Disregarding the effect of skin friction, a velocity diagram can be plotted from the experimental data available for each test run. A typical diagram is shown in Fig.

10 for which the significant quantities were computed as follows:

(1) The axial velocity component from the quantity of flow through the grid, neglecting the effect of blade thickness.

(2) The rotational component of velocity at discharge, the velocity at approach being in all cases axial, again neglecting the effect of blade thickness:

$$c_{u2} = \frac{N \sin \beta + T \cos \beta}{\rho t w_m}$$

where $N$ = normal force component per unit radial length of profile
$T$ = tangential force component per unit radial length of profile
$\rho$ = mass density
$t$ = pitch of blades.

(3) The mean relative velocity

$$w' = \sqrt{w_m^2 + [u - (c_{u2}/2)^2]}$$

using the notations of velocity vectors defined by the geometric relations of Fig. 10.

(4) The angle of attack $\alpha$ computed as the angle subtended by the geometrical chord and the mean relative velocity $\alpha = \beta - \beta'$.

The normal force may now be expressed in nondimensional form as follows:

$$C_N = N/[l(\rho w'^2/2)]$$

where $l$ = chord of blade, and correspondingly the tangential force

$$C_T = T/[l(\rho w'^2/2)]$$

From these quantities the lift coefficient is obtained:

$$C_L = c_N \cos \alpha - c_T \sin \alpha$$

Results of the computations of test data are given in Figs. 11a and 11b, which show lift coefficients versus angle of attack obtained from pressure distribution measurements at the mid-section of the blade, $r$ = 14 in. For purposes of comparison, both Figs. 11a and 11b show the lift coefficient curve of N.A.C.A. 4409 for infinite aspect ratio.

### *Pitch-Chord Ratios*

Three different pitch-chord ratios were investigated, namely, $t/l$ = 12 (one blade only in the wheel), $t/l$ = 1.83 (six blades), and $t/l$ = 0.915 (twelve blades). Tests of the two smaller pitch-chord ratios were made at one angular blade setting only—namely, at the setting for which the twist of the blade was designed on the basis of constant circulation along the radius. The tests at the largest pitch chord ratio, $t/l$ = 12, however, include one series at a blade angle smaller and one at a blade angle larger than the designed blade angle.

It should be stated here that the blade with a given twist can be expected to have constant circulation along its span at one particular value of the mid-section lift coefficient only. Only at this particular value of the lift coefficient is the condition of flow on coaxial surfaces of revolution, which underlies two-dimensional blade element theory, reasonably well fulfilled. At other lift coefficients, variation of circulation along the span of the blade may be expected to affect the flow past any particular blade section in a way that thus far eludes theoretic analysis.

While this consideration constitutes a severe limitation of the experimental method, it appears that for small variations of the lift coefficient the effect of spanwise variation of circulation is not so large as to deprive the results of their significance.

On the basis of these results the following conclusions can be derived:

(1) The lift characteristic of the mid-section of the blade for large pitch-chord ratios compares favorably with the lift characteristic of the same airfoil section in indefinite flow, reduced to infinite aspect ratio, in respect to angle of attack at zero lift and to slope.

(2) The maximum lift coefficient of the airfoil section in a widely spaced rotating grid is considerably

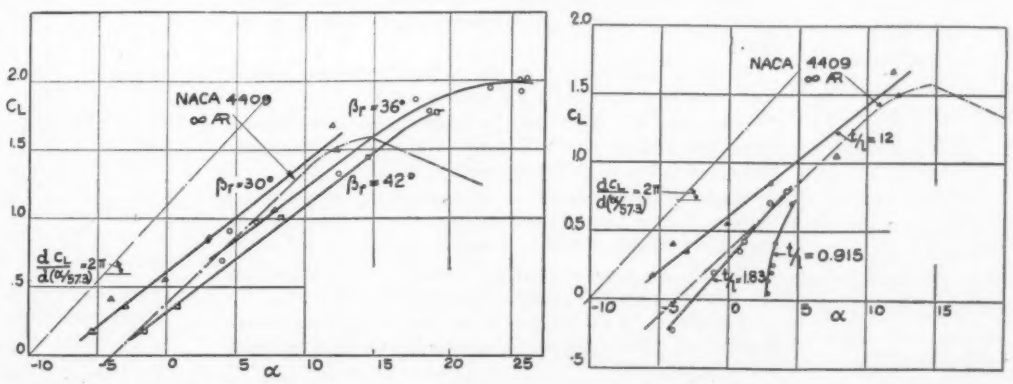


FIGS. 11a and 11b. Lift coefficients versus angle of attack for various blade spacings. FIG. 11a (*left*). $r$ = 14 in.; $t/l$ = 12. FIG. 11b (*right*). $r$ = 14 in.; $B_r$ = 30°.

larger than the maximum lift coefficient obtained in infinite flow in the wind tunnel.

It is suggested that this may be the result of the action of centrifugal acceleration upon the boundary layer. As the air in the boundary layer is retarded relative to the blade it acquires a larger angular velocity than the air in the free stream. Consequently, it is accelerated in a radial direction, and the resulting flow, which has been observed by means of smoke issued from bores in the airfoil, may retard the growth of the boundary layer and delay separation.

(3) The angle of attack at zero lift was found to increase as the pitch-chord ratio was decreased.

(4) The slope of the lift curve appears to increase as the pitch-chord ratio decreases.

The variation of blade characteristics with pitch-chord ratio can be explained qualitatively by effects of mutual interference of neighboring blades related to circulation[6] and by the effect of blade thickness.[7] The pressure distributions for blade grids at various spacings and angles of attack (Figs. 7 to 9) serve to show the effect of these factors in detail. The analysis of this evidence has not been completed.

## Wake Traverses

It has been stated above that because of the neglect of skin friction the functional relation between the lift coefficient and the angle of attack must be regarded as a first approximation.

Although this approximation is probably quite close, the method is inherently wanting in ultimate precision because of the technique employed—namely, the determination of aerodynamic forces from pressure distribution measurements, unless the profile drag is included.

In an attempt to supplement the information secured from pressure distribution measurements, particularly with regard to profile drag, wake traverses were obtained with a hot wire instrument. Sample records of wake traverses are shown in Fig. 12 which appear to indicate that, basically, this method is feasible provided it furnishes traverses of direction of flow as well as of velocity.

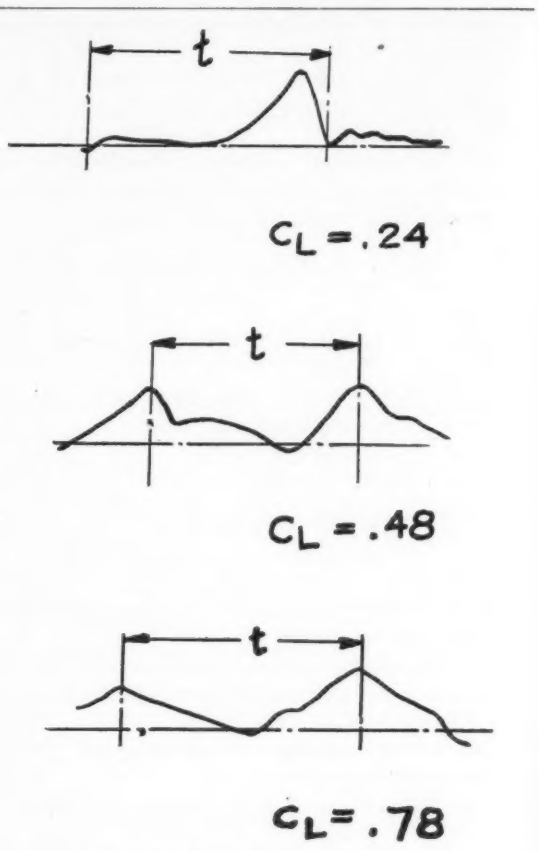


Fig. 12. Oscillographs of wake traverses; $r = 14$ in.; $B_r = 30°$; $t/l = 1.83$; 980 r.p.m.

## References

[1] Christiani, K., *Experimentelle Untersuchung eines Tragflugelprofils bei Gitteranordnung*, Luftfahrtforschung, Vol. 2, p. 91, 1928.

[2] Keller, C., and Marks, L. S., *Theory and Performance of Axial Flow Fans;* McGraw-Hill Book Company, 1937.

[3] Shimoyana, Y., *Experiments on Rows of Airfoils for Retarded Flow*, Transactions of the Society of Mechanical Engineers, Japan, Vol. 3, No. 13, p. 334, November, 1937.

[4] Kraft, H., and Berry, T. M., *Automatic Integrating Pressure Traverse Recorder for Study of Flow Phenomena in Steam Turbine Nozzles and Buckets*, A.S.M.E. Transactions, pp. 479–488, 1940.

[5] New, W. R., *An Investigation of Energy Losses in Steam Turbine Elements*, A.S.M.E. Transactions, pp. 489–502, 1940.

[6] Kawada, S., *A Contribution to the Theory of Latticed Wings*, Proceedings, Third Congress of Applied Mechanics, Stockholm, Vol. 1, p. 393, 1930.

[7] Betz, A., *Diagramme zur Berechnung von Flugelreihen*, Ing. Archiv, Vol. 2, p. 359, 1931.

# Tension Joints in Aircraft Structures

CLARENCE H. HOLLEMAN*
*Boeing Aircraft Company*

SUMMARY

The basic assumptions of conventional riveted joint design practice are discussed with respect to their applicability to aluminum alloys. Data are presented to establish the effect of holes on the tension efficiency of 24ST aluminum-alloy sheet, and values are proposed for use in riveted joint design. Information is presented showing the effect of hole size, hole type, number and spacing of holes, number of rows, and amount of stagger.

A series of tension tests of riveted skin splices is discussed, and suggestions are offered for obtaining the maximum possible efficiency in continuous joints.

## INTRODUCTION

MUCH SPACE in technical literature has been devoted to panel design and the design of compression surfaces, whereas the subject of tension surfaces and tension joints in aircraft structures has received little attention. The designer will, however, readily admit that the efficiency of a tension joint has an important bearing on structural weight and structural efficiency, since the efficiency of a monocoque structure can be but little higher than that of its weakest joint. The lack of emphasis on tension joints must therefore be attributed to a general belief that their behavior is well understood. The absence of instability failures and the extensive experience of engineers with riveted joints in boiler and tank design and in the design of steel structures lend credence to this belief.

It must, however, be recognized that the aluminum alloys and the mild steels used by the structural engineer are widely dissimilar materials. This dissimilarity has an important bearing on the relative efficiencies of steel and duraluminum joints. Evidence to support this contention will be developed in the discussion that follows.

## BASIC ASSUMPTIONS IN RIVETED JOINT ANALYSIS

The analysis of riveted boiler seams and riveted structural steel joints is commonly based on two assumptions:

(1) The efficiency of the joint material is not reduced at sections where material is removed for rivet holes; i.e., the same ultimate stress may be developed in the material at such sections as may be developed in an unperforated section.

(2) The load is distributed among the rivets in direct proportion to the ability of each rivet to resist load. Thus, if all rivets are critical in shear, the ultimate strength of a joint may be determined by summing the shear strengths of all rivets in the joint, irrespective of their size or of their position in the joint pattern.

The foregoing assumptions will be examined critically to see whether or not they are applicable to aluminum-alloy sheet or plate joined together by aluminum-alloy rivets.

## THE EFFECT OF HOLES ON THE STRENGTH OF TENSION MEMBERS

Analysis by the mathematical theory of elasticity indicates that the tensile stress at the edge of a circular hole in a plate subjected to uniform tensile stress is three times as large as the uniform tensile stress in the gross section. Various experimental methods, such as photoelasticity, the ductile material or Lueder's line method, and the brittle-material method, show values for the stress concentration factor ranging from 1.9 to 3.0. When load is applied to a plate by a pin through a hole in the plate, the concentration of stress at the edge of the hole is about the same as occurs when there is no pin in the hole.

It is generally assumed, and rightly so, that in a ductile material such as structural steel this concentration of stress has no significant effect on the ultimate stress that can be developed in the material. The ultimate load is, of course, reduced to the extent the cross-sectional area is reduced by the hole. When the stress at the edge of the hole reaches the yield point, the material continues to elongate in a ductile manner—i.e., without increased stress—until the stresses become approximately uniform over the entire cross section at which the hole occurs, and the load then progresses to the ultimate without further concentration of stress. It may be noted, however, that failure will still begin at the edge of the hole, since the material at this point must obviously have experienced the greatest elongation.

If, however, the perforated tension member is made from a material that does not possess a clearly defined ductile range (e.g., aluminum alloy), some concentration of stress must always exist at the edge of the hole. As a result, this more highly stressed material will reach the ultimate strength sooner than will the adjacent material, a localized rupture will develop, and a progressive tension failure will occur at the reduced section.

Presented at the Structures Session, Eleventh Annual Meeting, I.A.S., New York, January 25–29, 1943.

* Structural Development Engineer.

## The Effect of Holes on the Tensile Strength of 24ST Extrusions

Fig. 1 is a photograph of six tension specimens cut from a single length of a 24ST extrusion with a 0.60 by 3.0 cross section. Holes $^3/_4$ in. in diameter were drilled through all but one of these specimens, located as shown in the photograph. All specimens were pulled to failure in a testing machine.

The two specimens with single holes each failed at approximately the same load and, hence, at the same average stress on the net section. This stress was but 94.3 per cent of the ultimate stress for the unperforated specimen. The unsymmetric location of the hole in one specimen had no apparent effect on the efficiency of the member.

The specimens with two staggered holes failed at stresses lower than the ultimate stress for specimens with single holes. This was true even when the holes were separated sufficiently to cause rupture to occur across but one hole. Results for all specimens are shown in Table 1.

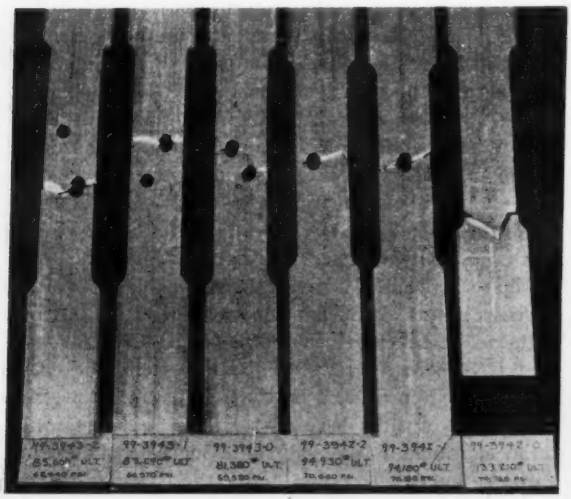

Fig. 1. Tension specimens cut from 24ST extrusions.

Table 1

Tensile Specimens of Heavy 24ST Extrusions with Staggered Holes

| Specimen | Cross Section (In. by In.) | Hole Diameter (In.) | Per Cent Holes Out | Ultimate Stress on Net Area (Lbs. per Sq.In.) | Efficiency of Net Area (Per Cent) |
|---|---|---|---|---|---|
| 99-3942-0 | 3.0 by 0.60 | 0.75 | 25 | 74,670 | 100 |
| -1 | 3.0 by 0.60 | 0.75 | 25 | 70,180 | 94.0 |
| -2 | 3.0 by 0.60 | 0.75 | 25 | 70,680 | 94.7 |
| 99-3943-0 | 3.0 by 0.60 | 0.75 | 25 | 59,530 | 79.8 |
| -1 | 3.0 by 0.60 | 0.75 | 25 | 60,970 | 81.6 |
| -2 | 3.0 by 0.60 | 0.75 | 25 | 62,940 | 84.4 |

## The Effect of Holes on the Tensile Strength of Sheet

Fig. 2 shows tensile specimens made from 24ST and 17ST aluminum-alloy sheet, and Fig. 3 shows specimens made from annealed X4130 steel sheet. Included are specimens with no holes, specimens with holes in the center only, and specimens with staggered holes. Results are tabulated in Table 2.

The average ultimate stress on the net area of sections with one hole out was lower than the ultimate stress on the unperforated sections in the case of both aluminum alloys, whereas the steel specimens with one hole out developed the same average stress on the net area at ultimate load as did the unperforated steel specimen. These results indicate that the assumption of no reduction in the efficiency of tension material owing to stress concentrations at holes is erroneous for aluminum alloys such as 17ST and 24ST but appears to be valid for a ductile material such as annealed X4130 steel.

Another result that has significance in the design of tension joints may be observed in the case of specimens

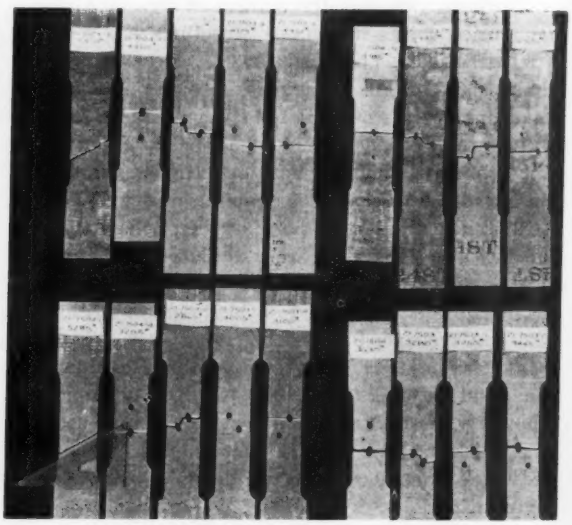

Fig. 2. Typical tension specimens. Aluminum alloy—17ST and 24ST.

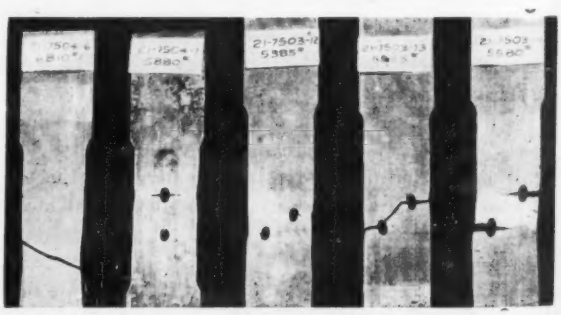

Fig. 3. Typical tension specimens. Steel—SAE X4130.

TABLE 2

Tensile Specimens with Staggered Holes

| Specimen | Material | Cross Section (In. by In.) | Hole Diameter (In.) | Per Cent Holes Out | Ultimate Stress (Lbs. per Sq.In.) Gross area | Ultimate Stress (Lbs. per Sq.In.) Net area | Efficiency (Per Cent) Gross area | Efficiency (Per Cent) Net area |
|---|---|---|---|---|---|---|---|---|
| 21-7504-3 | 24ST | 1.77 by 0.0502 | None | 0 | 66,400 | 66,400 | 100 | 100 |
| 1 | 24ST | 1.75 by 0.050 | 0.25 | 14.3 | 51,200 | 59,700 | 77.1 | 90.0 |
| 21-7503-3 | 24ST | 1.75 by 0.0505 | 0.25 | 14.3 | 45,100 | 52,600 | 68.0 | 79.2 |
| -4 | 24ST | 1.75 by 0.051 | 0.25 | 14.3 | 46,300 | 54,000 | 69.8 | 81.4 |
| -5 | 24ST | 1.75 by 0.051 | 0.25 | 14.3 | 48,200 | 56,300 | 72.6 | 84.8 |
| 21-7504-5 | 24ST | 1.77 by 0.0502 | 0.156 | 8.8 | 54,000 | 59,200 | 81.4 | 89.2 |
| 21-7503-9 | 24ST | 1.77 by 0.0505 | 0.156 | 8.8 | 48,500 | 53,200 | 73.1 | 80.1 |
| -10 | 24ST | 1.77 by 0.0505 | 0.156 | 8.8 | 49,500 | 54,300 | 74.6 | 81.8 |
| -11 | 24ST | 1.77 by 0.0505 | 0.156 | 8.8 | 48,500 | 53,100 | 73.1 | 80.0 |
| 21-7504 | 24ST | 1.44 by 0.0505 | 0.25 | 17.4 | 49,900 | 60,400 | 75.2 | 91.0 |
| 21-7503 | 24ST | 1.44 by 0.051 | 0.25 | 17.4 | 44,600 | 54,000 | 67.2 | 81.4 |
| 21-7503-1 | 24ST | 1.44 by 0.051 | 0.25 | 17.4 | 44,200 | 53,500 | 66.5 | 80.6 |
| -2 | 24ST | 1.44 by 0.051 | 0.25 | 17.4 | 46,900 | 56,800 | 70.7 | 85.5 |
| 21-7504-2 | 17ST | 1.77 by 0.0495 | None | 0 | 60,300 | 60,300 | 100 | 100 |
| -4 | 17ST | 1.45 by 0.0495 | 0.25 | 17.2 | 45,800 | 55,300 | 76.0 | 91.6 |
| 21-7503-6 | 17ST | 1.45 by 0.0495 | 0.25 | 17.2 | 39,900 | 48,200 | 66.2 | 80.0 |
| -7 | 17ST | 1.45 by 0.051 | 0.25 | 17.2 | 40,600 | 49,100 | 67.8 | 81.5 |
| -8 | 17ST | 1.45 by 0.0495 | 0.25 | 17.2 | 43,200 | 52,200 | 71.6 | 86.6 |
| 21-7504-6 | X4130 | 1.76 by 0.049 | None | 0 | 79,000 | 79,000 | 100 | 100 |
| -7 | X4130 | 1.75 by 0.0495 | 0.25 | 14.3 | 67,800 | 79,100 | 85.9 | 100.0 |
| 21-7503-12 | X4130 | 1.75 by 0.0498 | 0.25 | 14.3 | 61,900 | 72,100 | 78.4 | 91.3 |
| -13 | X4130 | 1.75 by 0.0490 | 0.25 | 14.3 | 64,900 | 75,600 | 82.2 | 95.7 |
| -14 | X4130 | 1.75 by 0.0495 | 0.25 | 14.3 | 64,500 | 75,100 | 81.6 | 95.1 |

with staggered holes. The presence of a second hole in the sheet always caused failure to occur at a lower average stress, based on the area of a section with one hole out, than when there was one hole only, even though failure occurred on a section through a single hole. Presumably, the section in line with the extra hole is unable to assume its full share of the load, thus causing an unequal distribution of stress across the section. This effect is likewise important in the case of the X4130 specimens.

### THE TENSION EFFICIENCY OF 24ST ALUMINUM-ALLOY SHEET WITH RIVET HOLE CUTOUTS

The foregoing examples may be construed as evidence that the material efficiency of aluminum alloys subjected to tensile loads is reduced by the presence of holes in the members. To obtain quantitative values of this reduced efficiency for use in joint design, a series of tests was inaugurated which embraced a large variety of riveting conditions; 0.081 gauge 24ST sheet was chosen as being representative of both size and material. Tests were designed to disclose the effect of hole type (cylindric or countersunk), hole size, number and spacing of holes, number of rows, and amount of stagger. All specimens were cut from the same sheet of material. Three unperforated specimens were tested in tension to provide a basis for computing the efficiencies of the specimens with holes.

Fig. 4 shows typical specimens with holes in one transverse row only. Pertinent data on dimensions and test results are shown in Table 3. Fig. 5 shows typical specimens with two transverse rows of staggered cylindric holes, and Fig. 6 shows typical specimens with staggered countersunk holes. Included also is one specimen with nine equal diameter holes in a single longitudinal row. Dimensions and test results for these specimens are shown in Table 4. Net areas were in all cases based on the transverse section having the larger number of holes, and nominal rivet dimensions were used as the dimensions of the holes.

In Fig. 7 the net area efficiencies of all specimens have been plotted against the percentage of material removed by holes. Values for both single and multiple rows of holes are shown, even though it is recognized that the two types are not entirely comparable because of the effect of a second row of holes on the efficiency of the material in the row at which the net area is computed. However, for the amount of stagger encountered in conventional riveted joints this effect is small enough to fall within the range of experimental variation (see Fig. 7). Therefore, the results for both types may be used to establish design criteria. A study of Fig. 7 and of Tables 3 and 4 reveals several significant trends.

(1) There is a small but perceptible increase in efficiency as the amount of material removed is increased.

(2) For a given decrease in area, greater efficiency is obtained if this decrease is produced by several holes rather than by a single large hole.

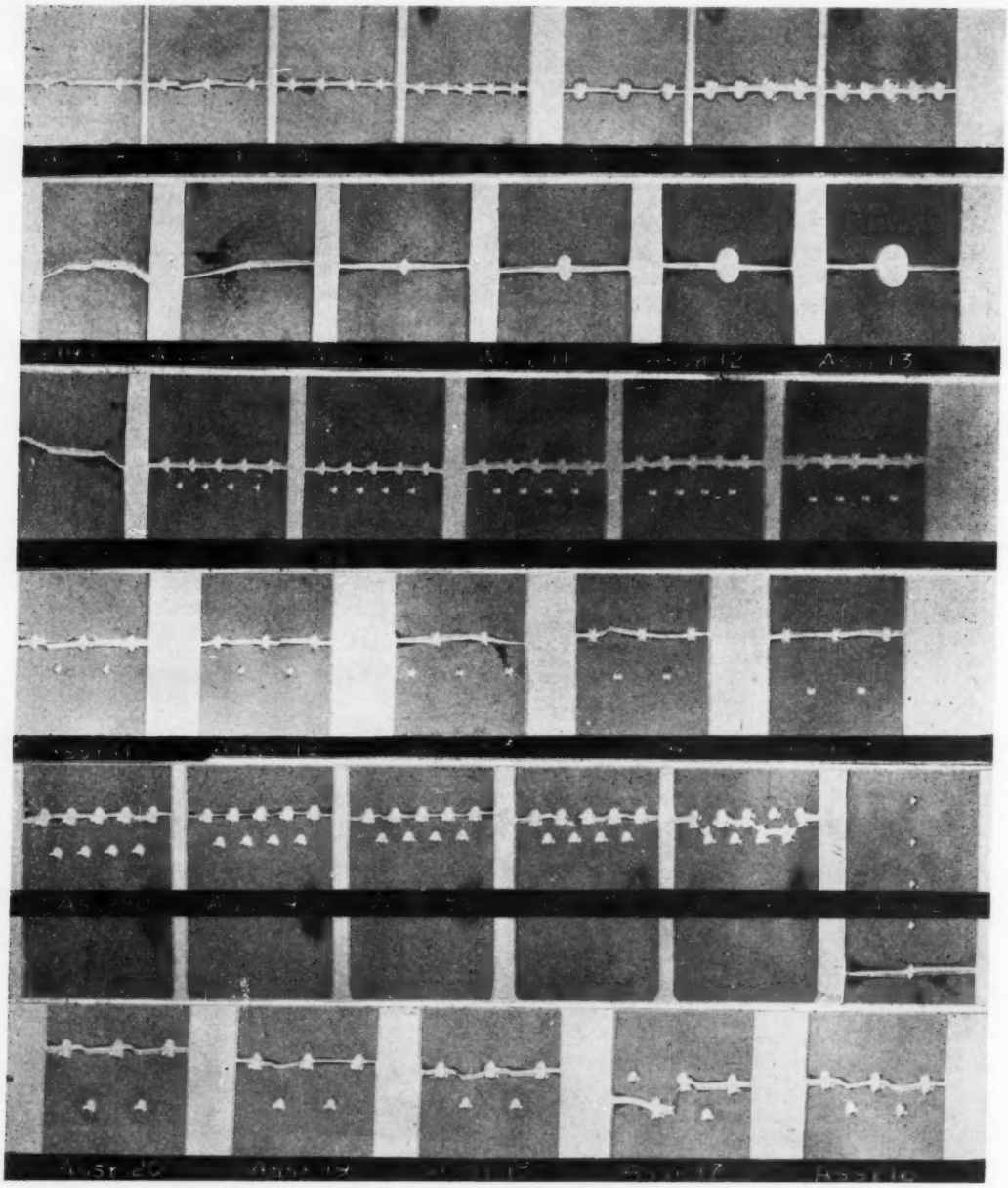

FIG. 4 (*top two strips*). Typical tension specimens with holes in one transverse row.
FIG. 5 (*center two strips*). Typical tension specimens with staggered cylindric holes in two transverse rows.
FIG. 6 (*bottom two strips*). Typical tension specimens with staggered countersunk holes in two transverse rows.

(3) Efficiencies tend to improve as the distance between transverse rows of staggered holes is increased.

(4) Countersunk holes have a somewhat more unfavorable effect on efficiency than do cylindric holes.

For design purposes it is recommended that the efficiency of 24ST aluminum alloy on transverse sections through rivet holes be assumed to be 90 per cent, where stresses are based on the net area and net area calculations are based on nominal rivet dimensions.

Fig. 8 shows the variation of overall efficiency with the area of material removed. The line representing 90 per cent net area efficiency may be used for design purposes.

## EFFICIENCY OF RIVETED JOINTS

A series of riveted skin splices, all made from 0.081 gauge 24ST aluminum-alloy sheet and 24ST rivets, was tested in tension. Joints were varied as to type (lap joints, single-strap butt joints, and double-strap butt joints), number of rows of rivets, size, type and number of rivets per row, and sheet width. Dimensions and

TABLE 3

Tensile Specimens with Holes in One Transverse Row

| Specimen | Cross Section (In. by In.) | Type of Hole | Number of Holes | Per Cent Holes Out | Ultimate Stress (Lbs. per Sq.In.) Gross area | Ultimate Stress (Lbs. per Sq.In.) Net area | Efficiency (Per Cent) Gross area | Efficiency (Per Cent) Net area |
|---|---|---|---|---|---|---|---|---|
| 1 | 4.20 by 0.082 | 1/4 cylindric | 5 | 29.4 | 47,600 | 67,500 | 67.3 | 95.5 |
| 2 | 4.00 by 0.081 | 1/4 cylindric | 4 | 25.0 | 48,800 | 65,000 | 69.1 | 92.0 |
| 3 | 4.60 by 0.081 | 1/4 cylindric | 4 | 21.7 | 54,400 | 69,500 | 77.0 | 98.4 |
| 4 | 4.00 by 0.081 | 1/4 cylindric | 3 | 18.8 | 53,700 | 65,900 | 76.0 | 93.3 |
| 5 | 4.32 by 0.080 | 1/4 countersunk | 5 | 39.0 | 40,100 | 65,950 | 56.7 | 93.3 |
| 6 | 4.12 by 0.082 | 1/4 countersunk | 4 | 32.0 | 44,500 | 65,400 | 63.0 | 92.5 |
| 7 | 4.72 by 0.081 | 1/4 countersunk | 4 | 28.3 | 44,530 | 62,000 | 63.0 | 87.7 |
| 8 | 4.12 by 0.082 | 1/4 countersunk | 3 | 24.0 | 47,300 | 62,300 | 67.0 | 88.1 |
| 9 | 4.00 by 0.079 | 1/8 cylindric | 1 | 3.2 | 61,100 | 63,100 | 86.5 | 89.3 |
| 10 | 4.00 by 0.081 | 1/4 cylindric | 1 | 6.2 | 58,800 | 62,700 | 83.2 | 88.7 |
| 11 | 4.00 by 0.081 | 1/2 cylindric | 1 | 12.6 | 56,200 | 64,300 | 79.5 | 91.0 |
| 11 | 4.00 by 0.081 | 1/2 cylindric | 1 | 12.6 | 56,800 | 65,000 | 80.4 | 92.0 |
| 12 | 4.00 by 0.080 | 3/4 cylindric | 1 | 19.1 | 51,400 | 63,200 | 72.7 | 89.5 |
| 13 | 4.00 by 0.081 | 1 cylindric | 1 | 25.0 | 48,100 | 64,200 | 68.0 | 90.9 |
| 14 | 5.00 by 0.082 | 1/4 cylindric | 3 | 14.9 | 53,400 | 62,800 | 75.5 | 88.9 |
| 15 | 3.50 by 0.081 | 1/4 cylindric | 2 | 14.1 | 53,200 | 61,800 | 75.3 | 87.5 |
| 16 | 4.32 by 0.081 | 1/4 countersunk | 5 | 38.6 | 41,800 | 68,100 | 59.2 | 96.4 |
| 17 | 4.12 by 0.082 | 1/4 countersunk | 4 | 31.9 | 44,970 | 66,100 | 63.6 | 93.5 |
| 18 | 4.00 by 0.082 | 1/4 cylindric | 2 | 12.2 | 55,500 | 63,200 | 78.5 | 89.5 |
| 19-1 | 3.50 by 0.081 | None | 0 | ... | 70,800 | ... | 100 | ... |
| 19-2 | 3.50 by 0.082 | None | 0 | ... | 70,700 | ... | 100 | ... |
| 19-2 | 3.50 by 0.082 | None | 0 | ... | 70,700 | ... | 100 | ... |

TABLE 4

Tensile Specimens with Staggered Holes

| Specimen | Cross Section (In. by In.) | Type of Hole | Number of Holes | Per Cent Holes Out | Ultimate Stress (Lbs. per Sq.In.) Gross area | Ultimate Stress (Lbs. per Sq.In.) Net area | Efficiency (Per Cent) Gross area | Efficiency (Per Cent) Net area |
|---|---|---|---|---|---|---|---|---|
| 1 | 4.20 by 0.082 | 1/4 cylindric | 4/5 | 29.2 | 47,400 | 67,000 | 67.0 | 94.8 |
| 2 | 4.20 by 0.082 | 1/4 cylindric | 4/5 | 29.2 | 47,700 | 67,400 | 67.5 | 95.4 |
| 3 | 4.20 by 0.082 | 1/4 cylindric | 4/5 | 29.2 | 49,000 | 69,300 | 69.3 | 98.0 |
| 4 | 4.20 by 0.082 | 1/4 cylindric | 4/5 | 29.2 | 48,400 | 68,500 | 68.5 | 97.0 |
| 5 | 4.20 by 0.081 | 1/4 cylindric | 4/5 | 29.7 | 45,300 | 64,400 | 64.1 | 91.0 |
| 6 | 4.32 by 0.082 | 1/4 countersunk | 4/5 | 38.2 | 39,700 | 64,100 | 56.2 | 90.6 |
| 7 | 4.32 by 0.082 | 1/4 countersunk | 4/5 | 38.2 | 41,500 | 67,100 | 58.7 | 95.0 |
| 8 | 4.32 by 0.081 | 1/4 countersunk | 4/5 | 38.6 | 39,900 | 64,900 | 56.5 | 91.8 |
| 9 | 4.32 by 0.080 | 1/4 countersunk | 4/5 | 39.0 | 40,600 | 66,600 | 57.4 | 94.2 |
| 10 | 4.32 by 0.079 | 1/4 countersunk | 4/5 | 39.6 | 43,400 | 71,800 | 61.4 | 101.5 |
| 11 | 4.00 by 0.081 | 1/4 cylindric | 2/3 | 18.8 | 49,400 | 60,800 | 69.9 | 86.0 |
| 12 | 4.00 by 0.081 | 1/4 cylindric | 2/3 | 18.8 | 52,200 | 64,200 | 73.9 | 90.9 |
| 13 | 4.00 by 0.082 | 1/4 cylindric | 2/3 | 18.5 | 54,700 | 67,200 | 77.4 | 95.1 |
| 14 | 4.00 by 0.082 | 1/4 cylindric | 2/3 | 18.5 | 50,900 | 62,600 | 72.0 | 88.5 |
| 15 | 4.00 by 0.081 | 1/4 cylindric | 2/3 | 18.8 | 54,900 | 67,600 | 77.7 | 95.6 |
| 16 | 4.12 by 0.080 | 1/4 countersunk | 2/3 | 24.6 | 47,700 | 63,200 | 67.5 | 89.5 |
| 17 | 4.12 by 0.081 | 1/4 countersunk | 2/3 | 24.2 | 47,900 | 63,200 | 67.8 | 89.5 |
| 18 | 4.12 by 0.081 | 1/4 countersunk | 2/3 | 24.2 | 45,900 | 60,700 | 65.0 | 86.0 |
| 19 | 4.12 by 0.082 | 1/4 countersunk | 2/3 | 24.0 | 49,700 | 65,300 | 70.3 | 92.4 |
| 20 | 4.12 by 0.082 | 1/4 countersunk | 2/3 | 24.0 | 51,200 | 67,300 | 72.5 | 95.2 |
| 21 | 4.00 by 0.081 | 1/4 cylindric | 9 | 6.2 | 56,500 | 60,200 | 80.0 | 85.2 |

test results are given in Table 5. Joint details are shown by the photographs in Figs. 9, 10, and 11.

It may be noted that the highest overall joint efficiencies obtained, on assemblies 107, 108 and 111, were all approximately 80 per cent. Rupture of these specimens occurred wholly or at least in part in the sheet at the outer row of rivets (see Fig. 9). At rupture the net area efficiencies were as high as or higher than might be expected for the percentage of material removed by rivet holes. It may be concluded that no change in rivet size, type, number or arrangement in

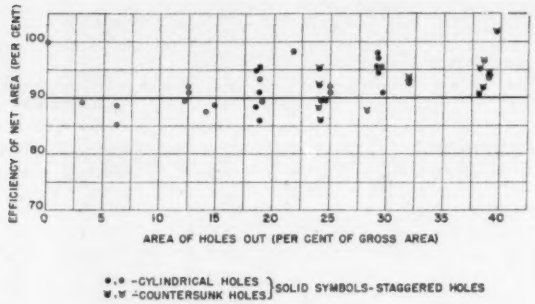
EFFICIENCY OF NET AREA (PER CENT)
AREA OF HOLES OUT (PER CENT OF GROSS AREA)
•,• -CYLINDRICAL HOLES
▼,▽ -COUNTERSUNK HOLES
SOLID SYMBOLS-STAGGERED HOLES

FIG. 7. Tension efficiency of 24ST sheet with holes in transverse rows.

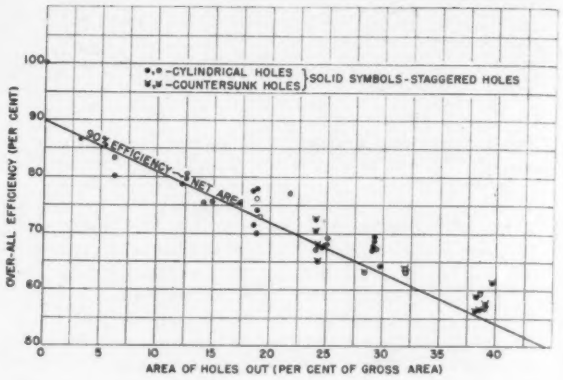
•,• -CYLINDRICAL HOLES
▼,▽ -COUNTERSUNK HOLES
SOLID SYMBOLS-STAGGERED HOLES
90% EFFICIENCY—S NET AREA
OVER-ALL EFFICIENCY (PER CENT)
AREA OF HOLES OUT (PER CENT OF GROSS AREA)

FIG. 8. Overall efficiency of 24ST sheet with holes in transverse rows.

the inner rows would materially improve the efficiency of these joints.

The only means by which the efficiency of assemblies 107, 108, and 111 could be improved would therefore either be a reduction in the percentage of holes out in the outer row or a change in the position of the outer rivets. The percentage of holes out may be lowered by (1) decreasing the size of the outer rivets, (2) increasing the pitch of the outer rivets, or (3) varying both rivet pitch and diameter in such a manner as to reduce the percentage of material removed.

The assumption previously mentioned—that each rivet assumes load in proportion to its ability to carry load—suggests the first method, i.e., decreasing the diameter of the outer rivets. The fallacy of this assumption is indicated by assemblies 101 and 105 (see Fig. 10), both of which failed by shearing the outer rivets prior to any failure in the inner rows. This type of failure may be attributed to the lack of ductility in 24ST aluminum alloy. Since higher stresses exist in the main plate between the first and second rows than in the butt plate between the same rows, unequal elongations must exist in the two plates. This inequality must exist at the expense of the outer rivets which must deform in shear and bearing, particularly

TABLE 5

Riveted Tension Joints—24ST

| Assy. | Cross Section (In. by In.) | Rivet Type | Joint Type | Per Cent Holes Out | Ultimate Stress (Lbs. per Sq.In.) Gross area | Ultimate Stress (Lbs. per Sq.In.) Net area | Efficiency (Per Cent) Gross area | Efficiency (Per Cent) Net area |
|---|---|---|---|---|---|---|---|---|
| 100A | 4.0 by 0.082 | 1/4 countersunk | Butt | 16.46 | 49,700 | 59,500 | 70.3 | 84.1 |
| 100A | 4.0 by 0.082 | 1/4 countersunk | Butt | 16.46 | 49,900 | 59,700 | 70.5 | 84.4 |
| 100B | 4.0 by 0.082 | 1/4 countersunk | Butt | 16.46 | 45,900 | 54,900 | 64.9 | 77.5 |
| 101A | 4.0 by 0.082 | 1/4 countersunk | Butt | 32.90 | 48,000 | (1) | 67.9 | (1) |
| 101A | 4.0 by 0.082 | 1/4 countersunk | Butt | 32.90 | 47,400 | (1) | 67.0 | (1) |
| 101B | 4.0 by 0.082 | 1/4 countersunk | Butt | 32.90 | 48,200 | (1) | 68.1 | (1) |
| 105 | 4.0 by 0.081 | 3/16 countersunk | Butt | ... | 43,800 | (1) | 61.9 | (1) |
| 106 | 4.0 by 0.082 | 1/4 countersunk | Butt | 24.70 | 40,700 | 54,000 | 57.5 | 76.3 |
| 107 | 4.0 by 0.081 | 1/4 R.H. | Lap | 12.96 | 56,500 | 64,900 | 79.8 | 91.7 |
| 107 | 4.0 by 0.081 | 1/4 R.H. | Lap | 12.96 | 56,600 | 65,100 | 80.0 | 92.0 |
| 108 | 4.0 by 0.081 | R.H. | Lap | 15.43 | 57,100 | 67,500 | 80.7 | 95.4 |
| 108 | 4.0 by 0.081 | R.H. | Lap | 15.43 | 58,000 | 68,600 | 82.0 | 97.0 |
| 111 | 3.98 by 0.082 | 3/16 R.H. | Butt | 9.20 | 56,600 | 62,300 | 80.0 | 88.0 |
| 111 | 3.98 by 0.082 | 3/16 R.H. | Butt | 9.20 | 56,700 | 62,500 | 80.2 | 88.4 |
| 112 | 4.0 by 0.081 | 1/4 R.H. | Butt | 6.48 | 54,000 | 57,800 | 76.4 | 81.6 |
| 116 | 5.0 by 0.081 | 1/4 R.H. | Butt | 20.00 | 45,900 | (2) | 65.2 | ... |
| 117 | 5.0 by 0.081 | 1/4 R.H. | Butt | 20.0 | 47,700 | (2) | 67.8 | ... |
| 118 | 5.0 by 0.081 | 1/4 R.H. | Butt | 20.0 | 53,100 | (2) | 75.5 | ... |
| 119 | 5.0 by 0.081 | 1/4 R.H. | Butt | 20.0 | 55,200 | 69,000 | 78.4 | 98.0 |
| 120 | 5.0 by 0.081 | 1/4 R.H. | Butt | 20.0 | 52,700 | 65,900 | 75.0 | 93.6 |
| 126 | 5.0 by 0.081 | 1/4 R.H. | Butt | 20.0 | 57,400 | 71,800 | 81.5 | 102.0 |
| 124 (3) | 7.0 by 0.104 | R.H. | Butt | 18.75 | 63,000 | 77,600 | 78.7 | 97.0 |
| 125 | 0.025 | Spot-welded joint | | ... | 59,650 | ... | 89.5 | ... |

(1) Failed in two rows.

(2) Failed in shear.

(3) 24SRT Sheet (Ultimate strength = 80,000 lbs per sq.in. by test).

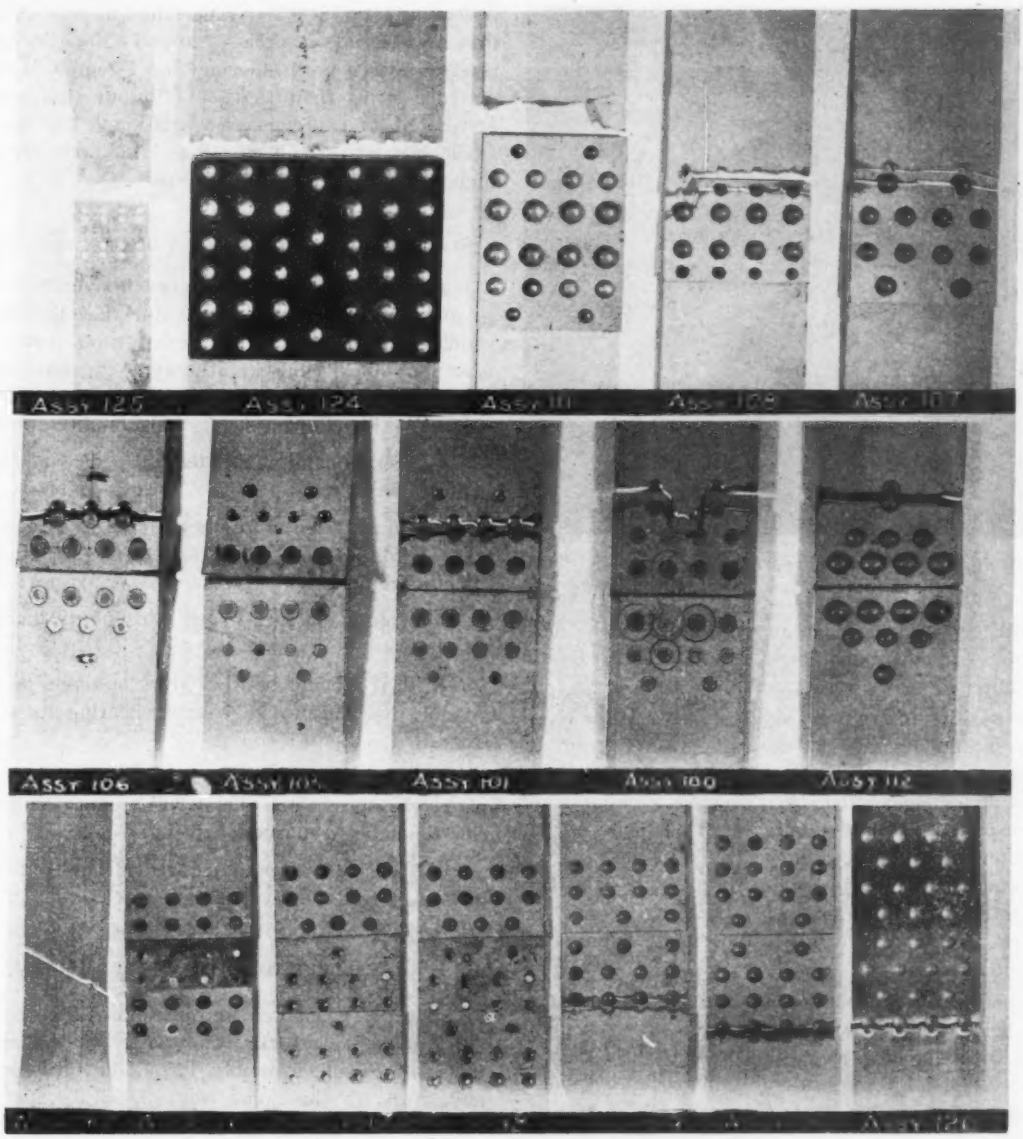


FIG. 9 (*top*). High efficiency joints.
FIG. 10 (*center*). Example of improperly designed joints.
FIG. 11 (*bottom*). Joints showing the effect of the number of rivets.

in shear. Since the total deformation possible in a small rivet is extremely low, it fails by shearing even though there may be no attendant failure at the second row of rivets. The second row, which generally has a greater reduction of area, must then carry the entire load on the joint and fails at a relatively low load. It should also be noted that the spacing between consecutive rows of rivets should be kept small, since large spacing results in greater differential elongation in the main and butt plates between the rows.

A typical example of the effect of extended spacing between rivets in the direction of the load is afforded by Fig. 12, showing typical tension failures in gussets. The outer rivet on assembly 6-4067-5 failed in shear at a load considerably below the ultimate load on the joint. This rivet was placed considerably farther from the remaining rivets than were the corresponding rivets in the other joints shown which failed in tension at the first rivet.

The second method for increasing net area at the outer row—i.e., by increasing the pitch of the outer rivets—is theoretically sound, but rivet pitch is often determined by adjoining structure such as wing surface stiffeners, so that only limited flexibility is afforded. The final selection of rivet diameter and pitch in the outer row will therefore be accomplished by method (3)

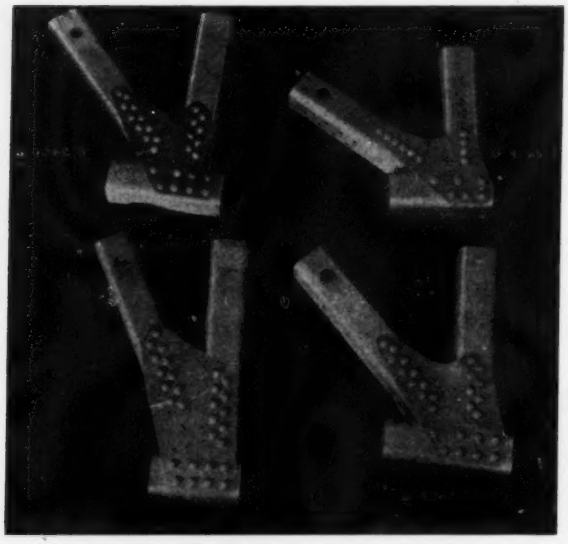

FIG. 12. Typical tension failures in gussets.

and will generally be a compromise between the most desirable size and spacing and the dimensional limitations imposed by the structure.

The position of the outer rivets relative to the rivets in the second row may have an important bearing on the net area efficiency. The effect of staggered holes on net area efficiency has been previously noted in the case of perforated tension specimens. When a rivet in the outer row subtends a large portion of the space between adjacent rivets in the second row, the stress flow across the joint must obviously be along severely restricted paths, thus causing abnormally high stress concentrations.

Assemblies 100 and 106 both show low net area efficiencies as the result of rivet stagger. In continuous joints with the same rivet size and pitch, these joints would very likely be considerably improved by placing the outer rivets on the same longitudinal line with the rivets in the inner rows. Both assemblies may be criticized for having too much material removed in the outer row to permit really high efficiency in any case.

The decreased efficiency resulting from too little material being removed at the outer row is exemplified by assembly 112. This joint has a fair overall efficiency (75.4 per cent), but the net area efficiency is lower than it should be. A smaller but more efficient net area might actually raise the overall efficiency.

The series of joints shown in Fig. 11 were designed to show that no increase in overall efficiency can be obtained by adding rivets after the minimum number necessary to provide against shear or bearing failure has been used. Rivet patterns in the first two rows were identical for all joints. Assemblies with 8, 9, and 10 rivets failed by shearing all rivets, as anticipated. Assembly 119, with 11 rivets, failed in tension at the first row, as did assemblies 120 and 126 with fourteen rivets. The overall efficiency of assembly 120 was actually lower than that of 119, but this must be attributed to experimental variation. The net area efficiencies for assemblies 119 and 126 were obviously higher than could normally be expected.

### Suggestions for the Design of Riveted Joints

It may be concluded that 80 per cent overall efficiency is approximately the highest value that the designer should expect to attain in the design of riveted 24ST aluminum-alloy joints (of the type encountered in a typical aircraft monocoque structure). To attain such efficiency, the following suggestions should be observed:

(1) Design for approximately 10 per cent holes out in the outer row.

(2) Make the outer rivets as large as is consistent with the dimensional limitations of the structure, i.e., avoid extremely small rivets.

(3) Avoid staggering rivets, particularly in the two outer rows.

(4) Keep spacing between rows of rivets as low as possible and still provide against shearing out between rows.

(5) Make gauge of butt plates as near to that of main plates as possible. (This will reduce differential elongation between rows of rivets.)

(6) Assume 90 per cent net area efficiency at all rivet rows when selecting rivet size and pitch.

### Efficiency of Spot-Welded Joints

One typical spot-welded joint joining 0.025 gauge to 0.032 gauge Alclad 24ST alloy is shown in the photograph of Fig. 9, assembly 125. The ultimate stress developed by this joint was 59,650 lbs. per sq.in., representing an efficiency of 89.5 per cent of the base metal ultimate strength of 66,675 lbs. per sq.in. It has been found possible to consistently maintain 80 per cent efficiency with this type of joint.

This joint is included because it illustrates several of the principles emphasized in the foregoing discussion of riveted joints. Since the welded spots are capable of little yielding, it is essential that differential elongation of the two sheets be avoided. With equal gauge sheets this can be done if only two rows of spots are used. However, insufficient shear strength is developed by two single rows of spots, so two double rows are used. By keeping the first and second rows of spots close to each other, the differential elongation of the two plates is kept sufficiently small to avoid shear failure of the spots in the first row.

*(Continued on page 310)*

# On the Torsional Damping Capacity of Solid Magnesium-Alloy Rods as Affected by Cold-Working

A. Ü. KUTSAY* AND A. J. YORGIADIS†

*Curtiss-Wright Corporation and Sonntag Scientific Equipment Corporation*

SUMMARY

The necessity of associating the damping capacity of magnesium in torsion, with both the shearing stress amplitude and the cold-work history of the material, is discussed.

Consideration is given to the relative merits of the "freely decaying vibrations" method, and the "sustained resonant vibrations" method for the dynamic testing of magnesium.

Test results on the torsional damping capacities and dynamic moduli of rigidity are given for two extruded magnesium alloys, O and J, tested under sustained resonant vibrations. The vibrations were induced to solid cylindric magnesium specimens by a mechanical oscillator driven by a synchronous motor.

The effect of various degrees of cold-work on the dynamic properties was investigated and found to be of utmost significance in that cold-working decreased the damping capacity considerably, thus showing the danger in neglecting the effect of cold-work on the induced stress in a member vibrating at resonance.

SYMBOLS USED

| | | |
|---|---|---|
| $b$ | = | in. (see Fig. 2) |
| $D$ | = | diameter of specimen, in. |
| $G$ | = | dynamic modulus of rigidity, lbs.in.$^{-2}$ |
| $I$ | = | moment of inertia of oscillator assembly, lb.in.sec.$^2$ |
| $J$ | = | polar moment of inertia of specimen cross section, in.$^4$ |
| $K$ | = | torsional spring constant, in.lbs.rad.$^{-1}$ |
| $L$ | = | free length of specimen, in. |
| $m$ | = | mass of one eccentric (see Fig. 2), lb.in.$^{-1}$sec.$^2$ |
| $r$ | = | eccentricity of $m$, in. (see Fig. 2) |
| $t$ | = | time, sec. |
| $T$ | = | maximum value of alternating oscillator torque, in.lbs. |
| $T_s$ | = | internal torque in test specimen, in.lbs. |
| $\Delta W$ | = | damping capacity, lb.in. per in.$^3$ (see Eq. (3)) |
| $\delta$ | = | logarithmic decrement, $= 0.5\,\psi$ approximately |
| $\theta$ | = | amplitude of torsional vibration, rad. |
| $\psi$ | = | specific damping capacity (see Eq. (4)) |
| $\tau_{max}$ | = | maximum shearing stress in specimen, lbs.in.$^{-2}$ |
| $\tau_s$ | = | static shearing stress corresponding to $T$ (see Eq. (6)) |
| $\omega$ | = | circular frequency, rad. per sec. |

## INTRODUCTION

THE KNOWLEDGE of the properties of materials under vibratory stresses is one of paramount importance to the designer of structures or machines that are subjected to dynamic stresses. One material may be more suitable than another for a certain purpose, but, if its properties under the working conditions are not fully known, then, from the point of view of the designer, it is either rejected or, if considered, full advantage of the material is not taken. In designing members subjected to vibratory loads of known amplitudes and fixed frequencies, it is possible to design a member of such rigidity that its natural frequencies do not correspond with the operating frequencies. In such a case the fatigue strength or fatigue limit of the material is the governing factor in the design. Nevertheless, in most actual cases, and particularly in airplane structures, the vibratory loads cannot be completely known in advance, with regard to either amplitude or frequency. In fact, the frequency of such loads may vary under wide ranges depending upon the operating conditions. The occurrence of resonance vibrations can hardly be entirely prevented. (See "Spectrum of Vibration Frequencies."[14])

### *Induced Load*

A point often missed is that at or near resonance the induced load in a member is the product of the applied load and the resonance amplification factor. The resonance amplification factor is a property of the material itself. Hence, the induced stress in the material is not a function of the applied vibratory load alone but a function of both the applied vibratory load and the dynamic properties of the material. The resonance amplification factor is proportional to the reciprocal of the damping capacity of the material, which in turn is a measure of the energy absorbed by internal friction during one stress cycle. Other factors remaining the same, a material of higher damping capacity is generally superior to one of lower damping capacity for use in a member subjected to vibratory stresses.[17] Often, if resonant vibrations are to be encountered, it may be advisable to use a material of lower fatigue strength but higher damping capacity than another. As Föppl[10] puts it, ". . . damping is, so to speak, a guarantee against the occurrence of unusually high stresses due to vibration."

### *Measuring Damping Capacity*

A number of methods have been devised to measure damping capacity, and these methods can be classified in different groups. It is beyond the scope of this

Presented at the Materials Session, Eleventh Annual Meeting, I.A.S., New York, January 25–29, 1943.

* Stress Analyst. Formerly Research Assistant, Engineering Experiment Station, The Pennsylvania State College.

† Research Engineer. Formerly Research Assistant, Engineering Experiment Station, The Pennsylvania State College.

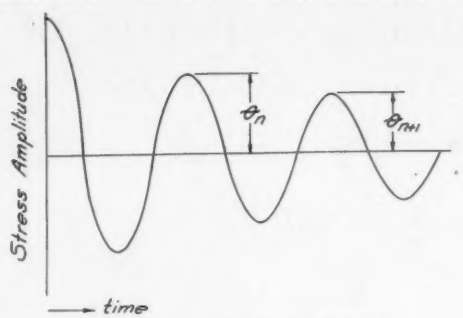


FIG. 1. Freely decaying vibrations.

paper to give a detailed account of all these methods.[3, 4, 5, 8, 10, 13, 20] Nevertheless, it is considered that a brief comparison of two of the most important methods for measuring damping is appropriate. One method uses the principle of freely decaying vibrations; the other uses that of forced or sustained near-resonant vibrations. The former is an old technique[1, 2] but still popular.[6, 7, 10] It consists of allowing the material to vibrate freely under specified conditions and measuring amplitudes of two successive vibrations. Since damping is present, the second amplitude $\theta_{n+1}$ is smaller than the first $\theta_n$ (see Fig. 1), and the logarithmic decrement $\delta$, a measure of the damping capacity, is $\delta = \log_e (\theta_n/\theta_{n+1})$.

The damping capacity is a function of the stress amplitude in that it increases as stress increases. Thus, for any given material a particular value of damping capacity should be associated with a definite value of stress. The value of $\delta$, obtained by the freely decaying vibrations method, is not associated with either of the stresses that correspond to the two amplitudes. Hence, this value of $\delta$ is not associated with its true value of stress. All that can be said about this stress is that it lies somewhere between the two observed stresses corresponding to the amplitudes $\theta_n$ and $\theta_{n+1}$. The discrepancy thus introduced is small for materials, and ranges of stress, of low damping capacity. Nevertheless, this discrepancy increases rapidly with increasing damping capacity. For example, in the case of the magnesium alloy O, vibrating torsionally (see Fig. 6), an approximate estimate indicates that in the vicinity of 5,000 lbs. per sq.in., two successive stress amplitudes differ by about 1,000 lbs. per sq.in., during which interval $\delta$ changes by 100 per cent.

The method of measuring damping by forced or sustained resonant vibrations dispenses with these difficulties. It consists of subjecting the material to forced resonant oscillations by using it as the spring or elastic member with a single degree of freedom. The oscillations are thus maintained at a constant amplitude by an oscillator. Hence, values of damping capacity obtained are associated with one particular value of stress amplitude. Furthermore, the measuring of damping by sustained vibrations is a more direct method than the rate of vibration decay method, since in practice it is the properties of materials under sustained vibrations that are of greater importance.[26]

The method of measuring damping by means of a mechanical oscillator, developed by B. J. Lazan[23,24,25] offers additional advantages when it comes to measuring the effect of the number of repeated stress cycles on the damping capacity. Normally, two machines have to be used for tests of this nature, as was done by Föppl in experiments on steel.[10] The specimen was subjected to repeated loads on a fatigue machine and was removed periodically to have its damping capacity measured on a decaying vibrations damping machine. The handling of the specimen back and forth from one machine to the other for every reading and the resulting difference in gripping were possible causes of error not present in Lazan's machine, which functions both as a fatigue and a damping machine at the same time. Hence, the method of forced or sustained vibrations in general and the mechanical oscillator of Lazan in particular were adopted for these tests.

## Statement of the Problem

The damping capacity of metals is a complex and sensitive physical property. There are a multitude of variables that might conceivably influence the damping capacity without a corresponding effect on other physical properties.[9] In view of the above, results on damping capacity are not expected to be so accurate and so consistent as the tensile strength. Previous work by the authors on the dynamic testing of magnesium revealed that cold-working had a great influence on the damping capacity of this material.[23,26]

On his dynamic tests with Elektron AZM and A9b specimens, W. Buchmann first observed a sudden temperature rise in his specimens, which stopped in 2 min. A gradual decrease in specimen temperature followed, with an advancing number of constant amplitude stress cycles. This phenomenon he reported as an index to a decrease in the damping capacity of this material due to cold-work.[16]

Consequently, to define the damping capacity of a magnesium alloy, it is necessary but not sufficient to specify the stress amplitude at which the measurement is taken; the past cold-working history of the specimen must also be stated.

In the tests reported in this paper, cold-working was accomplished by repeated stress cycles and was expressed in terms of stress amplitude and number of repetitions.

Preliminary tests had further shown that at any cold-working stress an equilibrium in damping was reached after certain number of cycles, beyond which further cyclic stress produced no significant change in damping. These tests are in agreement with theo-

retic attempts made to explain this peculiar behavior of materials.[15,21]

These tests were undertaken to determine completely the torsional damping capacity of magnesium alloys with reference to a particular stress and a particular stage of cold-working. The amount of cold-work required, at a given cold-working stress, to reach a stage of equilibrium with reference to damping was also studied.

The specimens used were of two magnesium alloys, alloy O and alloy J,[11] and were used in as-received condition without machining. All specimens were solid cylindric extruded rods, $^3/_4$ in. in diameter. A frequency of 18.75 cycles per sec. was adhered to throughout to avoid introduction of another variable.

## Apparatus and Test Procedure

The basic experimental setup was a single-degree-of-freedom system under forced torsional resonant oscillations.[18] The components of such a system are (see Figs. 2 and 3):

(1) *A torsional spring*, the angular deflection of which is a function of the applied torque. In these tests the magnesium specimens acted as the torsional spring whose characteristics depended upon the dimensions and properties of the magnesium rods, the relation between the applied torque and angular deflection being $T_s = JG\theta/L$.

(2) *A flywheel*, attached to the torsional spring, with moment of inertia $I$ about the axis of torsional oscillations. The motor-oscillator assembly provided the flywheel effect. Its moment of inertia was made adjustable by changing the positions of poises of mass $P$ (see Fig. 3) held to the oscillator body by threaded rods. The poises could be placed at any desired distance from the axis, making it possible to obtain any desired value of $I$ over a certain range. The moment of inertia of the oscillator assembly was determined accurately by the bifilar pendulum method.

(3) *The applied torque*, characterized by its amplitude $T$ and its frequency $\omega$. This torque was applied to the system by means of the mechanical oscillator driven by a synchronous motor, with its eccentrics $m$ arranged so as to produce a harmonic torque (see Fig. 2). An eccentric was placed at each of the two extremities of two parallel shafts rotating in opposite directions. The equal eccentric masses $m$ were attached 180° apart on each shaft, so that at any instant in the cycle the resultant force due to these masses was zero. The resultant torque $T$, however, about an axis perpendicular to the plane of the two shafts was sinusoidal, with a peak value of $T = 2mr\omega^2 b$, when the masses were in the plane of the two shafts (see Fig. 2).

The oscillator was driven by an 1,800-r.p.m. synchronous motor built integral with the oscillator. The speed ratio of the motor shaft to oscillator shafts could be altered by changing the gears connecting these shafts. A speed of 18.75 cycles per sec. was used throughout these tests.

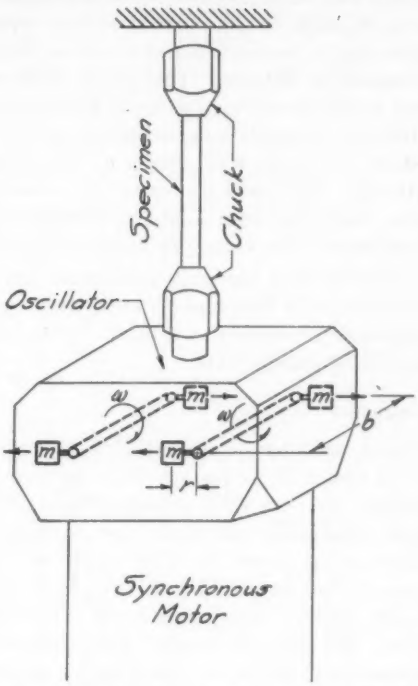


Fig. 2. Arrangement of rotating eccentrics $m$ to produce sinusoidal torque $T = 2mrb\omega^2$.

All the readings were taken when the system was at resonance, this being the setting at which the periodic torsional oscillations had a phase lag of 90° relative to the applied harmonic torque. This phase lag was determined by flashing the stroboscope at nearly the double frequency of vibrations. Two images of a mark on the oscillator were visible, moving in opposite phase. When these two images coincided, the dis-

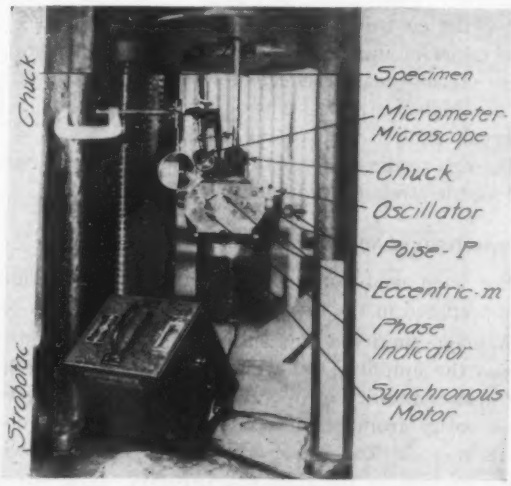


Fig. 3. Test setup.

placement was zero, and the angular position of the eccentrics $m$, read on the phase indicator, represented the phase lag between the forced harmonic torque and the torsional oscillations. This phase difference was adjusted to 90° by moving the poises $P$ toward or away from the axis of oscillations, depending upon whether the phase difference was greater or less than 90°, respectively. This was an extremely sensitive adjustment, far better than would be possible by means of a fixed inertia and a variable speed drive.

The amplitude of torsional oscillations $\theta$ in radians was measured with a micrometer microscope by reading the amplitude of motion of a mark on the oscillator, illuminated by oblique light.

### *Test Procedure*

The test procedure consisted of applying different values of torque $T$ to the specimen by changing the eccentricity $mr$. At each setting of eccentricity the position of the poises was adjusted to produce resonant vibrations as indicated by a 90° angle on the phase indicator. The amplitude of vibration was then measured under these conditions. The damping capacities and dynamic moduli were calculated from these observed values of eccentricity, amplitude of vibration, and position of poises in accordance with Eqs. (1) to (6).

The above procedure was first applied to a virgin specimen. Ideally, one specimen should have been used for every reading, since the stress cycles through which the specimen had gone during preceding readings had cold-worked the material to a certain extent. Nevertheless, one specimen was used for four or five readings, and this effect was kept to a minimum by taking the readings as fast as possible (one reading took about 30 sec. corresponding from 500 to 600 stress cycles). It was observed that at stresses lower than the cold-working stress the changes in dynamic properties were more pronounced than at stresses above the cold-working stress. Readings were therefore taken in increasing order of stress. In spite of these precautions the effect of cold-work was so rapid at the higher stresses that it was noticeable in the interval required to take one reading.

Enough readings were taken in this manner to cover the usable stress range of the material.

### *Preparations of Specimens*

For each cold-working stress a different specimen was prepared in the following manner:

A magnesium rod was subjected to repeated stress cycles the amplitude of which was closely controlled. To insure stability of operation this cold-working was done away from resonance. The progress of cold-work was checked at certain interyals by observing the variation in the damping capacity. The stresses at which these intermediate damping capacity readings were taken were kept below the cold-working stress, for, otherwise, the cold-work during the reading would contaminate the constant-stress cold-working. Cold-working was stopped when no further change in damping could be observed. The specimen thus prepared was subjected to the same procedure described for the virgin specimen. For each of the two alloys, three cold-working stresses were considered. A lower cold-working stress of approximately 2,000 lbs. per sq.in. was tried, but no measurable changes in the properties was noticed and these data were not reported.

## Available Data and Assumptions

The following test data were available:

Dimensions of the specimen: length $L$, in.; diameter $D$, in., kept at 0.75 in. throughout these tests; polar moment of inertia, $J$, in.$^4$

Moment of inertia of oscillator assembly: $I$, lb.-in.sec.$^2$, adjusted so as to keep the system at resonance.

Applied sinusoidal torque, $T$, in.lbs., of frequency 18.75 cycles per sec.

Amplitude of torsional oscillations, $\theta$, rad.

The following assumptions were made:

(1) That the elastic spring has linear characteristics—i.e., $T_s = K\theta$, where $K$, the torsional spring characteristic, is a constant over all ranges of $\theta$. In the actual system $K = JG/L$ and $G$ decreases as the stress increases, so that the actual system is one in which the spring constant decreases as the deflection increases.

(2) That the formulas for the resonant frequency of the undamped system hold for the system with damping—i.e.,

$$\omega^2 = GJ/IL \tag{1}$$

(3) That the vibration is a simple harmonic motion, so that the amplitudes of motion, velocity, and acceleration are $\theta$, $\theta\omega$, $\theta\omega^2$, respectively.

(4) That the distribution of the shearing stress in the solid cylindric specimen is linear.

## Formulas

Eq. (1) solved for the dynamic modulus of rigidity results in

$$G = L\omega^2 I/J \text{ lbs. per sq.in.} \tag{1a}$$

The maximum shearing stress from the fundamental stress-strain relation is

$$\tau_{max.} = DG\theta/2L \text{ lbs. per sq.in.} \tag{2}$$

The work done by the applied torque $T$ on the angular displacement $\theta$ is equal to the energy dissipated in the specimen due to damping. On the basis of the third assumption, this work is equal to $\pi T\theta$ for the resonant vibrations. The energy dissipated during

one complete cycle per cubic inch of material is, therefore,

$$\Delta W = 4T\theta/D^2L \text{ in.lb. per in.}^3 \quad (3)$$

The ratio between the energy dissipated due to damping and the elastic energy stored in the extreme position of the cycle is the relative damping

$$\psi = \pi DT/(J\tau)_{max.} \quad (4)$$

The logarithmic decrement $\delta$, which is another expression for damping, can be obtained from the approximate relation

$$\delta = 0.5\,\psi \quad (5)$$

A torque of magnitude $T$, applied statically, would cause a stress in the specimen,

$$\tau_s = DT/2J \text{ lbs. per sq.in.} \quad (6)$$

Eqs. (1a) to (6), inclusive, were used to calculate the quantities $G$, $\tau_{max.}$, $\Delta W$, $\psi$, $\delta$, and $\tau_s$, from the experimental data.

## Discussion of Results

The results of the tests are shown in Figs. 4 to 12, inclusive. Figs. 4 and 5 represent the damping capacity $\Delta W$ of alloys O and J, respectively, as a function of the maximum shear stress $\tau_{max.}$. Attention is called to the fact that since solid cylindric specimens were used, the exterior fibers were the only ones subjected to $\tau_{max.}$, the stress falling off to zero at the neutral axis. The damping capacity measured was therefore an integration of the damping capacities at the range of stress zero to $\tau_{max.}$. The upper curves, marked "No Cycles," are the curves representing the damping of the unworked specimens. These follow very nearly straight lines on the semilog coordinates. In Fig. 4, the next curve, marked "450,000 cycles," is broken at the range of stress 4,000 to 4,500 lbs. per sq.in. This is to indicate that before this damping curve was obtained, the specimen had been subjected to 450,000 cycles of cold-work at a $\tau_{max.}$ of 4,000 to 4,500 lbs. per sq.in. Similarly, the other curves of Figs. 4 and 5 represent the damping capacities of alloys O and J, respectively, cold-worked at stresses indicated by the broken portion of the curves.

The number of stress cycles was repeated until a state of equilibrium was attained, beyond which point further stress cycles had no effect on damping. In both alloys the higher the cold-working stress, the fewer number of cycles were required to reach this equilibrium. Each curve in these figures, therefore, represents very nearly the lowest value of damping capacity obtainable due to cold-work at the specified cold-working stress.

These curves reveal quantitatively the importance of cold-work in connection with the damping capacity of this material. For example, at the stress of 5,000

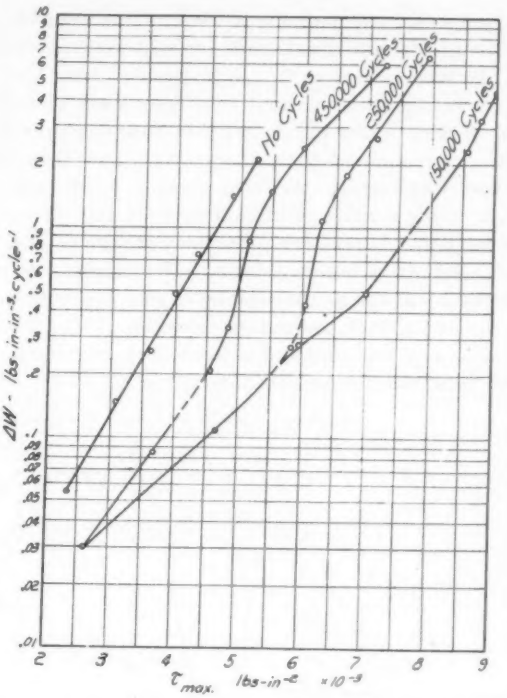


Fig. 4. The effect of cold-work on the torsional damping capacity $\Delta W$ of magnesium alloy O. (The dotted portion of the curve indicates the cold-working stress range.)

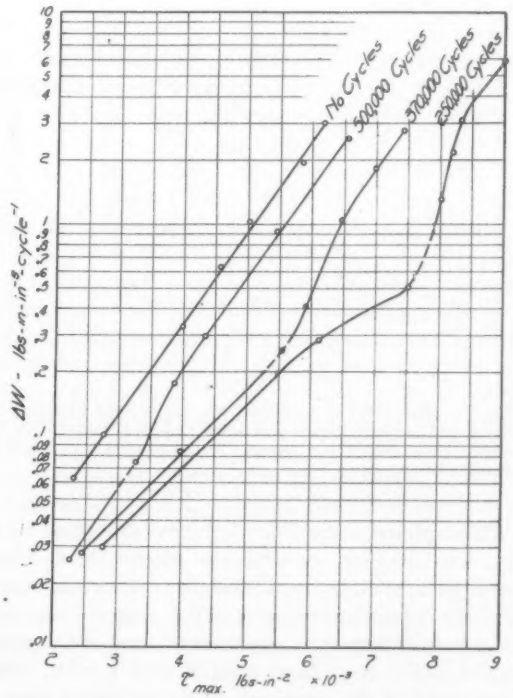


Fig. 5. The effect of cold-work on the torsional damping capacity $\Delta W$ of magnesium alloy J. (The dotted portion of the curve indicates the cold-working stress range.)

lbs. per sq.in., the damping of alloy O was reduced to one-tenth of its original value by cold-work at 6,000 lbs. per sq.in.

It is further observed that at stresses lower than the cold-working stress the decrease in damping capacity is more pronounced than at stresses higher than the cold-working stress, the cold-working stress, so to speak, being a range of discontinuity in the curves.

Figs. 6 and 7 represent the same test data as Figs. 4 and 5 but in a different form. The damping is expressed as $\psi$, the relative damping (see Eq. (4)), and $\delta$, the logarithmic decrement (see Eq. (5)). These curves are offered for the benefit of those more familiar with these two definitions of damping.

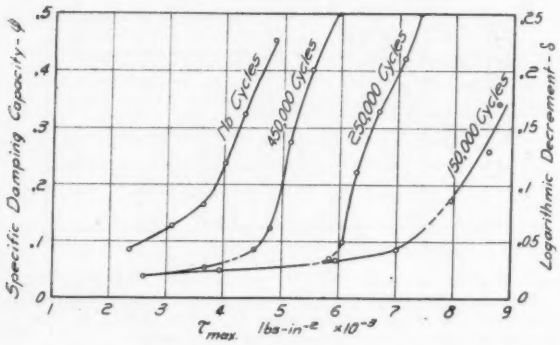


FIG. 6. The effect of cold-work on the specific damping capacity $\psi$ and the logarithmic decrement $\delta$ of magnesium alloy O in torsion. (The dotted portion of the curve indicates the cold-working stress range.)

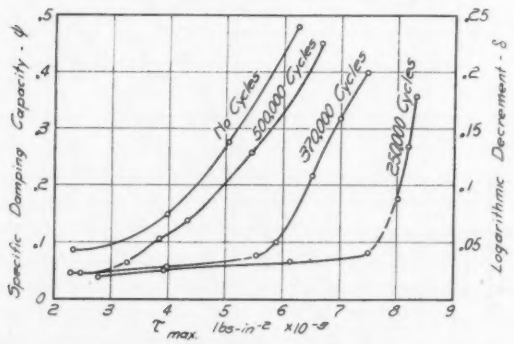


FIG. 7. The effect of cold-work on the specific damping capacity $\psi$ and the logarithmic decrement $\delta$ of magnesium alloy J in torsion. (The dotted portion of the curve indicates the cold-working stress range.)

While giving complete data on damping itself, Figs. 4 to 7 are not convenient to use for the designer. Given an applied dynamic torque of a certain amplitude, the immediate interest of the designer is to find the corresponding resonance stress induced in a member. Figs. 8 and 9 have been plotted with that in mind. $\tau_s$, an index of the amplitude of the applied torque, is the maximum stress that would exist in a cylindric specimen if the torque $T$ were applied statically. If

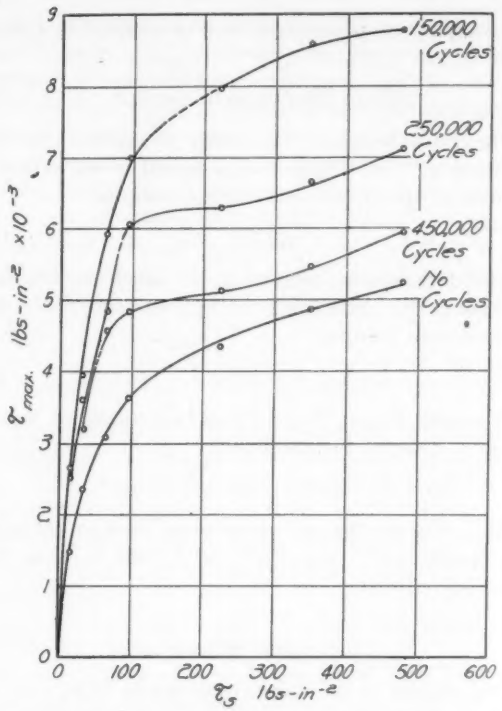


FIG. 8. The effect of cold-work on the variation of resonance stress $\tau_{max.}$ with the applied torque index $\tau_s = (D/2J)T$ for magnesium alloy O. (The dotted portion of the curve indicates the cold-working stress range.)

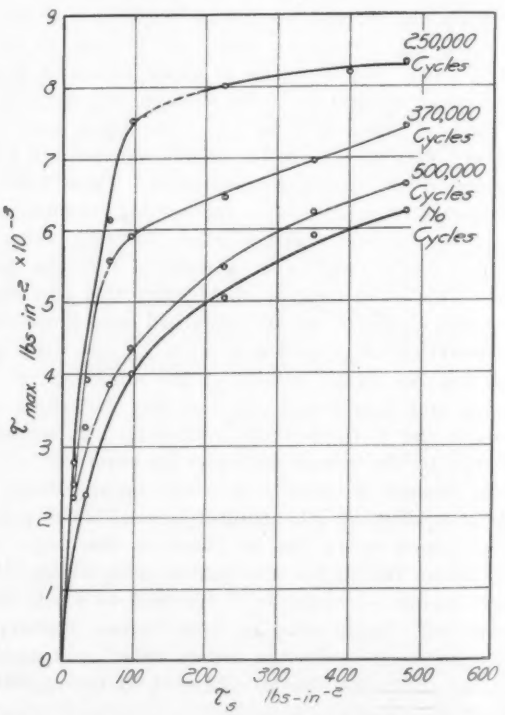


FIG. 9. The effect of cold-work on the variation of resonance stress $\tau_{max.}$ with the applied torque index $\tau_s = DT/2J$ for magnesium alloy J. (The dotted portion of the curve indicates the cold-working stress range.)

the values of $T$ of these tests were used directly, then these curves would only apply to solid rods $^3/_4$ in. in diameter. But through the relation of Eq. 6, induced resonance stresses in members of other size may be readily determined. These curves further show the danger in not taking into account the effect of cold-work history on the damping capacity. For example, if the effect of cold-work were ignored for alloy O, a member subjected to an applied torque corresponding to a $\tau_s$ of 100 lbs. per sq.in. would only have to withstand a $\tau_{max.}$ of 3,700 lbs. per sq.in. (see Fig. 8). In an extreme case of cold-working, however, this value of $\tau_{max.}$ may actually increase up to and beyond 7,000 lbs. per sq. in. because of the decrease in damping.

Fig. 10 shows the change in damping of alloys O and J, at a $\tau_{max.}$ of 6,000 lbs. per sq.in., due to cold-working at 7,500 to 8,000 lbs. per sq.in. The rate of change of the properties of the material due to cold-work is rapid at the earlier number of cycles; it decreases as the number of cycles increases until an equilibrium is reached. Further, alloy O is affected more rapidly than alloy J, and alloy O requires fewer cycles of cold-work to reach equilibrium, other factors remaining same.

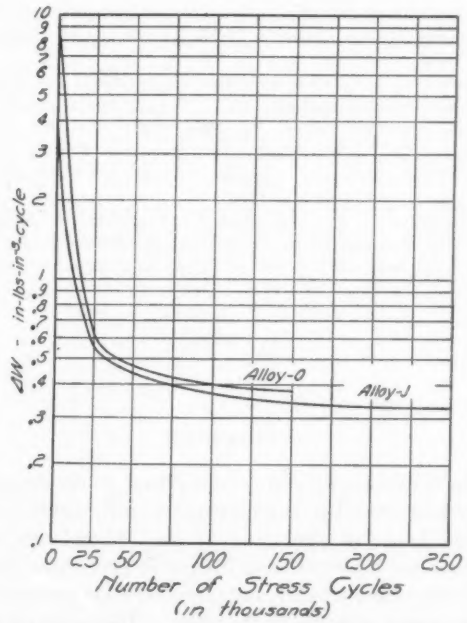


FIG. 10. Effect of repeated torsional stress cycles on the damping capacity $\Delta W$ of magnesium alloys. $\Delta W$ measured at $\tau_{max.}$ = 6,500 lbs. per sq.in. Cold-working stress = 7,500 to 8,000 lbs. per sq.in. (interpolated).

The variation of the dynamic modulus of rigidity for alloys O and J, with cold-work, is shown in Figs. 11 and 12. The effect of cold-work in this case is to increase the modulus, this increase being greatest for the specimen cold-worked at the highest stress. This phenomenon could be taken advantage of in case of a design of a superior rigidity. The material could

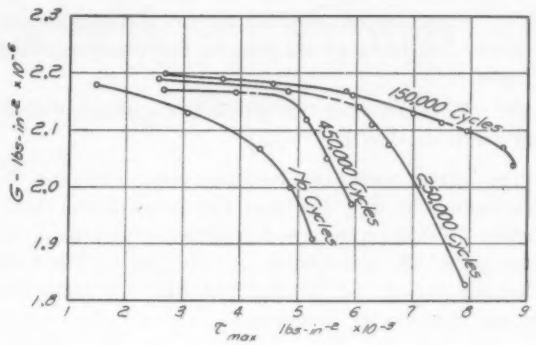


FIG. 11. Effect of cold-work on the dynamic modulus of rigidity $G$ of magnesium alloy O. (The dotted portion of the curve indicates the cold-working stress range.)

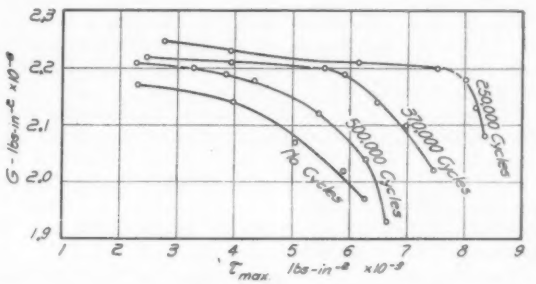


FIG. 12. The effect of cold-work on the dynamic modulus of rigidity $G$, of magnesium alloy J. (The dotted portion of the curve indicates the cold-working stress range.)

be made more rigid by cold-work before being put to use. Mechanical cold-work has been used in a different manner to strengthen magnesium propellers by Sachs.[18]

## CONCLUSIONS

The following conclusions were reached for the dynamic properties of magnesium alloys O and J in torsion:

(1) Damping capacity increases and dynamic modulus of rigidity decreases with increasing stress.

(2) Damping capacity decreases and dynamic modulus of rigidity increases with cold-working.

(3) The higher the cold-working stress, the lower is the damping capacity and the higher is the modulus of rigidity for any given stress.

(4) At stresses lower than the cold-working stress, the decrease in the damping capacity and the increase in the modulus of rigidity are more pronounced than at stresses higher than the cold-working stress.

(5) At any given cold-working stress, a certain number of stress cycles are required to attain a stage where additional stress cycles are ineffective.

(6) The rate of change of the properties of the material due to cold-work is rapid at the earlier number of cycles; it decreases as the number of cycles increases until an equilibrium is reached.

(7) At higher cold-working stresses this equilibrium is reached in fewer cycles than at lower cold-working stresses.

(8) Alloy O is more susceptible to the effects of cold-working than alloy J.

The authors wish to express their acknowledgment of indebtedness to B. J. Lazan of The Pennsylvania State College for making his research equipment available for these tests. Further thanks are also due to The Dow Chemical Company, Midland, Mich., for supplying the material for the specimens.

## References

[1] Voigt, K., *Über innere Reibung fester Körper, insbesondere der Metalle*, Annalen der Physik, Vol. 47, p. 671, 1892.

[2] Guye, M. Ch. E., *Le frottement interieur des Solides, ses Variations avec la Temperature*, Journal de Physique, p. 620, 1912.

[3] Honda, K., and Konno, S., *On the Determination of the Coefficient of Normal Viscosity of Metals*, Philosophical Magazine, Vol. 42, pp. 115–123, 1921.

[4] Quimby, S. C., *On the Experimental Determination of the Viscosity of Vibrating Solids*, Physical Review, Vol. 25, pp. 558–573, 1925.

[5] Canfield, R. H., *Internal Friction in Metals*, Physical Review, Vol. 32, pp. 520–530, 1928.

[6] Föppl, Ö., *Die Dampfung der Werkstoffe*, V.D.I., Vol. 74, No. 40, pp. 1391–1394, 1930.

[7] von Heydekampf, G., *Damping Capacity of Materials*, Proc. A.S.T.M., Vol. 31, Part 2, pp. 157–175, 1931.

[8] Wegel, R. L., and Walther, H., *Internal Dissipation in Solids for Small Cyclic Strains*, Journal of Applied Physics, Vol. 6, pp. 141–157, 1935.

[9] Brophy, G. R., *Damping Capacity, a Factor in Fatigue*, Trans. A S.M., Vol. 24, pp. 154–185, 1936.

[10] Föppl, Ö., *The Practical Importance of the Damping Capacity of Metals, Especially Steel*, Journal of the Iron and Steel Institute, Vol. 134, pp. 393–455, 1936.

[11] *Dowmetal Magnesium Alloys Handbook;* The Dow Chemical Company, Midland, Mich., October, 1937.

[12] Zener, C., *Internal Friction in Solids—IV, Relation Between Cold Work and Internal Friction*, Physical Review, Vol. 53, pp. 582–586, 1938.

[13] Sachs, G., *Improving Aircraft Propellers by Surface Rolling*, Metals and Alloys, Vol. 10, pp. 19–23, 1939.

[14] Arnstein, K., and Shaw, E. L., *Fatigue Problems in Aircraft Industry*, Metals and Alloys, Vol. 10, pp. 204–209, 1939.

[15] Read, Thomas A., *Internal Friction of Single Metal Crystals*, Physical Review, Vol. 58, pp. 371–380, 1940.

[16] Beck, A., *The Technology of Magnesium and Its Alloys;* translated from German, F. A. Hughes and Company, London, p. 205, Figs. 244 and 245, 1940.

[17] Fox, F. A., *Magnesium and Its Alloys*, Metal Industry (London), Vol. 57, pp. 7–11, 1940.

[18] den Hartog, J. P., *Mechanical Vibrations*, 2nd Edition, Chap. II; McGraw-Hill Book Company, New York, 1940.

[19] Kimball, A. L., *Vibration Problems, Part IV, Friction and Damping in Vibrations*, Trans. A.S.M.E., Journal of Applied Mechanics, Vol. 8, No. 1, March, 1941.

[20] Kimball, A. L., *Vibration Problems, Part V, Friction and Damping in Vibrations*, Trans. A.S.M.E., Journal of Applied Mechanics, Vol. 8, No. 3, September, 1941.

[21] Brick, R. M., and Philips, A , *Non-Ferrous Physical Metallurgy*, Mining and Metallurgy, Vol. 22, pp. 87–92, 1941.

[22] *Prevention of the Failure of Metals Under Repeated Stress;* by the Batelle Memorial Institute, John Wiley & Sons Inc., New York, 1941.

[23] Kutsay, A. Ü., *On the Torsional Damping Capacity of Three Magnesium Alloys;* Master's Thesis, University of Michigan, April, 1942.

[24] Lazan, B. J., *Mechanical Properties of Metals and Plastics Under Sustained Vibrations;* Ph.D. Thesis, The Pennsylvania State College, State College, Pa., May, 1942.

[25] Lazan, B. J., *Some Mechanical Properties of Plastics and Metals Under Sustained Vibrations;* Trans. A.S.M.E., Vol. 65, No. 2, pp 82–104, February, 1943.

[26] Yorgiadis, A., and Kutsay, A. Ü., Discussion of the paper *Some Mechanical Properties of Plastics and Metals Under Sustained Vibrations*, by B. J. Lazan.[25]

---

(*Continued from page 302*)

In general, it has been found desirable to avoid staggering the spots in the double rows. The annealing effect of the heat used in the spot-welding operation causes a weakening of the sheet similar to that caused by the holes in a riveted joint. As in the case of riveted joints, therefore, it is desirable to provide a direct path through the uninjured sheet material for the transfer of load across the double row of spots. Staggering the spots would appear to produce a tortuous path with resulting high stress concentrations.

## Conclusions

The conventional assumptions used in the design of riveted structural steel joints are not fully applicable to riveted joints in aluminum alloys. Allowances must be made for the reduced efficiency of perforated aluminum-alloy sheet which results from stress concentrations at the edges of holes in the sheet. If maximum joint efficiencies are to be obtained, the size, spacing, and position or pattern of the rivets must be carefully chosen.

# Contraction Cone for a Wind Tunnel

BOLESLAW SZCZENIOWSKI*
*French University, Montreal*

HSUE-SHEN TSIEN[1] has given a method for designing contraction cones for wind tunnels. This is quite accurate theoretically but requires complicated numerical calculations. A different solution[2] is given below. While equally exact, it is simpler and easier in its application.†

The stream function $\psi$ fulfils the equation:

$$\frac{\partial^2\psi}{\partial r^2} - \frac{1}{r}\frac{\partial\psi}{\partial r} + \frac{\partial^2\psi}{\partial x^2} = 0 \tag{1}$$

while the particular stream lines are obtained assuming $\psi$ = const. The velocities are

$$\left.\begin{aligned} u &= -(1/r)(\partial\psi/\partial r) \\ v &= (1/r)(\partial\psi/\partial x) \end{aligned}\right\} \tag{2}$$

Let

$$\psi = -\frac{(\mu+1)u_0 r^2}{4} + \frac{(\mu-1)u_0}{4} \times \sum_{n=1}^{\infty} \frac{(-1)^n n r^{2n}}{2^{2(n-1)}(n!)^2} f^{|2(n-1)|}(x) \tag{3}$$

where $u_0$ designates the arbitrary constant velocity, $\mu$ is the dimensionless coefficient unequal to unity; $a$ = arbitrary linear parameter and

$$f(x) = \tanh(x/a) \tag{4}$$

Therefore

$$\psi = -\frac{(\mu+1)u_0 r^2}{4} + \frac{(\mu-1)u_0}{4} \times \sum_{n=1}^{\infty} \frac{(-1)^n n r^{2n}}{2^{2(n-1)}(n!)^2} \left|\tanh\frac{x}{a}\right|^{|2(n-1)|} \tag{5}$$

$$u = \frac{(\mu+1)u_0}{2} + \frac{(\mu-1)u_0}{2} \times \sum_{n=1}^{\infty} \frac{(-1)^n n}{(n!)^2}\left(\frac{r}{2}\right)^{2(n-1)} \left|\tanh\frac{x}{a}\right|^{|2(n-1)|} \tag{6}$$

$$v = \frac{(\mu-1)u_0}{ar} \sum_{n=1}^{\infty} \frac{(-1)^n n}{(n!)^2}\left(\frac{r}{2}\right)^{2n} \left|\tanh\frac{x}{a}\right|^{|2n-1|} \tag{7}$$

Assuming

$$\left.\begin{aligned} \tanh\frac{x}{a} &= \frac{1-e^{-2(x/a)}}{1+e^{-2(x/a)}} = 1 + 2\sum_{m=1}^{\infty}(-1)^m e^{-2m(x/a)} \\ &\qquad \text{for } 0 \le \frac{x}{a} \le \infty \\ \tanh\frac{x}{a} &= \frac{e^{2(x/a)}-1}{1+e^{2(x/a)}} = -1 - 2\sum_{m=1}^{\infty}(-1)^m e^{2m(x/a)} \\ &\qquad \text{for } \ge \frac{x}{a} \ge -\infty \end{aligned}\right\} \tag{8}$$

the solution is obtained in a different form:

$$\psi = -\frac{\mu u_0 r^2}{4} + \frac{(\mu-1)u_0 a r}{2} \sum_{m=1}^{\infty} \frac{(-1)^{m-1}}{m^2} \times e^{-2m(x/a)} J_1\left(\frac{2mr}{a}\right) \tag{9}$$

$$u = \frac{\mu u_0}{2} - (\mu-1)u_0 \times \sum_{m=1}^{\infty} \frac{(-1)^{m-1}}{m} e^{-2m(x/a)} J_0\left(\frac{2mr}{a}\right) \tag{10}$$

$$v = (\mu-1)u_0 \sum_{m=1}^{\infty} \frac{(-1)^m}{m} e^{-2m(x/a)} J_1\left(\frac{2mr}{a}\right) \tag{11}$$

for $0 \le (x/a) \le +\infty$, and

$$\psi = -\frac{u_0 r^2}{4} - \frac{(\mu-1)u_0 a r}{2} \times \sum_{m=1}^{\infty} \frac{(-1)^{m-1}}{m^2} e^{2m(x/a)} J_1\left(\frac{2mr}{a}\right) \tag{12}$$

$$u = \frac{u_0}{2} + (\mu-1)u_0 \times \sum_{m=1}^{\infty} \frac{(-1)^{m-1}}{m} e^{2m(x/a)} J_0\left(\frac{2mr}{a}\right) \tag{13}$$

$$v = (\mu-1)u_0 \sum_{m=1}^{\infty} \frac{(-1)^m}{m} e^{2m(x/a)} J_1\left(\frac{2mr}{a}\right) \tag{14}$$

for $0 \ge \frac{x}{a} \ge -\infty$, where

$$J_0(\alpha) = \sum_{n=0}^{\infty} \frac{(-1)^n}{(n!)^2}\left(\frac{\alpha}{2}\right)^{2n}$$

and

* Associate Professor.

† This solution was applied in practice in the year 1928 in one of the largest then existing aerodynamic tunnels at the Warsaw Institute of Technology.

$$J_1(\alpha) = \frac{2}{\alpha}\sum_{n=1}^{\infty}\frac{(-1)^{n-1}n}{(n!)^2}\left(\frac{\alpha}{2}\right)^{2n}$$

are Bessel's functions. On the axis $x$ or for $r = 0$, $\psi = 0$, $v = 0$, and the velocity is the monotonic increasing function

$$(u)_{r=0} = \frac{(\mu+1)u_0}{2} + \frac{(\mu-1)u_0}{2}\tanh\frac{x}{a} \qquad (15)$$

Where $x = 0$, it is preferable to use Eq. (5), giving

$$(\psi/a^2u_0)_{x=0} = -[(\mu+1)/4](r/a)^2 \qquad (16)$$

Where the values $x$ approach 0, only the first two terms of Eq. (5) need be considered, and

$$\frac{\psi}{a^2u_0} \simeq -\frac{(\mu+1)}{4}\left(\frac{r}{a}\right)^2 - \frac{(\mu-1)}{32}\left(\frac{r}{a}\right)^2\frac{\sinh(x/a)}{\cosh^3(x/a)}\times\left[8\cosh^2\frac{x}{a} + \left(\frac{r}{a}\right)^2\right] \qquad (16a)$$

The series of Eqs. (9) and (12) become rapidly convergent; therefore it is sufficient to take the first two terms only, that is:

$$\left(\frac{\psi}{a^2u_0}\right)_{x>0} \simeq -\frac{\mu}{4}\left(\frac{r}{a}\right)^2 + \frac{(\mu-1)}{2}\left(\frac{r}{a}\right)\times\left[e^{-2(x/a)}J_1\left(\frac{2r}{a}\right) - \frac{1}{4}e^{-4(x/a)}J_1\left(\frac{4x}{a}\right)\right] \qquad (17)$$

$$\left(\frac{\psi}{a^2u_0}\right)_{x<0} \simeq -\frac{1}{4}\left(\frac{r}{a}\right)^2 - \frac{(\mu-1)}{2}\left(\frac{r}{a}\right)\times\left[e^{2(x/a)}J_1\left(\frac{2r}{a}\right) - \frac{1}{4}e^{4(x/a)}J_1\left(\frac{4x}{a}\right)\right] \qquad (18)$$

Applying Eqs. (16), (16a), (17), and (18) one can draw a number of lines $\psi$ = const. and then choose as the delineation of the walls of the contraction cone the value $\psi$, which gives a sufficiently slender contraction. Such a method does not cause any particular difficulties in calculation, as Eq. (16a) is solvable with regard to $r^2$ and Eqs. (17) and (18) are solvable with regard to $e^{2(x/a)}$. The values of $J_0$ and $J_1$ are given in many mathematical tables.[3]

The proposed form of the potential gives $V = u = u_0$ for $x = -\infty$ and $V = u = \mu u_0$ for $x = \infty$, where it can be $0 \leq \mu \leq \infty$.


References

[1] Tsien, Hsue-Shen, *On the Design of the Contraction Cone for a Wind Tunnel*, Journal of Aeronautical Sciences, Vol. 10, pp. 68–70, February, 1943.

[2] Szczeniowski, B., *Changement de la vitesse d'un courant uniforme*, Comptes Rendus de la Société Polytechnique de Varsovie, 1928 (in Polish with French extract).

[3] Jahnke-Emde, *Tables of Functions*, pp. 228–235; G. B. Teubner, Leipzig and Berlin, 1933.


# Letter to the Editor

Dear Sir:

I wish to draw your attention to an omission that was inadvertently made in the paper entitled "Aerodynamic Performance of the Towed Glider" recently published in the JOURNAL under the signatures of Walter C. Walling and myself.

This omission arose as a result of collaboration between two authors situated on the West and East coasts, respectively.

It was to have been in the form of an appendix referring to the splendid paper of Mr. W. Stepniewski of the DeHaviland Aircraft Company of Canada, calling attention to his paper on "Air Transport by Gliders" published in *The Aeroplane*, April 25, 1941.

Mr. Stepniewski is, as far as I know, the originator of the conception of sinking speed of the glider, virtual climb, and the like. While it is perfectly possible to bring out the aerodynamic characteristics of the glider in the tow in many ways, Mr. Stepniewski's ideas on the subject were exceedingly helpful, and, while one of the coauthors thought that more conventional presentation would be better, it was finally agreed that Mr. Stepniewski's methods are, in many respects, more convenient and more clarifying. His original paper in *The Aeroplane*, therefore, deserves careful study by anyone interested in the glider art.

It only remains for me to express admiration for Mr. Stepniewski's work and regret that full acknowledgment of his work did not appear in the paper "Aerodynamic Performance of the Towed Glider."


ALEXANDER KLEMIN
Professor of Aeronautical Engineering
Daniel Guggenheim School of Aeronautics
University Heights, New York, N.Y.

# A Multiple Recording Manometer

PAUL J. CAMPBELL*
*United Aircraft Corporation*

ABSTRACT

An instrument for recording the pressures encountered in wind-tunnel testing is described. The pressures to be measured are balanced against an accurately controlled variable pressure by means of thin leather diaphragms. The pressure at which each diaphragm becomes balanced is electrically recorded on a chart. Eighty pressures may be recorded in less than a minute.

## INTRODUCTION

WITH THE ADVENT of full-scale wind-tunnel testing of aircraft-engine installations, it has become necessary to develop new methods of observing and recording data. A large part of the data obtained from such tests is concerned with the flow of air through the various internal passages and cooling devices and over the external surfaces of the nacelle. A knowledge of these flows requires the measurement and recording of pressure at many locations. The number of such pressures to be recorded for each reading may exceed 100 on an average test. Because of the high cost of testing, the difficulty of maintaining constant operating conditions, and the urgent need for information, these pressures, like all other data, must be recorded in a minimum time.

Although many excellent pressure recording instruments have been developed, they are generally unsuitable for aircraft-engine research because they have been designed to record the time variation of one or two pressures rather than the momentary values of a large number of temporarily fixed pressures. One method that has been used to advantage in wind-tunnel work has been to photograph manometers. This method, however, has the disadvantage that the record is not available for some time after it has been taken, and the manometers are troublesome to connect. As none of the available instruments or methods of recording pressure was completely satisfactory, the Research Division of United Aircraft Corporation, with the cooperation of the Raymond Engineering Laboratory, undertook the development of a recording manometer designed specifically for wind-tunnel testing.

## REQUIREMENTS OF THE INSTRUMENT

In addition to the rapid and reliable recording of many pressures, the instrument must conform to a number of other requirements peculiar to wind-tunnel work. Connections between the nacelle and the control room must be compact and easy to install. The size of passage necessary to carry leads and controls to the engine will determine the minimum thickness of fairing between the nacelle and the tunnel wall, and compact leads are therefore necessary to reduce fairing interference. To reduce to a minimum the time of installing the test nacelle, it is desirable to complete as much of the installation as possible while the nacelle is in the shop and simply plug in to standardized panels after it has been placed in the tunnel. If pressure-sensitive pickups are to be placed within the nacelle, they must be insensitive to the vibration and temperature variations encountered near an engine. The record must be available to the operator immediately after it has been made without the necessity of any development or fixing, and it must be permanent. The recorded pressures must be easy to identify.

## DESCRIPTION OF THE MANOMETER

By combining several simple elements, an instrument has been developed which promises to meet these requirements. The elements, shown diagrammatically in Fig. 1, are: a number of limp diaphragms, to each of which is applied one of the pressures to be recorded; a compressor and regulator for applying a varying pressure to the back of the diaphragms; and a recording system to indicate on a chart the pressure necessary to balance each diaphragm against the pressure that it is measuring.

In operation, the pressure regulator automatically varies the balancing pressure that is applied simultaneously to the back of all diaphragms. A recording arm moves as this pressure is varied in such a way that its displacement is always precisely in proportion to the balancing pressure. The arm carries one stylus for each pressure to be recorded. The mark made by the stylus is controlled by an electrical circuit through the corresponding diaphragm. As the balancing pressure is gradually increased, it exceeds, one by one, the pressures on the opposite side of the diaphragms; as it does so, the electrical circuit through each is broken. Since the stylus is arranged to record only while its electrical circuit is closed, it marks on the chart a line whose length is proportional to the pressure measured by the diaphragm.

### *Connections*

Connections between the diaphragm cell and the recorder consist of one tube to transmit the balancing

Presented at the Radio and Instruments Session, Eleventh Annual Meeting, I.A.S., New York, January 25–29, 1943.

* Experimental Engineer, Research Division.

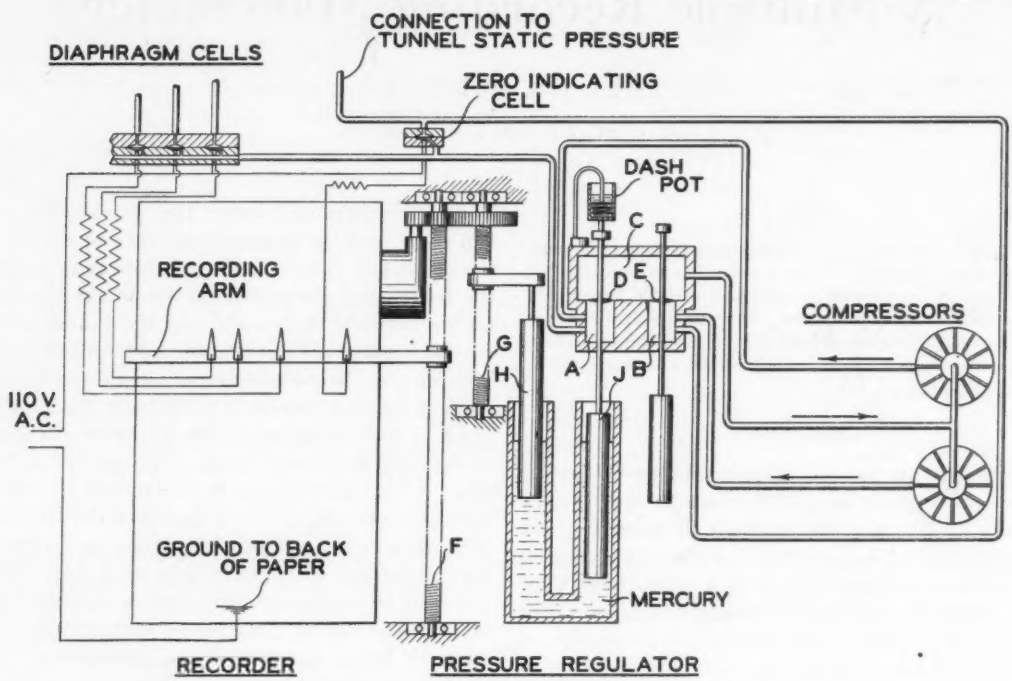


FIG. 1. Schematic view of the complete instrument.

pressure and a multiwire cable to carry electrical current from the diaphragms. The diaphragms are mounted in the nacelle and connected by small rubber tubes to the various points where pressure is to be measured.

### *The Diaphragm Cells*

The diaphragms are mounted in cells each containing ten diaphragms, although more could be used if desired. Fig. 2 shows a cross section through a single diaphragm, and Fig. 3 is a photograph of a complete cell. The diaphragms are small discs of colon leather. This material is extremely thin and limp, yet is adequately tough, airtight, and durable. The leather discs are clamped between lucite plates. Shallow concave surfaces machined in each plate at the locations of the diaphragms permit them to deflect a short distance in either direction. The spaces formed by these concave surfaces are connected on one side of the diaphragms to the pressures to be measured; on the other side, they communicate with a common passage leading to the balancing pressure. An extremely small pressure difference is sufficient to deflect a diaphragm from one wall to the other. As the diaphragm deflects, it opens or closes a circuit through a thin silver disc cemented to the center of the diaphragm. Two silver contact points imbedded in the lucite wall on the balancing-pressure side complete the circuit to the recording arm. The circuit is thus closed when balancing pressure is less than measured pressure.

### *The Pressure Regulator*

The function of the pressure regulator is to maintain the required proportionality between the position of the recording arm and the balancing pressure (Fig. 4). In most pressure recording or indicating instruments, the stylus or pointer is moved by the force due to the pressure applied. In this instrument, however, the process is reversed; the position of the stylus at all times determines the pressure. This method completely elimi-

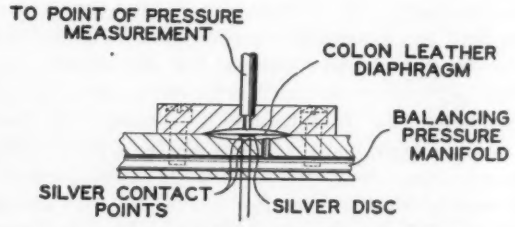


FIG. 2. Section through a pressure-sensitive cell.

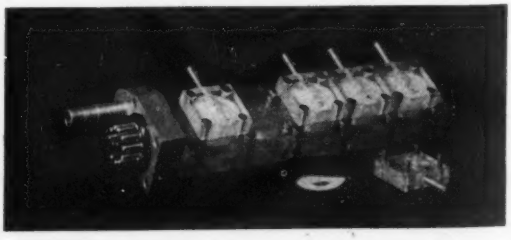

FIG. 3. Diaphragm cell.

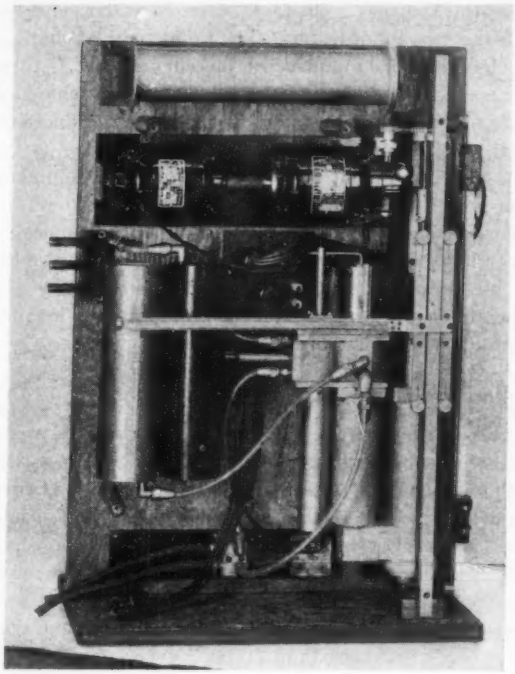

FIG. 4. Exposed view of instrument showing pressure regulator and recording arm drive.

nates any error due to friction of the numerous styluses. As the recording arm is driven by a motor across the chart, the balancing pressure is caused to vary accordingly.

## PRINCIPLE OF OPERATION

The principle of operation is shown in Fig. 1. The recording arm is moved across the chart by an accurately machined lead screw, F, driven by a small electric motor. Another lead screw, G, geared to the first, slowly lowers an iron bar, H, into a column of mercury and causes the mercury level to rise in proportion to the movement of the recording arm. The change in mercury level causes a proportional variation in the vertical force on a second iron bar, J, suspended at a fixed height, partly submerged in the mercury. The same result could be accomplished by stretching a spring if the instrument were designed for flight testing.

The varying force is applied to a floating piston, which, in turn, controls the balancing pressure that is applied to the diaphragms. The way in which a force applied to the piston accurately determines the pressure may be seen by referring to the pneumatic circuit in Fig. 1.

Two conical pistons, D and E, are mounted on slender rods in cylinders A and B, which are connected, respectively, to the balancing side of the diaphragms and to tunnel static pressure. The cylinders are machined side by side in a common block, and both open into a large space, E, at the top of the block. To reduce friction, the pistons are provided with enough clearance to prevent their touching the cylinder walls. The cylinders and the space above them are connected to two small motor-driven rotary vane compressors, as shown in Fig. 1.

The compressors pump air from the space above the pistons into the cylinders below them, thus lifting the pistons to the tops of their cylinders, where they come to rest because of the sudden increase in leakage at this point. The pressure difference across each piston is now equal to its effective weight divided by its area. Any change in the weight immediately causes a proportional change in pressure difference. Except for the slight flow due to leakage and variations in density, no air enters or leaves the system. Although cylinder B is open to tunnel static pressure, there is almost no flow through the opening.

## PISTON OPERATION

The two pistons serve different purposes. Piston E is restrained by a constant weight and serves only to maintain a constant negative pressure (relative to tunnel static pressure) in the space above piston D. The reason for maintaining a constant negative pressure in this space is to permit balancing pressure to extend to negative values. Piston D, however, is restrained by the weight which is partly immersed in mercury. When the mercury level is varied, the effective weight on the piston changes, and the pressure differential across the piston varies accordingly. Since the pressure in C is constant, relative to tunnel static pressure, the change in pressure differential across piston D amounts to a change in balancing pressure relative to tunnel static pressure.

The pistons were found to undergo a self-excited vertical vibration that could be started by any slight jarring of the instrument. This difficulty was eliminated from piston E by changing the force-displacement characteristics of the system. A small wedge-shaped notch was cut into the wall of cylinder B at the top so that leakage would increase gradually as the piston approached its equilibrium position. This remedy was not permissible for piston D, however, because its equilibrium position must remain definitely fixed. Here it was necessary to resort to damping. An oil-filled dash pot was mounted on the piston rod in such a way that mechanical contact between moving parts was impossible. This dash pot introduces no friction unless there is motion, and yet it completely eliminates the vibration.

## METHOD OF RECORDING

The record is made on "Teledeltos" paper, an electrically conductive paper that turns black at any point where an electric current is carried to its surface. Standard 110-volt alternating current is used for the re-

cording. A 4,000-ohm resistance in the circuit through each stylus and diaphragm prevents excessive current from burning the paper or arcing at the diaphragm contact points. The current is brought to the styluses on the recording arm through a multiwire flexible cable. A ground wire connecting the back of the paper to all diaphragms completes the circuit. The styluses are simply small cantilever springs with rounded contact points bearing lightly against the paper.

Since the datum for all measurements is tunnel static pressure, it is necessary to record this pressure on the chart as a zero from which to measure the other pressures. To register this point, a single diaphragm unit is connected across the cylinders, A and B, of the pressure regulator. The current from this diaphragm is carried to styluses at each side of the chart. When balancing pressure becomes equal to tunnel static pressure, the lines drawn by these styluses are terminated; a horizontal zero line may later be drawn with pencil between the two recorded points. Recording the instrument zero automatically on each record is a distinct advantage in that it eliminates error due to variations in zero or to improper location of the chart.

The recording paper is mounted in a roll at the top of the instrument. From here it passes over the recording platen and under a knife at the bottom. After each recording the paper is pulled out of the bottom and torn off against the knife. The size of each record is $10^1/_2$ in. wide by 17 in. high.

The maximum number of pressures which can be recorded on this size sheet is determined by the desired ease of reading the record. Eighty lines at a spacing of $^1/_8$ in. appear to be about the maximum. However, there is adequate power to drive many more styluses, so this number can be increased either by closer spacing or by increasing the width of the sheet.

The paper is not ruled. In interpreting the record, a horizontal line is drawn through the zero point, and the heights of the individual lines are measured from this zero line. To facilitate this measurement, it is planned to construct a transparent plastic plate ruled with horizontal lines corresponding to the scale of pressure.

## Operation

To make a record, the operator closes one switch that controls the lead screw drive motor. After the recording arm has traveled the length of the chart, the current to the styluses is automatically turned off and the motor is reversed. The arm then returns to its original position, where it is stopped by a limit switch. The chart may then be pulled out and another record made.

### *Scale and Range*

The scale and range of the instrument may be made almost any desired values within the limits of the compressors and diaphragms. In the instrument's present form, the range is −26 to +36 in. of water, and the scale is 1 to 4 in. of water. The range may be changed by changing the quantity of mercury in the U-tube. Changes in the scale may be made either by changing gears on the lead screws or by changing the diameter of either of the bars immersed in the mercury.

As the instrument is still undergoing development, it is not possible to give any final figures on its accuracy or speed of recording. Accuracy is somewhat dependent on speed, and the optimum compromise has not yet been determined. The overall accuracy also depends on the sensitivity of the diaphragms and the accuracy of the pressure regulator.

### *Diaphragms*

The diaphragms are remarkably sensitive; a unit 1 in. in diameter will respond to a pressure of less than 0.01 in. of water. The diaphragms employed at present are $^3/_4$ in. in diameter, and their sensitivity is somewhat poorer. A small size is advantageous, however, and further efforts are being made to combine good sensitivity with small size. The silver contact points have shown no signs of deterioration. Two of the diaphragms were tested to more than 200,000 cycles, making and breaking a 110-volt circuit, with no evidence of loss in sensitivity.

Friction in the piston rods of the pressure regulator can cause errors. However, because of the fact that the pistons do not touch the cylinder walls, this error is small and can be practically eliminated by a slight vibration.

### *Speed of Recording*

If the instrument is operated too fast, an error can presumably be caused by a flow of air due to rapid changes in density. As the air in the balancing chamber at the diaphragm cell is compressed, some air must flow from the regulator into the cell. The only place where this air can enter the system is through the tunnel static connection. If these flows are too rapid, the resulting pressure drops may cause errors. However, at the present recording speed, there is no evidence of any error due to this cause.

The instrument is now designed to make a complete record in 1 min. For engine testing, this speed is fast enough because the engine must be held at constant conditions for longer than a minute to permit temperatures to be recorded. A faster speed would be desirable, however, for other wind-tunnel testing where temperatures are not measured. The maximum permissible speed of the instrument has not yet been investigated.

### *Errors*

In the limited testing that has been done, the greatest observed error was 0.4 per cent of full scale. This error was evidently due mainly to friction in the pres-

sure regulator and perhaps to poor sensitivity of the diaphragms. With these faults corrected, it is thought possible to reduce the error to less than 0.1 per cent of full scale.

Although there is a slight leakage of air through the diaphragms, it does not affect accuracy because the leakage becomes zero when balancing pressure equals measured pressure. It may be a source of difficulty, however, when another manometer is connected to the same point of pressure measurement. This difficulty was noticed when attempting to check the instrument against a water manometer. Both were connected in parallel to a total-head tube made of hypodermic tubing. Under these conditions, the leakage of the diaphragm was large enough compared to the flow out of the total-head tube to cause an error in the height of the water manometer. This error disappeared, however, when the balancing pressure approached the measured pressure, and the true pressure was recorded correctly.

### *Fluctuating Pressures*

If the measured pressure is fluctuating, the instrument will give a fair idea of the magnitude and frequency of the fluctuation and permit a reasonable estimate to be made of the mean. The recorded line, instead of terminating at a definite point, will end in a series of dashes that become shorter until they disappear. The lowest break in the line represents the minimum of the fluctuation and the highest dot, the maximum.

## Conclusion

Although this instrument has been developed to record relatively low air pressures, it could be modified to record some of the higher pressures encountered in engine testing. For intermediate pressures, such as those found in the induction system, it would probably be necessary only to provide smaller pistons in the pressure regulator and use diaphragm material that was resistant to oil and gasoline. For higher pressures, such as those of the lubricating oil and torque measuring devices, it might be necessary to replace the pneumatic system with a hydraulic one.

For flight testing, a number of modifications in the design would be necessary, but the same basic principles could be retained. The mercury displacement system could be replaced by a spring. Errors due to the inertia of the regulator pistons could be eliminated by replacing them with diaphragm-controlled valves. If all parts were carefully designed to eliminate the effects of inertia and gravity, the instrument could be used for recording pressures during maneuvers and at various flight attitudes that cannot be measured by conventional manometers.

---

# Letters to the Editor

Dear Sir:

Referring to the article, "A Tabular Method of Propeller Blade Stress Analysis," by Joseph Stuart, III (Journal of the Aeronautical Sciences, April, 1943), it is to be noted that by use of a simple algebraic means no estimation of trial root moment is necessary. Mr. Stuart's method of stress analysis calculated in this manner becomes a direct method rather than a method of successive approximations, thus eliminating the difficulties that arise in the analysis of unusual type blades and in cases where accurate evaluation of tip bending moments becomes necessary.

Let the moment at the blade root be called $M_1$, and carry through the processes of finding the moments along the blade, as outlined in Mr. Stuart's article, in terms of $M_1$. This results in each moment being expressed as

$$M_n = a_n M_1 - b_n$$

where $a_n$ and $b_n$ are constants determined in the tabular computation process for the bending moment $M_n$ at station $n$. Enforcing the condition that the tip moment should equal zero allows evaluation of $M_1$,

$$M_1 = b_{tip}/a_{tip}$$

and thus evaluation of every bending moment.

Mr. Stuart has suggested that to facilitate computation the tabular algebraic method discussed above may be separated into two tables, one involving the solution of the constants $a_n$ and the other the constant $b_n$. By this means the method lends itself extremely well to routine computation. Two persons may work simultaneously on the two different tables, enabling direct results to be obtained in approximately $1^1/_2$ hours' time.

The numerical computation must be carried through to at least six significant figures if one wishes to be

TABLE 1

Computation of $a_n$

| (1) Station | (2) $a_n$ | (3) $\frac{36}{EI} \times 10^6$ | (4) $\frac{36}{EI} \times a_n \times 10^6$ | (5) $(Z_2 - Z_1)_a \times 10^6$ | (6) C.F. | (7) $(z_2 - z_1)_a \times$ C.F. |
|---|---|---|---|---|---|---|
| (6) | | | | 0 | | |
| 9 | 1.000 | 0.1267 | 0.1267 | | | |
| (12) | | | | 0.1267 | 74,000 | 0.009376 |
| 15 | 1.009376 | 0.1267 | 0.12789 | | | |
| (18) | | | | 0.25459 | 65,700 | 0.016727 |
| 21 | 1.026103 | 0.4320 | 0.44328 | | | |
| (24) | | | | 0.69787 | 58,300 | 0.040686 |
| 27 | 1.066678 | 0.9930 | 1.05932 | | | |
| (30) | | | | 1.75719 | 50,800 | 0.089265 |
| 33 | 1.156054 | 1.855 | 2.14448 | | | |
| (36) | | | | 3.90167 | 42,700 | 0.166601 |
| 39 | 1.32266 | 3.268 | 4.32245 | | | |
| (42) | | | | 8.22412 | 34,300 | 0.28209 |
| 45 | 1.60475 | 5.214 | 8.36717 | | | |
| (48) | | | | 16.59129 | 26,000 | 0.431374 |
| 51 | 2.03612 | 8.271 | 16.8407 | | | |
| (54) | | | | 33.4320 | 18,000 | 0.601776 |
| 57 | 2.6379 | 14.43 | 38.065 | | | |
| (60) | | | | 71.497 | 10,600 | 0.757868 |
| 63 | 3.3958 | 27.58 | 93.6561 | | | |
| (66) | | | | 165.1531 | 3,400 | 0.56152 |
| 69 | 3.95732 | | | | | |

*Computation Procedure:* [NOTE: $(3)_{15}$ means item in column (3) station 15.] *Given:* Columns (3) and (6), $(2)_9 = 1.000$ (that is, $a_n$ at root = 1.000); $(5)_{(6)} = 0$. *Find:* $(4)_9 = (2)_9 \times (3)_9$, $(5)_{(12)} = (5)_{(6)} + (4)_9$, $(7)_{(12)} = (5)_{(12)} \times (6)_{(12)}$, $(2)_{15} = (2)_9 + (7)_{(12)}$, $(4)_{15} = (2)_{15} \times (3)_{15}$, $(5)_{(18)} = (5)_{(12)} + (4)_{(15)}$, $(7)_{(18)} = (5)_{(12)} \times (6)_{(18)}$, $(2)_{21} = (2)_{15} + (7)_{(18)}$, etc.

TABLE 2

Computation of $b_n$ and $M$

| (1) Station | (2) $-b_n$ | (3) $\frac{36}{EI} \times 10^6$ | (4) $-\frac{36}{EI} \times b_n$ | (5) $6\left(\frac{dz}{dr}\right)_b$ | (6) $Z_2 - Z_1$ | (7) $(z_2 - z_1)_b$ | (8) C.F. | (9) $\frac{(z_1 - z_1)_b \times}{\text{C.F.}}$ | (10) 65 | (11) $a_n M_1$ | (12) $M$ |
|---|---|---|---|---|---|---|---|---|---|---|---|
| (6) | | | | 0.03140 | | | | | | | |
| 9 | 0 | 0.1267 | 0 | | | | | | | 28,030.4 | 28,030.4 |
| (12) | | | | 0.03140 | −0.169 | −0.13760 | 74,000 | −10,182.4 | −7,680 | | |
| 15 | −17,862.4 | 0.1267 | −0.002263 | | | | | | | 28,293.2 | 10,430.8 |
| (18) | | | | 0.02914 | +0.182 | +0.21114 | 65,700 | +13,871.9 | −7,630 | | |
| 21 | −11,620.5 | 0.4320 | −0.00502 | | | | | | | 28,762.1 | 17,141.6 |
| (24) | | | | 0.02412 | −0.013 | +0.01112 | 58,300 | +648.3 | −7,330 | | |
| 27 | −18,302.2 | 0.9930 | −0.018174 | | | | | | | 29,902.5 | 11,600.3 |
| (30) | | | | 0.005946 | 0 | +0.00595 | 50,800 | +302.3 | −6,860 | | |
| 33 | −24,859.9 | 1.855 | −0.046115 | | | | | | | 32,404.7 | 7,544.8 |
| (36) | | | | −0.040169 | +0.006 | −0.03417 | 42,700 | −1,459.0 | −6,140 | | |
| 39 | −32,459.0 | 3.268 | −0.106076 | | | | | | | 37,074.7 | 4,615.7 |
| (42) | | | | −0.146245 | +0.004 | −0.14225 | 34,300 | −4,879.0 | −5,200 | | |
| 45 | −42,538.0 | 5.214 | −0.221793 | | | | | | | 44,981.8 | 2,443.8 |
| (48) | | | | −0.368038 | −0.003 | −0.37104 | 26,000 | −9,647.0 | −4,085 | | |
| 51 | −56,270.0 | 8.271 | −0.465409 | | | | | | | 57,073.3 | 803.3 |
| (54) | | | | −0.833447 | −0.012 | −0.84545 | 18,000 | −15,218.0 | −2,790 | | |
| 57 | −74,278.0 | 14.43 | −1.07183 | | | | | | | 73,941.4 | −336.6 |
| (60) | | | | −1.90528 | +0.001 | −1.90428 | 10,600 | −20,185.4 | −1,375 | | |
| 63 | −95,838.4 | 27.58 | −2.64322 | | | | | | | 95,185.6 | −652.8 |
| (66) | | | | −4.54850 | +0.213 | −4.3355 | 3,400 | −14,740.7 | −346 | | |
| 69 | −110,925.1 | | | | | | | | | 110,925.1 | 0 |

*Computation Procedure: Given:* $(5)_{(6)} = 0.08140$ (blade tilt); $(2)_9 = 0$; columns (3), (6), (8), (10). *Find:* $(4)_9 = (2)_9 \times (3)_9$, $(5)_{(12)} = (5)_{(6)} + (4)_9$, $(7)_{(12)} = (5)_{(12)} + (6)_{(12)}$, $(9)_{(12)} = (7)_{(12)} \times (8)_{(12)}$, $(2)_{15} = (2)_9 + (9)_{(12)} + (10)_{(12)}$, $(4)_{15} = (2)_{15} \times (3)_{15}$, etc. Compute first ten columns first. $M_1 = b_{69}/a_{69}$, column (11) now found from $M_1 \times$ column (2), Table 1, $(12)_n = (11)_n + (2)_n$ ($n$ = any station).

accurate in any degree in the evaluation of the tip moments.

An analysis of the same blade for the same conditions as used by Mr. Stuart in his Table 1 is given in Tables 1 and 2 on page 318.)

SYDNEY D. BLACK
Project Engineer, Aerodynamics Branch,
Propeller Laboratory, Engineering Div.,
A.A.F. Matériel Command
Wright Field, Dayton, O.

---

Dear Sir:

I have read with interest the article "A Tabular Method of Propeller Blade Stress Analysis" by Mr. Joseph Stuart, III, which appeared in the April issue of the JOURNAL OF THE AERONAUTICAL SCIENCES, and I wish to suggest some improvements in the proposed method of analysis.

All trial-and-error methods can be avoided by performing the following calculations:

(1) Assume no thrust in the propeller, all c. g. of sections located on the axis ($Z = 0$) and the axis perfectly radial at the root of the propeller blade ($\theta = 0$). Assume an arbitrary bending moment at the root, say $M_0 = 100$ in.lbs., and perform the tabular calculations outlined by Mr Stuart. The tip bending moment obtained from this calculation will be, say, $M_{T1}$, and the bending moments obtained at all other sections will be the ones resulting from $M_{T1}$ at the tip and the centrifugal force. The moments along the rotating blade due to a unit bending moment at the tip will then be obtained by dividing all the above bending moments by $M_{T1}$. Call the bending moments thus obtained along the blade $M'$.

(2) Make the same assumptions as above except that now the blade axis at the root leans forward an arbitrary amount, say, $\theta = 0.01$ rad. and $M_0 = 100$ in.lbs. After performing the tabular calculations there will result a tip bending moment of $M_{T2}$. Due to the linear form of the stress equations, however, this may easily be removed by subtracting the bending moments $M_{T2}M'$ from those last obtained. Call the bending moments thus obtained along the blade $M''$. These bending moments will then simply be the ones resulting from a rotating blade leaning forward 0.01 rad. at the root.

(3) Now perform the complete calculation with the thrust and the eccentricities of the centers of gravity of the sections included, but with $\theta = 0$. Assume an arbitrary bending moment at the root. The bending moment at the tip is now $M_{T3}$, but this may be removed by subtracting $M_{T3}M'$ from the ones just found. Let us call the bending moments thus obtained $M$. These will be the correct bending moments for the blade in question with $\theta = 0$ at root. If $\theta \neq 0$, the correct bending moments will merely be $M + \theta M''$. If it is not desired to investigate the effect of varying $\theta$, calculation No. 2 may be omitted since a fixed value of $\theta$ can be considered together with the thrust in calculation No. 3. In this case, therefore, only two tabular calculations will be necessary to obtain the correct bending moments along the propeller blade.

I have some doubt as to the validity of Mr. Stuart's assumption that the distance $Z$ that the center of gravity of a section is forward of the blade axis may be considered to be unchanged by the centrifugal force. The centrifugal force will have a powerful tendency to straighten the blade out, so to speak, which may result in a considerable reduction in the eccentricities of the blade sections and a consequent reduction in the bending moments resulting therefrom. The exact effect of blade section eccentricity can, however, easily be found by the following procedure.

Put $Z = 0$ in calculations No. 3 described above. Load this fictitious propeller blade statically in such a way that its originally straight axis bent into the shape described by the centers of gravity of the real blade. The bending moment thus obtained is given by $M_F = EI(d^2Z/dr^2)$ and the shear force by $S_F = -dM_F/dr$. With this fictitious loading perform tabular calculation No. 4. Use the above calculated value of $S_F$ and assume a root bending moment. Correct for the tip bending moment as previously described and obtain a bending moment distribution $M_C$. The bending moment due to eccentricity alone will then be $M_E = M_F - M_C$, which should be added to the previously obtained bending moment $M$ (with eccentricity neglected). The total bending moment is then $M + M_E$.

N. O. MYKLESTAD
Research Associate in Aeronautics,
California Institute of Technology,
Pasadena, Calif.

---

Dear Sir:

Concerning the article, "A Tabular Method of Propeller Blade Stress Analysis" by Joseph Stuart, III, appearing in the April issue of the JOURNAL, I should like to offer the following suggestions:

It should be noted first that if the quantities $z_1$, $z_2$ . . . . are eliminated from the equations of the type (3), (5), and (7), the resulting system is a set of linear equations of the "triangular" type in the $n$ variables $M_1$, $M_2$ . . . . $M_N$ (assuming $N$ stations). The author adopts the standard method of solution for such a system—namely, that of determining the last $N - 1$ variables as functions of the first—but fails to take full advantage of the linearity for interpolation at every station. Only two guesses of the root moment are necessary to determine correct moments at every station by linear interpolation or extrapolation, whereas the

author suggests interpolation only at the tip and uses this interpolation only to find a third accurate guess.

It may also be pointed out that the "one-fourth" rule offered is not practical for all blades. Indeed, for one type of propeller blade for which I carried out the computations, the slope of the graph shown in Fig. 4 was 40 rather than 4. The computation for any blade is reduced somewhat if this slope is found directly first, one guess then being sufficient to determine the graph similar to Fig. 4 for each station.

DR. R. C. RAND
Chief Analyst
Engineering and Research Corporation
Riverdale, Md.

---

Dear Sir:

In the March issue of the Journal, F. Theilheimer published a paper, "The Influence of Sweep on the Spanwise Lift Distribution of Wings." This paper interests me particularly since I have studied the same topic and arrived at the same—or essentially the same—expressions as Mr. Theilheimer. My reason for not publishing my results was and still is that my formulations invariably lead to nonexisting integrals. This seems to have also been the experience of Hermann Blenk, who reports in "Der Eindecker als tragende Wirbelfläche," *Zeitsch. f. Angew. Math. u. Mech.*, Vol. 5, p. 36: "Yawing wings and wings curved in the direction of flight could not be calculated with this first approximation (referring to the lifting *line* concept). For such wings the chordwise distribution must be taken into consideration." (My translation.)

If one takes Mr. Theilheimer's expression for $\Delta w_s - \Delta w$ on the bottom of page 102 and applies it for the actually existing continuous vortex sheet the following is obtained:

$$w_s - w = \frac{1}{4\pi} u \left[ \int_0^{b_2} \frac{\Gamma(y)'}{y'} dy \int_0^{b_2} \frac{\Gamma(y)'}{|y - y'|} dy - \ldots \right]$$

The integrals all stay within bounds provided $\Gamma'(y)$ is bounded which is commonly accepted as a valid assumption. One of the integrals—namely, the one with the absolute value of $y - y'$ in the denominator—makes a notable exception: This integral has a singularity in the interval of integration. This singularity makes the integral infinite and (contrary to the case of a straight wing) makes even the principal value of the integral nonexistent.

Mr. Theilheimer seems to circumvent this difficulty by taking a finite sum of $N$ distinct vortices instead of the continuous vortex sheet. In the mathematical sense he approximates the Riemann integral—which we just recognized as nonexisting—by a finite sum. It seems to me that if one were to write the limit of the sum as of the top of page 103 for $N \to \infty$ one would have the formal definition of the above integral.

This question now arises: For which value of $N$ does Mr. Theilheimer's sum approach the correct result? His numerical calculations suggest $N = 8$ as the answer. However, no justification is given for this choice, and so it seems that any result whatsoever could be obtained by that sum depending on the choice of $N$.

In view of the great importance of this lift distribution problem, I suggest that Mr. Theilheimer disclose his convergence proof, if not in public for reasons of wartime secrecy then certainly to the aeronautical industry, which is in danger of being misled by Mr. Theilheimer's results in case the convergence of his formula cannot be established.

As a more positive contribution to the problem of yawing and swept wings, I call the industry's attention to the paper of H. Blenk as quoted above. Blenk's results are cumbersome but unquestionably converging except at the very wing tips. Experimental proof for Blenk's results was furnished by the Doctor Dissertation of Mr. Sergio Del Proposto. This dissertation was published in an all too brief excerpt in the July, 1934, issue of the JOURNAL OF THE AERONAUTICAL SCIENCES.

ALBERT GAIL
Assistant Professor
Illinois Institute of Technology
Chicago, Ill.

---

Dear Sir:

Professor Gail objects to the use of a vortex system consisting of a finite number of vortices, because the formula for the induced velocity—if applied to a continuous lift distribution—leads to an integral containing a singularity. Exactly the same situation, however, prevails in the classic case of the straight lifting line and, just as there, it can be shown here that the integral in question has a principal value:

The expression for $\Delta w_s$ (in the middle of page 102) contains the term

$$\{(-u/|y - y'|) + [1/(y - y')]\}(-\Delta\Gamma)$$

where $u = \sin \Lambda$. This leads in the case of continuous loading to the integral

$$-\int_0^{y'} [(1 + u)d\Gamma/(y - y')] - \int_0^{b/2} \times [(1 - u)d\Gamma/(y - y')]$$

The vorticity distribution $\Gamma$ shall be assumed to be given as a trigonometric polynomial

$$\Gamma = \Sigma A_n \sin n\theta$$

where $\theta$ is introduced by means of the familiar substitution

$$y = (b/2) \cos \theta$$

and likewise

$$y' = (b/2) \cos \varphi$$

Since $\cos n\theta$ can be written as a sum of powers of $\cos \theta$, the division by $\cos \theta - \cos \varphi$ in the integrand can be carried out, so that there remains only one term that requires closer examination—namely,

$$J = \int_{\pi/2}^{\varphi} \frac{(1 + u)d\theta}{\cos \theta - \cos \varphi} + \int_{\varphi}^{\pi} \frac{(1 - u)d\theta}{\cos \theta - \cos \varphi}$$

A principal value can be ascribed to $J$ by writing

$$J = \lim_{\substack{\delta \to 0 \\ \epsilon \to 0}} \left[ \int_{\pi/2}^{\varphi - \delta} \frac{(1 + u)d\theta}{\cos \theta - \cos \varphi} + \int_{\varphi + \epsilon}^{\pi} \frac{(1 - u)d\theta}{\cos \theta - \cos \varphi} \right]$$

and choosing $\delta$ and $\epsilon$ such that

$$(1 + u) \log \sin (\pi/2) = (1 - u) \log \sin (\epsilon/2)$$

Noting that

$$\frac{d\theta}{\cos \theta - \cos \varphi} = \frac{1}{\sin \varphi} d \log \frac{\sin [(\varphi + \theta)/2]}{\sin [(\varphi - \theta)/2]}$$

the principal value of $J$ is found to be

$$\frac{1}{\sin \varphi} \left[ 2u \log \sin \varphi + (1 + u) \log \frac{1 - \sin \varphi}{-\cos \varphi} \right]$$

For $u = 0$ this reduces to the same expression that is used in the theory of the straight lifting line.

FEODOR THEILHEIMER
Trinity College
Hartford, Conn.

---

(*Continued from page 284*)

count for yielding thus only emphasizes the need for more tests and calculations of shear lag on typical examples including the effects of such factors as skin camber, taper in plan form, and different typical spanwise variations of beam shear per inch.

REFERENCES

[1] A.S.T.M. Standards, Part I, *Metals*, 1939.
[2] Shanley, F. R., *Elastic Theory in Sheet Metal Forming Problems*, Journal of the Aeronautical Sciences, Vol. 9, No. 9, pp. 313–333, July, 1942.
[3] Frocht, *Photoelasticity*, Vol. I, pp. 220–223; John Wiley & Sons, New York, 1941.
[4] Kirsch, Prof. G., *Die Theorie der Elastizität und die Bedürfnisse der Festigkeitslehre*, Zeitschrift des Vereines Deutscher Ingenieure, Vol. 42, p. 797, 1898.
[5] Winny, H. F., *The Distribution of Stress in Monocoque Wings*, R. & M. No. 1756, 1936.

---

(*Continued from page 288*)

frequencies with each separate control, filtering them at the receiving end. The carrier system is more satisfactory for a large number of channels, and the individual frequency band system is applicable for operation of two to four channels. Any type of vehicle could be positively controlled by this system because the control is continuous and not intermittent or based upon a step-by-step arrangement.

## CONCLUSION

It is hoped that this paper illustrates the resonant-control principle and some of its typical applications. Operating models that have been constructed have demonstrated many applications of the principle. Development is continuing and any suggestions for further applications and uses from the field would be gratefully received.

# SUGGESTIONS FOR CONTRIBUTORS TO THE PUBLICATIONS *of the* INSTITUTE *of the* AERONAUTICAL SCIENCES

The Institute of the Aeronautical Sciences invites both members and nonmembers from any country to submit papers for publication in the JOURNAL OF THE AERONAUTICAL SCIENCES and the AERONAUTICAL ENGINEERING REVIEW The Institute, following the practice of other societies, does not pay for contributions.

The following directions for the preparation of papers, if followed by authors, will save correspondence, avoid the return of papers for changes, minimize the work of preparation for the printer, and save the expense due to the charges made for "author's corrections."

---

MANUSCRIPTS: Papers must be written in English, in original typewriting on one side only of white paper sheets, consecutively numbered and be double or triple spaced with wide margins. Manuscripts should be prepared with great care so that they will be typographically accurate. Paragraphing should be given special attention. Papers should be written in the third person, reference to the writer being made as "the author." Avoid the use of the words "I," "we," and "you." Blueprint copies of papers are unacceptable as it is impossible to mark directions to the printer on them. Correcting, changing, or adding to papers after they are in type is costly. It is, therefore, imperative that papers submitted be in final form. Typographical errors may be corrected on proofs, but if authors wish to add material, they may do so at their own expense. In mailing, drawings may be rolled, but manuscripts should be sent flat. Send by first class mail (register if you wish for your own protection) to the Editorial Office, Institute of the Aeronautical Sciences, 1505 RCA Bldg. West, 30 Rockefeller Plaza. New York 20, N. Y. All manuscripts will be examined by the Editorial Committee and by the Editor. Authors will be advised as promptly as possible whether the paper is acceptable for publication.

TITLES: The title of the paper should be brief. The name and initials of the author should be written as he prefers. The use of the full name of an author is advocated because of the frequent duplication of initials and surnames which sometimes makes it difficult to establish the identity of the author. This is particularly important for large annual indexing and abstracting services. All titles and degrees or honors are omitted. The name of the organization with which the author is associated should be placed after his name on a separate line. The date on which the paper is received will be inserted by the Editor.

SUMMARIES OR ABSTRACTS: An abstract to be printed at the beginning should accompany each article. It should be adequate as an *index* and as a *summary*. It should contain a statement of major conclusions reached, since summaries in many cases constitute the only source of information used in compiling scientific reference indexes. Abstracts printed in other journals, especially foreign, in most cases, consist of summaries from printed papers. The summary should explain as adequately as possible the major conclusions to a nonspecialist in the subject. The summary should contain from 100 to 300 words, depending on the length of the paper.

SUBHEADINGS: Subheadings should be inserted by the author at frequent intervals. The work of editorial preparation will be simplified by the author providing many subheadings. Owing to the breaking of columns and the insertion of illustrations, some of the subheadings may have to be omitted.

SHORTENING OF PAPERS: Some papers, at the end, fill in only a portion of a page. This leaves much wasted blank space as succeeding articles are started at the top of a page. Authors should indicate by notation on the left-hand side of the page what matter may be omitted when "runovers" occur. This request is important as the Journal cannot afford in the future, as it has in its earlier issues, to have blank half pages or more at the end of papers.

MATTER USUALLY DELETED: Acknowledgments of assistance in preparation of paper, except by collaborators. Photographs or illustrations of little technical interest and not showing advances in general practice. Too detailed tabular matter (general results of such tables may be included in the text). Lengthy descriptions of materials or processes or of preliminary experiments or theories that preceded final results; salient features only are of interest.

REFERENCES AND FOOTNOTES: References should appear as footnotes only, numbered consecutively, grouped together at the end of the manuscript. The arrangement should be as follows: (for books)—[1] Durand, W. F., *Aerodynamic Theory*, 1st Edition, Vol 1, p. 23; Julius Springer, Berlin, 1934. (For magazines)—

[1]Englund, C. R., Crawford, A. B., and Mumford, W. W., *Some Results of a Study of Ultra-Short-Wave Transmission Phenomenon*, Proc. I. R. E., Vol. 20, No. 12, pp. 481 and 482, March, 1933. Please give author, title, edition, volume, page, publisher and date of publication as indicated. Omission of one required fact causes much extra editorial work and possible inaccuracies. All references are grouped at the end of the article.

ILLUSTRATIONS: Illustrations should accompany manuscripts and each should always be referred to in the text, preferably by number. Drawings or graphs should not be larger than 12 × 16 inches, and must be made with jet black India Ink on white paper or tracing cloth, the latter being preferred. *Do not use typewriter for lettering.* The smallest lettering on 8 × 10 inch figures should be no less than 1/4 inch high. Cross-section paper (white with black lines) may be used, but should not have more than 4 lines per inch. If finer ruled paper is used, the major division lines should be drawn in with black ink, omitting the finer divisions In the case of finely ruled paper, only blue-lined paper can be accepted. *Tracing paper and blueprints* are not acceptable. Lettering and all markings must be large enough to be readable after reduction. Mail rolled or flat, never fold. Drawings that cannot be reproduced (including pencil drawings) will be returned to the author for redrawing, thus delaying publication of the paper. Photographs should be very distinct and show clear black and white contrasts. They must be on glossy white paper. Avoid round and oval photographs.

CAPTIONS AND LEGENDS: Legends or captions must accompany each drawing or photograph submitted If written on the drawing or photograph, they should be placed below and well outside the part to be reproduced. It is better to place them on separate sheets of paper pasted to the back of the drawings or photographs. Each table should have a caption such as Table 1, Table 2, Table 3, etc. Captions should be complete in themselves so as to make the data intelligible to the reader without reference to the text. A duplicate list of captions for figures should be included as the last page of the manuscript. Use "Fig. 1" (not Figure 1), Figs. 3 and 4, etc., in both the text and the numbering of illustrations. In the text, "Eq. (1)," or "Eqs. (1) and (2)" are preferable to "Equation (1)." In captions and legends, except for "Fig." and "Eq." and table headings, write all words in full; do not abbreviate. Avoid placing explanatory written matter in the drawings; it should be in the text.

MATHEMATICAL WORK: Only the simplest formulas should be typewritten; all others should be carefully written in pen and ink, the writing to be large enough so that ample room is provided to mark mathematical matter for the printer. A considerable space for marking should be allowed above and below all equations. All complicated equations should be repeated on separate sheets with plenty of space left for marking. The solidus should be used for simple fractions appearing within the text. Make all expressions clear to the typesetter. Greek letters used in formulas should be clearly designated by name on the margin of the manuscript. All symbols should be clearly written and carefully checked. The difference between capital and lower-case letters should be clearly distinguished and care taken to avoid confusion between zero (0) and the letter (o), between the numeral (one) and the letter (ell) and the prime ('), between alpha and a, kappa and k, u and mu, v and nu, n and eta. All subscripts and exponents should be clearly marked and dots and bars over letters or mathematical expressions should be avoided. Avoid complicated exponents and subscripts. When it is necessary to repeat a complicated expression, it should be represented by some convenient symbol.

NOMENCLATURE AND ABBREVIATIONS: The National Advisory Committee for Aeronautics Nomenclature should be used in preference to any others. Standard abbreviations should be used, and it should be noted that most abbreviations are lower case, such as m.p.h., b.m.e.p., i.hp., b.hp., hp., . . . etc.

# Index to Volume 10

## Journal of the Aeronautical Sciences

Numbers 1–8, January, 1943–October, 1943


No. 1, January, 1943, pages 1– 40
No. 2, February, 1943, pages 41– 72
No. 3, March, 1943, pages 73–104
No. 4, April, 1943, pages 105–136
No. 5, May, 1943, pages 137–168
No. 6, June, 1943, pages 169–200
No. 7, July, 1943, pages 201–232
No. 8, October, 1943, pages 233–326


Material that has appeared in the above volume has been indexed under a general subject heading and by author and has been further cross-indexed under various specialized subheadings.


ABBOT, C. G. The 1914 Tests of the Langley "Aerodrome". 31

**Aerodynamics—**

*Aerodynamic Performance of the Towed Glider*, Alexander Klemin and Walter C. Walling 185
*Aspect Ratio Corrections*, K. D. Wood 270
*Characteristics of Airfoils in a Cylindric Axial Flow Grid*, John R. Weske and Frank E. Marble 289
*On the Design of the Contraction Cone for a Wind Tunnel*, Hsue-Shen Tsien 68
*Flight Testing for Performance and Stability*, Edmund T. Allen 1
*Graphic Determination of Distance in Accelerated Airplane Motion*, G. A. Mokrzycki 36
*Induced Drag of a Twisted Wing*, H. W. Sibert 71
*The Influence of Sweep on the Spanwise Lift Distribution of Wings*, F. Theilheimer 101
*Letters to the Editor*
Foa, Joseph V 90
Gail, Albert 320
Klemin, Alexander 321
Nagel, Felix 199
Theilheimer, F 321
*Maneuverability Criteria Through Turning Performance*, John E. Goode, Jr 73
*A New Method of Longitudinal Control for Aircraft by Use of an Adjustable Angle of Attack Balance*, Roland J. White 152
*Regions of Infinite Acceleration and Flow Realms in a Compressible Fluid*, Max G. Scherberg 223
*Three-Dimensional Wing Flutter Analysis*, Alexander H. Flax 41
*Torsional and Aileron Flutter*, Zbigniew Krzywoblocki 161

Airfoils in a cylindric axial flow grid, characteristics of 289
Air-speed indicators, graphical analysis of delay of response in 91
ALLEN, EDMUND T. Flight Testing for Performance and Stability 1
Altimeter setting indicator 250
Aluminum-alloy columns and plates, buckling of 218
Aluminum alloy, 24S, elevated temperature aging of 180
Aluminum alloy, 24ST, effect of cold-work and heat-treatment on 86
Aspect ratio corrections 270

Bending strength in the plastic range 137
BERGEN, WILLIAM B. Experimental Investigations in Aircraft Dynamics 233
BLACK, SYDNEY D. Letter to the Editor (Propellers) 319
CAMPBELL, PAUL J. A Multiple Recording Manometer 313
CARSON, LEON D., WALTER R. MILES, AND S. S. STEVENS. Vision, Hearing, and Aeronautical Design 127
CARTER, RICHARD H. Letter to the Editor (Design) 208
——— Space Limitations and Optimum Conditions in Aircraft Spring Design 51
Climb calculations, rate of 48
COLMAN, PHILIP. Temperature Effects on Turbine Supercharger Installations 261
COLVIN, CHARLES H. Altimeter Setting Indicator 250
Compressible fluid, regions of infinite acceleration and flow realms in a 223
Constant-speed propellers, dynamics of 58
Control, longitudinal, for aircraft by use of an adjustable angle of attack balance, a new method of 152
Control systems, resonant electrical 285
COZZONE, FRANK P. Bending Strength in the Plastic Range 137
Cylinders, monocoque, general instability of 105

DEHAVEN, HUGH R., WILLIAM E. RUSSELL, AND JOHN R. ERWIN. Medical Research in Some Aspects of Aircraft Design 227
DEJUHASZ, KALMAN J. Graphical Analysis of Delay of Response in Air-Speed Indicators 91

**Design—**

*Letter to the Editor*
Carter, Richard H 208
*Medical Research in Some Aspects of Aircraft Design*, William E. Russell, John R. Erwin, and Hugh R. DeHaven 227
*A New Method of Longitudinal Control for Aircraft by Use of an Adjustable Angle of Attack Balance*, Roland J. White 152
*Space Limitations and Optimum Conditions in Aircraft Spring Design*, Richard H. Carter 51
*The 1914 Tests of the Langley "Aerodrome,"* C. G. Abbot 31
*Vision, Hearing, and Aeronautical Design*, Leon D. Carson, Walter R. Miles, and S. S. Stevens 127
DOMMASCH, DANIEL O. General Equations for the Analysis of Elliptical Rings 119

**Engines—**

*Letters to the Editor*
Manley, R. G. (Pendulum-Type Vibration Absorbers) 38
Shieh, A. H 135
*Temperature Effects on Turbine Supercharger Installations*, Philip Colman 261
ERWIN, JOHN R., WILLIAM E. RUSSELL, AND HUGH R. DEHAVEN. Medical Research in Some Aspects of Aircraft Design 227

FARRAH, JERE T. Problems of Routine Propeller Balancing ..... 209
FLAX, ALEXANDER H. Three-Dimensional Wing Flutter Analysis ..... 41
Flutter analysis, wing, three-dimensional ..... 41
Flutter, torsional and aileron ..... 161
FOA, JOSEPH V. Letter to the Editor (Aerodynamics) ..... 90
FULLER, FORREST B., AND TURE T. OBERG. Fatigue Characteristics of Natural and Resin-Impregnated, Compressed, Laminated Woods ..... 81

GAGGE, A. P., L. H. NEWBURGH, AND L. P. HERRINGTON. Limits of Human Heat Regulation ..... 197
GAIL, ALBERT. Letter to the Editor (Aerodynamics) ..... 320
Glider, towed, aerodynamic performance of the ..... 185
GOODE, JOHN E., JR. Maneuverability Criteria Through Turning Performance ..... 73
Graphic determination of distance in accelerated airplane motion ..... 36
GRAY, HAMILTON, AND RICHARD S. SMITH. Design-Strengthened Materials ..... 213

Helicopter performance, a method for rapid estimation of ..... 131
HERRINGTON, L. P., L. H. NEWBURGH, AND A. P. GAGGE. Limits of Human Heat Regulation ..... 197
HOFF, N. J. General Instability of Monocoque Cylinders ..... 105
HOLLEMAN, CLARENCE H. Tension Joints in Aircraft Structures ..... 295

**Instruments—**
*Altimeter Setting Indicator*, Charles H. Colvin ..... 250
*Graphical Analysis of Delay of Response in Air-Speed Indicators*, Kalman J. DeJuhasz ..... 91
*A Multiple Recording Manometer*, Paul J. Campbell ..... 313
*Resonant Electrical Control Systems*, David William Moore, Jr. ..... 285

KAMAN, CHARLES H. Aerodynamic Considerations of Rotors in Hovering and Vertical Climb Conditions ..... 201
KLEMIN, ALEXANDER. Letter to the Editor (Aerodynamics) 321
KLEMIN, ALEXANDER, AND WALTER C. WALLING. Aerodynamic Performance of the Towed Glider ..... 185
KOEGLER, RICHARD K., AND ARTHUR SCHNITT. Effects of Yielding and Perforations on a Wing Tension Surface ..... 273
KRZYWOBLOCKI, ZBIGNIEW. Torsional and Aileron Flutter 161
KUTSAY, A. Ü., AND A. J. YORGIADIS. On the Torsional Damping Capacity of Solid Magnesium-Alloy Rods as Affected by Cold-Working ..... 303

LANGHAAR, HENRY L. Buckling of Aluminum-Alloy Columns and Plates ..... 218
Langley "Aerodrome," 1914 tests of the ..... 31
Lift distribution of wings, spanwise, the influence of sweep on the ..... 101
LINCOLN, R. A., AND W. H. MATHER. Mechanical Properties of Austenitic Stainless Steels ..... 253

Magnesium-alloy rods, solid, as affected by cold-working, on the torsional damping capacity of ..... 303
Maneuverability criteria through turning performance ..... 73
MANLEY, R. G. Letter to the Editor (Pendulum-Type Vibration Absorbers) ..... 38
Manometer, a multiple recording ..... 313
MARBLE, FRANK E., AND JOHN R. WESKE. Characteristics of Airfoils in a Cylindric Axial Flow Grid ..... 289

**Materials—**
*Design-Strengthened Materials*, Richard S. Smith and Hamilton Gray ..... 213
*Effect of Cold-Work and Heat-Treatment on 24ST Aluminum Alloy*, Bruce Mitchell ..... 86
*Elevated Temperature Aging of 24S Aluminum Alloy*, Paul P. Mozley ..... 180
*Fatigue Characteristics of Natural and Resin-Impregnated, Compressed, Laminated Woods*, Forrest B. Fuller and Ture T. Oberg ..... 81
*Mechanical Properties of Austenitic Stainless Steels*, R. A. Lincoln and W. H. Mather ..... 253
*On the Torsional Damping Capacity of Solid Magnesium-Alloy Rods as Affected by Cold-Working*, A. Ü. Kutsay and A. J. Yorgiadis ..... 303
MATHER, W. H., AND R. A. LINCOLN. Mechanical Properties of Austenitic Stainless Steels ..... 253
**Medicine and Physiology—**
*Limits of Human Heat Regulation*, L. H. Newburgh, L. P. Herrington, and A. P. Gagge ..... 197
*Medical Research on Some Aspects of Aircraft Design*, William E. Russell, John R. Erwin, and Hugh R. DeHaven 227
*Vision, Hearing, and Aeronautical Design*, Leon D. Carson, Walter R. Miles, and S. S. Stevens ..... 127
MILES, WALTER R., LEON D. CARSON, AND S. S. STEVENS. Vision, Hearing, and Aeronautical Design ..... 127
MITCHELL, BRUCE. Effect of Cold-Work and Heat-Treatment on 24ST Aluminum Alloy ..... 86
MOKRZYCKI, G. A. Graphic Determination of Distance in Accelerated Airplane Motion ..... 36
Monocoque cylinders, general instability of ..... 105
MOORE, DAVID WILLIAM, JR. Resonant Electrical Control Systems ..... 285
MOZLEY, PAUL P. Elevated Temperature Aging of 24S Aluminum Alloy ..... 180
MYKLESTAD, N. O. Letter to the Editor (Propellers) ..... 319

NAGEL, FELIX. Letter to the Editor (Aerodynamics) ..... 199
NEWBURGH, L. H., L. P. HERRINGTON, AND A. P. GAGGE. Limits of Human Heat Regulation ..... 197

OBERG, TURE T., AND FORREST B. FULLER. Fatigue Characteristics of Natural and Resin-Impregnated, Compressed, Laminated Woods ..... 81
OTTEN, G. Rate of Climb Calculations ..... 48

**Performance—**
*Flight Testing for Performance and Stability*, Edmund T. Allen ..... 1
*Maneuverability Criteria Through Turning Performance*, John E. Goode, Jr ..... 73
*A Method for Rapid Estimation of Helicopter Performance*, Quentin Wald ..... 131
*Rate of Climb Calculations*, G. Otten ..... 48
**Propellers—**
*Dynamics of Constant-Speed Propellers*, Herbert K. Weiss 58
*Letters to the Editor*
Black, Sydney D ..... 319
Myklestad, N. O ..... 319
Rand, R. C ..... 320
*Problems of Routine Propeller Balancing*, Jere T. Farrah ..... 209
*A Tabular Method of Propeller Blade Stress Analysis*, Joseph Stuart, III ..... 115

RAND, R. C. Letter to the Editor (Propellers) ..... 320
Rings, elliptical, general equations for the analysis of ..... 119

**Rotary Wing Aircraft—**
*Aerodynamic Considerations of Rotors in Hovering and Vertical Climb Conditions*, Charles H. Kaman..... 201
*A Method for Rapid Estimation of Helicopter Performance*, Quentin Wald..... 131
RUSSELL, WILLIAM E., JOHN R. ERWIN, AND HUGH R. DEHAVEN. Medical Research in Some Aspects of Aircraft Design..... 227

SCHERBERG, MAX G. Regions of Infinite Acceleration and Flow Realms in a Compressible Fluid..... 223
SCHNITT, ARTHUR, AND RICHARD K. KOEGLER. Effects of Yielding and Perforations on a Wing Tension Surface.. 273
SHIEH, A. H. Letter to the Editor (Engines)..... 135
SIBERT, H. W. Induced Drag of a Twisted Wing..... 71
SMITH, RICHARD S., AND HAMILTON GRAY. Design-Strengthened Materials..... 213
Spring design, aircraft, space limitations and optimum conditions in..... 51
Stability and performance, flight testing for..... 1
Steels, austenitic stainless, mechanical properties of..... 253
STEVENS, S. S., LEON D. CARSON, AND WALTER R. MILES. Vision, Hearing, and Aeronautical Design..... 127
**Stress Analysis and Structures—**
*Bending Strength in the Plastic Range*, Frank P. Cozzone. 137
*Buckling of Aluminum-Alloy Columns and Plates*, Henry L. Langhaar..... 218
*Effects of Yielding and Perforations on a Wing Tension Surface*, Richard K. Koegler and Arthur Schnitt..... 273
*Experimental Investigations in Aircraft Dynamics*, William B. Bergen..... 233
*General Equations for the Analysis of Elliptical Rings*, Daniel O. Dommasch..... 119
*General Instability of Monocoque Cylinders*, N. J. Hoff.... 105
*Significance of the Secant and Tangent Moduli of Elasticity in Structural Design*, Don S. Wolford..... 169
*A Tabular Method of Propeller Blade Stress Analysis*, Joseph Stuart, III..... 115
*Tension Joints in Aircraft Structures*, Clarence H. Holleman..... 295
STUART, JOSEPH, III. A Tabular Method of Propeller Blade Stress Analysis..... 115
Supercharger installations, turbine, temperature effects on. 261

SZCZENIOWSKI, BOLESLAW. Contraction Cone for a Wind Tunnel..... 311

Tension joints in aircraft structures..... 295
THEILHEIMER, F. The Influence of Sweep on the Spanwise Lift Distribution of Wings..... 101
———— Letter to the Editor (Aerodynamics)... 321
TIFFORD, ARTHUR N. Wind-Tunnel Cooling..... 98
TSIEN, HSUE-SHEN. On the Design of the Contraction Cone for a Wind Tunnel..... 68

WALD, QUENTIN. A Method for Rapid Estimation of Helicopter Performance..... 131
WALLING, WALTER C., AND ALEXANDER KLEMIN. Aerodynamic Performance of the Towed Glider..... 185
WEISS, HERBERT K. Dynamics of Constant-Speed Propellers..... 58
WESKE, JOHN R., AND FRANK E. MARBLE. Characteristics of Airfoils in a Cylindric Axial Flow Grid..... 289
WHITE, ROLAND J. A New Method of Longitudinal Control for Aircraft by Use of an Adjustable Angle of Attack Balance..... 152
**Wind Tunnels—**
*Contraction Cone for a Wind Tunnel*, Boleslaw Szczeniowski..... 311
*On the Design of the Contraction Cone for a Wind Tunnel*, Hsue-Shen Tsien..... 68
*Wind-Tunnel Cooling*, Arthur N. Tifford..... 98
Wing flutter analysis, three-dimensional..... 41
Wings, the influence of sweep on the spanwise lift distribution of..... 101
Wing tension surface, effects of yielding and perforations on a..... 273
Wing, twisted, induced drag of a..... 71
WOLFORD, DON S. Significance of the Secant and Tangent Moduli of Elasticity in Structural Design..... 169
WOOD, K. D. Aspect Ratio Corrections..... 270
Woods, natural and resin-impregnated, compressed, laminated, fatigue characteristics of..... 81

YORGIADIS, A. J., and A. Ü. KUTSAY. On the Torsional Damping Capacity of Solid Magnesium-Alloy Rods as Affected by Cold-Working..... 303

# Services of the Aeronautical Archives of the Institute of the Aeronautical Sciences

The services of the Aeronautical Archives are available to all members of the Institute, to Corporate Members, to advertisers in the Aeronautical Engineering Review and, under usual library limitations, to the public. Four specialized services are available.

## The Paul Kollsman Library

This lending library service makes available, *without charge*, the latest and more important aeronautical books.

As far as the facilities permit, any person in the United States over 18 years of age who can furnish references which certify to his or her responsibility may become a member of the library.

Members may request the loan of any aeronautical or technical book they wish to borrow. Through an exchange agreement with the Engineering Societies Library, any book on general engineering may be borrowed from its great collection of over 160,000 volumes.

A photostating service is available at usual library rates.

Applications for membership in the library and further information will be sent on request.

## The Burden Reference Library

This reference library contains over 14,000 aeronautical books, magazines, pamphlets, photographs, reports, and clippings gathered from world-wide sources and is one of the most complete aeronautical libraries in the world. Material from this library is not available for loan but may be used for reference purposes at the Aeronautical Archives.

## The Pacific Aeronautical Library

6715 Hollywood Boulevard
Hollywood, California

Established in cooperation with the aircraft companies the library serves. The leading aircraft companies in or near Los Angeles participate in its support and operation.

This service library for aeronautical research is available to the public for reading privileges. Source material includes aerodynamic and structural research reports, as well as books on drafting, production methods, history, and allied sciences. It furnishes books, periodicals, and pamphlet material to the participating aircraft companies to supplement their engineering libraries.

## The Aeronautical Archives Technical Information Service

This service has experienced personnel under the supervision of trained aeronautical engineers to compile any information desired. The services range from listing specialized reference books to the preparation of exhaustive bibliographies, digesting of reports, and general surveys of any aeronautical subject. Some of the available services are:

Bibliographies on any aeronautical subject.
Reports on any aeronautical subject.
Digests of aeronautical books, papers, periodicals, and references.
Translations.
Engineering investigations of special aeronautical subjects.
Biographies of individuals engaged in aeronautics.
Photostats of any aeronautical or general engineering material.
Microfilms made on special order.
Photographs made from the Institute's photographic collection.
Drawings and tracings made.

In addition to the services mentioned any commission which comes within the scope of the Service will be accepted. Special arrangements may be made for work requiring several weeks or months.

Translators are available for accurate transcriptions of all foreign language data. Translations are carefully edited by trained engineers.

Reproductions of any material in the Aeronautical Archives of the Institute may be ordered at standard photostat rates.

INSTITUTE OF THE AERONAUTICAL SCIENCES
1505 RCA BUILDING WEST
30 ROCKEFELLER PLAZA, NEW YORK 20, N. Y.

L629.05
J82

# JOURNAL OF THE AERONAUTICAL SCIENCES

INSTITUTE OF THE AERONAUTICAL SCIENCES

GE JOHN CRERAR
OCT 27 1943
LIBRARY

VOLUME 10 OCTOBER, 1943 NUMBER 8

## CONTENTS

Experimental Investigations in Aircraft Dynamics . . . . . WILLIAM B. BERGEN 233
Altimeter Setting Indicator . . . . . CHARLES H. COLVIN 250
Mechanical Properties of Austenitic Stainless Steels . . . . . R. A. LINCOLN AND W. H. MATHER 253
Temperature Effects on Turbine Supercharger Installations . . . . PHILIP COLMAN 261
Aspect Ratio Corrections . . . . . K. D. WOOD 270
Effects of Yielding and Perforations on a Wing Tension Surface . . . . . RICHARD K. KOEGLER AND ARTHUR SCHNITT 273
Resonant Electrical Control Systems . . . . . DAVID WILLIAM MOORE, JR. 285
Characteristics of Airfoils in a Cylindric Axial-Flow Grid . . . . . JOHN R. WESKE AND FRANK E. MARBLE 289
Tension Joints in Aircraft Structures . . . . . CLARENCE H. HOLLEMAN 295
On the Torsional Damping Capacity of Solid Magnesium-Alloy Rods as Affected by Cold-Working . . . . . A. Ü. KUTSAY AND A. J. YORGIADIS 303
Contraction Cone for a Wind Tunnel . . . . . BOLESLAW SZCZENIOWSKI 311
A Multiple Recording Manometer . . . . . PAUL J. CAMPBELL 313
Letters to the Editor . . . . . 312, 317
Index to Volume 10 . . . . . 323

*Published Quarterly by the*

INSTITUTE OF THE AERONAUTICAL SCIENCES INC.

# JOURNAL OF THE AERONAUTICAL SCIENCES

VOL. 10 OCTOBER, 1943 NO. 8

PUBLISHED QUARTERLY BY THE INSTITUTE OF THE AERONAUTICAL SCIENCES INC.

*Chairman of the Editorial Board:* HUGH L. DRYDEN, *Chief of Mechanics and Sound Division, National Bureau of Standards*

*Editor:* ROBERT R. DEXTER *Manager:* JOSEPH J. MAITAN

The Institute of the Aeronautical Sciences publishes the JOURNAL OF THE AERONAUTICAL SCIENCES quarterly, in January, April, July, and October, and the AERONAUTICAL ENGINEERING REVIEW monthly.

The JOURNAL OF THE AERONAUTICAL SCIENCES prints papers of scientific and technical interest to Institute members and subscribers. In general, it provides an opportunity for specialists to publish articles disclosing new knowledge and new applications in the field of the aeronautical sciences. The JOURNAL restricts itself to the aeronautical aspects of advances in science and engineering, and papers printed have either been submitted directly to the JOURNAL or have been previously presented at a meeting of the Institute.

The AERONAUTICAL ENGINEERING REVIEW keeps members and subscribers informed regarding the contents of new books and current periodicals in the field of aeronautics. It reviews new developments in the aircraft industry and reports on progress from house organs and catalogues published by aircraft and engine manufacturers and other companies engaged in aeronautical activities. It publishes papers on applied engineering and aircraft production. News of Institute activities is published in the REVIEW.

Statements and opinions expressed in the JOURNAL are to be understood as individual expressions of the authors and not those of the Institute.

**SUBSCRIPTION RATES**

**Journal of the Aeronautical Sciences**
**Published Quarterly**

| United States and Possessions | | Foreign Countries Including Canada (American Currency Rates) | |
|---|---|---|---|
| 1 Year | $7.00 | 1 Year | $9.00 |
| Single Copies | 2.00 | Single Copies | 2.50 |

**Aeronautical Engineering Review**
**Published Monthly**

| United States and Possessions | | Foreign Countries Including Canada (American Currency Rates) | |
|---|---|---|---|
| 1 Year | $3.00 | 1 Year | $3.50 |
| Single Copies | 0.30 | Single Copies | 0.35 |

Notices of change of address should be sent to the Institute at least 30 days prior to actual change of address.

Manuscripts for publication, proofs, and all correspondence should be addressed to the Editorial Office of the JOURNAL.

Correspondence regarding subscriptions may be addressed to Publication Office, 20th and Northampton Sts., Easton, Pa., or to the Editorial Office of the JOURNAL OF THE AERONAUTICAL SCIENCES, 1505 RCA Building West, 30 Rockefeller Plaza, New York 20, New York.

Entered as Second-Class Matter at the Post Office, Easton, Pa., May 1, 1937. Acceptance for mailing at a special rate of Postage provided for in the Act of August 24, 1912. Authorized April 29, 1937.

# INSTITUTE of the AERONAUTICAL SCIENCES

*President*
HUGH L. DRYDEN

*Assistant to the President*
GEORGE R. FORMAN

*Vice-Presidents*
J. L. ATWOOD
ERNEST R. BREECH
SHERMAN M. FAIRCHILD
EARL D. OSBORN

*Past-Presidents*
J. C. HUNSAKER
CHARLES L. LAWRANCE
D. W. DOUGLAS
GLENN L. MARTIN
CLARK B. MILLIKAN
T. P. WRIGHT
GEORGE W. LEWIS
JAMES H. DOOLITTLE
FRANK W. CALDWELL
HALL L. HIBBARD

*Executive Vice-President*
BENNETT H. HORCHLER

*Secretary*
ROBERT R. DEXTER

*Treasurer*
ELMER A. SPERRY, JR.

*Controller*
JOSEPH J. MAITAN

## COUNCIL

LESTER D. GARDNER, *Chairman*

P. R. BASSETT
W. A. M. BURDEN
CHARLES H. COLVIN
R. T. GOODWIN
R. PAUL HARRINGTON
C. S. JONES
ROGER WOLFE KAHN
W. WALLACE KELLETT
JAMES H. KIMBALL
JOHN C. LESLIE
R. D. MACCART
ARTHUR NUTT

## ADVISORY BOARD

JOHN D. AKERMAN
LAWRENCE D. BELL
DON R. BERLIN
LYMAN J. BRIGGS
WILLIAM K. EBEL
JACK FRYE
P. G. JOHNSON
TH. VON KÁRMÁN
J. H. KINDELBERGER
F. K. KIRSTEN
PAUL KOLLSMAN
ARNOLD M. KUETHE
WILLIAM LITTLEWOOD
THOMAS A. MORGAN
RICHARD W. PALMER
W. A. PATTERSON
A. E. RAYMOND
F. W. REICHELDERFER
J. T. TRIPPE
J. G. VINCENT
E. P. WARNER

## HONORARY MEMBERS

H. H. ARNOLD
GRIFFITH BREWER
LYMAN J. BRIGGS
W. A. M. BURDEN
ARTEMUS L. GATES
HARRY F. GUGGENHEIM
J. C. HUNSAKER
ROBERT A. LOVETT
JOHN S. MCCAIN
GEORGE B. PEGRAM
GEORGE W. LEWIS
L. WELCH POGUE
D. C. RAMSEY
F. W. REICHELDERFER
T. P. WRIGHT

## HONORARY FELLOWS

A. CAQUOT
G. A. CROCCO
D. W. DOUGLAS
HUGH L. DRYDEN
W. F. DURAND
HUGO ECKENER
A. H. R. FEDDEN
J. C. HUNSAKER
B. MELVILL JONES
TH. VON KÁRMÁN
GEORGE W. LEWIS
GLENN L. MARTIN
GEORGE J. MEAD
LUDWIG PRANDTL
D. R. PYE
IGOR I. SIKORSKY
G. I. TAYLOR
ORVILLE WRIGHT

## BENEFACTOR MEMBERS

E. E. ALDRIN
HART O. BERG (Deceased)
E. L. CORD
D. W. DOUGLAS
SHERMAN M. FAIRCHILD
C. R. FAIREY
R. H. FLEET
FLORENCE GUGGENHEIM
C. D. HANSCOM
BELLA C. LANDAUER
GROVER LOENING
EDMUND C. LYNCH (Deceased)
F. W. MAGIN
PAUL KOLLSMAN
GLENN L. MARTIN
GEO. J. MEAD
S. A. REED (Deceased)
L. S. ROCKEFELLER
EDWARD P. WARNER

## AMERICAN FELLOWS

EDWIN E. ALDRIN
KARL ARNSTEIN
J. L. ATWOOD
RALPH S. BARNABY
P. R. BASSETT
REX B. BEISEL
G. M. BELLANCA
DON R. BERLIN
HENRY A. BERLINER
B. C. BOULTON
GEORGE W. BRADY
LYMAN J. BRIGGS
W. G. BROMBACHER
CHARLES P. BURGESS
FRANK W. CALDWELL
CHARLES H. CHATFIELD
ALLAN CHILTON
V. E. CLARK
CHARLES H. COLVIN
KARL T. COMPTON
JOHN W. CROWLEY, JR.
A. V. DE FOREST
RALPH S. DAMON
SMITH J. DE FRANCE
J. P. DEN HARTOG
WALTER S. DIEHL
J. H. DOOLITTLE
C. S. DRAPER
WILLIAM K. EBEL
C. L. EGTVEDT
FREDRIC FLADER
GARLAND FULTON
R. F. GAGG
LESTER D. GARDNER
RICHARD C. GAZLEY
MICHAEL E. GLUHAREFF
MELVIN N. GOUGH
LEROY R. GRUMMAN
R. M. HAZEN
ALBERT F. HEGENBERGER
S. D HERON
HALL L. HIBBARD
L. S. HOBBS
PAUL E. HOVGAARD
WILLIAM HOVGAARD
ROBERT INSLEY
EASTMAN N. JACOBS
CLARENCE L. JOHNSON
PAUL H KEMMER
J. H. KIMBALL
J. H. KINDELBERGER
ARTHUR L. KLEIN
ALEXANDER KLEMIN
W. B. KLEMPERER
PAUL KOLLSMAN
OTTO C. KOPPEN
S. M. KRAUS
I. MACHLIN LADDON
E. S. LAND
CHARLES L. LAWRANCE
JOHN G. LEE
CHARLES A. LINDBERGH
WILLIAM LITTLEWOOD
GROVER LOENING
R. D. MACCART
WM. H. MCAVOY
C. J MCCARTHY
RICHARD VON MISES
LESSITER C. MILBURN
CLARK B. MILLIKAN
ROBERT J. MINSHALL
JOSEPH S. NEWELL
ALFRED S. NILES
JOHN K. NORTHROP
ARTHUR NUTT
ROBERT R. OSBORN
W. BAILEY OSWALD
GEORGE A. PAGE, JR.
F. W. PAWLOWSKI
F. W. PENNOYER, JR.
A. A. PRIESTER
ARTHUR E. RAYMOND
F. W. REICHELDERFER
ELLIOTT G. REID
H. J. E. REID
H. C. RICHARDSON
C. E. ROSENDAHL
C.-G. ROSSBY
WILLIAM T. SCHWENDLER
MAC SHORT
IGOR ALEXIS SIKORSKY
ELMER A. SPERRY, JR.
HARRY A. SUTTON
WILLIAM B. STOUT
C. FAYETTE TAYLOR
EDWARD S. TAYLOR
PHILIP B. TAYLOR
TH. THEODORSEN
T. E. TILLINGHAST
S. TIMOSHENKO
STARR TRUSCOTT
L. B. TUCKERMAN
RALPH H. UPSON
EDWARD P. WARNER
W. W. WEBSTER
P. V. H. WEEMS
FRED E. WEICK
R. D. WEVERBACHER
JOHN B. WHEATLEY
ANDREW V. WILLGOOS
DONALD H. WOOD
ROBERT J. WOODS
T. P. WRIGHT
JOHN E. YOUNGER
ALBERT F ZAHM
STEPHEN J. ZAND

# *An Appreciation*

## TO CORPORATE MEMBERS OF THE INSTITUTE OF THE AERONAUTICAL SCIENCES

Listed below are the leading aeronautical and industrial companies who make possible the publication of the *Journal of the Aeronautical Sciences* and the *Aeronautical Engineering Review*.

They enable the Institute to publish scientific and technical papers in the *Journal* and to devote its pages exclusively to editorial material.

The *Aeronautical Engineering Review* provides technical articles and brief reviews of current aeronautical books, magazines, house organs, and government publications, thus saving the aeronautical engineer engaged in war work valuable time. Advertising defrays the editorial and publishing cost.

The above publications provide a source of comprehensive technical information for the benefit of the aeronautical profession and industry.

ACADEMY OF AERONAUTICS
ADEL PRECISION PRODUCTS CORPORATION
AERO INSURANCE UNDERWRITERS
AERO PARTS MANUFACTURING COMPANY
AERONAUTICAL PRODUCTS, INC.
AIRCRAFT ACCESSORIES CORPORATION
  AIRCRAFT ACCESSORIES CORPORATION OF MISSOURI
AIRCRAFT INDUSTRIES COMPANY
AIRCRAFT RADIO CORPORATION
AIRESEARCH MANUFACTURING COMPANY
  AIRESEARCH MANUFACTURING COMPANY OF ARIZONA, INC.
ALLIS-CHALMERS MANUFACTURING COMPANY
ALUMINUM COMPANY OF AMERICA
AMERICAN AIRLINES, INC.
AMERICAN BOSCH CORPORATION
THE AMERICAN ROLLING MILL COMPANY
AMERICAN TUBE BENDING COMPANY, INC.
ASSOCIATED AVIATION UNDERWRITERS
BAKER STEEL & TUBE COMPANY
BAUSCH & LOMB OPTICAL COMPANY
BEECH AIRCRAFT CORPORATION
THE BG CORPORATION
BELL AIRCRAFT CORPORATION
BENDIX AVIATION CORPORATION
  BENDIX AVIATION LTD.
  BENDIX PRODUCTS DIVISION
  BENDIX RADIO CORPORATION
  ECLIPSE-PIONEER DIVISION
  EXPORT DIVISION
  JULIEN P. FRIEZ & SONS DIVISION
  SCINTILLA MAGNETO COMPANY
BOEING AIRCRAFT COMPANY
BOEING SCHOOL OF AERONAUTICS
BOLTON MANUFACTURING CORPORATION
BOOTS AIRCRAFT NUT CORPORATION
BREEZE CORPORATIONS, INC.
  ESSEX TOOL & DIE COMPANY
  FEDERAL LABORATORIES, INC.
BREWSTER AERONAUTICAL CORPORATION
EDWARD G. BUDD MANUFACTURING COMPANY
CANADIAN PACIFIC AIR LINES LTD.
CESSNA AIRCRAFT COMPANY
CHANDLER EVANS CORPORATION
CHASE NATIONAL BANK OF THE CITY OF NEW YORK
THE CLEVELAND PNEUMATIC TOOL COMPANY
  AUTOMOTIVE-AIRCRAFT DIVISION
CONSOLIDATED VULTEE AIRCRAFT CORPORATION
  NASHVILLE DIVISION
  STINSON AIRCRAFT DIVISION
CONTINENTAL MOTORS CORPORATION
CULVER AIRCRAFT CORPORATION
CURTISS-WRIGHT CORPORATION
  AIRPLANE DIVISION
  PROPELLER DIVISION
  WRIGHT AERONAUTICAL CORPORATION
THE DENISON ENGINEERING COMPANY
DOAK AIRCRAFT COMPANY, INC.
DOUGLAS AIRCRAFT COMPANY, INC.
  EL SEGUNDO PLANT
  LONG BEACH PLANT
THE DOW CHEMICAL COMPANY
EASTERN AIR LINES, INC.
EATON MANUFACTURING COMPANY
EDO AIRCRAFT CORPORATION
ELASTIC STOP NUT CORPORATION OF AMERICA
THE ELECTRIC AUTO-LITE COMPANY
ELECTRO INCORPORATED
ENGINEERING AND RESEARCH CORPORATION
ETHYL CORPORATION
THE FAFNIR BEARING COMPANY
FAIRCHILD AVIATION CORPORATION
  FAIRCHILD AERIAL SURVEYS, INC.
FAIRCHILD ENGINE & AIRPLANE CORPORATION
  DURAMOLD AIRCRAFT CORPORATION
  FAIRCHILD AIRCRAFT DIVISION
  RANGER AIRCRAFT ENGINES DIVISION
FEDERAL TELEPHONE & RADIO CORPORATION
FIRESTONE AIRCRAFT COMPANY
FLEETWINGS DIVISION, KAISER CARGO, INC.
FLETCHER AVIATION CORPORATION
GENERAL AVIATION EQUIPMENT COMPANY, INC.
GENERAL ELECTRIC COMPANY
GENERAL INSTRUMENT CORPORATION
GENERAL MOTORS CORPORATION
  AC SPARK PLUG DIVISION
  AERORODUCTS DIVISION
  ALLISON DIVISION
  BUICK MOTOR DIVISION
  CADILLAC MOTOR CAR DIVISION
  CHEVROLET MOTOR DIVISION
  DELCO PRODUCTS DIVISION
  DELCO-REMY DIVISION
  EASTERN AIRCRAFT DIVISION
  FISHER BODY DIVISION
  FRIGIDAIRE DIVISION
  HARRISON RADIATOR DIVISION
  RESEARCH LABORATORIES DIVISION
  ROCHESTER PRODUCTS DIVISION
GENERAL TIRE & RUBBER COMPANY
THE B. F. GOODRICH COMPANY
THE GOODYEAR TIRE & RUBBER COMPANY
GRUMMAN AIRCRAFT ENGINEERING CORPORATION
GUIBERSON DIESEL ENGINE COMPANY
W. & L. E. GURLEY
HAMMOND AIRCRAFT COMPANY
HASKELITE MANUFACTURING CORPORATION
HAYES INDUSTRIES, INC.
HIGGINS AIRCRAFT, INC.
HUB INDUSTRIES, INC.
INTERCONTINENT AIRCRAFT CORPORATION
THE INTERNATIONAL NICKEL COMPANY
INTERSTATE AIRCRAFT & ENGINEERING CORPORATION
  WILSHIRE DIVISION
  EL SEGUNDO DIVISION
  DE KALB DIVISION
JACOBS AIRCRAFT ENGINE COMPANY
CASEY JONES SCHOOL OF AERONAUTICS, INC.
JORDANOFF AVIATION CORPORATION
KELLETT AIRCRAFT CORPORATION
KENYON INSTRUMENT COMPANY, INC.
KOLLSMAN INSTRUMENT DIVISION, SQUARE D COMPANY
LEAR AVIA, INC.
LOCKHEED AIRCRAFT CORPORATION
THE MARQUETTE METAL PRODUCTS COMPANY
THE GLENN L. MARTIN COMPANY
WARREN McARTHUR CORPORATION
McDONNELL AIRCRAFT CORPORATION
MENASCO MANUFACTURING COMPANY
MINNEAPOLIS-HONEYWELL REGULATOR COMPANY
MOORE DROP FORGING COMPANY
NASH-KELVINATOR CORPORATION
NATIONAL CITY BANK OF NEW YORK
NATIONAL MACHINE PRODUCTS
THE NATIONAL SCREW & MANUFACTURING COMPANY
NORMA-HOFFMANN BEARINGS CORPORATION
NORTH AMERICAN AVIATION, INC.
  NORTH AMERICAN AVIATION, INC., OF TEXAS
NORTHROP AIRCRAFT, INC.
NORTHWEST AIRLINES, INC.
OTTO AVIATION CORPORATION
PACKARD MOTOR CAR COMPANY
PAN AMERICAN AIRWAYS SYSTEM
THE PARKER APPLIANCE COMPANY
PHILLIPS PETROLEUM COMPANY
PIONEER PARACHUTE COMPANY, INC.
PRATT, READ & COMPANY, INC.
PUMP ENGINEERING SERVICE CORPORATION DIVISION, BORG-WARNER CORPORATION
THE PURE OIL COMPANY
REPUBLIC AVIATION CORPORATION
RIDGEFIELD MANUFACTURING CORPORATION, AIRCRAFT DIVISION
JOHN A. ROEBLING'S SONS COMPANY
ROHR AIRCRAFT CORPORATION
ROOSEVELT FIELD, INC.
SCOTT AVIATION CORPORATION
SHAKESPEARE PRODUCTS COMPANY
SHELL OIL COMPANY, INC.
SOCONY-VACUUM OIL COMPANY
SOLAR AIRCRAFT COMPANY
SPERRY GYROSCOPE COMPANY, INC.
STANDARD OIL COMPANY OF CALIFORNIA
STANDARD OIL COMPANY (INDIANA)
STANDARD OIL COMPANY OF NEW JERSEY
STEWART-WARNER CORPORATION
SUMMERILL TUBING COMPANY
SWEDLOW-AEROPLASTICS CORPORATION
SWITLIK PARACHUTE COMPANY
TELEFLEX LIMITED
THE TEXAS COMPANY
THOMPSON PRODUCTS, INC.
TRANSCONTINENTAL & WESTERN AIR, INC.
UNITED AIRCRAFT CORPORATION
  CHANCE VOUGHT AIRCRAFT DIVISION
  HAMILTON STANDARD PROPELLERS DIVISION
  PRATT & WHITNEY AIRCRAFT DIVISION
  PRATT & WHITNEY AIRCRAFT CORPORATION OF MISSOURI
  SIKORSKY AIRCRAFT DIVISION
UNITED AIR LINES TRANSPORT CORPORATION
UNITED-CARR FASTENER CORPORATION
UNITED STATES AVIATION UNDERWRITERS, INC.
UNITED STATES RUBBER COMPANY
  DOMINION RUBBER COMPANY, LTD.
UNIVERSAL MOULDED PRODUCTS CORPORATION
VEGA AIRCRAFT CORPORATION
WARNER AIRCRAFT CORPORATION
THE WEATHERHEAD COMPANY
WESTERN AIRLINES, INC.
WESTINGHOUSE ELECTRIC & MANUFACTURING COMPANY
WESTON ELECTRICAL INSTRUMENT CORPORATION
WHITING CORPORATION, AVIATION DIVISION
WOLVERINE TUBE DIVISION, CALUMET & HECLA CONSOLIDATED COPPER COMPANY
WYMAN-GORDON COMPANY

## EDITORIAL AND PROFESSIONAL ACTIVITIES COMMITTEE

HUGH L. DRYDEN, *Chairman*

### Aerodynamics

William Bollay
Walter S. Diehl
Hugh L. Dryden
P. R. Harrington
P. E. Hemke
Eastman N. Jacobs
Th. von Kármán
Alexander Klemin
W. B. Klemperer
Otto C. Koppen
A. M. Kuethe
John G. Lee
John R. Markham
Clark B. Millikan
Richard von Mises
Shatswell Ober
W. Bailey Oswald
Manfred Rauscher
H. J. E. Reid
Benjamin F. Ruffner
G. B. Schubauer
Abe Silverstein
R. H. Smith
Th. Theodorsen
M. J. Thompson
Starr Truscott
Michael Watter
K. D. Wood

### Air Transport

Charles Froesch
Melvin N. Gough
J. A. Herlihy
William Littlewood
A. A. Priester
Paul E. Richter
N. F. Scudder

### Aircraft Design

Karl Arnstein
Rex B. Beisel
B. C. Boulton
C. P. Burgess
C. H. Chatfield
J. W. Crowley, Jr.
R. C. Gazley
Leroy R. Grumman
Hall L. Hibbard
A. L. Klein
Montgomery Knight
Otto C. Koppen
I. M. Laddon
John G. Lee
C. J. McCarthy
William H. Miller
R. H. Prewitt
Igor I. Sikorsky
E. A. Stalker
Th. Troller
Starr Truscott
R. H. Upson
Fred B. Weick
Robert J. Woods
T. P. Wright

### Aircraft Production

John L. Atwood
W. E. Beall
Ralph Damon
Carl de Ganahl
W. K. Ebel
Fredric Flader
Hall L. Hibbard
Guy A. Luburg
C. J. McCarthy
A. E. Raymond
W. T. Schwendler
Harry A. Sutton
John Tjaarda
Robert J. Woods
T. P. Wright

### Radio

C. S. Draper
Lloyd Espenschied
C. G. Fick
Lewis M. Hull
Haraden Pratt
F. X. Rettenmeyer

### Physiologic Problems

H. G. Armstrong
Louis H. Bauer
David B. Dill
Eugene Du Bois
W. Randolph Lovelace, II
Ross A. McFarland
A. D. Tuttle

### Power Plants and Propellers

M. A. Biot
George W. Brady
Frank W. Caldwell
Ivan H. Driggs
Louis H. Enos
David Gregg
L. S. Hobbs
Albert R. Jacobs
Carleton Kemper
H. M. McCoy
W. C. Nelson
Arthur Nutt
Shatswell Ober
David R. Shoults
C. Fayette Taylor
E. S. Taylor
Th. Theodorsen
A. V. Willgoos
D. H. Wood

### Structures and Materials

M. A. Biot
C. P. Burgess
George W. DeBell
A. V. de Forest
Paul D. Ffield
Richard C. Gazley
W. C. Geer
J. P. Den Hartog
N. J. Hoff
Zay Jeffries
Th. von Kármán
E. E. Lundquist
C. J. McCarthy
C. F. Nagel, Jr.
J. S. Newell
Alfred S. Niles
Thomas D. Perry
W. Ramberg
F. R. Shanley
H. W. Sibert
S. Timoshenko
George Tweney
J. A. Wise
J. E. Younger

### Meteorology

C. F. Brooks
Karl O. Lange
D. M. Little
E. J. Minser
Sverre Petterssen
F. W. Reichelderfer
A. F. Spilhaus
P. V. H. Weems
H. C. Willett

### Education

R. P. Harrington
C. S. Jones
Alexander Klemin
Montgomery Knight
Clark B. Millikan
W. C. Nelson
George B. Pegram
R. H. Smith
E. A. Stalker
Ben D. Wood

### Fuels and Oils

D. P. Barnard
A. L. Beall
J. H. Doolittle
Graham Edgar
Luis de Florez
R. Goodwin
Raymond Haskell
S. D. Heron
A. M. Rothrock
D. H. Young

### Instruments

P. R. Bassett
W. G. Brombacher
Charles H. Colvin
C. S. Draper
Lucien L. Friez
Walter McKay
W. A. Reichel
C. F. Savage
A. F. Spilhaus
S. J. Zand

---

## I.A.S. REPRESENTATIVES TO OTHER ORGANIZATIONS

*Aeronautical Chamber of Commerce of America*—CHARLES MARCUS
*American Association for the Advancement of Science*—J. C. HUNSAKER
*American Institute of Mining & Metallurgical Engineers*—A. V. DE FOREST
*American Society of Mechanical Engineers*—JOHN E. YOUNGER
*American Standards Association*—P. R. BASSETT
*Greater New York Safety Council*—WILLIAM LITTLEWOOD
*Daniel Guggenheim Medal Board of Award*—CHARLES H. COLVIN, LESTER D. GARDNER, ELMER A. SPERRY, JR.
*Institute of Radio Engineers*—L. M. HULL
*Manufacturers Aircraft Association*—J. T. HARTSON
*National Aeronautic Association*—WILLIAM P. REDDING
*National Safety Council*—JEROME LEDERER
*National Research Council Engineering Division*—FRANK W. CALDWELL
*New York Museum of Science and Industry*—LESTER D. GARDNER
*Society of Automotive Engineers*—EDWARD P. WARNER

# INSTITUTE *of the* AERONAUTICAL SCIENCES
## 1932–1943

Since its incorporation in October, 1932, as a scientific membership society to advance the art and science of aeronautics, the Institute of the Aeronautical Sciences, in over ten years of service to aviation, has become the representative technical society for the aviation industry and profession. It is the only organization in the United States which brings together all of the sciences and branches of engineering and technology which are applied to aeronautics.

### Activities

In this year, coincident with the great increase in aeronautical production and research in the nation's war effort, the Institute is expanding its membership and activities in keeping with the greater demands made upon its services. Beginning with aeronautical students, the Institute has increased the number and activities of Student Branches. Members of the Institute in aeronautical centers are organized in local Sections which hold their own meetings. More of these Sections are being formed this year and additional services provided for members. The Annual Meeting and other national meetings provide forums where specialists in all the aeronautical sciences may present and receive reports on progress made in their particular fields and learn of developments in other fields that have a bearing on their own work. All meetings are held with proper safeguards to prevent any unauthorized publicizing of important information. Several annual awards and honors are conferred by the Institute to recognize and encourage outstanding achievement in the aeronautical sciences.

### Publications

Papers presented at meetings or submitted to the Editorial Board are published in the Institute's two publications—the JOURNAL OF THE AERONAUTICAL SCIENCES and the AERONAUTICAL ENGINEERING REVIEW. The JOURNAL prints in each issue several full length scientific papers on new research and developments in various fields applied to aviation. The REVIEW keeps members and subscribers up to date on aeronautical news and literature through reviews of new books and periodical articles, government publications and trade literature and publishes papers on applied engineering and aircraft production.

### Research Facilities

Through the Aeronautical Archives of the Institute, members have for their use the most complete aeronautical library and reference research facilities maintained by any technical society. At Institute headquarters in New York, the W. A. M. Burden Reference Library of books, reports and periodicals, the Aeronautical Index of subject files, biographic files and bibliography, and the historical and art collections in the Archives are available for study. The Pacific Aeronautical Library at 6715 Hollywood Boulevard, Los Angeles, maintains a reference collection and reading room for members and loans books to company libraries in the area. Through the Paul Kollsman Library, aeronautical books are lent by mail without charge to members anywhere in the continental United States. In addition to a very complete collection of standard aeronautical reference works, the Kollsman Library has available for loan new aviation books as they are reviewed in the AERONAUTICAL ENGINEERING REVIEW.

### Membership

In addition to membership in professional societies representing their particular fields, specialists applying their knowledge and experience to aeronautics find membership in the Institute of great value in the contacts made with others engaged in aeronautical work and in the broad coverage of all aeronautical problems furnished through its meetings and publications. All applications for membership are carefully reviewed by the Admissions Committee, which recommends the grade of membership for which the applicant is found eligible. There are advanced grades of membership—Associate Fellow, Fellow, Honorary Fellow—to which members may be elected as their experience warrants. Thus, a member receives due recognition—more valuable because it is given by his colleagues—for his contributions to the progress of aeronautics. New applicants may be elected initially by the Admissions Committee to the grade of MEMBER if they are engineering graduates with at least three years of experience or have had over five years' experience in research, engineering, or other special work applied to aviation; to the grade of Industrial Member if they have acquired a recognized standing in an administrative capacity in the aviation industry; to the grade of Technical Member if they are recent engineering school graduates or are engaged in technical aeronautical work. For those interested or engaged in aeronautics or fields related to aeronautics who wish to participate in the activities of the Institute, the grade of Affiliate is provided. Student Members are admitted by application through Student Branches organized at their schools. Aeronautical companies, as well as individuals, are affiliated with, and participate in, the support of the Institute through Corporate Membership.

### Dues

An entrance fee of $5.00 is required of all new members who apply for admission to a grade of membership to be specified by the Admissions Committee (Corporate Members, Student Members, and those who apply specifically for the grade of Affiliate being excepted).

Annual membership dues for the various grades of membership are as follows: Fellows—$15; Associate Fellows—$11; MEMBERS—$9.00; Industrial Members—$9.00; Technical Members—$5.00; Affiliates—$5.00.

The regular subscription price for the JOURNAL OF THE AERONAUTICAL SCIENCES and the AERONAUTICAL ENGINEERING REVIEW is $7.00 and $3.00 per year, respectively. Members may subscribe to the JOURNAL or the REVIEW or both at one-half the regular subscription rates.

Those who are engaged in aeronautical work or who have an interest in any technical phase of aviation will find the services of the Institute to be a necessary aid in keeping abreast of developments in these times of such rapid progress. An application form and further information about membership can be obtained from an Institute member or by writing to the Secretary.

INSTITUTE OF THE AERONAUTICAL SCIENCES
1505 RCA BUILDING WEST
30 ROCKEFELLER PLAZA
NEW YORK 20, N. Y.